Measurement of incoherently produced J/ψ polarisation in ultra-peripheral Pb–Pb collisions with ALICE and characterisation of the Muon Forward Tracker

Lucrezia Camilla Migliorin

THÈSE de DOCTORAT DE
L'UNIVERSITÉ CLAUDE BERNARD LYON 1

Ecole Doctorale : N°52
Physique et Astrophysique (PHAST)

Discipline : Physique des Particules

Soutenue publiquement le 29/11/2022, par :
Lucrezia Camilla Migliorin

Mesure de la polarisation des J/ψ incohérents en collisions Pb–Pb ultra-périphériques avec ALICE et caractérisation du Muon Forward Tracker

Devant le jury composé de :

ARNALDI Roberta Chercheuse, Università e INFN di Torino	**Examinatrice**
AUGIER Corinne Professeure des Universités, IP2I Lyon	**Présidente du jury**
BASTID Nicole Professeure des Universités, LPC Clermont	**Rapporteuse**
CHESHKOV Cvetan DR-HDR, CNRS, IP2I Lyon	**Directeur de thèse**
PANEBIANCO Stefano Matthias DR-HDR, CEA Saclay	**Rapporteur**
URAS Antonio CR, CNRS, IP2I Lyon	**Co-Directeur de thèse**

Our freedom to doubt was born out of a struggle against authority in the early days of science. It was a very deep and strong struggle: permit us to question — to doubt — to not be sure. I think that it is important that we do not forget this struggle and thus perhaps lose what we have gained.

— Richard Feynman

Alla mia famiglia.

Remerciements

VOGLIO iniziare questa tesi nella mia lingua per ringraziare mia mamma e mio papà per avermi dato la possibilità di fare tutto ciò che ho sempre voluto fino al raggiungimento di questo traguardo cosi importante per me. E voglio anche ringraziare la mia famiglia iniziando nonno Armando, nonna Assunta, zia Lucia e zio Ivano che mi sono sempre vicini anche se ora non ci vediamo più cosi spesso. Senza di loro, che mi hanno sempre ascoltato e aiutato non sarei mai arrivata a questo giorno.

Je veux dans la suite remercier l'équipe ALICE qui m'a donné la possibilité de faire ma thèse au sein de leur équipe. Merci surtout à Cvetan et Antonio pour avoir accepté d'être mes encadrants au cours de la thèse et d'avoir eu la patience de m'aider avec mon analyse qui n'a pas été toujours très facilement compréhensible. Un grand merci à Brigitte qui a été toujours la maman du groupe et je ne peux pas oublier Sarah, Robin et Yanchun qui ont partagé avec moi cette aventure.

Je veux aussi remercier chaleureusement Nicole et Stefano d'avoir accepté d'être mes rapporteurs. Entre les membres du jury je veux aussi remercier du plus profond de mon cœur Roberta pour avoir été si disponible et bienveillante et Corinne, la meilleure présidente du jury de l'UCBL.

La pandémie a changé le sujet de ma thèse mais je ne peux pas oublier toutes les personnes avec qui j'ai travaillé lors de la caractérisation du MFT. Tout d'abord Max, grazie per tutto. C'est sûrement grâce à toi que j'ai pu continuer mon parcours dans la Collaboration ALICE. Merci pour m'avoir acceptée en stage et de m'avoir appris plein de choses. Une autre personne qui sera toujours dans mon cœur est Raphael. La vie parfois nous fait prendre des décisions qui nous éloignent des autres mais t'avoir vu assister a ma soutenance a été le meilleur cadeau de thèse que tu aurais pu m'offrir. Après il y a ma chère Andry, avec qui j'ai galéré en installant O2 mais on s'est toujours amusées ensemble. Stefano ancora tu! Grazie per essermi stato vicino anche quando

avevo i capelli blu! Merci à Charlotte pour avoir patiente avec moi quand il y avait des erreurs dans le remplissage des tests et d'être venue à ma thèse. Après un dernier merci a toute l'équipe de Nantes surtout un gros câlin virtuel a Rita, Maxime et Guillaume.

J'ai eu la possibilité en étant représentante des doctorant.e.s et des membres non-permanents de côtoyer beaucoup de monde dans l'IP2I a partir de la direction. Merci a Anne et Jacques pour avoir été toujours bienveillants vers moi, Sylvie et Dany pour m'avoir fait confiance dans mon rôle au sein du labo et du conseil de l'ED, Bruno et Clément pour tout leur aide et leur gentillesse, Viola pour sa sympathie et ses conseils. Entre les doctorant.e.s il y a des personnes spéciales qui seront toujours dans mon cœur : Leo pour tout ce qu'on a vécu ensemble, Denis, JB et Phil qui sont devenus mes petits amis du cœur, Elisa, Marco et Giulia qui m'ont amené en Italie lors de nos conversations parce que notre pays est le meilleur, mon Amelie chérie, Laurita et Quentin pour avoir partage plein de ragots avec moi et tout.e.s les autres qui ont toujours été la.

Et enfin, je veux remercier mes ami.e.s! La liste est longue mais j'essaie d'aller vite. Flami, Arabella, Giulia C., Giulia P. e Ylenia, le mie amiche di sempre. La mejor familia latina que una italiana de Latina podría tener: mis Nutrias queridas ! Sofi , grazie per aver avuto il coraggio di leggere tutte queste pagine. Mis hermanas Sol y Ines por el amor tan grande que me dan cada día. Quiero darles las gracias a Diego y Brissa que estuvieron conmigo los días anteriores a mi soutenance . Mi familia colombiana: un besito grande por todo el cariño que dieron en Medallo. Pau y Manuel por la buenas vibras que me mandaron desde Colombia. Les Soutes pour les petites visios-ragots. Ana y Adri por su amistad tan bonita. Eddy por haber corregido mis errores de gramática.Et soyez pas tristes si j'oublie quelqu'un.

Lyon, 29 Novembre 2022 L. C. M.

Abstract

THE primary goal of the ALICE experiment at the CERN LHC is to investigate and characterise the Quark-Gluon Plasma (QGP), a deconfined state of quarks and gluons, created in ultra-relativistic collisions of heavy nuclei. The heavy-ion beams at the LHC are sources of strong flux of quasi-real photons and thus provide a unique possibility to study also photo-induced interactions. These studies are usually performed in Ultra-Peripheral Collisions (UPC), in which the impact parameter is larger than the sum of the nuclear radii and the hadronic interactions are suppressed. The J/ψ vector meson is a bound state of charm and anti-charm quarks. Its photo-production is sensitive to the gluon contents of the target nucleus. The J/ψ meson is produced coherently when the incident photon interacts with the nucleus as a whole. In this case, its spin is expected to inherit the polarisation of the photon. This is known as *s*-channel helicity conservation (SCHC). The incoherent production of J/ψ results from interactions between the photon and a single nucleon inside the nuclear target. It can be accompanied by nucleon dissociation. The measurement of the polarisation of incoherently produced J/ψ allows to investigate possible deviations from the SCHC and eventually the dependence on the momentum transfer of the interaction. It has been performed using a large sample of Pb–Pb UPC collisions at $\sqrt{s_{\mathrm{NN}}} = 5.02$ TeV collected by the ALICE experiment in 2015 and 2018. The results are compatible with pure transverse polarisation of incoherent J/ψ and also with the corresponding results for coherent J/ψ. They are consistent with the SCHC scenario, although possible momentum-transfer dependence of the polarisation can not be excluded.

The physics programme of the LHC continues with Runs 3 and 4. All the experiments have upgraded or will upgrade their detector systems. In ALICE, one of the major upgrades is the installation of a new silicon detector, placed in front of the muon spectrometer, called Muon Forward Tracker (MFT). Thanks to its about thousand large pixel sensors, the MFT will add vertex-determination capacity to the muon arm and thus significantly enrich the physics programme of the experiment. Calibration work has been done studying the analog and digital components of the sensor chips. The detector configuration has been studied in order to optimize the signal-to-noise ratio. The MFT has been entirely characterised and a detailed map of the dead and noisy pixels has

been produced. Several parameter sets have been tested with the aim to improve and to streamline the data flux from the detector.

Key words: polarisation, ALICE, J/ψ, ultra-peripheral collisions, silicon tracker

Résumé

L'objectif principal de l'expérience ALICE au LHC du CERN est d'étudier et de caractériser le plasma des quarks et gluons (PQG), un état déconfiné de quarks et de gluons, créé lors de collisions ultra-relativistes de noyaux lourds. Les faisceaux d'ions lourds au LHC sont des sources de flux intense de photons quasi-réels et offrent ainsi une possibilité unique d'étudier également les interactions photo-induites. Ces études sont généralement réalisées dans les collisions ultra-périphériques, dans lesquelles le paramètre d'impact est supérieur à la somme des rayons nucléaires des deux noyaux en collision et les interactions hadroniques sont supprimées. Le méson vecteur J/ψ est un état lié des quarks charmé et anti-charmé. Sa photoproduction est sensible au contenu en gluons du noyau cible. Le méson J/ψ est produit de manière cohérente lorsque le photon incident interagit avec le noyau dans son ensemble. Dans ce cas, son spin devrait hériter de la polarisation du photon. Ceci est connu sous le nom de conservation de l'hélicité du canal-s (SCHC). La production incohérente de J/ψ résulte des interactions entre un photon et un nucléon à l'intérieur du noyau cible. Elle peut s'accompagner d'une dissociation du nucléon. La mesure de la polarisation du J/ψ produit de manière incohérente permet d'étudier les déviations possibles par rapport au SCHC et éventuellement la dépendance de l'interaction avec le transfert d'impulsion. Elle a été réalisée à partir d'un large échantillon de collisions Pb–Pb ultra-périphériques à $\sqrt{s_{\mathrm{NN}}} = 5.02$ TeV collectées par l'expérience ALICE en 2015 et 2018. Les résultats sont compatibles avec une polarisation purement transverse pour les J/ψ cohérents et incohérents. Ils sont compatibles avec le scénario SCHC, bien qu'une éventuelle dépendance de la polarisation avec le transfert d'impulsion ne puisse être exclue.

Le programme de physique du LHC se poursuit avec les prises de données des Runs 3 et 4. Toutes les expériences ont mis ou mettront à niveau leurs systèmes de détection. Dans ALICE, l'une des améliorations majeures est l'installation d'un nouveau détecteur en silicium, placé devant le spectromètre à muons, appelé Muon Forward Tracker (MFT). Grâce à un millier de capteurs à pixels, le MFT ajoutera une capacité de détermination de vertex au bras muon et enrichira ainsi considérablement le programme de physique de l'expérience. Des travaux d'étalonnage ont été effectués en étudiant les composants analogiques et numériques des puces du capteur. La configuration du détecteur a été étudiée afin d'optimiser le rapport signal sur bruit. Le MFT a été en-

tièrement caractérisé et une carte détaillée de l'état des pixels a été réalisée. En outre, plusieurs jeux de paramètres ont été testés dans le but d'améliorer et d'organiser le flux de données provenant du détecteur.

Mots clefs : polarisation, ALICE, J/ψ, collisions ultra-périphériques, trajectographe en silicium

Sintesi

L' obiettivo principale dell'esperimento ALICE, istallato nell'LHC del CERN è quello di studiare e caratterizzare il Plasma di Quark e Gluoni (PQG), stato *deconfinato* dei quark e dei gluoni, creato grazie alle collisioni ultra-relativistiche degli ioni pesanti. I fasci di ioni pesanti dell'LHC possono essere considerati come delle sorgenti di fotoni quasi-reali ed offrono una possibilità unica per lo studio delle interazioni foto-indotte. Questo tipo d'interazioni può essere studiato soprattutto grazie alle collisioni ultra-periferiche, nelle quali il parametro d'impatto è superiore alla somma dei raggi nucleari dei due nuclei incedenti alla collisione e le interazioni adroniche sono quasi completamente nulle. Il mesone vettore J/ψ è uno stato composto da un quark charm e un antiquark charm. La foto-produzione di questo mesone è collegata alla presenza del gluone nel nucleo *bersaglio*. Quando il fotone incidente interagisce con tutto il nucleo, chiamato nucleo *bersaglio*, è prodotto in maniera coerente. In questo caso, ci si aspetta che lo spin del J/ψ possieda la stessa polarizzazione del fotone. Questo fenomeno è noto come elicità del canale-s (SCHC). La produzione è detta incoerente quando emerge dall'interazione tra un fotone e un nucleone contenuto nel nucleo bersaglio. Questo fenomeno può essere accompagnato dalla dissociazione del nucleone stesso dal nucleo. La misura della polarizzazione del mesone J/ψ prodotto in maniera incoerente permette di studiare le possibili deviazioni dalla teoria del SCHC e di, eventualmente, mettere in luce la dipendenza dell'interazione dal trasferimento dell'impulso. Questa misura è stata realizzata grazie ad un grande campione di collisioni Pb-Pb ultra-periferiche, a $\sqrt{s_{\mathrm{NN}}} = 5.02$ TeV, ottenuto dall'esperimento ALICE nel 2015 e nel 2018. I risultati sono compatibili con una polarizzazione esclusivamente trasversa sia per i mesoni J/ψ coerenti, che per quelli incoerenti. Questi risultati sono compatibili con lo scenario di SCHC, sebbene non è stato possibile escludere nessuna dipendenza tra la polarizzazione e il trasferimento dell'impulso.

Il programma di fisica dell'LHC continua grazie ai periodi di acquisizione dei dati dei Run 3 e 4. Tutti i grandi esperimenti hanno migliorato o miglioreranno i loro sistemi di rilevazione. Nell'esperimento ALICE, uno dei cambiamenti più importati è stato l'installazione di un nuovo rivelatore in silicio, collocato davanti allo spettrometro a muoni, chiamato Muon Forward Tracker (MFT). Grazie al suo migliaio di sensori a pixel, il rivelatore MFT aumenterà la capacità di determinare il vertice di produzione dello

spettrometro arricchendo, in maniera considerevole, il programma di fisica dell'esperimento. Diverse misure di calibrazione sono state effettuate, studiando in maniera accurata le componenti analogiche e numeriche dei pixel situati nel sensore. La configurazione del rivelatore è stata studiata per ottimizzare il rapporto segnale-rumore. Il rivelatore MFT è stato completamente caratterizzato e una mappa dettagliata dello stato dell'arte dei pixel è stata prodotta. In aggiunta, diversi parametri sono stati studiati per migliorare ed organizzare il flusso di dati provenienti dal rivelatore.

Parole chiave: polarizzazione, ALICE, J/ψ, collisioni ultra-periferiche, tracker in silicio

Resumen

El objetivo principal del experimento ALICE, situado en el LHC del CERN, es estudiar y caracterizar el plasma de quark-gluones (QGP), fase deconfinada de los quarks y de los gluones, creado gracias a las colisiones ultra-relativistas entre los iones pesados. Los haces de iones pesados del LHC pueden ser considerados como una fuente de fotones casi-reales y ofrecen una posibilidad única para estudiar las interacciones foto-inducidas. Ese tipo de interacciones puede ser estudiada gracias a las colisiones ultra-periféricas en las cuales el parámetro de impacto es superior a la suma de los radios nucleares entre los dos núcleos incidentes a la colisión y las interacciones hadrónicas son casi completamente nulas. El mesón vector J/ψ es un estado compuesto de un quark charm y un antiquark charm. La foto-producción de este mesón está conectada con la presencia de un gluon en el núcleo *blanco*. El mesón J/ψ es creado en manera coherente cuando el fotón incidente interactúa con todo el núcleo blanco. En este caso, el espín del J/ψ tendría que tener la misma polarización del fotón. Este fenómeno es conocido como helicidad del canal-*s* (SCHC). La producción es llamada incoherente cuando surge de la interacción entre un fotón y un nucleón contendido en el núcleo blanco. Este fenómeno puede ser acompañado de la disociación del nucleón mismo en el núcleo. Las medidas de polarización del mesón J/ψ creado en manera incoherente permiten estudiar las desviaciones posibles de la teoría de SCHC y de, eventualmente, poner de relieve una dependencia de la interacción con la transferencia del momento. Esta medida ha sido realizada gracias a una gran cantidad de colisiones Pb-Pb ultra-periféricas, a $\sqrt{s_{\mathrm{NN}}} = 5.02$ TeV, obtenida en 2015 y en 2018 por el experimento ALICE. Los resultados son compatibles con una polarización exclusivamente transversa con respeto a las muestras coherente e incoherente. Estos resultados son compatibles con el escenario de SCHC, aunque no ha sido posible excluir ninguna dependencia entre la polarización y la transferencia del momento.

El programa de física del LHC continúa gracias a periodos de adquisición de datos (Runs 3 y 4). Todos los grandes experimentos han mejorado o mejorarán sus sistemas de detección. En el experimento ALICE, uno de los cambios más importantes ha sido la instalación de un nuevo detector en silicio, situado al frente del espectrómetro a muones, llamado Muon Forward Tracker (MFT). Gracias a su millar de sensores de

pixeles, el detector MFT aumentará la capacidad de determinar el cumbre de producción del espectrómetro, enriqueciendo de manera considerable el programa de física del experimento. Diferentes medidas de calibración han sido realizadas, estudiando de manera precisa los componentes analógicos y digitales de los pixeles situados en el sensor. La configuración del detector ha sido estudiada para optimizar la relación entre señal y ruido. El detector MFT ha sido completamente caracterizado y un mapa detallado del estado del arte de los pixeles ha sido producido. Adicionalmente, diferentes parámetros han sido estudiados para mejorar y organizar el flujo de datos provenientes del detector.

Palabras claves: polarización, ALICE, J/ψ, colisiones ultra-periféricas, tracker en silicio

Contents

Synthèse en français

Chapitre 1 : Du modèle standard au plasma de quark et gluons

Les collisions d'ions lourds visent à mieux comprendre la matière hadronique, en particulier dans des conditions de densité énergétique extrême. En effet, la Chromodynamique Quantique – théorie qui explique le fonctionnement de la force nucléaire forte – prédit une transition de la matière hadronique vers un état déconfiné : le plasma de quarks et de gluons (PQG), même si on ne connaît pas encore la nature et l'ordre de cette phase de transition. Cet état de la matière nucléaire aurait été celui de l'Univers quelques micro-secondes après le Big Bang mais nous supposons qu'il existe aujourd'hui uniquement au cœur des étoiles à neutrons.

Toutefois, grâce aux progrès scientifiques du dernier siècle, un PQG peut être répliqué à une échelle infiniment plus petite, en collisionnant des noyaux lourds accélérés à des vitesses ultra-relativistes au sein d'accélérateurs de particules tels que le *Super Proton Synchrotron* (SPS, CERN, Genève, Suisse), le *Relativistic Heavy Ion Collider* (RHIC, *Brookhaven National Laboratory*, New York, États-Unis) ou encore le *Large Hadron Collider* (LHC, CERN, Genève, Suisse). Quand la température et la densité d'énergie sont suffisamment élevées pour produire un changement de phase, les quarks et les gluons ne sont plus confinés au sein des hadrons mais évoluent librement. Avant la collision, les ions lourds – qui sont en réalité des noyaux privés de tous leurs électrons – peuvent être représentés par deux disques plats, perpendiculaires à la direction du faisceau à cause de la contraction de Lorentz. Au moment de la collision, des multiples interactions ont lieu en créant un système qui se trouve dans une phase de pré-équilibre où les collisions inélastiques peuvent éventuellement conduire à une thermalisation du système. Lorsque la densité d'énergie dans un volume donné est assez importante, un état déconfiné apparaît en formant un PQG sur une échelle de taille de l'ordre de 10 fm et avec une durée de l'ordre de 10 fm/c. Avec le refroidissement du système, les quarks

et les gluons se recombinent pour former des hadrons qui seront mesurés au sein des détecteurs de l'expérience.

À cause de la durée de vie extrêmement courte du PQG, aucune observation directe ne peut être réalisée et ses propriétés doivent être extraites à partir des particules à l'état final qui sont détectées par l'expérience. Les particules qui caractérisent la création d'un état déconfiné sont dites observables et on en différencie deux types principaux : les sondes molles et les sondes dures. Les premières correspondent à des interactions associées à des impulsions relativement faibles et sont les plus abondamment produites. Elles reflètent les propriétés globales de la collision et fournissent des informations sur la collectivité et ses propriétés. Les secondes sont produites à larges impulsions pendant les premiers instants de la collision. Parmi celles-ci, on y retrouve les quarkonia, comme le méson J/ψ.

Chapitre 2 : Les collisions ultra-périphériques

Entre tous les types d'interaction qu'on peut produire lors des collisions ultra-relativistes d'ions lourds, on retrouve les collisions ultra-périphériques (CUP), caractérisées par un paramètre d'impact plus grand que la somme des deux rayons des noyaux. Dans ce type de collision, on produit principalement des mésons vecteurs (comme le méson J/ψ), lors de l'interaction d'un photon γ issu d'un noyau avec l'autre noyau, appelé cible. Durant ces interactions, le photon peut interagir avec le noyau tout entier et on dit, alors, qu'il s'agit d'un processus *cohérent*, ou avec un seul nucléon du noyau, formant ainsi des mésons vecteurs produits de manière *incohérente*.

La photo-production de mésons vecteurs dans les collisions ultra-périphériques offre également une possibilité unique de mesurer la fonction de distribution des gluons dans le noyau et de mettre en lumière un phénomène physique aussi important que la saturation des gluons.

Chapitre 3 : L'expérience ALICE au CERN

Le plus grand et le plus puissant accélérateur de particules au monde se trouve à la frontière franco-suisse, appelé LHC. Avec ses 27 km de diamètre et sa position à 100 m sous le sol, grâce à un système cryogénique et un puissant champ magnétique, il permet de produire un grand nombre de collisions lorsque les deux faisceaux, circulant dans des directions opposées et contenant des paquets d'environ 200 millions d'ions de Pb, ren-

trent en collision jusqu'à 4000 fois par seconde. Il y a quatre grandes expériences au LHC et la seule qui se dédie à l'étude des collisions d'ions lourds pour caractériser le PQG est ALICE, qui signifie justement "expérience sur un grand collisionneur d'ions".

Composée d'une vingtaine de détecteurs de tailles différentes, elle est constituée d'une partie centrale et d'un spectromètre à muons à rapidité à l'avant. Dans ce manuscrit de thèse on s'intéresse à l'étude des J/ψ produits de manière incohérente qui se désintègrent en dimuon et donc, le détecteur le plus utilisé dans cette analyse est le spectromètre à muons, situé à rapidité avant ($-4 < \eta < -2{,}5$) et permettant de mesurer les muons émis avec un angle polaire $171° < \theta < 178°$ par rapport à l'axe du faisceau. Il est composé d'un absorbeur frontal, de 10 plans de détection regroupés deux par deux dans 5 chambres proportionnelles multifilaires, d'un aimant dipolaire autour de la troisième station et d'un déclencheur à muons précédé d'un filtre à muons.

Chapitre 4 : L'analyse de la polarisation des J/ψ incohérentes en collisions Pb–Pb ultra-périphériques

Les CUP offrent un terrain de recherche très singulier, car, lors de ces collisions, il est possible d'étudier des phénomènes physiques particuliers comme la polarisation. Le photon qui entre en jeu pour la création d'un méson vecteur est polarisé et il est donc légitime de se demander si les particules produites le seront aussi. Lors d'une désintégration en deux corps, comme celle du J/$\psi \longrightarrow \mu^+\mu^-$, la distribution angulaire des muons produits, exprimée en termes des angles polaire et azimutal dans le centre de masse du méson vecteur J/ψ parent, reflète la polarisation de ce méson. L'analyse de cette distribution permet de mesurer les paramètres de polarisation ($\lambda_\theta, \lambda_\varphi, \lambda_{\theta\varphi}$) et déterminer si le méson J/ψ est polarisé transversalement, longitudinalement ou n'est pas polarisé.

L'analyse menée pendant cette thèse est basée sur les données colletées par l'expérience ALICE pendant les collisions Pb–Pb du *Run* 2 du LHC en 2015 et 2018. La stratégie suivie pour analyser ces données est la suivante : on définit une série de *bins* associée à des variables angulaires, on crée des spectres de masse invariante pour chacun de ces *bins*, on extrait le nombre de J/ψ trouvés dans chaque *bin* grâce à des *fits*, on ajuste les spectres en impulsion transverse (p_T) et rapidité (y), obtenus par une simulation Monte-Carlo (MC) et, enfin, on trouve les paramètres de polarisation.

Pour sélectionner les données associées à des CUP, une série de coupures a été appliquée, en incluant une sélection sur les *triggers*. Une production MC avec un spectre

en p_{T} plat a été générée entre 0 et 2,5 GeV/c. Pour sélectionner les J/ψ produits de manière incohérente, on prend les données reconstruites avec un $p_{\mathrm{T}} > 0{,}35$ GeV/c. Les spectres de masse invariante ont été *fittés* avec une double fonction *Crystal Ball* pour le J/ψ et le ψ' et trois fonctions ont été testés pour mieux décrire le fond.

Une fois les spectres de masse invariante obtenus, les spectres de p_{T} et de y simulés grâce à la méthode MC ont été soumis une procédure d'ajustement. Finalement, en utilisant la méthode appelée *template fit*, on a réussi à extraire les paramètres de polarisation en partant de la distribution angulaire générée $W(\cos\theta, \varphi)$. La procédure du *template fit* a été validée et les résultats ont donc pu être obtenus.

Chapitre 5 : Résultats de l'analyse de la polarisation des J/ψ incohérents en collisions Pb–Pb ultra-périphériques

LES résultats sur la polarisation des J/ψ produits de manière incohérente ont été obtenus après une étude approfondie des effets systématiques. Quatre sources d'erreurs systématiques ont été identifiées et calculées. Ces sources sont dues aux variations de la façon dont les *fits* de la masse invariante sont effectués sur les données qui constituent le fond; à la simulation imparfaite de la réponse de *trigger* du muon à très bas p_{T}; à l'incertitude dans l'ajustement des spectres p_{T} et y en MC; à la présence de polarisation dans MC.

Afin de vérifier si les résultats ne sont pas affectés par une contamination significative du fond, une série de tests a été produite. Ces études nous ont permis de conclure qu'il n'y a aucune contamination significative provenant des collisions hadroniques. L'unique source d'erreur systématique qui pourrait être ajoutée est celle générée par la décroissance des J/ψ et ψ' produits de manière cohérente, même s'il s'agirait d'une erreur systématique négligeable.

La simulation MC, qui a été produite pour cette analyse, a été comparée avec une autre simulation MC générée avec le générateur `STARlight` , utilisée dans les analyses de production de particules créées de manière cohérente en CUP. Les résultats sont comparables, ce qui permet de valider encore une fois la méthode du *template fit* et la production MC correspondante.

Les résultats, obtenus grâce à cette analyse, nous ont permis de conclure que les J/ψ produits de manière incohérente sont polarisés transversalement. Ainsi, ces résultats sont entièrement compatibles avec ceux obtenus pour les mésons J/ψ cohérents.

Même si cette concordance entre les résultats cohérents et incohérents laisse entrevoir une absence de dépendance du transfert d'impulsion de la cible nucléaire, une telle dépendance ne peut être exclue du fait des incertitudes expérimentales importantes.

Chapitre 6 : Le futur d'ALICE : les nouveaux *upgrades* pour les Runs 3 et 4 du LHC

QUAND le LHC atteindra son maximum en termes d'énergie et de luminosité, l'expérience ALICE aura besoin de nouveaux détecteurs capables de collecter un flux de données plus important et d'améliorer sa résolution. Le cœur du détecteur a été changé, en utilisant des pixels de silicium plus performants.

Cette technologie a été employée aussi pour la création d'un tout nouveau trajectographe qui est nécessaire pour améliorer la reconstruction spatiale de l'expérience ALICE, en exploitant les informations sur les vertex de production, positionné devant le spectromètre à muons, le *Muon Forward Tracker* (MFT), conçu et calibré à l'IP2I de Lyon[1]. Le programme de physique du MFT se focalise sur la dynamique des *quarkonia*, la thermalisation des quarks lourds et leur perte d'énergie au sein du PQG, la physique de la beauté et l'étude de la brisure de symétrie chirale et sa restauration *via* les mesures de vecteurs de basse masse. Le MFT va permettre d'exploiter pleinement l'intervalle cinématique du spectromètre à muons en faisant face à plusieurs de ses limitations intrinsèques. Il consiste en deux demi-cônes, placés le long du tube-faisceau, avec chacun de ces demi-cônes constitué de cinq demi-disques.

Les capteurs choisis se basent sur la technologie *CMOS*[2] qui présente des caractéristiques intéressantes en termes de granularité, d'épaisseur du matériau, de vitesse de lecture, de consommation de puissance et de résistance aux radiations, en intégrant à la fois le volume de détection et l'électronique de lecture sur un unique composant et permettant, ainsi, l'optimisation de la surface entre le volume sensible et l'électronique.

[1] La conception, la réalisation technique et l'installation du MFT a été réalisée grâce a la collaboration de differents instuts francais de physique. lL'IN2P3 a mobilisé trois de ses laboratoires l'IP2I à Lyon, le LPC à Clermont-Ferrand et Subatech à Nantes pour réaliser une importante partie de ses éléments. Des dizaines de scientifiques et technicien·nes de 14 institutions à travers le monde ont participé à ce projet dont l'IN2P3 et l'Irfu au CEA.

[2] *Complementary Metal Oxide Semiconductor.*

Chapitre 7 : Calibration et caractérisation du MFT pendant le *commissioning* en surface

AFIN de connaître les performances que le MFT aura pendant la prise de données, une série de tests a été réalisée pour qualifier le détecteur sur sa surface active. Chaque capteur a été soumis à cinq tests de caractérisation, en testant les parties digitale et analogique contenues dans chaque capteur. Les niveaux de consommation du courant ont été contrôlés tout le long des tests et 929 senseurs sur les 936 installés sur le détecteur MFT ont été validés. Grâce à l'ajustement de deux paramètres DAQ qui font partie du circuit électrique placé dans chaque pixel, on arrive à avoir une surface active qui enregistre tous les signaux qui dépassent les 100 électrons, en obtenant de cette manière un seuil de détection homogène. On a identifié les pixels *CMOS* les moins performants afin de les masquer pendant l'acquisition pour ne pas compromettre la qualité des données collectées.

Un long travail d'analyse sur les résultats de performance de capteurs a été réalisé, il en découle que le détecteur MFT est efficace à plus de 99%. Il pourra donc reconstruire de manière fiable les trajectoires des particules chargées avant leur passage dans l'absorbeur du spectromètre à muons.

Introduction

FROM the beginning of time, Humans have had an innate need to understand, explore and control the Nature up to the Cosmos. The physics has the objective to study the matter and its behaviour, on a scale from the microscopic to the extremely large.

But the history of physics suggests that it is false to believe that we will eventually discover a limited set of equations that cannot be refuted by experiment. Each established theory eventually reveals its limitations and gets incorporated into a broader theory. Despite the fact that there are no perfect theories, capable of explaining "everything" today, there are two that accurately explain the fundamental building blocks of matter: the Standard Model of particle physics and Quantum Chromodynamics.

We were able to comprehend and observe in the lab a matter state in which quarks and the gluons, the building blocks of hadrons, are free. According to the widely recognised "Big Bang" theory, during the first microseconds following the formation of our Universe, nuclear matter was in a state known as Quark-Gluon Plasma (QGP) a in which the quarks and gluons were deconfined. This excited and highly hot and dense state of matter is created in the lab in the largest particle accelerators in the World – as the LHC at CERN – by means of ultra-relativistic heavy ion collisions.

To investigate the QGP in ultra-relativistic heavy ion collisions, it is essential to recognise and understand the initial conditions, global dynamics, and available energy density. The measurement of global variables, such as the number of charged particles created by a collision or the event's centrality, is fundamental. In addition, the QGP's brief lifetime limits its direct observation. To examine its characteristics, one must be interested in the experimental signatures left in the final state by the production of a medium so dense and hot. One of the most important observable is the J/ψ meson, formed by a $c\bar{c}$ pair.

This Ph.D. work is based on the study of incoherent J/ψ polarisation in Ultra-Peripheral Collisions (UPC). This kind of collisions, when the impact parameter b is $b > R_1 + R_2$,

where R_1 and R_2 are the radii of the two nuclei. These mesons have been studied in their dimuon channel, reconstructed by the Muon Spectrometer of ALICE experiment. The majority of the figures presented in the analysis will be published in an ALICE Collaboration article.

Despite the excellent results obtained by the ALICE Collaboration during the first two Runs of LHC, a series of new detectors has been designed and installed to increase the quality of the data collected. One of these new detectors is the Muon Forward Tracker installed in front of the Muon Spectrometer, to increase the tracking before the selection of the muons in the muons chambers. The qualification and the calibration of this detector have been also studied during this three years of Ph.D. thesis.

This manuscript is organised into seven chapters and provides a summary of the work accomplished over the last three years. Each begins with a recall of the table of contents and concludes with a list of bibliographical references cited in the text.

1. **Chapter 1 : From the Standard Model to the Quark-Gluon Plasma**

   This chapter provides a theoretical and experimental context for the physics examined in this research. Consequently, one can find an explanation of the theory of strong interaction, the QGP, as well as a brief description of the associated experimental probes. In addition, the motivations for using heavy ion collisions are further upon. Finally, the dynamics and physical repercussions resulting from such collisions are described briefly.

2. **Chapter 2 : Ultra-Peripheral Collisions and polarisation measurements**

   This chapter gives an overview of the physics relevant for the UPC and a detailed review of the previous results obtained by different experiments is presented.

3. **Chapter 3 : ALICE experiment at the LHC**

   The environment in which this Ph.D. work was performed is described here. It provides details on the LHC and the ALICE experiment and its working environment. All the subdetectors are briefly described, in particular on the Muon Spectrometer, which reconstructed the data used in the analysis. This makes it possible to clearly define the experimental context of this work.

4. **Chapter 4 : J/ψ polarisation in Pb–Pb collisions**

   In this chapter, the polarisation phenomenon is explained and one can find all the procedure followed to extract the polarisation parameters, needed to characterised the J/ψ mesons polarisation. In particular, all the steps of the analysis are detailed to better understand how the data-set was prepared for interpretation of results.

5. **Chapter 5 : Results on J/ψ polarisation in Pb–Pb collisions analysis**

   This chapter described the results obtained during the analysis. In addition, there is a description of any systematic errors that have been identified. This chapter ends with the interpretation of the results.

6. **Chapter 6 : The ALICE future : the new upgrades for LHC Runs 3 and 4**

   In chapter, the scientific program of upgrades, developed by the ALICE Collaboration, is described. In particular, all attention is paid on a new silicon detector called Muon Forward Tracker (MFT), which is described and all its expected physics performances are reported.

7. **Chapter 7 : MFT calibration and qualification during the commissioning on surface**

   In the last chapter of this thesis, there is a description of all the tests that have been created to calibrate and qualify the MFT detector during surface commissioning. The last part describes a selection of the results obtained in order to give an opinion on this new detector.

1 From the Standard Model to the Quark-Gluon Plasma

If I have seen further than others,
it is because I am surrounded by dwarfs.
Murray Gell-Mann (1929 – 2019)

Contents

THE study of the Quark-Gluon Plasma (QGP), a deconfined state of hadronic matter, allows one to investigate how the Universe was like around few micro-seconds after the Big Bang, when the Universe was very hot and filled with a "primordial soup" of deconfined quarks and gluons, before expanding and cooling down converting it self in the ordinary hadronic state, organized in complex structures like atoms, stars, planets, and even human beings.

Thanks to the collisions of ultra-relativistic heavy-ions, lab experiments, like the ALICE experiment, located in the LHC, can study the QGP matter state where a QGP fireball can be generated. These experiments are conducted to investigate and describe the properties of this hot and dense phase of hadronic matter.

In this Chapter, the main concepts of QGP physics will be shortly reviewed.

1.1 The Standard Model of particle physics

THE Standard Model (SM) of particle physics is the theory providing the best description (as of today) of the interactions between fundamental particles — outside gravity. The SM was conceived in the second half of the XX century and proved, in the mid-1970s, with experimental confirmation of quarks existence [1] or the most recent proof of top quark (in 1995 [2]) and tau neutrino (in 2000 [3]) existence. The last piece of the SM was discovered in 2012 when CMS [4] and ATLAS [5] experiments observed the Higgs boson [6, 7], which was theoretically predicted by R. Brout, F. Englert, P. Higgs, G. S. Guralnik, C. R. Hagen and T. W. B. Kibble in 1964 [8, 9]. This discovery confirmed the validity of the SM theory, which is now commonly accepted as the most accurate theoretical framework for the electro-weak and strong interactions.

The SM separates the fundamental matter constituents, all of them being *fermions*, into two categories: *quarks* and *leptons*. Particles which are sensitive to the same forces are classified according to a specific family and each force is exerted *via* the exchange of a mediator *boson*. Both lepton and quark categories contain six particles that can be grouped in three pairs (families), as shown in Figure 1.1. All fermions have a half-integer spin of $^1/_2$ and respect the Pauli exclusion principle. For each fermion, there is an opposite-charge particle, called *antiparticle*.

What substantially differentiates a lepton from a quark is the fact that the latter has one additional charge, called "colour" charge, which will be described in more detail in

Section 1.2.

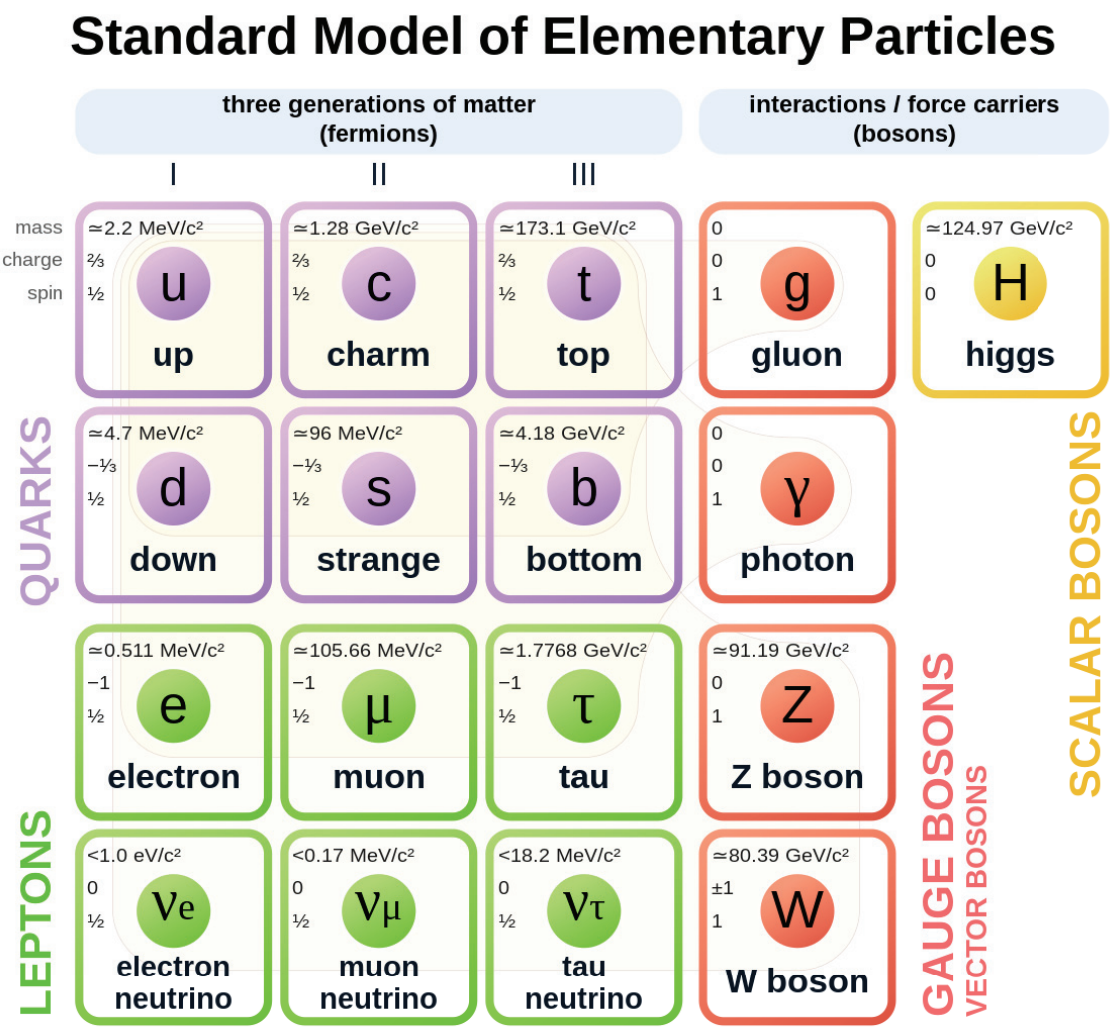

FIGURE 1.1. Standard Model of elementary particles: the 12 fundamental fermions, 5 gauge bosons and the Higgs boson in yellow. Brown loops indicate which bosons (red) couple to which fermions (purple and green), from [10].

Let us see how the SM is composed, starting from the fermions, described in green and purple groups in Figure 1.1. The first family [1] contains the lighter and more stable particles, whereas the second and third families include the heavier and more unstable ones. Second and third generation particles all decay into first family particles, hence, do not constitute the bulk of *ordinary matter*.

As already mentioned, three out of the four fundamental forces, represented by their

[1] 1st quark family : up and down. 1st lepton family : electron and electron neutrino.

corresponding mediator bosons (marked in red in Figure 1.1), are included in the SM: the *electromagnetism*[2], the *weak*[3] force and the *strong*[4] force.

The Higgs boson is a SM element in its own right, the only identified scalar boson. It is represented in yellow in Figure 1.1. It is the mediator of the Higgs field, responsible for the mass of the known elementary particles.

From a mathematical point of view, the SM is a gauge-invariant theory with 19 free parameters[5] [11] and $SU(3) \times SU(2) \times U(1)$ gauge group[6]. It is renormalizable and theoretically self-consistent, and provides predictions in many contexts of elementary physics, but does not account for *gravity*, the fourth fundamental force.

Despite its immense and ongoing success in predicting experimental results, however, the SM left several unexplained phenomena even beyond the aforementioned problem of gravity. For this reason, a significant number of models, called *Beyond the Standard Model* theories, such as the super-symmetry [12] or the string theory [13], have been proposed to broaden the scope of the SM. For some of these approaches, the ultimate goal is to develop a theory capable of explaining our world, including general relativity, addressing the limitations of the SM to reach the so-called theory of everything [14].

1.2 QCD formalism and its characteristics

THE QCD theory [15] etymology is derived from the Greek word $\chi\rho\hat{\omega}\mu\alpha$, meaning colour. Indeed, the fundamental symmetry of QCD is colour [16] symmetry. Extraneous to the everyday meanings of colour and charge, the colour charge has three fundamental values: red, blue and green. Together with these "values", the corresponding anti-colour charges must also be considered: anti-red, anti-blue and anti-green. In the following Sections, the basic concepts of the QCD will be shortly discussed.

[2] The electromagnetic force boson is the photon, which is massless.

[3] For the weak force, 3 different massive bosons have been identified : Z^0, W^+ and W^-.

[4] The gluons carry the colour charge and they are identified as the mediator gauge bosons of the strong force. More information about the gluons is reported in Section 1.2.

[5] The neutrino masses are assumed to be zero in this scenario. The model number of free parameters grows when including non-zero neutrino masses.

[6] Quantum field theories are formalized as gauge theories, using local symmetry groups, taking the form of complex Lie groups each underlying the modeled gauge symmetries. Thereby : QED has made it possible to describe *electromagnetism* within the framework of an abelian gauge theory with the unitary group $U(1)$; the *weak* interaction is described with the unitary special group $SU(2)$ and, so, the *electroweak* interaction is described with the gauge group $SU(2) \times U(1)$; QCD is done with the $SU(3)$ group. Finally, the SM is developed with the gauge group $SU(3) \times SU(2) \times U(1)$.

1.2.1 QCD matter

QUARKS are, as of today, the most fundamental constituents of nuclear matter and carry a fraction of the elementary electrical charge. Due to the confinement mechanism which characterises the strong interaction, quarks and their "glue", the gluon bosons (carriers of the strong interaction), are not directly detectable with experimental techniques. Quarks and gluons combine together to form more complex particles, known as *hadrons*, having a neutral color charge and being thus experimentally detectable. Characterised by different masses and lifetimes, hadrons are divided into two principal groups :

- **mesons**, composed of a pair of quark-antiquark ($q\overline{q}$), like the J/ψ meson ($c\overline{c}$) relevant for the analysis presented in this Ph.D. thesis.
- **baryons**, composed of a triplet of quarks (or antiquark). The most common baryons are the protons (uud) and the neutrons (udd).

Aside from mesons and baryons, other types of hadrons have been identified, including the so-called tetraquark[7] and pentaquark[8] states. These exotic particles, however, are not the "normal" constituents of the hadronic matter, that surrounds us.

If one wants to find a state of matter in which quarks and gluons are free and not "confined" together in hadronic structures, the temperatures and densities studied have to been chosen to be different from normal ones, that's to say extremely high. This phase is the Quark-Gluon Plasma (QGP) [19], and can be created at high temperature or net baryonic density. This state of matter dominated the Universe a few microseconds after the Big Bang [20]. To give the proper context to the study of the QGP, it is convenient to discuss the features of the strong force, as described in the SM by Quantum-Chromo-Dynamics (QCD).

1.2.2 QCD formalism

AS just said, quarks may exist in six distinct "colour"[9] states. The introduction of the colour quantum number is based on empirical evidence. Indeed, some baryons, as

[7] The first tetraquark discovered is $Z(4430)$, which is a mesonic resonance, found by the Belle experiment [17].

[8] Only two pentaquark states have been discovered $P_c^+(4380)$ and $P_c^+(4450)$, by LHCb Collaboration [18].

[9] 3 colour and 3 anti-colour states.

Δ^{++}, which has a spin of $^3/_2$ and is made up of three u quarks in the same spin state, would violate the Pauli exclusion principle, if an extra colour quantum number was not supplied: the quarks of these particles all have identical quantum numbers apart from that of colour. This concepts apply, among others, to the following particles:

$$\Delta^{++} = (uuu)\,, \qquad \Delta^{-} = (ddd)\,, \qquad \Omega^{-} = (sss)\,.$$

Mathematically speaking, the existence of the colour quantum number is described by the Lie group $SU(3)_c$ [21], a special unitary group of degree 3, suited to describe colour invariance (the index c stands for "colour").

Gluons are defined as vector fields and their colour charge is a combination of colour and anticolour, for example red and antigreen:

$$\begin{cases} (r\bar{b}+b\bar{r})/\sqrt{2} & -i(r\bar{b}-b\bar{r})/\sqrt{2} \\ (r\bar{g}+g\bar{r})/\sqrt{2} & -i(r\bar{g}-g\bar{r})/\sqrt{2} \\ (b\bar{g}+g\bar{b})/\sqrt{2} & -i(b\bar{g}-g\bar{b})/\sqrt{2} \\ (r\bar{r}-b\bar{b})/\sqrt{2} & (r\bar{r}+b\bar{b}-2g\bar{g})/\sqrt{6}. \end{cases}$$

Gluons form a colour octet represented by 3×3 Hermitian Gell-Mann matrices, having a zero trace [22].

Let us see, in more detail, the dynamics that governs quarks and gluons. The gauge-invariant QCD Lagrangian ($\mathscr{L}_{\mathrm{QCD}}$) is the following one:

$$\mathscr{L}_{\mathrm{QCD}} = \sum_f \bar{\psi}_f \left(i\gamma^\mu D_\mu - m_f\right)\psi_f - \frac{1}{4}G^a_{\mu\nu}G^{\mu\nu}_a, \tag{1.1}$$

where the index f indicates a sum over quark flavours and a index represents the eight gluons; ψ is the quark field, a dynamical function of spacetime, in the fundamental representation of the $SU(3)$ gauge group [23]; m_f is the mass of the quark with flavour f and D_μ is the gauge covariant derivative [24], which takes the form :

$$D_\mu = \delta_\mu - i\, g A^a_\mu t^a, \tag{1.2}$$

where g is the bare QCD coupling; A^a_μ are the eight gluon fields and $t^a = \frac{1}{2}\lambda^a$ are the generators of $SU(3)$. Combining equations 1.1 and 1.2, the QCD Lagrangian is equal to:

$$\mathscr{L}_{\mathrm{QCD}} = \sum_f \bar{\psi}_f \left(i\delta_\mu\gamma^\mu - m_f\right)\psi_f + \sum_f \bar{\psi}_f g A^a_\mu t^a \psi_f - \frac{1}{4}G^a_{\mu\nu}G^{\mu\nu}_a. \tag{1.3}$$

- The term $\sum_f \bar{\psi}_f \left(i\delta_\mu \gamma^\mu - m_f\right)\psi_f$ comes from Dirac's equation. It represents the Lagrangian of a free fermion of mass m, represented by the field $\psi(t,\vec{r})$.
- The element $\sum_f \bar{\psi}_f g A^a_\mu t^a \psi_f$ is the Yukawa coupling term [25], that describes the interaction of the quark field with the gluons. The t^a is expressed from the Gell-Mann matrices [22]: $t^a = \lambda^a/2$.
- Finally, the $G^a_{\mu\nu}$ is the gluon field tensor written as $G^a_{\mu\nu} = \left(\delta_\mu A^a_\nu - \delta_\nu A^a_\mu + g f^{abc} A^b_\mu A^c_\nu\right)$ [26], where the coefficients f^{abc} are the structure constants of $SU(3)$ and g is the bare coupling constant of the strong interaction. The first part of $G^a_{\mu\nu}$ is the $\left(\delta_\mu A^a_\nu - \delta_\nu A^a_\mu\right)$ that describes the propagation of gluon fields – analogue to Quantum-Electro-Dynamics (QED) *i.e.* the gluon kinematics.

  The term $\left(g f^{abc} A^b_\mu A^c_\nu\right)$ derives from QCD's non-Abelian nature and translates the capacity of gluons to interact with one another.

The main difference between QED and QCD is the fact that photons have no electric charge, while gluons have a colour charge. This property of the gluon, the coupling of the colour field with itself, is at the origin of confinement and makes it impossible to detect quarks and gluons as free particles.

1.2.3 The coupling constant α_s

THE mathematical framework of QCD theory needs a renormalization due to some divergences that appear in the calculations. In fact, each interaction must be renormalized by the quantum fluctuations, which are of two kinds: the fermion-antifermion fluctuations (similar to QED) and the fluctuations which come from the self-interaction of the gluons (specific to QCD). For a particular interaction, three coupling constants can exist: the "bare", "renormalized" and "effective" constants [27].

The most interesting one is the effective coupling constant α_s, which changes depending on the energy scale Q^2 of the process that is being looked at. It is described in the following way :

$$\alpha_s\left(Q^2\right) = \frac{12\pi}{11N_c - 2N_f \ln\left(\frac{Q^2}{\Lambda^2_{QCD}}\right)}$$

with N_c the number of colours (equal to 3); N_f the number of quark flavours (equal to 6); Λ_{QCD}, the fundamental scale parameter of the QCD determined experimentally to

be approximately equal to 200 MeV.

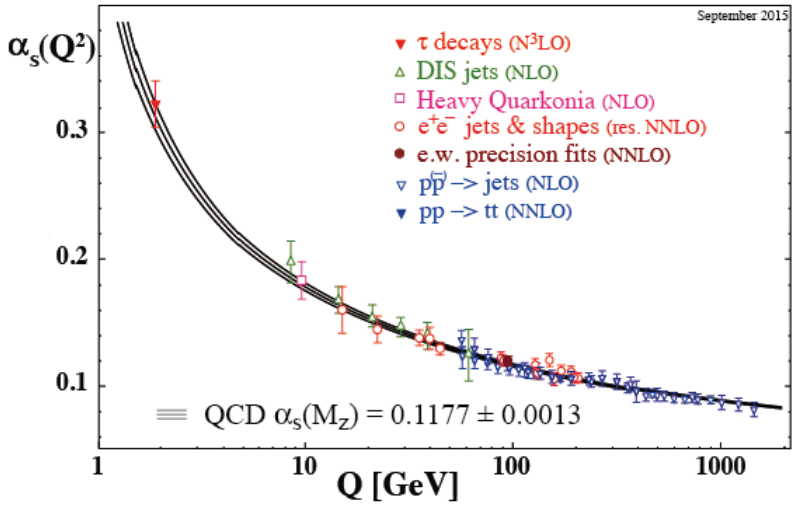

FIGURE 1.2. Summary of measurements of α_s as a function of the energy scale Q. The respective degree of QCD perturbation theory used in the extraction of α_s is indicated in brackets (next-to-leading order (NLO), next-to-next-to leading order (NNLO), NNLO matched with resummed next-to-leading logs (res. NNLO) and next-to-NNLO (N^3LO))[10], from [28].

The value of α_s significantly depends on the energy scale involved in the considered process, as shown in Figure 1.2. Above 1 GeV, there is the region of *asymptotic freedom*. Below 1 GeV, there is the regime of *colour confinement*. Both of these regimes will be detailed in the next two Sections.

1.2.3.1 Asymptotic freedom

FIGURE 1.2 shows that the coupling constant α_s approaches to zero in the region of high energy (or at short distances), defining the regime of asymptotic freedom: because of this, the QCD perturbative theory may be used [32] to perform analytical calculations. Quarks have weak interactions with their neighbours in this regime, when they are close to each other, and they act as quasi-free particles.

[10] Leading order refers to an approximation to a given function, usually under assumptions about the inputs being very small or very large. When a single approximation is not enough, it may be necessary to also retain the set of next largest term. These can be called the next-to-leading order terms [29, 30]. The next set of terms down after that can be called the next-to-next-to leading order terms [31].

1.2.3.2 Colour confinement

At low energies and, hence, at large distances ($\gtrsim$1 fm), the coupling constant α_s diverges and the interaction between quarks becomes intense.

This effect can be explained introducing the QCD potential $V(r)$, that is a function of the distance between quarks r:

$$V(r) \simeq -\frac{4}{3}\frac{\alpha_s}{r} + \sigma r. \tag{1.4}$$

From equation 1.4, two different behaviour of the potential $V(r)$ can be identified. At a small distance ($r \longrightarrow 0$), the Coulomb term ($1/r$) dominates, the α_r becomes small and the quarks are quasi-free: this is the asymptotic freedom, described in Section 1.2.3.1. one can see that when the distance between quarks becomes large ($r \longrightarrow \infty$), the term (σr) dominates and the potential increases linearly with the distance. In this case, σ can be assimilated to the tension of a string and translates the effect of confinement for long distances. Therefore, it means that an infinite amount of energy is needed to split two quarks away from each other. Trying to separate quarks, indeed, leads to the creation of a new $q\overline{q}$ pair, so the inter-quark distance diminishes, the potential $V(r)$ returns to a lower intensity and the quarks can rearrange themselves inside the hadrons. One can notice, indeed, that the hadrons that constitute the matter are "white", it means that are composed of coloured quarks [33], resulting in a "white" charge[11].

Due to the large values taken by the coupling constant at large distances, the perturbative theory cannot be used to describe the mechanism of confinement, and effective [34] or lattice-QCD [35] approaches are needed. It is thanks to lattice-QCD calculations, in particular, that we know the value of the critical temperature T_c ~155 MeV beyond which quarks and gluons cannot be confined anymore inside hadrons: this temperature marks the transition to the QGP state of matter.

1.2.4 Parton distribution function

Hadrons can be considered themselves as a statistical "soup" of partons, in which $q\overline{q}$ pairs are constantly created and destroyed. In other words, it is a misuse of the term to

[11] By analogy with conventional colours: red + green + blue = white, a neutral colour with a net colour charge of zero.

say that protons are made of two u quarks and one d quark: it would be more accurate to say that its composition can be represented as the combination of two u quarks and one d quark at an energy scale just above the one at which the proton appears to behave as a point-like particle. Increasing the energy regime, then decreasing the associated wavelength of the particle probing the content proton, the inner structure must be described by the so-called Parton Distribution Functions (PDFs), providing the density of each parton species as a function of Bjorken-x, the fraction of the hadron momentum.

The PDFs are estimated experimentally, using fits to experimental data. Inelastic lepton scattering experiments on hadrons, such as the HERA [36] experiments, play a significant role in the fitting of PDFs. As already noticed, in fact, the PDFs are dependent on the Bjorken-x[12] variable, which corresponds to the fraction of energy carried by a considered parton, as well as on the energy scale of the process Q^2. In terms of Q^2, x is defined as

$$x \equiv \frac{Q^2}{2p \cdot q},$$

where $Q^2 = -q_\mu q^\mu$, q_μ being the 4-momentum of the exchanged photon and p is the momentum of the hadron [37].

With regard to the gluons, thanks to HERA measurements (see Figure 1.3), we know that at small values of x the gluon distribution in the proton increases extremely rapidly with decreasing x[13]. QCD predicts that this evolution results in a large number of gluons that interact with each other and eventually in a *saturation*, where this term refers to the point of balance between gluon generation and annihilation. Studying this point can help to understand the gluon distribution function. With the advent of the LHC, it becomes possible to analyse the gluon distribution of lead nuclei at small-x values for perturbative Q^2 scales and the saturation point would be detectable. More information on gluon distribution functions will be given in Section 2.2.4.

1.3 Thermodynamics of QCD: the Quark-Gluon Plasma

HADRONIC matter undergoes a phase transition to a state in which quarks and gluons are deconfined, under circumstances of large energy density and temperature, according to the QCD-based predictions. Quark-Gluon Plasma (QGP) [39, 40] is the name given to this state of matter, which is made up of quarks and gluons rather than hadrons (baryons and mesons). Not accessible at ordinary temperature and density, the first

[12] The Bjorken-x is proportional to the ratio of the momentum carried by a gluon or quark in the nucleon (nucleus) to the nucleon (or nucleus) overall momentum.

[13] Deep Inelastic Scattering (DIS) is an effective approach for investigating PDFs at small-x.

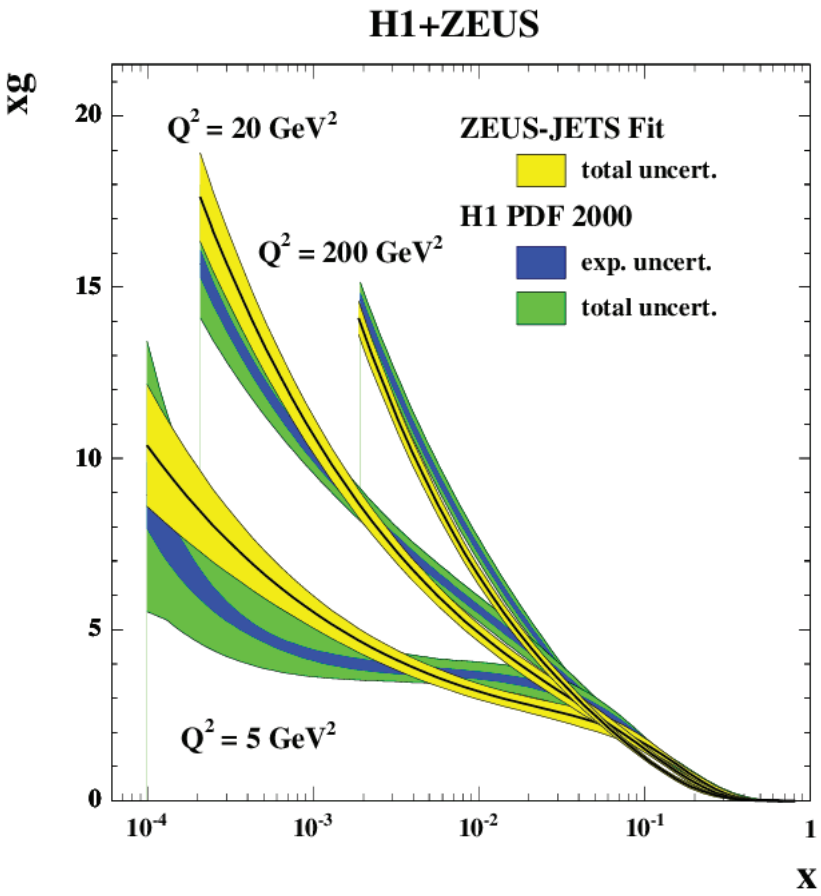

FIGURE 1.3. Gluon distributions extracted at HERA (H1 and ZEUS experiments) as a function of x in three bins of Q^2, from [38]. The significant increase in gluon distribution at small-x is easily visible.

hints of this state of matter were observed in the laboratory in 2000 at SPS [41]. In the next Sections, a thermodynamics approach to the study of QGP will be shortly discussed.

1.3.1 Hadronic matter phase diagram

USING a phase diagram of nuclear matter, in the temperature-baryonic chemical potential plane, as reported in Figure 1.4, makes it easy to observe the transition to a QGP state. Ordinary nuclear matter consists of regions with low temperatures (T) and baryonic chemical potentials (μ_B), in the hadronic phase.

In this theory, the Big Bang represents the start of the Universe expansion from a sin-

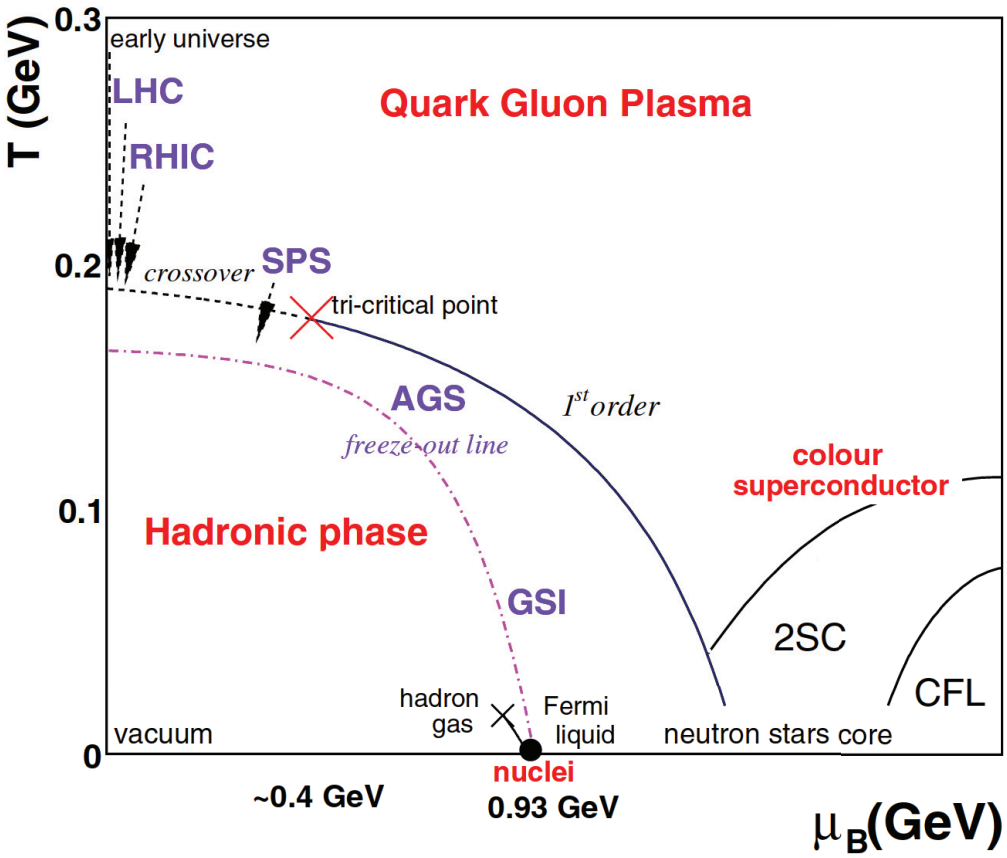

FIGURE 1.4. Hadronic phase diagram of nuclear matter in the temperature/baryonic density plane, from [42].

gularity, in a very hot environment. The QCD critical temperature (T_c ~0.2 GeV), from which the Universe passed from a deconfined state to the hadronic state of nuclear matter, is believed to have been reached, in the early cosmos, some microseconds after the Big Bang. After the first microseconds, matter transitioned from a QGP state to a hadron gas phase, always at almost zero baryon chemical potential. The cosmos froze out, reaching the current temperature of the cosmos[14], according to measurements of the cosmic microwave background [43], 13 orders of magnitude lower than the critical temperature.

The right side of Figure 1.4 represents conditions of temperatures and μ_B that are found in neutron stars: the pressure and μ_B in the cores of neutron stars [44] are believed to surpass the critical value of μ_B, squeezing the nucleons so closely together that the constituent quarks cannot be allocated to one or another nucleon.

These two specific conditions, the earliest seconds after the Big Bang and the cores of

[14]The current cosmos temperature is $2.725\,\mathrm{K} \simeq 2.3 \times 10^{-13}$ GeV.

neutron stars are, of course, not observable. To reproduce the characteristics of QGP in the laboratory, relativistic heavy-ion collisions are used. The arrows and the purple texts, in Figure 1.4, depict the zones of the hadronic phase diagram, that different heavy-ion accelerators (LHC[15], RHIC[16], SPS[17], AGS[18] and GSI[19]) can investigate.

1.3.2 Transition phase

SEVERAL questions on how to achieve the QGP are still being studied. Among these, there is undoubtedly the characterisation of the transition state for nuclear matter.
At very small μ_B values, lattice-QCD calculations have shown that the phase transition is a "crossover"[20] phase transition and at large baryon potentials $(\mu_B > 360\,\text{MeV})$ [45], the transition phase should be of the first order[21].

Currently the nature of this transition phase is unknown and the crossover is still being studied, for example at RHIC and LHC accelerators.

1.4 Heavy-ion collisions

DURING the first microseconds of the Universe, it was completely opaque, making cosmological research of the QGP impossible[22]. Likewise, when the baryonic density is sufficiently high, the presence of the QGP is expected in the cores of neutron stars, as already explained in Section 1.3.1. There is no way to conduct an experimental investigation of the QGP there, for obvious reasons.

For these reasons, the collisions of ultra-relativistic heavy-ions with accelerators such as the SPS, RHIC or LHC provide the necessary temperatures and energy densities for the production of a QGP fireball in the laboratory. Such collisions may be carried out

[15] Located in Geneva, Switzerland.
[16] Located in Upton, New York, USA.
[17] Located in Geneva, Switzerland.
[18] Located in Upton, New York, USA.
[19] Located in Darmstadt, Germany.
[20] In a crossover, no *canonical* "phase transition" occurs, although there is a drastic change in the phase of the system. It is thus not associated with a change of symmetry or a discontinuity in the free energy functional. Typically, it occurs in a region of the phase diagram, rather than a singular point. Microscopically, in a crossover, the ground-state of the system changes radically but in a very *smooth* manner; *i.e.* , without any discontinuity in the thermodynamic observables.
[21] First-order phase transitions exhibit a discontinuity in the first derivative of the free energy with respect to some thermodynamic variable.
[22] The Universe's radiation-matter decoupling occurred just 3×10^5 years after the Big Bang.

using one of two technologies (Table 1.1): on fixed targets (AGS, SPS) or in colliders (RHIC, LHC).

Fixed target experiment	Collider experiment
The obtained luminosity is very high.	The total energy of the two beams is available for producing new particles.
All kinds of particles (stable or not) can be used to create collisions.	The referential of the center of mass and the laboratory coincide for symmetric systems.

TABLE 1.1. Main characteristics of fixed and collider experiments creating heavy-ion collisions.

The principle of collisions between ultra-relativistic heavy nuclei is the following. By increasing the energy per nucleon over 100 GeV, the nuclei flow through one another, resulting in very high temperatures but very low baryonic densities: this is referred to as the *transparency* regime [46]. Before the collision, the ions have a velocity close to the speed of light along the beam axis and can be seen as thin "pancakes", owing to the Lorentz contraction. Following the impact, inelastic scattering occurs.

The Bjorken formula (equation 1.5), using the rapidity explained in Section 1.4.1, may be used to determine the energy density created. Here, the Bjorken formula is reported:

$$\epsilon = \frac{1}{\tau_f A}\langle m_T \rangle \frac{\mathrm{d}N}{\mathrm{d}y}, \tag{1.5}$$

where τ_f is the formation time of the particles; A is the section of the nuclei and $\langle m_T \rangle$ is the average transverse mass $\langle m_T \rangle = \left(\sqrt{E^2 - p_z^2}\right) = \left(\sqrt{m^2 + p_{\mathrm{T}}^2}\right)$.

Let us try to characterise the various stages of the collisions between heavy nuclei. Figure 1.5 shows the time evolution of the heavy-ion collisions [47].

All steps of the collision are represented on the left side of Figure 1.5, from the bottom to the top: the nuclei, with a "pancake" shape and a speed $v \simeq c$, collide at $\tau = 0$. Starting from $\tau = \tau_0$, the QGP is created and, after the transition phase, the hot matter returns smoothly to hadronic matter.
On the right side, each step is identified by a hyperbola $\left(\tau = \sqrt{c^2 t^2 - z^2}\right)$, where τ is the proper time. The evolution of the different steps of the QGP creation is described here :

1. The nuclei collide and begin to flow through each other, due to the transparency regime. This happens at $\tau = 0$.

2. A state of *pre-equilibrium* forms, in which the partons create heavy quarks, mainly

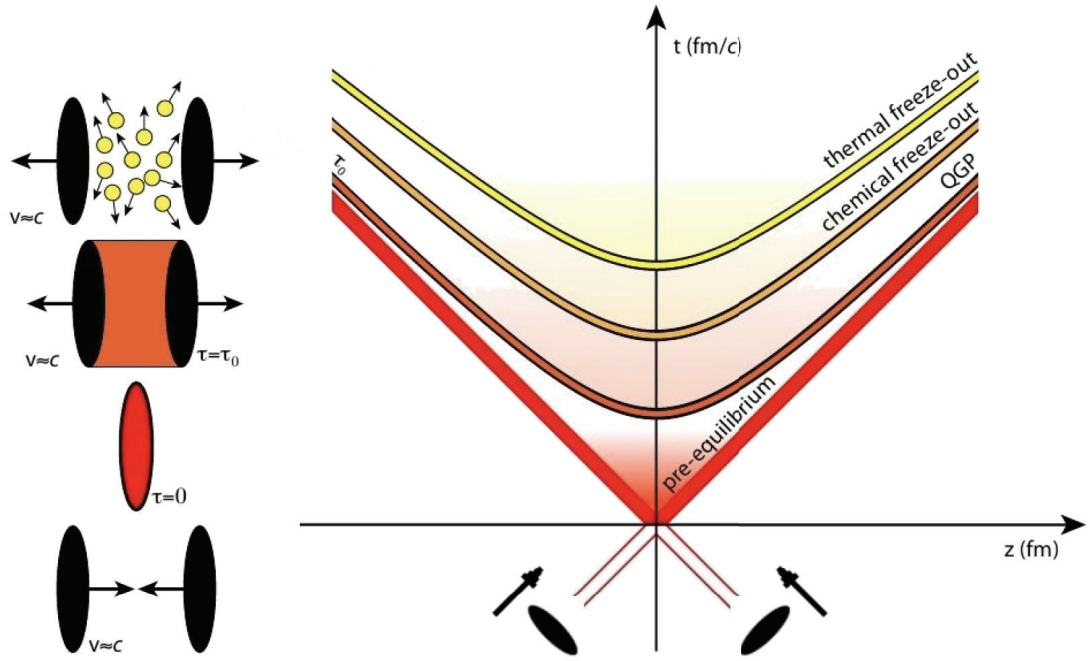

FIGURE 1.5. Space-time evolution of an heavy-ion collision, from [48].

charm and beauty. This phase, which lasts around 1 fm/c[23], is one of the less well-known to date.

3. Multiple scattering, among nucleons and their components, leads to a parton deconfinement, if the energy density is enough. Then, a thermodynamic equilibrium may be reached, permitting the production of plasma, with a lifetime of up to 10 fm/c at the LHC.

4. The plasma, then, cools down and starts to hadronise. A mixed-phase is developed, in which there is a coexistence of partonic matter and hadrons.

5. Finally, a gas of free hadrons is formed. This hadron gas undergoes elastic and inelastic interactions. When the inelastic scattering ends, the system experiences its initial freeze-out phase. It is the chemical freeze-out, since the system *chemical* composition is then frozen. The second freezing is a *thermal* or *kinetic* one and relates to the end of the hadronic elastic scattering. The produced in this way hadrons are then observed with detectors.

[23] 1 fm/c ~ 10^{-24} s.

1.4.1 The rapidity in heavy-ion collisions

THE rapidity y is defined in Equation 1.6 :

$$y = \frac{1}{2}\ln\left(\frac{E+p_z}{E-p_z}\right), \tag{1.6}$$

where E and p_z are the components of the Lorentz energy-impulsion quatrivector $\vec{p} = (E, p_x, p_y, p_z)$. In heavy-ion collisions, it is more common to use the *pseudo-rapidity* η, which is equivalent to rapidity, in the ultra-relativistic limit.

$$\eta = \frac{1}{2}\ln\left(\frac{|p|+p_z}{|p|-p_z}\right) = \frac{1}{2}\ln\left(\frac{1+\frac{p_z}{|p|}}{1-\frac{p_z}{|p|}}\right) = -\ln\left(\tan\frac{\theta}{2}\right), \tag{1.7}$$

where θ is the emission polar angle of the particle.

1.4.2 The centrality of heavy-ion collisions

AN important parameter used to describe the heavy-ion collisions is the *centrality*. The term "centrality" refers to the transverse overlap of the two nuclei that collide. Two variables can describe the collision, by the Glauber model [49]: the impact parameter b and the number of nucleons participating in the collision N_{part}. One can also calculate the N_{coll} that gives the number of binary collisions between participant nucleons.

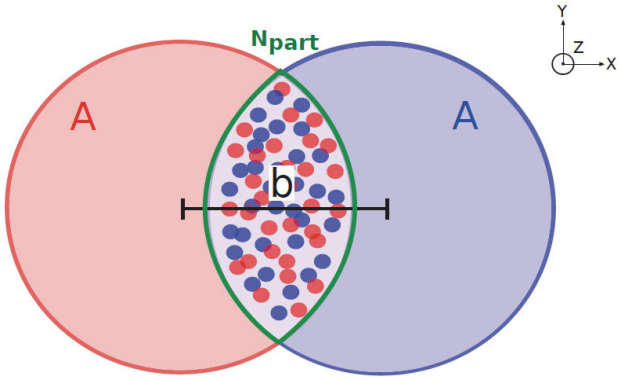

FIGURE 1.6. Diagram of a heavy-ion collision in the transverse plane, from [50].

In Figure 1.6, the distance between the centres of the two nuclei is defined by the impact parameter b and the overlap zone (green area) specifies the number of nucleons N_{part} involved in the collision. The biggest overlap represents a more *central* collision with the lowest value of b which means $b < R_1 + R_2$. A collision is called *peripheral* when b is large ($b = R_1 + R_2$). The collision is considered to be ***ultra-peripheral*** when $b > R_1 + R_2$, where R_1 and R_2 are the radii of the two nuclei. This kind of interaction will be discussed in Chapter 2.

1.5 The QGP observables

As already said in the previous Sections, the QGP lifetime is brief and, experimentally, it is impossible to observe it. The unique elements that can be used to characterise the QGP are the hadrons or decay particles, produced when the hot matter freezes out. In this Section, some of the known QGP observables will be described.

1.5.1 Soft probes

Particles produced in low-Q^2 processes are usually referred to as soft probes. They are sensitive to the QGP evolution and characterise the medium in terms of mechanisms for hadron production, statistical/thermal features and collective phenomena. The soft probes form the bulk of the particle production in heavy-ion collisions.

The study of soft probes is important to characterise the collective behaviour of the QGP. The initial-state spatial anisotropies of the colliding nuclei are transformed into the final-state particle momentum anisotropies by the pressure gradients in the QGP. Measurements of these momentum anisotropies (known as particle flow, see Figure 1.7) allowed us to observe that the QGP created at the LHC behaves as an nearly perfect fluid, and to determine its shear and bulk viscosity.

The study of the yields of various hadrons produced in heavy-ion collisions provides information about the thermodynamic properties of the QGP medium. At the hadronisation stage, the colliding system is close to thermal equilibrium and then rapidly freezes out. The hadron yields are thus described extremely well by a thermal (known as Statistical Hadronization [52]) model. Moreover, a fit of the hadron yields provides a precise estimate of the temperature of the system at the chemical freeze-out (Figure 1.8).

Another soft probe that characterises the QGP is the thermal photons [54]. They are

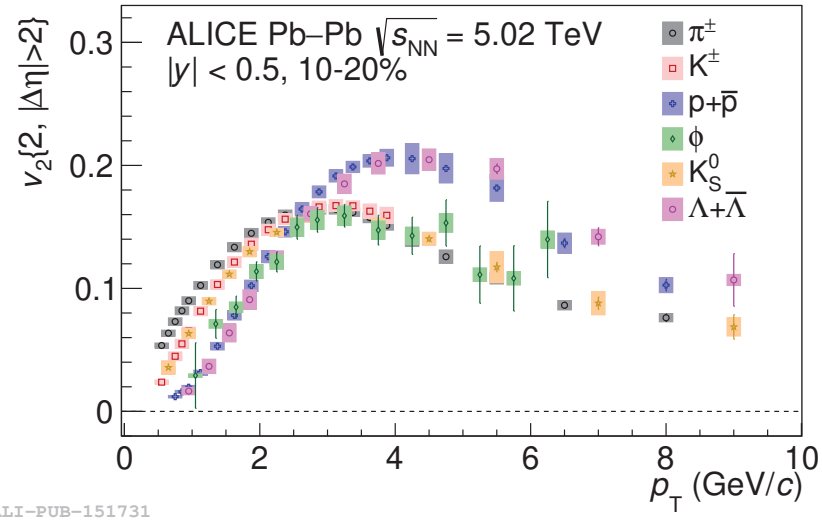

FIGURE 1.7. The measured elliptic flow v_2 of various hadrons as a function of p_T for 10-20% centrality in Pb–Pb collisions at $\sqrt{s_{NN}}$ = 5.02 TeV, from [51].

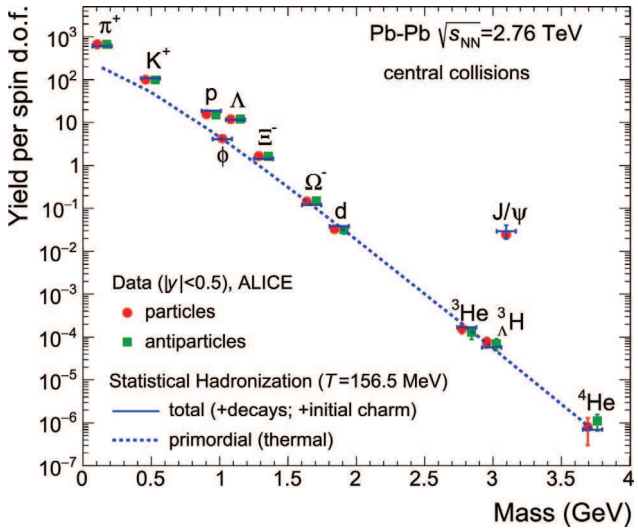

FIGURE 1.8. Yields of various hadrons, normalised to the spin degeneracy, as a function of their mass calculated within the Statistical Hadronization Model for Pb–Pb collisions as $\sqrt{s_{NN}}$ = 2.76 TeV. The temperature at the chemical freeze-out is obtained by a fit of the model calculations to the experimental data, from [53].

emitted during the evolution of the hot QGP medium and escape the fireball without interacting with it. Their spectrum is approximately exponential, with an inverse slope equal to the effective temperature of the QGP during its evolution.

In hadronic collisions, strange quarks are produced *via* $q\bar{q} \longrightarrow s\bar{s}$ or $gg \longrightarrow s\bar{s}$ processes

and the yields of strange particles, especially multi-strange ones, are usually relatively low. Due to the partial chiral symmetry restoration in the QGP, the energy required to create a $s\bar{s}$ pair becomes as low as about twice the mass of the s quark. This energy is at the order of or smaller with respect to the temperatures reached during the QGP evolution. This fact, coupled to the abundance of gluons in the QGP, increases significantly the strangeness content of the QGP and hence enhances the yield of strange particles. This enhancement is illustrated in Figure 1.9, where one can clearly see the smooth evolution of the strange particle production from pp to Pb–Pb collisions. It is worth noting that higher is the strangeness content of the particle, the steeper is its enhancement.

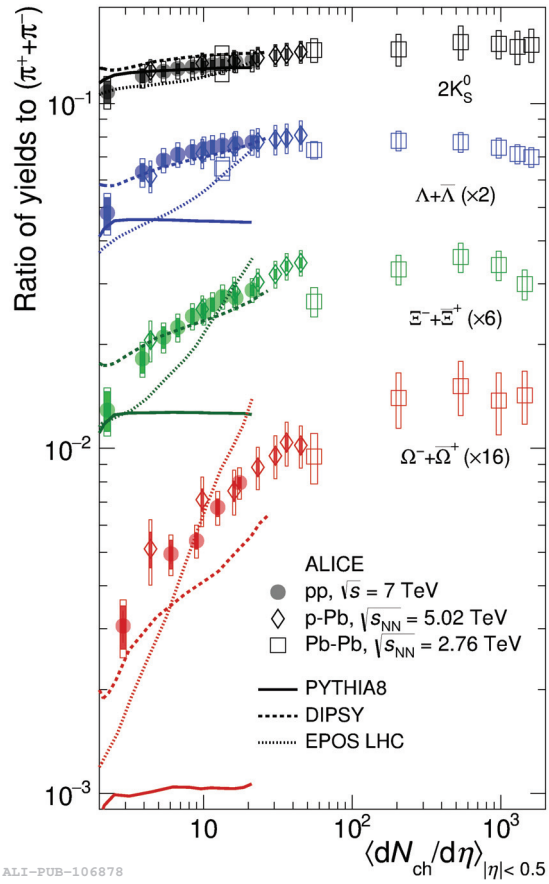

FIGURE 1.9. p_{T}-integrated yield ratios of strange and multi-strange hadrons to $(\pi^+ + \pi^-)$ as a function of $< \mathrm{d}N_{\mathrm{ch}}/\mathrm{d}\eta >$ measured in the rapidity interval $\eta < 0.5$, from [55].

1.5.2 Hard probes

OBSERVABLES that are associated with perturbative QCD processes are known as hard probes. Such processes have a characteristic scale smaller than $\Lambda_{\mathrm{QCD}}^{-1}$. Therefore, the

hard probes originate from the early stages of the collision and experience the entire evolution of the QGP. The modifications in the production of hard probes in the QGP are usually quantified by the so-called nuclear modification factor R_{AA} defined as

$$R_{AA} = \frac{1}{< N_{\text{coll}} > \dfrac{\mathrm{d}^2 N_{pp}}{\mathrm{d}y\,\mathrm{d}p_{\mathrm{T}}}} \times \frac{\mathrm{d}^2 N_{AA}}{\mathrm{d}y\,\mathrm{d}p_{\mathrm{T}}},$$

where $< N_{\text{coll}} >$ is the average number of binary nucleon-nucleon collisions, and $\mathrm{d}^2 N_{AA}/\mathrm{d}y\,\mathrm{d}p_{\mathrm{T}}$ and $\mathrm{d}^2 N_{pp}/\mathrm{d}y\,\mathrm{d}p_{\mathrm{T}}$ represent the yields of a given hard probe for a given centrality in A-A and p-p collisions, respectively.

Let us start with the parton energy loss and the jet quenching. The jets are streams of collimated particles originating from highly energetic partons created *via* hard scattering processes at the early collision stages. During the propagation of the jets through the hot and dense QGP medium, they interact with the surrounding colour charges which leads to parton energy loss or the so-called *jet quenching*. The jet quenching manifests itself in various ways: the suppression of the yield of high-p_{T} jets, hadrons, and decay particles, the modification of back-to-back jet and hadron correlations, the modification of the jets substructure. The jet quenching increases with the traversed path length inside the QGP.

The heavy c and b quarks are also created in the initial stages of the collision (no significant thermal production). Their interaction with the QGP constituents lead to both collective and energy-loss effects. Due to their high masses they undergo a sort of Brownian motion inside the QGP, leading to an incomplete thermalisation encoded in the so-called diffusion coefficient. The diffusion coefficient can be constrained *via* simultaneous measurements of the heavy-quark hadron nuclear modification factor and flow (Figure 1.10). At high p_{T}, inelastic processes, like gluon radiation, dominate and result in energy loss.

An important family of particles are the quarkonia, corresponding to $c\overline{c}$ (charmonia) and $b\overline{b}$ (bottomonia) bound states. In hadronic collisions, they are produced essentially *via* the gluon fusion. Inside the QGP, the suppression of these bound states is owing to the $q\overline{q}$ potential colour screening; when the temperature rises, the interaction potential changes and becomes repulsive. The temperature when this happens depends on the binding energy of each specific bound state. The quarkonia suppression, thus, serves as a thermometer of the medium. At the LHC energies, there is a counterbalancing process that enhances the production of charmonia. The large number of charm quarks and antiquarks in the QGP (about a hundred in central Pb–Pb collisions)

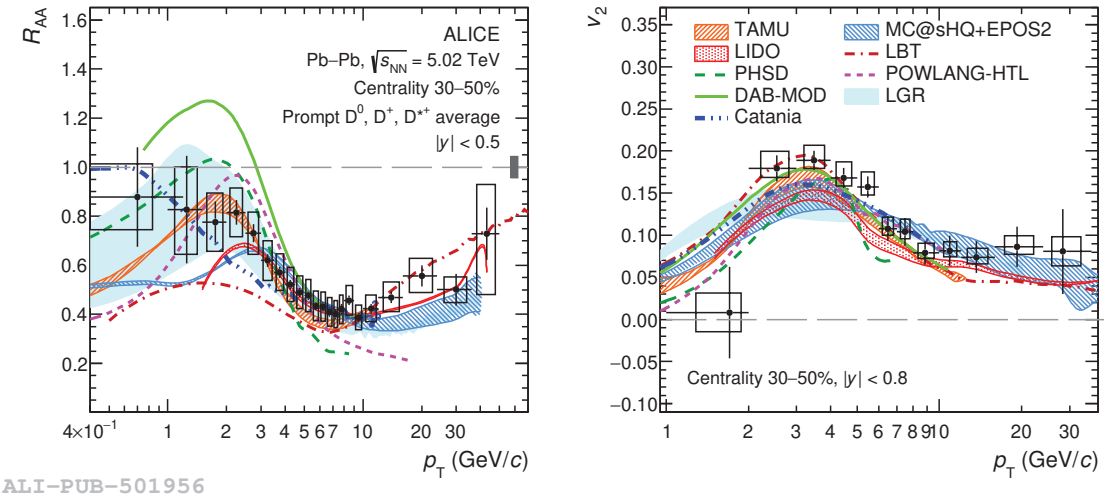

FIGURE 1.10. Average R_{AA} (left) and elliptic flow v_2 (right) of prompt D^0, D^+, and D^{*+} mesons for 30-50% centrality in Pb–Pb collisions at $\sqrt{s_{NN}}$ = 5.02 TeV compared with predictions of models implementing the charm-quark transport in a hydrodynamically expanding QGP, from [56].

gives rise to charmonia production *via* recombination.

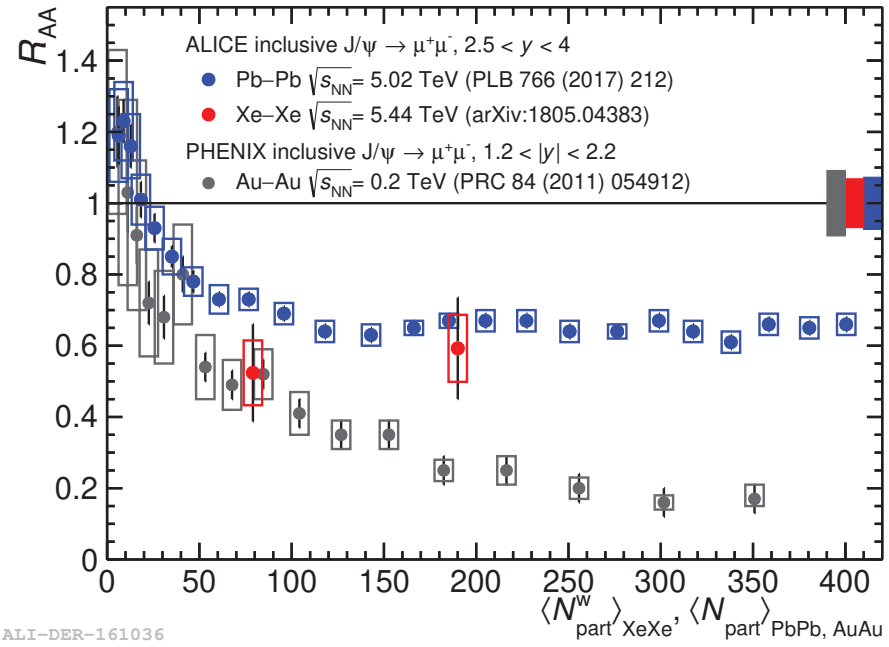

FIGURE 1.11. Inclusive J/ψ R_{AA} as a function of centrality in Xe-Xe and Pb-Pb collisions as measured by ALICE. The results are compared with J/ψ R_{AA} measured by Phenix in Au-Au collisions at RHIC, from [57].

As Figure 1.11 reveals, the ALICE measurement of J/ψ R_{AA} in Pb–Pb collisions at $\sqrt{s_{\mathrm{NN}}} = 5.02$ TeV shows a significantly lower suppression of the J/ψ in more central collisions compared to the results of the PHENIX[24] experiments at lower energies at RHIC. This is an important ALICE result as it demonstrates the J/ψ production *via* recombination and suppression with the deconfined medium.

[24] Located in Ridge, New York, USA.

References

[1] M. K. Gaillard, P. D. Grannis Paul D., and F. J. Sciulli. "The Standard model of particle physics". In: *Rev. Mod. Phys.* 71 (1999), S96–S111. DOI: 10.1103/RevModPhys.71.S96. arXiv: hep-ph/9812285 (cit. on p. 2).

[2] C. Campagnari and M. Franklin. "The Discovery of the top quark". In: *Rev. Mod. Phys.* 69 (1997), pp. 137–212. DOI: 10.1103/RevModPhys.69.137. arXiv: hep-ex/9608003 (cit. on p. 2).

[3] T. Patzak. "First direct observation of the tau-neutrino". In: *Europhys. News* 32 (2001), pp. 56–57. DOI: 10.1051/epn:2001205 (cit. on p. 2).

[4] S. Chatrchyan et al. "The CMS Experiment at the CERN LHC". In: *JINST* 3 (2008), S08004. DOI: 10.1088/1748-0221/3/08/S08004 (cit. on p. 2).

[5] G. Aad et al. "ATLAS Collaboration". In: *Nuclear Physics A* 932 (2014). Hard Probes 2013, pp. 572–594. ISSN: 0375-9474. DOI: https://doi.org/10.1016/S0375-9474(14)00601-0. URL: https://www.sciencedirect.com/science/article/pii/S0375947414006010 (cit. on p. 2).

[6] G. Aad et al. "Observation of a new particle in the search for the Standard Model Higgs boson with the ATLAS detector at the LHC". In: *Phys. Lett. B* 716 (2012), pp. 1–29. DOI: 10.1016/j.physletb.2012.08.020. arXiv: 1207.7214 [hep-ex] (cit. on p. 2).

[7] S. Chatrchyan et al. "Observation of a New Boson at a Mass of 125 GeV with the CMS Experiment at the LHC". In: *Phys. Lett. B* 716 (2012), pp. 30–61. DOI: 10.1016/j.physletb.2012.08.021. arXiv: 1207.7235 [hep-ex] (cit. on p. 2).

[8] P. W. Higgs. "Broken Symmetries and the Masses of Gauge Bosons". In: *Phys. Rev. Lett.* 13 (1964). Ed. by J. C. Taylor, pp. 508–509. DOI: 10.1103/PhysRevLett.13.508 (cit. on p. 2).

[9] P. W. Higgs. "Spontaneous Symmetry Breakdown without Massless Bosons". In: *Phys. Rev.* 145 (1966), pp. 1156–1163. DOI: 10.1103/PhysRev.145.1156 (cit. on p. 2).

[10] Wikipedia. *Standard model of elementary particles*. <link>. 2019 (cit. on p. 3).

[11] L. Lusanna and P. Valtancoli. "Dirac's observables for the SU(3) × SU(2) × U(1) standard model". In: *Int. J. Mod. Phys. A* 13 (1998), pp. 4605–4690. DOI: 10.1142/S0217751X98002213. arXiv: hep-th/9707072 (cit. on p. 4).

[12] P. Fayet and S. Ferrara. "Supersymmetry". In: *Phys. Rept.* 32 (1977), pp. 249–334. DOI: 10.1016/0370-1573(77)90066-7 (cit. on p. 4).

[13] J. Polchinski. "What is string theory?" In: (Nov. 1994). arXiv: hep-th/9411028 (cit. on p. 4).

[14] F. De Aquino. "Gravitation and electromagnetism: Correlation and grand unification". In: *J. New Energy* 5 (2000), pp. 76–84. arXiv: gr-qc/9910036 (cit. on p. 4).

[15] H. D. Politzer. "Reliable Perturbative Results for Strong Interactions?" In: *Phys. Rev. Lett.* 30 (1973). Ed. by J. C. Taylor, pp. 1346–1349. DOI: 10.1103/PhysRevLett.30.1346 (cit. on p. 4).

[16] H. Fritzsch, M. Gell-Mann, and H. Leutwyler. "Advantages of the Color Octet Gluon Picture". In: *Phys. Lett. B* 47 (1973), pp. 365–368. DOI: 10.1016/0370-2693(73)90625-4 (cit. on p. 4).

[17] S. K. Choi et al. "Observation of a resonance-like structure in the $pi^{\pm}\psi'$ mass distribution in exclusive $B \to K\pi^{\pm}\psi'$ decays". In: *Phys. Rev. Lett.* 100 (2008). Ed. by Dongchul Son and Sun Kun Oh, p. 142001. DOI: 10.1103/PhysRevLett.100.142001. arXiv: 0708.1790 [hep-ex] (cit. on p. 5).

[18] R. Aaij et al. "Observation of $J/\psi p$ Resonances Consistent with Pentaquark States in $\Lambda_b^0 \to J/\psi K^- p$ Decays". In: *Phys. Rev. Lett.* 115 (2015), p. 072001. DOI: 10.1103/PhysRevLett.115.072001. arXiv: 1507.03414 [hep-ex] (cit. on p. 5).

[19] B. Muller. *The physics of the quark - gluon plasma*. Vol. 225. 1985, p. 1 (cit. on p. 5).

[20] J. Rafelski. "Connecting QGP-Heavy Ion Physics to the Early Universe". In: *Nucl. Phys. B Proc. Suppl.* 243-244 (2013). Ed. by Roberto Battiston and Sergio Bertolucci, pp. 155–162. DOI: 10.1016/j.nuclphysbps.2013.09.017. arXiv: 1306.2471 [astro-ph.CO] (cit. on p. 5).

[21] B. L. Inscoe and J. L. Lancaster. "Introducing SU(3) color charge in undergraduate quantum mechanics". In: *Am. J. Phys.* 89.2 (2021), pp. 172–184. DOI: 10.1119/10.0002004. arXiv: 1907.12520 [physics.ed-ph] (cit. on p. 6).

[22] M. Gell-Mann. "Symmetries of baryons and mesons". In: *Phys. Rev.* 125 (1962), pp. 1067–1084. DOI: 10.1103/PhysRev.125.1067 (cit. on pp. 6, 7).

[23] F. Halzen and A. D. Martin. *Quarks and leptons : an introductory course in modern particle physics*. 1984. ISBN: 978-0-471-88741-6 (cit. on p. 6).

[24] D. Bleecker. *Gauge theory and variational principles*. 1981 (cit. on p. 6).

[25] H. Yukawa. "On the Interaction of Elementary Particles I". In: *Proc. Phys. Math. Soc. Jap.* 17 (1935), pp. 48–57. DOI: 10.1143/PTPS.1.1 (cit. on p. 7).

[26] W. Greiner and A. Schaefer. *Quantum chromodynamics*. 1995. ISBN: 978-3-540-57103-2 (cit. on p. 7).

[27] A. Deur, S. J. Brodsky, and G. F. de Teramond. "The QCD Running Coupling". In: *Nucl. Phys.* 90 (2016), p. 1. DOI: 10.1016/j.ppnp.2016.04.003. arXiv: 1604.08082 [hep-ph] (cit. on p. 7).

[28] D. d'Enterria and P. Z. Skands, eds. *Proceedings, High-Precision α_s Measurements from LHC to FCC-ee: Geneva, Switzerland, October 2-13, 2015*. Geneva: CERN, Dec. 2015. arXiv: 1512.05194 [hep-ph] (cit. on p. 8).

[29] J. M. Campbell and R. K. Ellis. "Next-to-Leading Order Corrections to W^+ 2 jet and Z^+ 2 Jet Production at Hadron Colliders". In: *Phys. Rev. D* 65 (2002), p. 113007. DOI: 10.1103/PhysRevD.65.113007. arXiv: hep-ph/0202176 (cit. on p. 8).

[30] S. Catani and M. H. Seymour. "The Dipole formalism for the calculation of QCD jet cross-sections at next-to-leading order". In: *Phys. Lett. B* 378 (1996), pp. 287–301. DOI: 10.1016/0370-2693(96)00425-X. arXiv: hep-ph/9602277 (cit. on p. 8).

[31] N. Kidonakis. "Next-to-next-to-next-to-leading-order soft-gluon corrections in hard-scattering processes near threshold". In: *Phys. Rev. D* 73 (2006), p. 034001. DOI: 10.1103/PhysRevD.73.034001. arXiv: hep-ph/0509079 (cit. on p. 8).

[32] C. Patrignani et al. "Review of Particle Physics". In: *Chin. Phys. C* 40.10 (2016), p. 100001. DOI: 10.1088/1674-1137/40/10/100001 (cit. on p. 8).

[33] T. Muta. *Foundations of Quantum Chromodynamics: An Introduction to Perturbative Methods in Gauge Theories, (3rd ed.)* 3rd. Vol. 78. World scientific Lecture Notes in Physics. Hackensack, N.J.: World Scientific, 2010. ISBN: 978-981-279-353-9 (cit. on p. 9).

[34] D. Ki Hong. "An Effective field theory of QCD at high density". In: *Phys. Lett. B* 473 (2000), pp. 118–125. DOI: 10.1016/S0370-2693(99)01472-0. arXiv: hep-ph/9812510 (cit. on p. 9).

[35] F. Karsch. "Lattice QCD at high temperature and density". In: *Lect. Notes Phys.* 583 (2002). Ed. by Willibald Plessas and L. Mathelitsch, pp. 209–249. DOI: 10.1007/3-540-45792-5_6. arXiv: hep-lat/0106019 (cit. on p. 9).

[36] H. Abramowicz and A. Caldwell. "HERA collider physics". In: *Rev. Mod. Phys.* 71 (1999), pp. 1275–1410. DOI: 10.1103/RevModPhys.71.1275. arXiv: hep-ex/9903037 (cit. on p. 10).

[37] R. C. Hwa and X. N. Wang, eds. *Quark-gluon plasma 3*. Singapore: World Scientific, 2004. ISBN: 978-981-238-077-7, 978-981-4488-08-2. DOI: 10.1142/5029 (cit. on p. 10).

[38] M. Dittmar et al. “Working Group I: Parton distributions: Summary report for the HERA LHC Workshop Proceedings”. In: (Nov. 2005). arXiv: hep-ph/0511119 (cit. on p. 11).

[39] E. V. Shuryak. “Quark-Gluon Plasma and Hadronic Production of Leptons, Photons and Psions”. In: *Phys. Lett. B* 78 (1978), p. 150. DOI: 10.1016/0370-2693(78)90370-2 (cit. on p. 10).

[40] F. Karsch. “Lattice results on QCD thermodynamics”. In: *Nucl. Phys. A* 698 (2002). Ed. by T. J. Hallman, D. E. Kharzeev, J. T. Mitchell, and T. S. Ullrich, pp. 199–208. DOI: 10.1016/S0375-9474(01)01365-3. arXiv: hep-ph/0103314 (cit. on p. 10).

[41] U. W. Heinz and M. Jacob. “Evidence for a new state of matter: An Assessment of the results from the CERN lead beam program”. In: (Jan. 2000). arXiv: nucl-th/0002042 (cit. on p. 11).

[42] G. L. Bayatian et al. “CMS physics technical design report: Addendum on high density QCD with heavy ions”. In: *J. Phys. G* 34 (2007). Ed. by David G. d’Enterria et al., pp. 2307–2455. DOI: 10.1088/0954-3899/34/11/008 (cit. on p. 12).

[43] J. C. Mather, D. J. Fixsen, R. A. Shafer, C. Mosier, and D. T. Wilkinson. “Calibrator design for the COBE far infrared absolute spectrophotometer (FIRAS)”. In: *Astrophys. J.* 512 (1999), pp. 511–520. DOI: 10.1086/306805. arXiv: astro-ph/9810373 (cit. on p. 12).

[44] A. Rosenhauer, E. F. Staubo, L. P. Csernai, T. Oevergard, and E. Oestgaard. “Neutron stars, hybrid stars and the equation of state”. In: *Nucl. Phys. A* 540 (1992), pp. 630–645. DOI: 10.1016/0375-9474(92)90177-L (cit. on p. 12).

[45] Z. Fodor and S. D. Katz. “The Phase diagram of quantum chromodynamics”. In: (Aug. 2009). arXiv: 0908.3341 [hep-ph] (cit. on p. 13).

[46] N. N. Nikolaev. “Color transparency: A Novel test of QCD in nuclear interactions”. In: *Surveys High Energ. Phys.* 7 (1994), pp. 1–92. DOI: 10.1080/01422419408241243. arXiv: nucl-th/9304015 (cit. on p. 14).

[47] A. K. Chaudhuri and U. W. Heinz. “Hydrodynamical evolution of dissipative QGP fluid”. In: *J. Phys. Conf. Ser.* 50 (2006). Ed. by B. Sinha, J. Alam, and T. K. Nayak, pp. 251–258. DOI: 10.1088/1742-6596/50/1/030. arXiv: nucl-th/0504022 (cit. on p. 14).

[48] H. Satz. “The SPS heavy ion programme”. In: *Phys. Rept.* 403-404 (2004), pp. 33–50. DOI: 10.1016/j.physrep.2004.08.009. arXiv: hep-ph/0405051 (cit. on p. 15).

[49] M. L. Miller, K. Reygers, S. J. Sanders, and P. Steinberg. "Glauber modeling in high energy nuclear collisions". In: *Ann. Rev. Nucl. Part. Sci.* 57 (2007), pp. 205–243. DOI: 10.1146/annurev.nucl.57.090506.123020. arXiv: nucl-ex/0701025 (cit. on p. 16).

[50] M. Guilbaud. "Etude de la densité de particules chargées et des mésons vecteurs de basses masses en collisions Pb-Pb à $\sqrt{s_{\mathrm{NN}}}$ = 2.76 TeV dans ALICE au LHC". PhD thesis. Lyon 1 University, 2013. URL: http://cds.cern.ch/record/1696853 (cit. on p. 16).

[51] S. Acharya et al. "Anisotropic flow of identified particles in Pb-Pb collisions at $\sqrt{s_{\mathrm{NN}}}$ = 5.02 TeV". In: *JHEP* 09 (2018), p. 006. DOI: 10.1007/JHEP09(2018)006. arXiv: 1805.04390 [nucl-ex] (cit. on p. 18).

[52] F. Becattini. "An Introduction to the Statistical Hadronization Model". In: *International School on Quark-Gluon Plasma and Heavy Ion Collisions: past, present, future*. Jan. 2009. arXiv: 0901.3643 [hep-ph] (cit. on p. 17).

[53] A. Andronic, P. Braun-Munzinger, Markus K. Köhler, K. Redlich, and J. Stachel. "Transverse momentum distributions of charmonium states with the statistical hadronization model". In: *Phys. Lett. B* 797 (2019), p. 134836. DOI: 10.1016/j.physletb.2019.134836. arXiv: 1901.09200 [nucl-th] (cit. on p. 18).

[54] K. Reygers. "Experimental overview of electromagnetic probes in ultra-relativistic nucleus-nucleus collisions". In: *29th International Conference on Ultra-relativistic Nucleus-Nucleus Collisions*. Dec. 2022. arXiv: 2212.01220 [nucl-ex] (cit. on p. 17).

[55] J. Adam et al. "Enhanced production of multi-strange hadrons in high-multiplicity p-p collisions". In: *Nature Phys.* 13 (2017), pp. 535–539. DOI: 10.1038/nphys4111. arXiv: 1606.07424 [nucl-ex] (cit. on p. 19).

[56] S. Acharya et al. "Prompt D^0, D^+, and D^{*+} production in Pb–Pb collisions at $\sqrt{s_{\mathrm{NN}}}$ = 5.02 TeV". In: *JHEP* 01 (2022), p. 174. DOI: 10.1007/JHEP01(2022)174. arXiv: 2110.09420 [nucl-ex] (cit. on p. 21).

[57] F. Noferini. "ALICE Highlights". In: *MDPI Proc.* 13.1 (2019), p. 6. DOI: 10.3390/proceedings2019013006. arXiv: 1906.02460 [hep-ex] (cit. on p. 21).

2 Ultra-Peripheral Collisions

It is no good to try to stop knowledge from going forward.
Ignorance is never better than knowledge.
Enrico Fermi (1901 – 1954)

Contents

ITALIAN Nobel Prize winner Enrico Fermi postulated, in 1924, a theory [58] that is still used successfully today. When a charged particle flows, it is surrounded by a magnetic field and is encircled radially by an electric field. This field mimics an authentic photon behaviour. Thus, Fermi decided to treat it as a flux of virtual photons. In the 1930s, Weizsacker and Williams extended Fermi's theory to the relativistic charged particles [59, 60].
As already explained in Section 1.4, when the particle velocity approaches the speed of light, any extended particle and also the electromagnetic field lines become Lorentz contracted in the direction of movement. At LHC energies, protons and ions carry an electromagnetic field, which may be considered a source of photons. In other words, a photon, produced by one of these hadrons, may interact with another photon or with a hadron. This kind of interactions are well observed using Ultra-Peripheral Collisions (UPC) at the LHC.

Polarisation is one of the most important observables that can be studied in heavy-ion collisions. On the one hand, theoretical predictions portray it as the ideal probe for shedding light on the long-standing subject of the process of quarkonium creation in elementary collisions. On the other hand, due to the possibility that it is sensitive to the environment in which particle creation happens, it might be used to explore the impact of a deconfined medium on the development of a bound state of two heavy quarks. This versatility is somewhat compensated by the challenges in describing the experimental data, which extend back to the initial measurements conducted at Tevatron.

In this Chapter, the physics behind the UPC is described.

2.1 The photon flux

OBTAINED from a Lorentz transformation of a 4-vector potential A^{μ}, the electric field components in relativistic collisions are equal to

$$\begin{cases} E_{\text{long}}(t,b) = \dfrac{-Ze\gamma_L vt}{\left(b^2+(\gamma vt)^2\right)^{\frac{3}{2}}}, \\ E_{\text{transv}}(t,b) = \dfrac{-Ze\gamma_L b}{\left(b^2+(\gamma vt)^2\right)^{\frac{3}{2}}}, \end{cases}$$

where b, is the impact parameter; v the speed; γ_L the Lorentz's factor[1]; Z the atomic number and e the electron charge. In these equations, E_{long} and E_{transv} are the longitudinal and the transverse components of E-field, respectively. As the γ_L factor increases, the E-field gets oriented within a more narrow cone with angular width γ_L with respect to the transverse plane. The corresponding magnetic field is perpendicular to the E-field and has the same strength, since the particle velocity is close to the speed of light. Using the Weizsacker-Williams method, the relativistic expression of the electromagnetic field components are equal to

$$\begin{cases} E_{\text{long}}(\omega, b) = \sqrt{\dfrac{2}{\pi}} \dfrac{eZ}{4\pi\varepsilon_0} \dfrac{\omega}{\gamma^2 v^2} K_0\left(\dfrac{\omega b}{\gamma_L v}\right), \\ E_{\text{transv}}(\omega, b) = \sqrt{\dfrac{2}{\pi}} \dfrac{eZ}{4\pi\varepsilon_0} \dfrac{\omega}{\gamma v^2} K_1\left(\dfrac{\omega b}{\gamma_L v}\right), \\ B_{\text{long}}(\omega, b) = 0, \\ B_{\text{transv}}(\omega, b) = \dfrac{E_{\text{transv}}}{c}, \end{cases} \tag{2.1}$$

where ω is the photon frequency; K_0 and K_1 are the modified Bassel functions.

At this point, one can describe the electromagnetic field in terms of a photon flux. Considering that each photon energy is $E_\gamma = \hbar\omega$, the flux of equivalent photons, emitted by a charged ion, is calculated using a Fourier transform of the time-dependent electromagnetic field. To observe the ions' field lines, which resemble a superposition of real photons when observed from a sufficient distance to the beam ions, one can analyse the Ultra-Peripheral Collisions [61], described in Figure 2.1, in which the impact parameter b (reported in Section 1.4.2) is larger than the sum of the two radii, so $b > R_A + R_B$. In this kind of interactions, the fm range of the strong force and the weakness of the gravitational and weak forces make them almost inexistent and the collisions are mediated exclusively by the electromagnetic interaction.

The photon flux is given by

$$N(\omega, b) = \frac{\mathrm{d}N^2}{\mathrm{d}\omega \mathrm{d}b} = \frac{Z^2\alpha}{\pi^2\beta^2\omega b^2}\zeta^2\left(\frac{1}{\gamma_L^2}K_0^2(\zeta) + K_1^2(\zeta)\right), \tag{2.2}$$

where α is the fine structure constant and $\zeta = \frac{b\omega}{\beta\gamma_L}$. For ultra-relativistic particles, $K_1^2 \gg$

[1] $\gamma_L = \left(1 - v^2/c^2\right)^{-1/2}$.

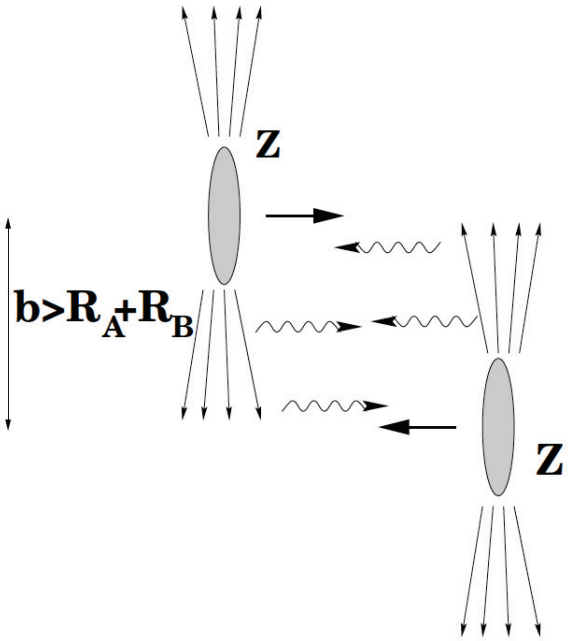

FIGURE 2.1. Schematic diagram of Ultra-Peripheral Collisions, from [62]. The impact parameter b is larger than the sum of the radii of A and B ions (in our case $A = B$ =Pb): $b > R_A + R_B$. Lorentz contraction occurs in the electromagnetic fields of very energetic charges. These fields can be treated as a flux of real (or quasi-real) γ.

$\frac{1}{\gamma_L^2} K_0^2$, so the transverse direction component is dominant. The maximum energy of a photon flux in the laboratory frame is

$$\omega^{\max} = \frac{\hbar}{\Delta t} \sim \frac{\hbar \gamma_L v}{b} \approx \frac{\gamma_L}{R},$$

where R is the nucleus radius[2]. The photon energy spectrum is determined by the shortest distance between the target and the charge, as well as the particle velocity.

Since there are many equivalent photons in each collision, the single photon cross-section must be converted into an effective multi-photon cross-section [63] as follows

$$\sigma = \int \frac{n(\omega)}{\omega} \sigma^{\gamma}(\omega) \mathrm{d}\omega, \tag{2.3}$$

where σ is the multi-photon cross-section; $n(\omega)$ is the equivalent photon flux and σ^{γ} the cross-section of a single photon.
The $n(\omega)$ term can be calculated with a Fourier transform and can be expressed via the

[2] $R = 1.2A^{1/3}$ fm where A is the nucleon number.

integration of $N(\omega)$ (that is the equivalent flux of photons per unit area (Equation 2.2)) over the impact parameter

$$n(\omega) = \int_{b>2R_A} N(\omega, b) \mathrm{d}^2 b = \frac{2\alpha Z^2}{\pi E_\gamma} \left(x K_0 K_1 - \frac{1}{2} x^2 (K_1^2(x) - K_0^2(x)) \right), \tag{2.4}$$

with $x = \frac{2RE_\gamma}{\beta\gamma}$. The behavior of the E-field of the nucleus at $v = 0$ and $v \sim c$ is shown in Figure 2.2.

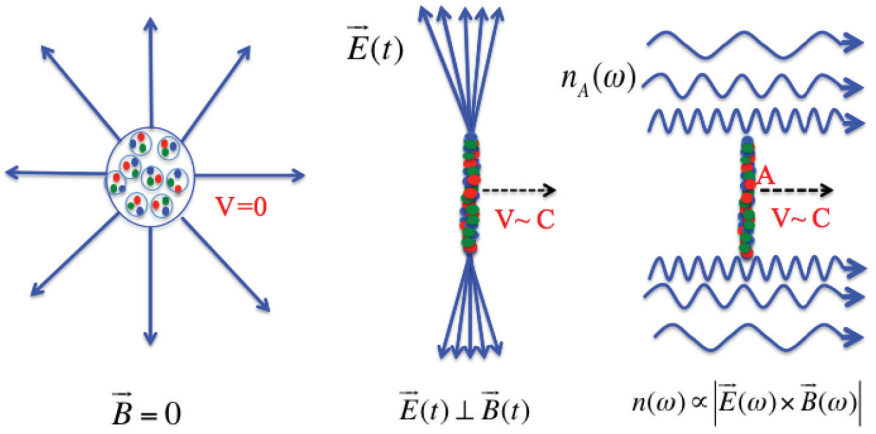

FIGURE 2.2. *Left*: the E-field at $v = 0$ is isotropic and the B-field is equal to 0. *Center*: the E_{transv} at $v \sim c$ is the unique component of the E-field and the B-field is perpendicular to it. *Right*: the $n(\omega)$ photon spectrum at $v \sim c$, from [64]. Since the E-field is more intense when b grows, the photons with higher energy are created far from the nucleus.

2.2 Photo-nuclear processes

FOR many decades, photo-nuclear reactions have been studied and are regarded as critical processes for understanding of the nuclear structure and the basic dynamics of the nucleonic system.

Photon interactions with nuclei may be categorized as direct or resolved from the perspective of a Fock space decomposition [65]. In direct interactions, the photon operates as a point-like particle ("bare photon"), whereas in resolved interactions, it fluctuates into a $q\overline{q}$ state or an even more complicated partonic configuration composed of quarks and gluons. Figure 2.3 shows these two processes that will be described in Sections 2.2.1 and 2.2.2.

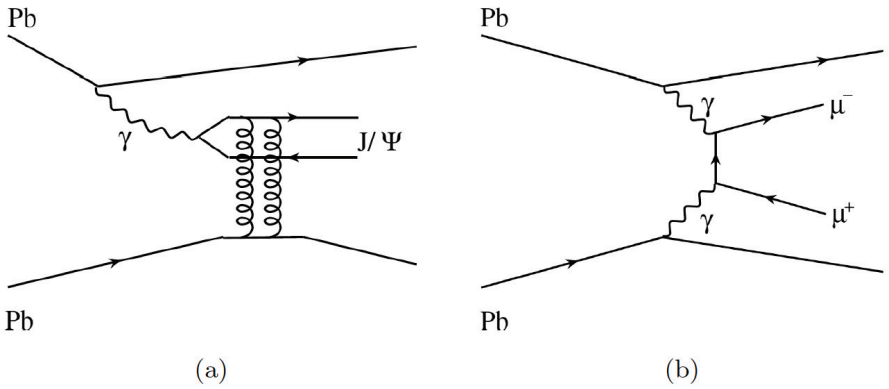

FIGURE 2.3. Feynman diagrams for the photoproduction of vector mesons, like J/ψ, (*a*) and the two-photon process (*b*) in ultra-peripheral Pb-Pb collisions.

In general, three different kinds of photoproduction reactions are identified: the *elastic* interaction where the ion target remains intact, the *nucleus dissociation* into low-mass systems and the *nucleus break-up with a colour transfer* in the *inelastic collision* case. In this Ph.D. thesis, the focus will be on the *elastic scattering interactions*, described by the following formula

$$\gamma + \mathrm{Pb} \longrightarrow J/\psi + \mathrm{Pb}.$$

2.2.1 $\gamma\gamma$ interactions

WHEN two photons collide, they generate new particles without any hadronic interaction, as illustrated in Figure 2.4. The $\gamma\gamma$ interactions cross-section is given by

$$\sigma_{\mathrm{direct}} = \int \mathrm{d}\omega_1 \mathrm{d}\omega_2 \frac{n(\omega_1)}{\omega_1} \frac{n(\omega_2)}{\omega_2} \sigma^{\gamma\gamma \longrightarrow X}, \tag{2.5}$$

here $n(\omega_1)$ and $n(\omega_2)$ represent the photon densities of the two ions and $\sigma^{\gamma\gamma \longrightarrow X}$ represents the interaction cross-section between two photons. The final state X might be composed of lepton pairs like $\mu^+\mu^-$ [66].

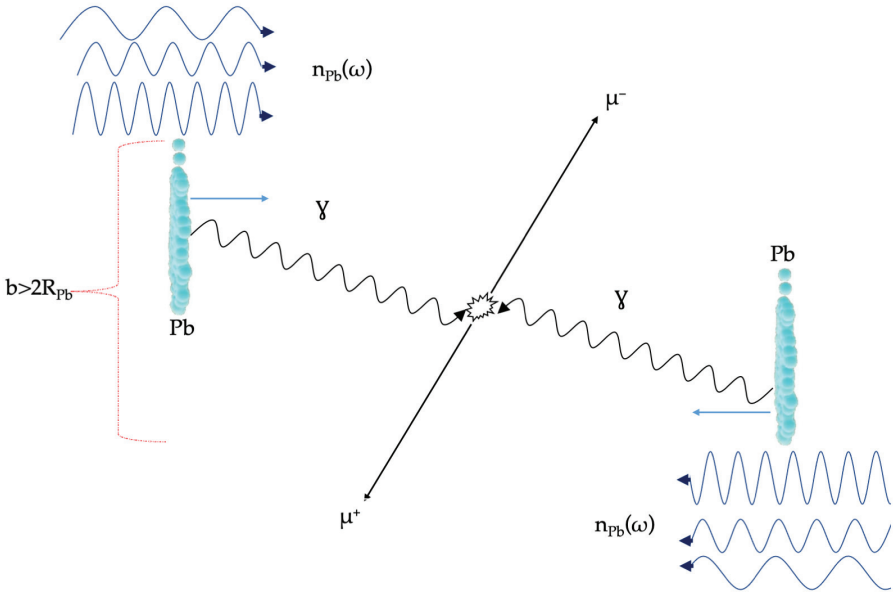

FIGURE 2.4. UPC $\gamma\gamma$ interaction. Two photons from Pb nuclei interact creating a dilepton (such as $\mu^+\mu^-$).

2.2.2 γA interactions

THE "cloud" of photons around the nucleus at ultra-relativistic collisions looks like a beam of virtual photons, that can interact with the other nucleus. The incident γ can fluctuate into a $q\overline{q}$ pair, which then interacts hadronically with the other ion target, producing a vector meson, or into a virtual vector meson, which exchanges momentum with the target, causing production of a real meson, as depicted in Figure 2.5.

The cross-section of this process can be obtained equivalently to Equation 2.5, with the cross-section of the vector production in γA interaction written as [62]

$$\frac{d\sigma^{\gamma \mathrm{Pb} \longrightarrow X\mathrm{Pb}}}{dt} = \frac{d\sigma}{dt}\bigg|_{t=0} |F_{\mathrm{Pb}}(t)|^2, \tag{2.6}$$

where $\frac{d\sigma}{dt}\Big|_{t=0}$ is the forward scattering amplitude which carries the dynamical information and $F_{\mathrm{Pb}}(t)$ is the form factor that affects the momentum transfer of the elastic scattering. The form factor is dependent on the spatial characteristics of the target nucleus and is equal to the Fourier transform of the charge density of the target.

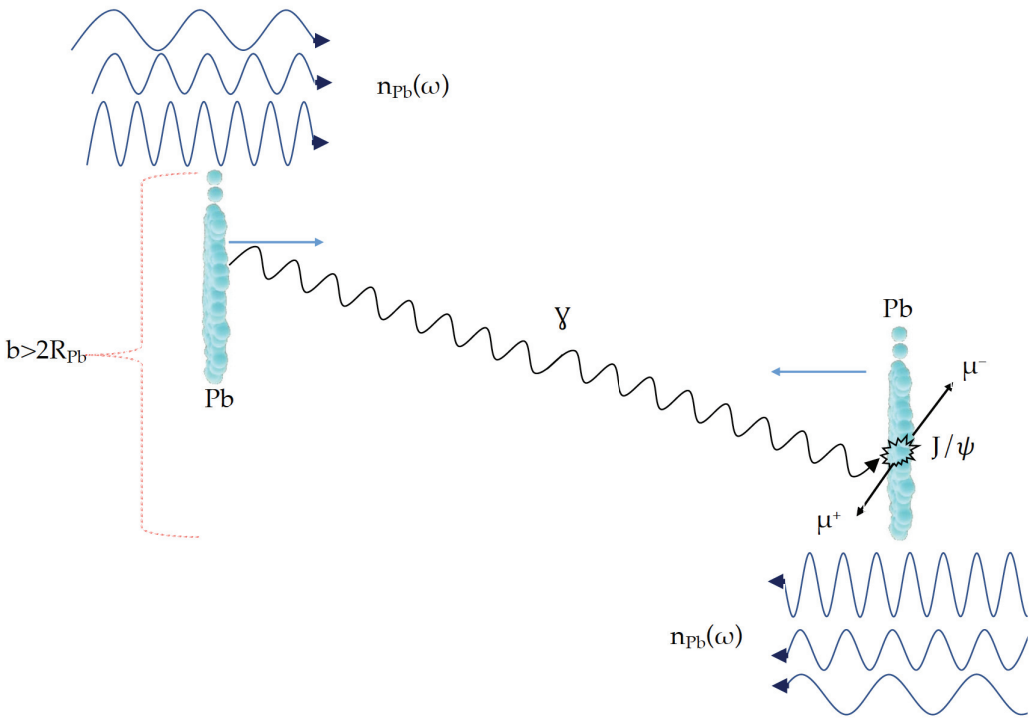

FIGURE 2.5. UPC γA interaction. The photon from one of the two Pb nuclei fluctuates into a J/ψ meson which further decays into a $\mu^+\mu^-$ pair.

2.2.3 Vector meson production

DURING a photo-nuclear interaction, a vector meson production can be produced in the final state. This process can be understood within the Vector Meson Dominance (VMD) theory [67]: a photon can fluctuate into a $q\overline{q}$ pair and because the photon has spin 1 and negative parity, the fluctuation will most likely turn into a vector meson.

Before any interaction, the photon is transformed into a virtual vector meson. Figure 2.6 depicts a graphical illustration of elastic meson production. The photon fluctuates into a vector meson, which scatters off of the proton via pomeron[3] exchange. Donnachie and Landshoff [69] found the parameters of the pomeron by a global fit to pho-

[3]Well before the quark model became the general paradigm in particle physics, the notion of Regge poles [68] was the prevalent model for elementary particle scattering. The Regge pole theory fits scattering cross-sections using the complex plane and Regge trajectories, with the poles corresponding to resonances with particular spins near the resonance mass but arbitrary spins off. The exchange of Regge poles was fitted using scattering cross-section data (instead of single particles). At a period when it seemed that the Regge pole model would be the model for hadronic interactions, it was required to account for elastic scattering, i.e., when nothing else occurred than energy exchange. The pomeron trajectory was employed for this application of the Regge trajectory.

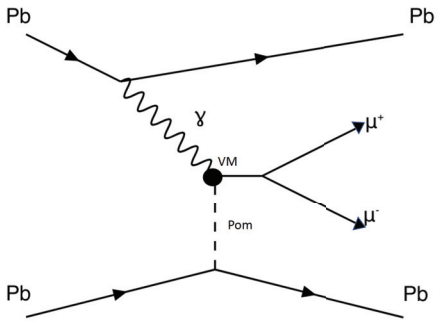

FIGURE 2.6. The photon fluctuates into a vector meson that scatters off of a Pb nucleus via an exchange of a pomeron.

toproduction data. For small values of Q^2, the exchange of the "soft" pomeron governs the production of light vector mesons ρ^0, ω, ϕ [70]. At high values of Q^2, the production of heavy vector mesons $J/\psi, \psi', \Upsilon$ is driven by the interchange of two pomerons [71].

The left side of Figure 2.3 shows the photo-nuclear process studied in this Ph.D. thesis: the J/ψ meson photoproduction in UPC at $\sqrt{s} = 5.02$ TeV. Nuclei photoproduction has two channels of vector mesons production : the *coherent* and *incoherent* [72, 73, 74, 75].

- *Coherent photoproduction* : the emitted photon interacts with the target nucleus as a whole. The transverse impulsion p_T is of the order of $1/2\ R_{Pb}$, so $p_T \sim 0.06$ GeV/c.
- *Incoherent photoproduction* : the photon interacts with a single nucleon, not with the entire nucleus. Since the radius of the nucleon is lower than the radius of the nucleus, the generated system has a greater transverse momentum, at the order of ~0.3 GeV/c.

In Figure 2.7, one can observe the different components of the p_T spectrum and the coherent and incoherent photoproduction regions. The templates used to fit the p_T spectrum were modelled using STARlight event generator and represent the various production mechanisms: coherent J/ψ, incoherent J/ψ, feed-down J/ψ from coherent ψ' decays, feed-down J/ψ from incoherent ψ' decays and continuum dimuons from the $\gamma\gamma \longrightarrow \mu^+\mu^-$process. In order to describe the high-p_T tail of the spectrum, the incoherent J/ψ photoproduction accompanied by nucleon dissociation (magenta line in Figure 2.7) was also taken into consideration using a template based on the H1 parametrisation [77].

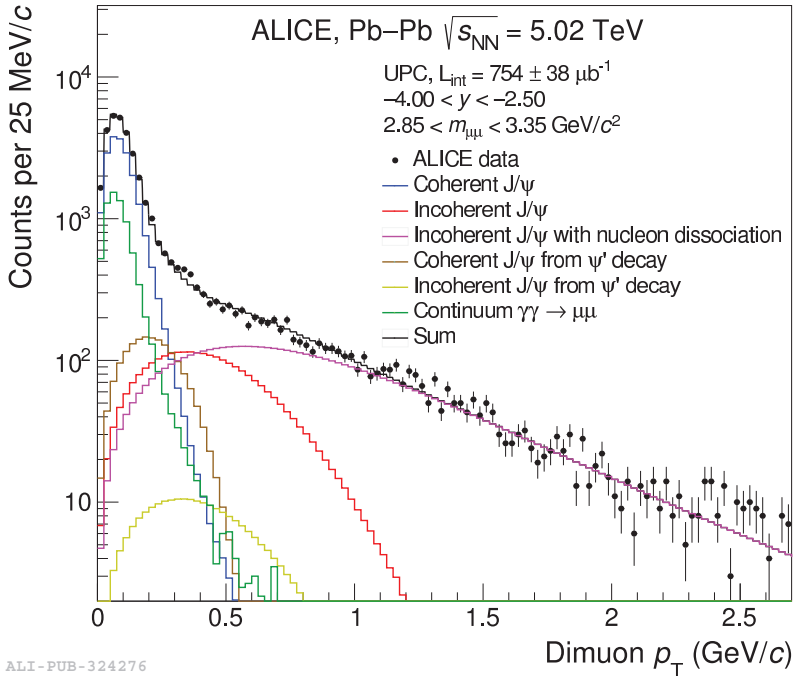

FIGURE 2.7. Transverse momentum distribution of muon pairs in the range $2.85 < m < 3.35$ GeV/c^2 (around the J/ψ mass), from [76].

In the present manuscript, the analysis of incoherent data in the p_T range between 0.35 and 2 GeV/c will be presented.

2.2.4 The gluon distribution function

IN Section 1.2.4, the Parton Distribution Functions (PDFs) have been briefly described. Thanks to the HERA measurements as a function of Bjoken-x and Q^2, it was observed that the gluon distribution of the proton grows very fast at small x values. QCD predicts that this growth will eventually lead to high gluon density and eventually a "saturation", which is the point of balance between gluon generation and annihilation. Because of the significantly higher gluon densities in the nucleus than in the proton, the photo-nucleus interactions are a perfect tool to study the gluon saturation. Moreover, at the LHC energies, the study the gluon distribution of Pb nuclei at small values of x became possible also for perturbative scales Q^2.

The motivation for studying the photoproduction of J/ψ is its link with the gluon distribution function in Pb at $Q^2 \sim \frac{M_{J/\psi}^2}{4}$. Starting from Equation 2.6, the expression for the

forward scattering amplitude in leading order QCD [78] with two-gluon exchange is

$$\frac{\mathrm{d}\sigma(\gamma\mathrm{Pb} \longrightarrow V\mathrm{Pb})}{\mathrm{d}t}\Big|_{t=0} \propto \left[x g_{\mathrm{Pb}}(x,Q^2)\right]^2, \tag{2.7}$$

where $x = \frac{M_V^2}{W_{\gamma\mathrm{Pb}}^2}$ is the longitudinal fractional momentum carried by the gluons, $g_{\mathrm{Pb}}(x,Q^2)$ is the gluon distribution function of the nucleus and $W_{\gamma\mathrm{Pb}}$ is the γ-Pb center of mass energy. It is evident that vector meson production is a particularly sensitive probe of the gluon distribution of the nucleus.

It is worth noting that the gluon distribution of the nucleus cannot be determined by simply scaling the gluon distribution of the proton. For Bjorken x values below 0.1, the so-called shadowing occurs and the ratio of the nucleus structure function to the proton structure function drops.

The LHC, that will be described in Chapter 3, provides the highest energy collisions created in a laboratory, resulting in a greater range of x for a given value of Q^2. The Bjorken-x of the pomeron is connected to the rapidity of coherently generated J/ψ. The process is sensitive to $x \sim 10^{-3}$ for Run 1 energies and $x \sim 6 \cdot 10^{-4}$ for Run 2 energies at midrapidity. The collinear PDFs do not include information regarding the distribution of gluons in the transverse plane. In this plane, saturation models anticipate intriguing signatures [79]. To get this information, it is necessary to measure the cross-section's dependency on $|t|$[4] at various rapidities. In case of vector meson production in UPC at LHC, one can approximate $t \approx {p_{\mathrm{T}}}^2$.

2.2.5 Mandelstam variables

KINEMATICS of any type $A+B \Longrightarrow C+D$ dispersion process may be represented using the three Mandelstam's variables [80, 81].

$$\begin{cases} s = -c^2(p_A + p_B)^2 + (E_A + E_B)^2, \\ t = -c^2(p_A - p_C)^2 - (E_A - E_C)^2, \\ u = -c^2(p_A - p_D)^2 + (E_A - E_D)^2. \end{cases}$$

[4] t stands for the Mandelstam variable corresponding to the momentum transfer from the target nucleus.

Lorentz invariance applies to all variables. In the center of mass system $(p_A + p_B)$ variable s is reduced to:

$$s = (E_A + E_B)^2$$

Therefore, s is the square of the total energy in the mass-center system and may be specified for any type of particle collision. If s and t are known, u may be expressed as a function of s and t using the equation $s + t + u = (m_A^2 + m_B^2 + m_C^2 + m_D^2)c^4$, where m_A, m_B, m_C and m_D are the masses of the incident and scattered particles, respectively.

The variable t indicates the momentum transported to the core, which is approximated by $t = {p_T}^2$ for the vector meson.

2.3 Experimental results for J/ψ photoproduction

DIFFERENT experiments studied the photoproduction processes for the J/ψ mesons. Here, an overview will be reported.

2.3.1 First observation of photoproduction

IN 2002 [82], the STAR collaboration [83] observed the exclusive coherent ρ^0 production which was one of the earliest observations of vector meson photoproduction in UPCs. The source nucleus generated a virtual photon that fluctuated into a ρ^0 meson that

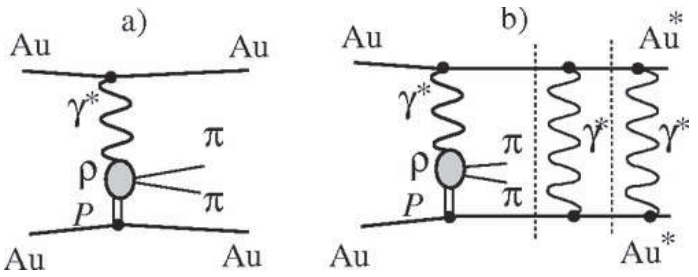

FIGURE 2.8. Diagram for (a) exclusive ρ^0 production in UPCs and (b) ρ^0 production with nuclear excitation. The dashed lines indicate factorization, from [82]. P corresponds to the pomeron.

scatters elastically off the target nucleus. The ρ^0 decayed into a pair of pions with opposing charges. In the STAR tracker, these pions left two back-to-back tracks. Figure 2.8 shows the processes highlighted by the STAR Collaboration.

2.3.2 J/ψ photoproduction in small systems

2.3.2.1 Results from $p\overline{p}$ collisions

THE first interesting result on J/ψ photoproduction in $p\overline{p}$ collisions at $\sqrt{s_{\mathrm{NN}}} = 1.96$ TeV at the Tevatron by the CDF collaboration [84] and it is showed in Figure 2.9.

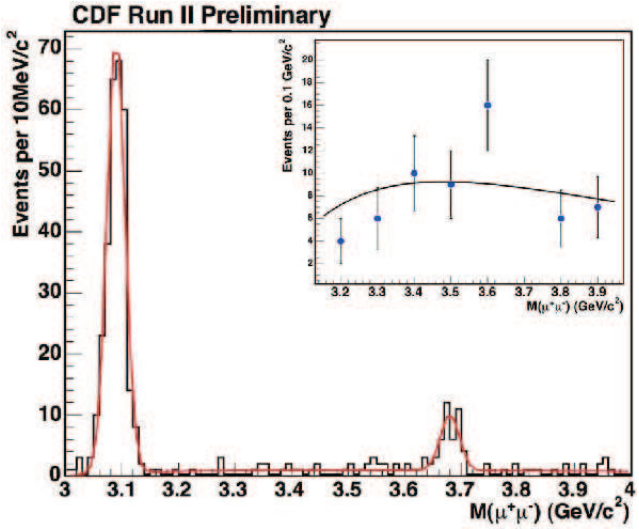

FIGURE 2.9. Mass $M_{\mu\mu}$ distribution of 402 exclusive events, with no EM shower (histogram), together with a fit to two Gaussians for the J/ψ and ψ', and a QED continuum. All three shapes are predetermined, with only the normalizations floating. Inset: Data above the J/ψ and excluding $3.65 < M_{\mu\mu} < 3.75$ GeV/c^2 [ψ'] with the fit to the QED spectrum times acceptance (statistical uncertainties only), from [84].

The found cross section $\frac{\mathrm{d}\sigma}{\mathrm{d}y}\Big|_{y=0}$ is equal to 3.92±0.25(stat)±0.52(syst) nb. The data are consistent with a power law in $W_{\gamma p}$ with $\delta = 0.72$ [85].

2.3.2.2 Results from HERA - ep collisions

CONCERNING HERA collider, H1 detector [86] measured the J/ψ photoproduction using electron-proton collisions in the range $40 \leq W_{\gamma p} \leq 305$ GeV and $40 \leq W_{\gamma p} \leq 160$ GeV. The data fit a power law in $W_{\gamma p}$ with $\delta = 0.754 \pm 0.033$ (stat)$\pm$ 0.032 (syst), and the result reveals no Q^2 dependence [87]. The ZEUS collaboration, for its part, measured the J/ψ photoproduction using ep collisions in the range $20 \leq W_{\gamma p} \leq 290$ GeV and the data are consistent also with a power law in $W_{\gamma p}$ with $\delta = 0.69 \pm 0.02$(stat) $\pm$ 0.03(syst) [88].

The cross sections results from H1 and ZEUS experiments are reported in Figure 2.11b.

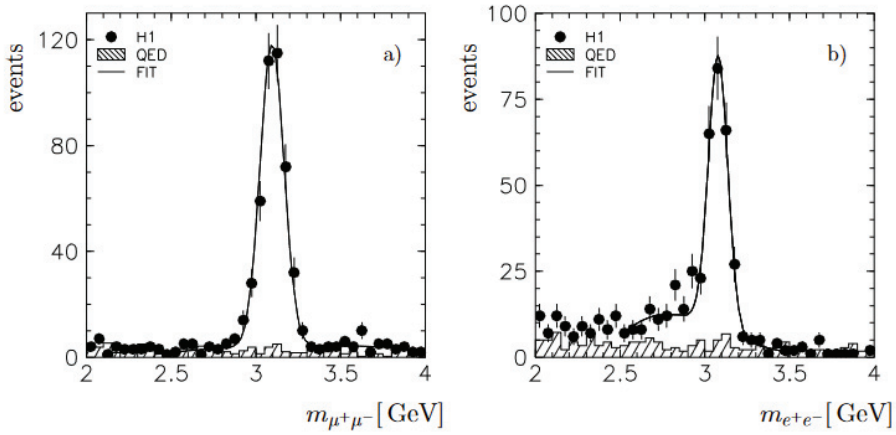

FIGURE 2.10. Mass distribution for $\mu^+\mu^-$ (a) and e^+e pairs (b) for the two track selection above 2 GeV. The curves are fits of a Gaussian plus a polynomial background to the J/ψ mass region. The shaded histogram shows the contribution of QED lepton pairs. For $\mu^+\mu^-$ the maximum of the fit is at 3.10 ± 0.01 GeV with a width of 76 MeV. For e^+e the maximum is at 3.08 ± 0.02 GeV and the width is 77 MeV. For both cases the detector simulation yields a width of 65 MeV, from [87].

2.3.2.3 Results from the LHC collaboration in pp collisions

AT $\sqrt{s} = 7$ TeV, the LHCb collaboration observed exclusive photoproduction of the J/ψ in pp collisions [89]. The cross section times the branching fraction to two muons with pseudorapidities ranging from $2.0 < \eta < 4.5$ is 307±21±36 pb for exclusive J/ψ. The results are compatible with a power law dependence and existing H1 and ZEUS conclusions [89], as shown in Figure 2.12b.

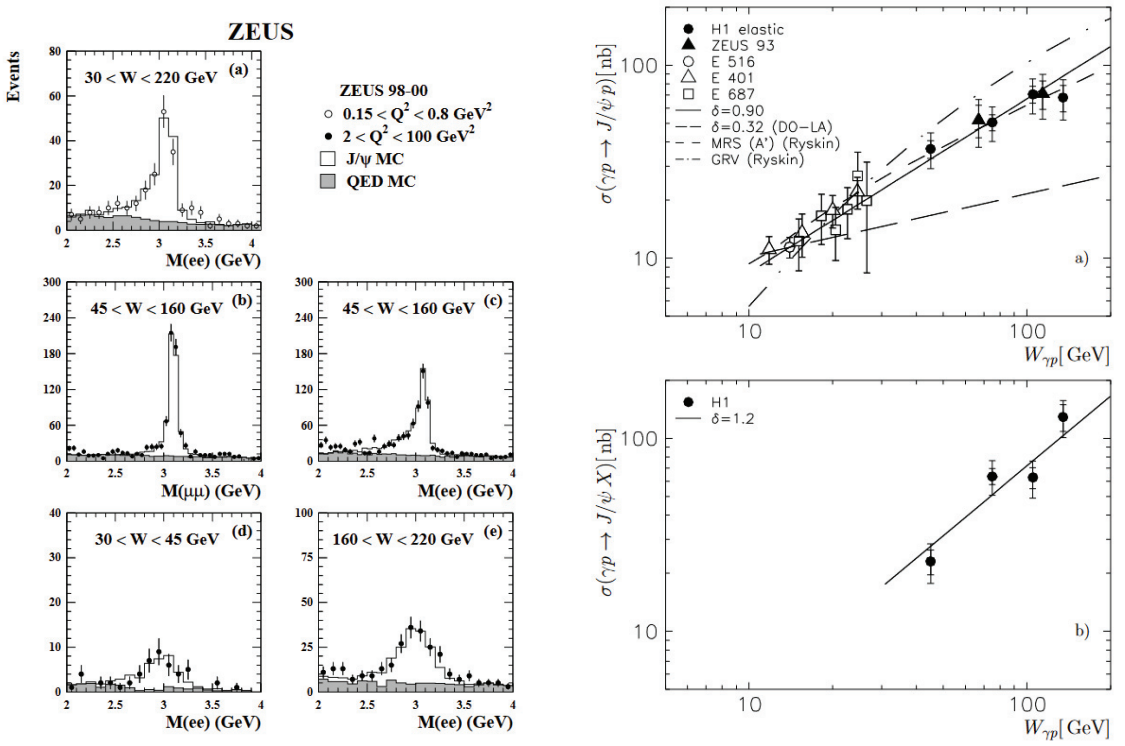

(A) (B)

FIGURE 2.11. (A) - Left : Invariant mass distributions of the lepton pairs for (a) the low-Q^2 sample and (b)-(e) the high-Q^2 sample. The shaded histograms are the QED MC distributions and the open histograms the sum of the J/ψ and QED MC events.The small excess of data at low mass is due to background from pions. The error bars indicate the statistical uncertainties, from [88]. (B) - Right : a) Total cross section for elastic J/ψ photoproduction. b) Total cross section for J/ψ-production with proton dissociation, from [87].

2.3.2.4 Results from the ALICE collaboration in pPb collisions

USING proton-lead UPc at $\sqrt{s_{\mathrm{NN}}}$ = 5.02 TeV, the ALICE collaboration detected the exclusive photoproduction of J/ψ [90]. Figure 2.13 depicts the dimuon invariant mass spectra in two rapidity ranges. Both data sets clearly show the J/ψ peak, which is nicely represented by a Crystal Ball parametric. As expected from two-photon creation of continuum $\gamma\gamma \longrightarrow \mu^+\mu^-$, the dimuon continuum is well represented by an exponential.

In Figure 2.14a, predictions for the non-exclusive (red), (green) and Pb (pink) contributions are presented alongside the dimuon p_{T} spectra for J/ψ candidates. For both the ALICE data and the H1 and ZEUS observations from the HERA ep collider, the cross section $\sigma(\gamma$+p$\longrightarrow$ J/ψ + p) *vs* the pp center of mass energy $W_{\gamma p}$ is shown in Figure 2.14b.

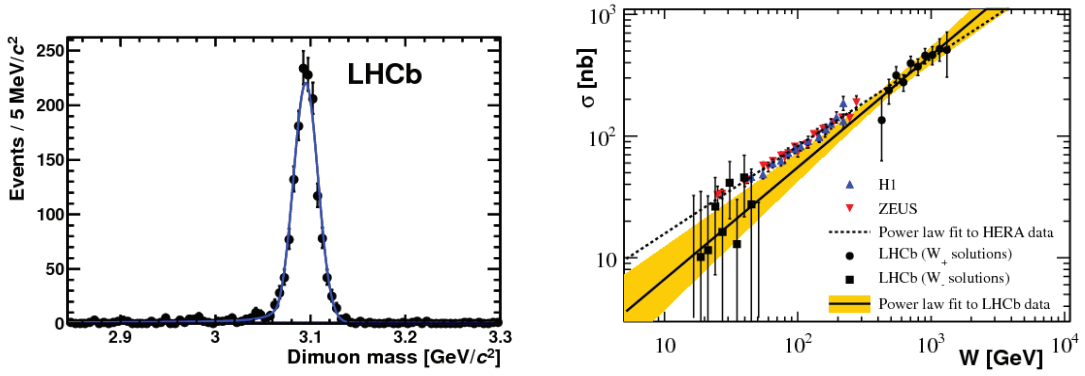

(A) (B)

FIGURE 2.12. (A) Invariant mass distributions in the regions of the J/ψ mass peaks for events with exactly two tracks, no photons and a dimuon with p_T below 900 MeV/c. The overall fits to the data are shown by the full curves while the dashed curves show the background contributions. (B) Dependence of J/ψ photoproduction cross-section on the centre-of-mass energy of the photon-proton system. The blue (red) triangles represent the data from H1 (ZEUS). The black dots and squares are derived from the LHCb differential cross-section as a function of rapidity. The dashed and full lines are the power law dependences determined from the HERA and LHCb data, respectively. The uncertainty on the LHCb power law determination is shown by the shaded band, from [89].

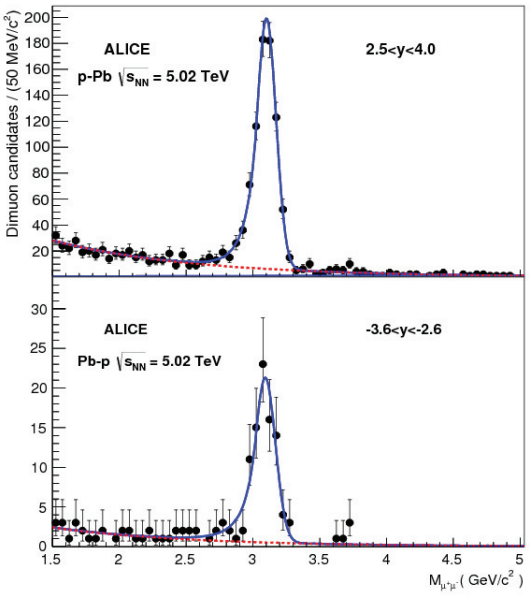

FIGURE 2.13. Invariant mass distribution for events with two oppositely charged muons, for both forward (top panel) and backward (bottom panel) dimuon rapidity samples, from [90].

Several theoretical models' predictions are also provided. The data cover an energy range of 20 to 700 GeV, corresponding to Bjorken-x values ranging between $x \sim 10^{-3}$ and $x \sim 10^{-5}$. The data from the three experiments has also been fitted to a power law of the form $\sigma \propto W^{\delta}$.

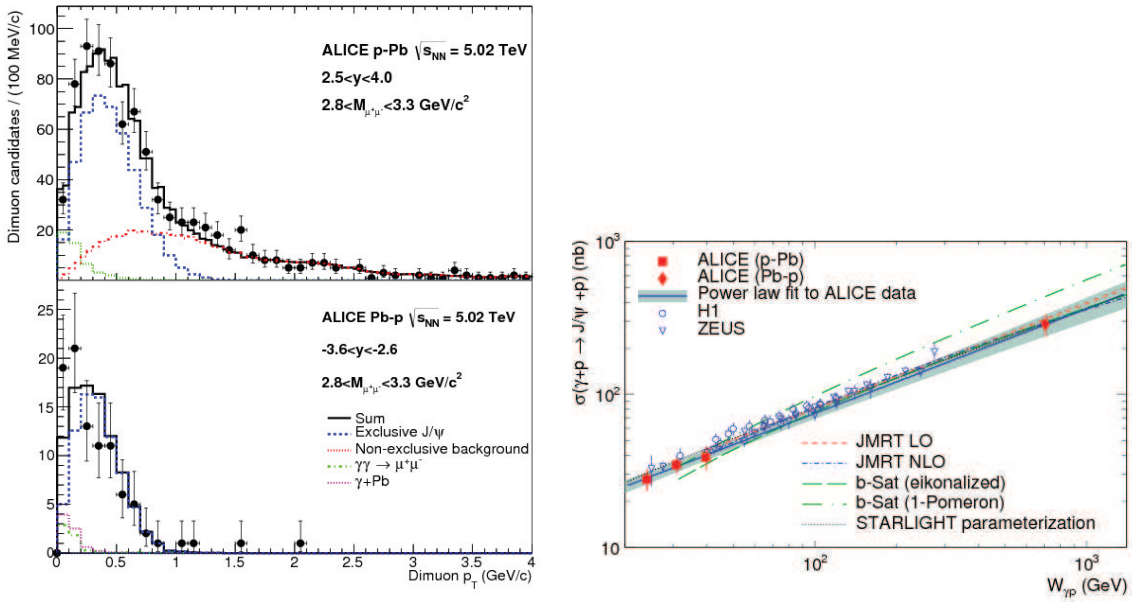

(A) (B)

FIGURE 2.14. (A) - Left : Transverse momentum distribution for events with two oppositely charged muons, for both forward (top panel) and backward (bottom panel) dimuon rapidity samples, from [90]. (B) - Right : Exclusive J/ψ photoproduction cross section off protons measured by ALICE and compared to HERA data. Comparisons to STARLIGHT, JMRT and the b-Sat models are shown. The power law fit to ALICE data is also shown, from [90].

Fitting the ALICE data provides $\delta = 0.68 \pm 0.06$ (stat+syst). As a result, there is no noticeable difference in the evolution of gluon density between HERA and LHC energies for protons.

2.3.3 J/ψ photoproduction in heavy ions collisions

2.3.3.1 BNL results

THE PHENIX collaboration measured the photoproduction cross section of J/ψ in ultra-peripheral Au-Au collisions at $\sqrt{s_{\mathrm{NN}}} = 200$ GeV at mid-rapidity in coincidence with forward neutrons [91]. The J/$\psi \longrightarrow e^+e^-$ decay channel was used for their measurement. The invariant mass distribution of the e+e couples is seen in Figure 2.15a. The results clearly reveal a J/ψ peak above an exponential background. Figure 2.15b depicts the data's p_{T} spectrum.

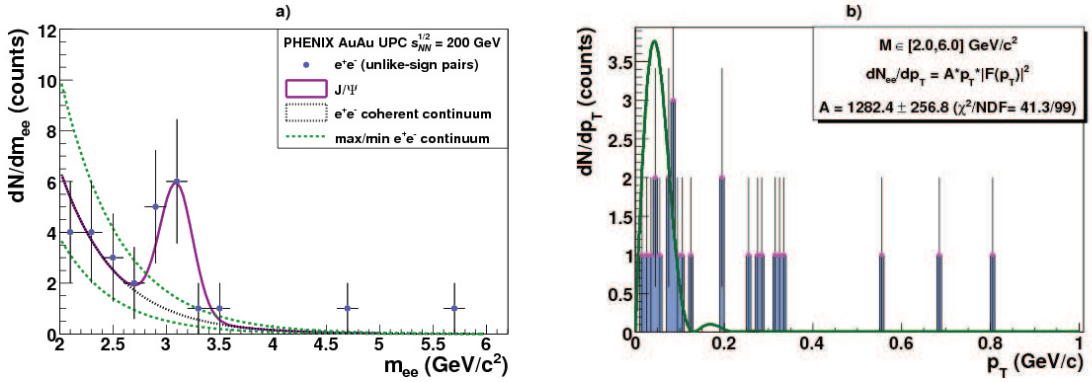

(A) (B)

FIGURE 2.15. (A) Invariant mass distribution of e^+e^- pairs fitted to the combination of a di-electron continuum (exponential distribution) and a J/ψ (Gaussian) signal. The two additional dashed curves indicate the fit results with the maximum and minimum continuum contributions considered in the analysis. (B) dN/dp_{T} distribution of the pairs with $m_{e^+e} > 2$ GeV/c^2 fitted to the Au nuclear form factor, from [91].

There is an enhancement of events with very low transverse momentum, consistent with coherent production, but also a significant number of higher p_{T} events. These are thought to be caused by incoherent production, which occurs when a photon interacts with a single nucleon.

The PHENIX J/ψ $+X_n$ cross section is compared to various theoretical models in Figure 2.16. Unfortunately, the number of events is too low to differentiate between the models.

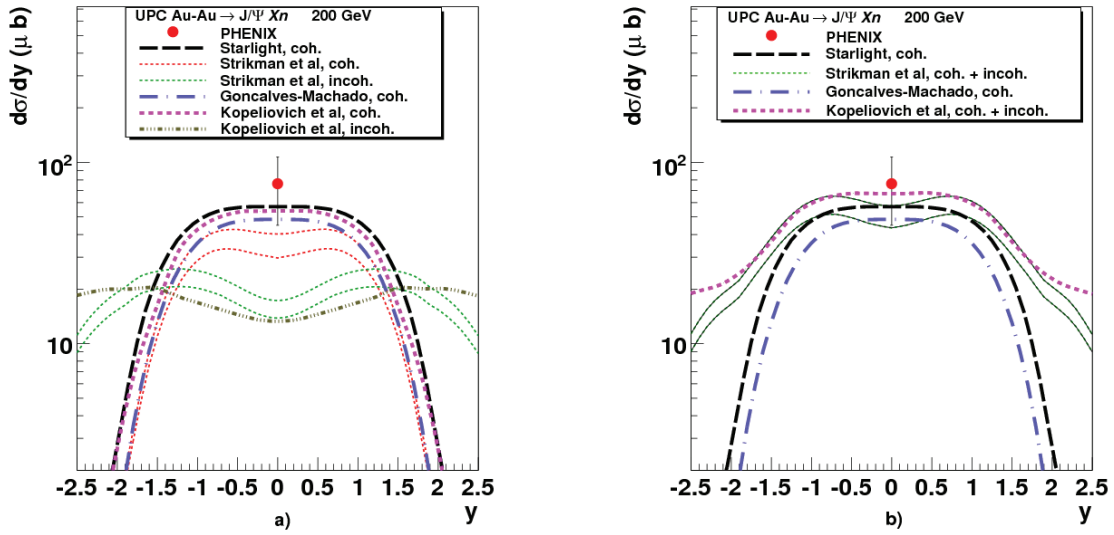

(A) (B)

FIGURE 2.16. Cross section of J/ψ +X_n production at midrapidity in UPC Au+Au collisions at $\sqrt{s_{\mathrm{NN}}}$ = 200 GeV compared to theoretical calculations. The error bar (box) shows the statistical (systematical) uncertainties of the measurement. When available, the theoretical calculations for the coherent and incoherent components are shown separately in (A), and summed up in (B), from [91].

2.3.3.2 ALICE and CMS collaborations results

In 2015, the ALICE and CMS collaborations explored ultra-peripheral coherent the J/ψ photoproduction using 2011 Pb-Pb data at $\sqrt{s_{\mathrm{NN}}}$ = 2.76 TeV [92, 93].

Figure 2.17 illustrates the dimuon invariant mass and p_{T} from the CMS decay of coherent J/ψ.

This first measurement at forward rapidity of J/ψ photo-producted by the ALICE collaboration yielded a total of about a hundred potential coherent J/ψ candidates, as shown in Figure 2.18a. The related p_{T} spectrum in Figure 2.18b reveals a low p_{T} excess consistent with coherent J/ψ photoproduction expectations. Visual inspection of incoherent J/ψ photoproduction is also possible at higher p_{T}.

The cross section for coherent J/ψ photoproduction, for γ+ p$\longrightarrow$ J/ψ + p, has a power-law dependency on the photon-proton center-of-mass energy. Such information may be used to determine the gluon distribution in the proton as a function of Bjorken-x [94], as shown in Figure 2.14b from [90]. The UPC J/ψ photoproduction cross section in a nucleus-nucleus collision may be estimated using the heavy-ion impulse approxi-

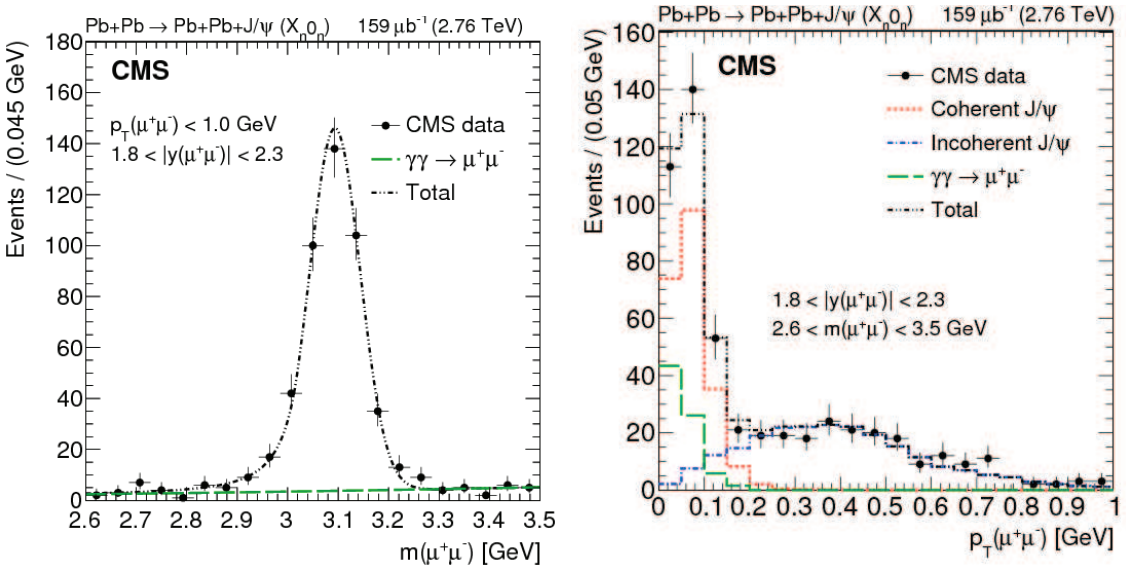

(A) (B)

FIGURE 2.17. Results from the simultaneous fit to dimuon invariant mass (A) and p_T (A) distributions from opposite-sign muon pairs with $p_T < 1.0$ GeV/c, $1.8 < y < 2.3$ and $2.6 < m(\mu^+\mu^-) < 3.5$ GeV/c^2. In the left panel the green curve represents the $\gamma+\gamma$ component (second-order polynomial) and the black curve the sum of the $\gamma+\gamma$, incoherent J/ψ, and coherent J/ψ components (see text for details). In the right panel the green, red, and blue curves represent $\gamma+\gamma$, coherent J/ψ, and incoherent J/ψ components, respectively. The black curve represents the sum of the $\gamma+\gamma$, coherent J/ψ, and incoherent J/ψ components. Only statistical uncertainties are shown. The data are not corrected by acceptance and efficiencies, and the MC templates are folded with the detector response simulation, from [93].

mation [95]. By scaling up the photon-nuclear cross section calculated from electron-proton collisions at HERA and the LHC, the impulse approximation shows the nucleus as a sum of protons and neutrons [96].

The ALICE and CMS collaborations' studies of UPC J/ψ photoproduction reveal that the measured cross section is compatible with nucleus models that combine moderately strong gluon shadowing, specifically EPSO9 [97, 98]. The cross sections obtained by ALICE and CMS are contrasted to theoretical models in Figure 2.19. The data clearly contradict the impulse approximation prediction. The cross sections show that the nuclear gluon density is suppressed in comparison to the proton at the energy scale of the J/ψ mass [99]. During Run 1, the midrapidity measurement of coherent J/ψ by the ALICE collaboration was more successful in distinguishing across models [100]. As illustrated in Figure 2.20, the single available midrapidity point is incompatible with models that have no or extremely significant nuclear shadowing effects. As a result, the ALICE collaboration has concluded that the data indicate moderate nuclear shadowing.

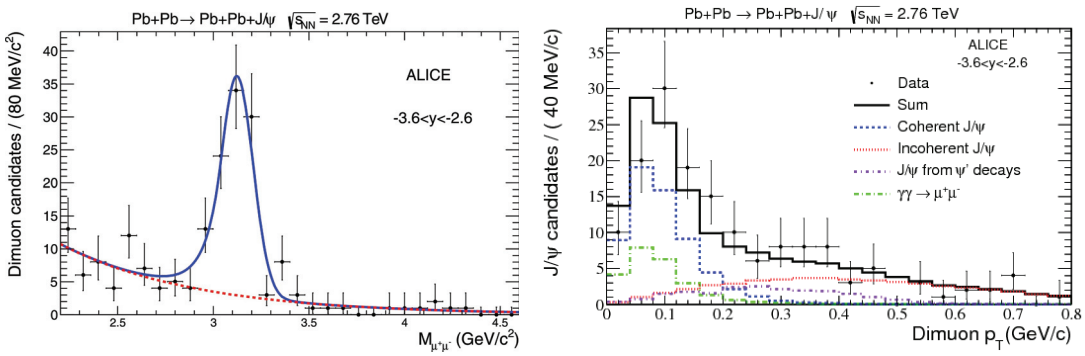

(A) (B)

FIGURE 2.18. (A) Summary of the contributions to the systematic uncertainty for the integrated J/ψ cross section measurement. The error for the coherent signal extraction includes the systematic error in the fit of the invariant mass spectrum and the systematic errors on f_D and f_I. (B) Dimuon p_T distribution for events satisfying the event selection described in the text. The data points are fitted summing four different Monte Carlo templates: coherent J/ψ production (dashed - blue), incoherent J/ψ production (dotted - red), J/ψs from ψ' decay (dash-dotted - violet), and $\gamma+\gamma \longrightarrow \mu^+\mu^-$ (dash-dotted - green). The solid histogram (black) is the sum, from [92].

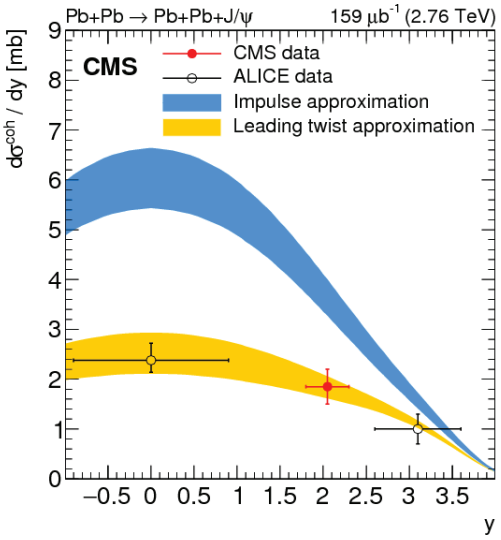

FIGURE 2.19. Differential cross section versus rapidity for coherent J/ψ production in ultra-peripheral PbPb collisions at $\sqrt{s_{\rm NN}} = 2.76$ TeV, measured by ALICE and CMS. The vertical error bars include the statistical and systematic uncertainties added in quadrature, and the horizontal bars represent the range of the measurements in y, from [97].

It is already intriguing to try to extract the so-called nuclear shadowing factor $S_{\rm Pb}$, de-

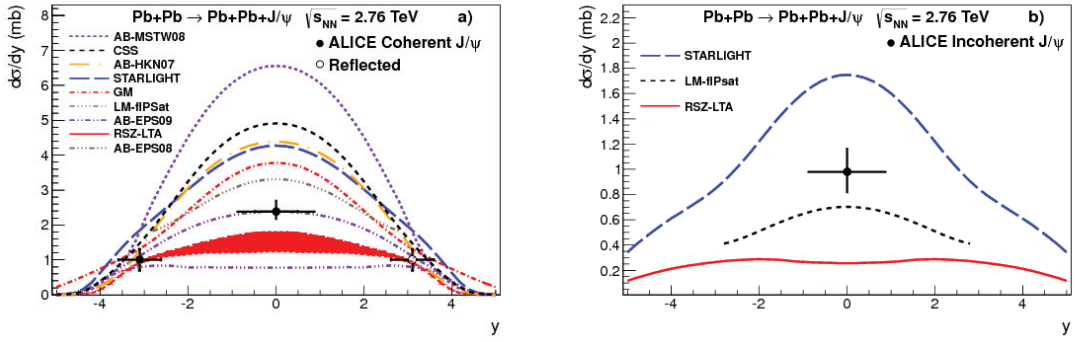

(A) (B)

FIGURE 2.20. Measured differential cross section of J/ψ photoproduction in ultra-peripheral Pb-Pb collisions at $\sqrt{s_{\mathrm{NN}}}$ = 2.76 TeV at -0.9 < y < 0.9 for coherent (A) and incoherent (B) events. The error is the quadratic sum of the statistical and systematic errors.

fined from the data as shown in the following Eq.

$$S_{\mathrm{Pb}} = \sqrt{\frac{\mathrm{d}\sigma_{\mathrm{data}}/\mathrm{d}y}{\mathrm{d}\sigma_{\mathrm{IA}}/\mathrm{d}y}},$$

where $\mathrm{d}\sigma_{\mathrm{data}}/\mathrm{d}y$ is the measured cross-section and $\mathrm{d}\sigma_{\mathrm{IA}}/\mathrm{d}y$ is the cross-section from the Impulse Approximation model [101][5], in which the nucleus is seen as a superposition of nucleons, all of which contribute to the interaction but have no nuclear effects. As shown in Figure 2.20b, the measurement of incoherent J/ψ photoproduction cross-section has been supplied by the ALICE Collaboration at midrapidity. No model can account for both coherent and incoherent J/ψ photoproduction trends.

The nuclear suppression factor, which is equivalent to the nuclear PDF calculation as a function of Bjorken-x, was calculated using ALICE and CMS data. The LHC results show nuclear gluon shadowing at low Q^2 and low Bjorken-x. Figure 2.21 compares results from ALICE and CMS to theoretical models of nuclear shadowing to the S_{Pb} ratio of the Pb PDF to the proton PDF as a function of Bjorken-x. This is the first experimental demonstration of shadowing effects in the Pb nucleus at high energies.

Additionally, results for coherent ψ' photoproduction at midrapidity with Run 1 data have been made public by the ALICE Collaboration [103]. The measurement was carried out in the channels $\psi' \longrightarrow l^+l^-, \mu^+\mu^-\pi^+\pi^-, e^+e^-\pi^+\pi^-$ where $l = e, \mu$, as shown in Figures 2.22, 2.23 and 2.24. The cross section is shown in Figure 2.25.

[5] In Figure 2.20, the Impulse Approximation is referred to as AB-MSTW08.

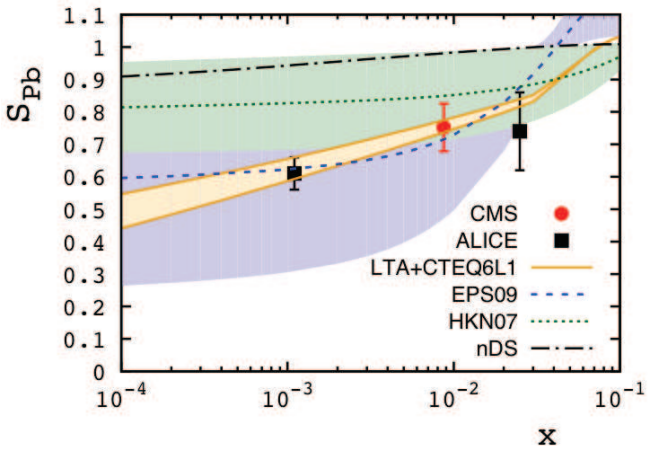

FIGURE 2.21. Measurements of nuclear shadowing, extracted from the CMS and ALICE data, compared with the EPS09 parameterization. Also shown is a leading twist calculation of shadowing, from [102].

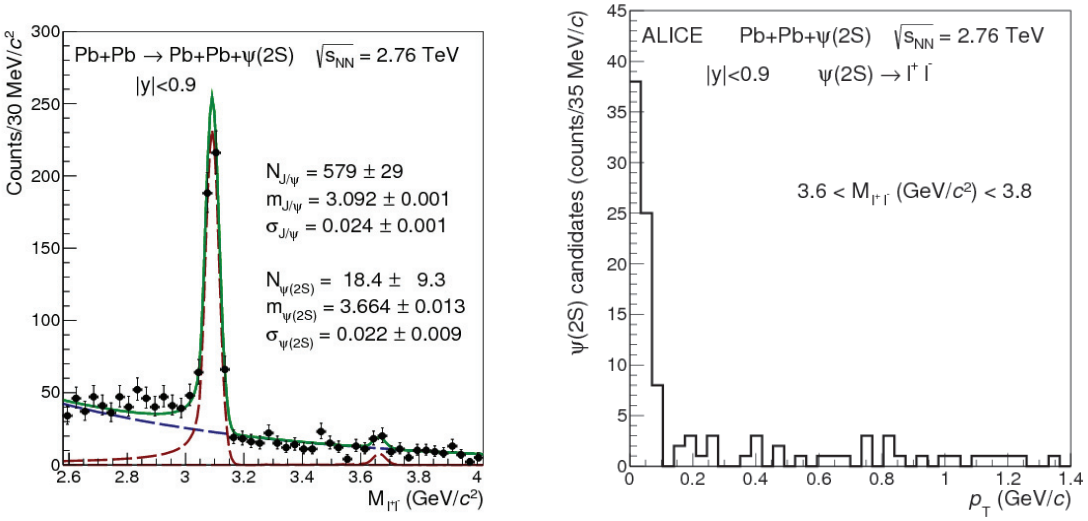

(A) (B)

FIGURE 2.22. Invariant mass (left) and p_T distributions (right) of ψ' for ultra-peripheral Pb–Pb collisions at $\sqrt{s_{NN}}$ = 2.76 TeV and $0.9 < y < 0.9$ for events satisfying the event selection. The channels $\psi' \longrightarrow l^+ l$, are shown l($l^+ l^{=e^+ e}$ and $\mu^+\mu^-$), from [103].

The ψ' has a nuclear shadowing factor equivalent to the J/ψ. ALICE finds a ratio for the

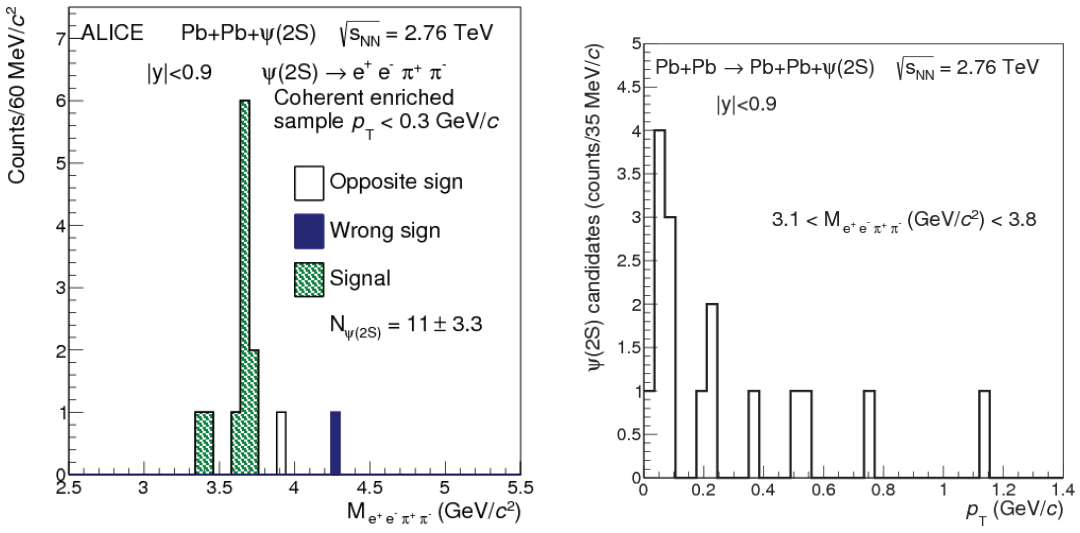

(A) (B)

FIGURE 2.23. Invariant mass (left) and p_T distributions (right) of ψ' for ultra-peripheral Pb–Pb collisions at $\sqrt{s_{NN}}$ = 2.76 TeV and $0.9 < y < 0.9$ for events satisfying the event selection. The $\psi' \longrightarrow \pi^+\pi^-\mu^+\mu^-$ channel is shown, from [103].

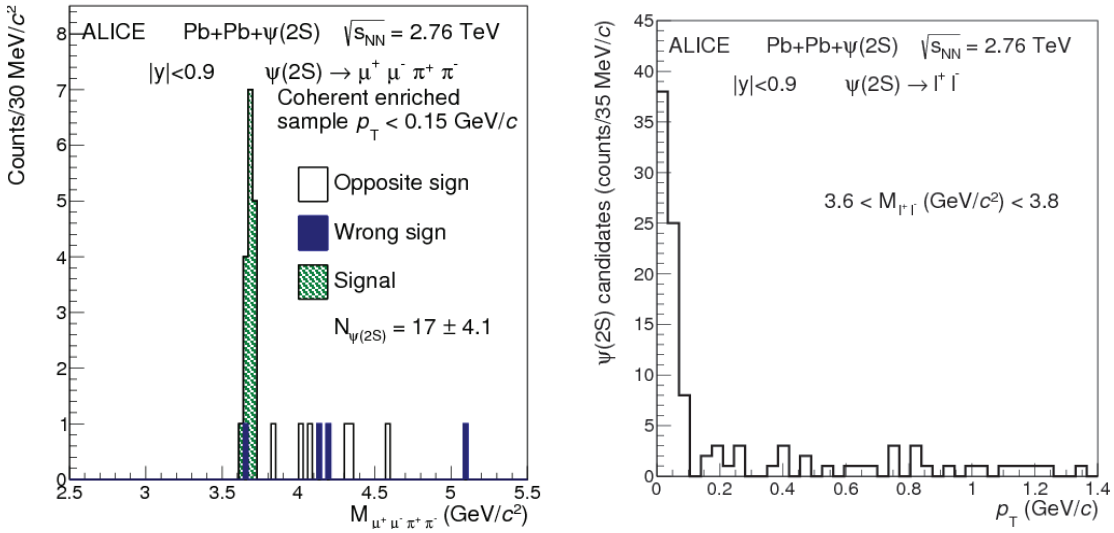

(A) (B)

FIGURE 2.24. Invariant mass (left) and p_T distributions (right) of ψ' for ultra-peripheral Pb–Pb collisions at $\sqrt{s_{NN}}$ = 2.76 TeV and $0.9 < y < 0.9$ for events satisfying the event selection. The channel $\psi' \longrightarrow \pi^+\pi^- e^+ e^-$ in shown, from [103].

ψ' to J/ψ coherent photoproduction cross sections equal to

$$R[\psi'/\mathrm{J}/\psi] = \sqrt{\frac{1}{\frac{\mathrm{d}\sigma^{\mathrm{coh}}_{\mathrm{J}/\psi}}{\mathrm{d}y}} \frac{\mathrm{d}\sigma^{\mathrm{coh}}_{\psi'}}{\mathrm{d}y}} = 0.34^{0.08}_{-0.07}(\text{ stat.+sys.}),$$

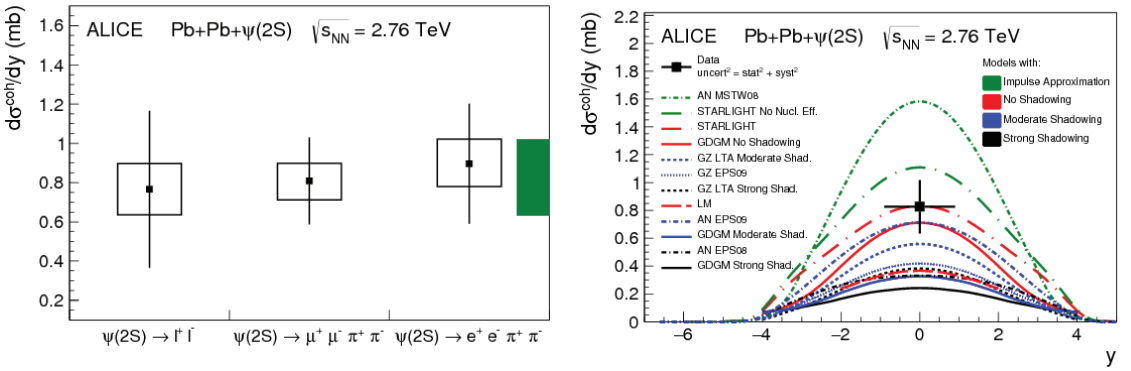

(A) (B)

FIGURE 2.25. Measured differential cross section of ψ' photoproduction in Pb–Pb ultra-peripheral collisions at $\sqrt{s_{\mathrm{NN}}} = 2.76$ TeV at $0.9 < y < 0.9$ in three different channels. The square represents the systematic uncertainties while the bar represents the statistic uncertainty, from [103].

as shown also in Figure 2.26.

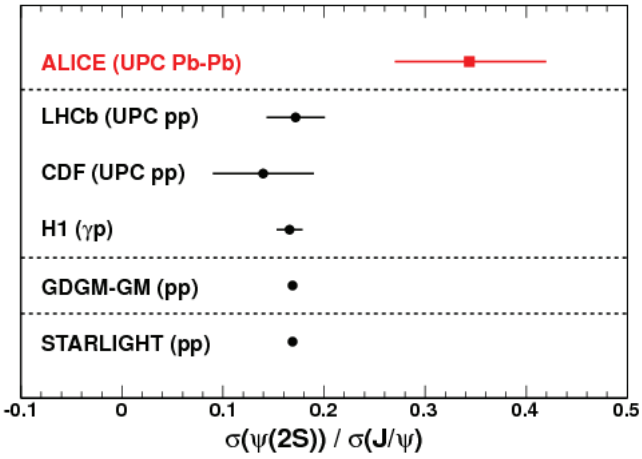

FIGURE 2.26. Ratio of the ψ' to J/ψ cross section for pp and γp interactions compared to theoretical predictions. The ALICE ratio measured in PbPb collisions is shown as well, from [103].

References

[58] E. Fermi. "On the Theory of the impact between atoms and electrically charged particles". In: *Z. Phys.* 29 (1924), pp. 315–327. DOI: 10.1007/BF03184853 (cit. on p. 29).

[59] C. F. von Weizsacker. "Radiation emitted in collisions of very fast electrons". In: *Z. Phys.* 88 (1934), pp. 612–625. DOI: 10.1007/BF01333110 (cit. on p. 29).

[60] E. J. Williams. "Nature of the high-energy particles of penetrating radiation and status of ionization and radiation formulae". In: *Phys. Rev.* 45 (1934), pp. 729–730. DOI: 10.1103/PhysRev.45.729 (cit. on p. 29).

[61] A. J. Baltz. "The Physics of Ultraperipheral Collisions at the LHC". In: *Phys. Rept.* 458 (2008). Ed. by G. Baur et al., pp. 1–171. DOI: 10.1016/j.physrep.2007.12.001. arXiv: 0706.3356 [nucl-ex] (cit. on p. 30).

[62] G. Baur, K. Hencken, D. Trautmann, S. Sadovsky, and Y. Kharlov. "Coherent gamma gamma and gamma-A interactions in very peripheral collisions at relativistic ion colliders". In: *Phys. Rept.* 364 (2002), pp. 359–450. DOI: 10.1016/S0370-1573(01)00101-6. arXiv: hep-ph/0112211 (cit. on pp. 31, 34).

[63] C. A. Bertulani, S. R. Klein, and J. Nystrand. "Physics of ultra-peripheral nuclear collisions". In: *Ann. Rev. Nucl. Part. Sci.* 55 (2005), pp. 271–310. DOI: 10.1146/annurev.nucl.55.090704.151526. arXiv: nucl-ex/0502005 (cit. on p. 31).

[64] A. A. Al-Bataineh. "J/ψ production in ultra-peripheral proton-lead and lead-lead collisions with CMS". PhD thesis. Kansas U., 2017 (cit. on p. 32).

[65] R. Honegger and A. Rieckers. *Photons in Fock space and beyond*. World Scientific, 2015 (cit. on p. 32).

[66] C. A. Bertulani and G. Baur. "Electromagnetic Processes in Relativistic Heavy Ion Collisions". In: *Phys. Rept.* 163 (1988), p. 299. DOI: 10.1016/0370-1573(88)90142-1 (cit. on p. 33).

[67] D. Schildknecht. "Vector meson dominance". In: *Acta Phys. Polon. B* 37 (2006). Ed. by R. Brenner, C. P. de los Heros, and J. Rathsman, pp. 595–608. arXiv: hep-ph/0511090 (cit. on p. 35).

[68] T. Regge. "Introduction to complex orbital momenta". In: *Nuovo Cim.* 14 (1959), p. 951. DOI: 10.1007/BF02728177 (cit. on pp. 35, 89).

[69] A. Donnachie and P. V. Landshoff. "Total cross-sections". In: *Phys. Lett. B* 296 (1992), pp. 227–232. DOI: 10.1016/0370-2693(92)90832-O. arXiv: hep-ph/9209205 (cit. on p. 35).

[70] J. Breitweg et al. "ZEUS results on the measurement and phenomenology of F(2) at low x and low Q**2". In: *Eur. Phys. J. C* 7 (1999), pp. 609–630. DOI: 10.1007/s100529901084. arXiv: hep-ex/9809005 (cit. on p. 36).

[71] A. Donnachie and P. V. Landshoff. "Small x: Two pomerons!" In: *Phys. Lett. B* 437 (1998), pp. 408–416. DOI: 10.1016/S0370-2693(98)00899-5. arXiv: hep-ph/9806344 (cit. on p. 36).

[72] V. Guzey and M. Zhalov. "Rapidity and momentum transfer distributions of coherent J/ψ photoproduction in ultraperipheral pPb collisions at the LHC". In: *JHEP* 02 (2014), p. 046. DOI: 10.1007/JHEP02(2014)046. arXiv: 1307.6689 [hep-ph] (cit. on p. 36).

[73] L. Frankfurt, M. Strikman, and M. Zhalov. "Large t diffractive ρ meson photoproduction with target dissociation in ultraperipheral pA and AA collisions at LHC". In: (Dec. 2006). arXiv: hep-ph/0612072 (cit. on p. 36).

[74] A. J. Baltz, S. R. Klein, and J. Nystrand. "Coherent vector meson photoproduction with nuclear breakup in relativistic heavy ion collisions". In: *Phys. Rev. Lett.* 89 (2002), p. 012301. DOI: 10.1103/PhysRevLett.89.012301. arXiv: nucl-th/0205031 (cit. on p. 36).

[75] S. R. Klein and J. Nystrand. "Photoproduction of quarkonium in proton proton and nucleus nucleus collisions". In: *Phys. Rev. Lett.* 92 (2004), p. 142003. DOI: 10.1103/PhysRevLett.92.142003. arXiv: hep-ph/0311164 (cit. on p. 36).

[76] S. Acharya et al. "Coherent J/ψ photoproduction at forward rapidity in ultra-peripheral Pb-Pb collisions at $\sqrt{s_{\mathrm{NN}}} = 5.02$ TeV". In: *Phys. Lett. B* 798 (2019), p. 134926. DOI: 10.1016/j.physletb.2019.134926. arXiv: 1904.06272 [nucl-ex] (cit. on pp. 37, 94, 100, 128, 130).

[77] C. Alexa et al. "Elastic and Proton-Dissociative Photoproduction of J/ψ Mesons at HERA". In: *Eur. Phys. J. C* 73.6 (2013), p. 2466. DOI: 10.1140/epjc/s10052-013-2466-y. arXiv: 1304.5162 [hep-ex] (cit. on p. 36).

[78] M. Klasen. "Theory of hard photoproduction". In: *Rev. Mod. Phys.* 74 (2002), pp. 1221–1282. DOI: 10.1103/RevModPhys.74.1221. arXiv: hep-ph/0206169 (cit. on p. 38).

[79] S. Munier, A. M. Stasto, and Alfred H. Mueller. "Impact parameter dependent S matrix for dipole proton scattering from diffractive meson electroproduction". In: *Nucl. Phys. B* 603 (2001), pp. 427–445. DOI: 10.1016/S0550-3213(01)00168-7. arXiv: hep-ph/0102291 (cit. on p. 38).

[80] S. Mandelstam. "Determination of the pion-nucleon scattering amplitude from dispersion relations and unitarity. General theory". In: *Memorial Volume for Stanley Mandelstam*. World Scientific, 1958, pp. 151–167 (cit. on p. 38).

[81] S. Mandelstam. "Analytic properties of transition amplitudes in perturbation theory". In: *Physical Review* 115.6 (1959), p. 1741 (cit. on p. 38).

[82] C. Adler et al. "Coherent rho0 production in ultraperipheral heavy ion collisions". In: *Phys. Rev. Lett.* 89 (2002), p. 272302. DOI: 10.1103/PhysRevLett.89.272302. arXiv: nucl-ex/0206004 (cit. on p. 39).

[83] J. W. Harris. "Physics of the STAR experiment at the relativistic heavy ion collider". In: *8th Winter Workshop on Nuclear Dynamics*. Jan. 1992 (cit. on p. 39).

[84] T. Aaltonen et al. "Observation of exclusive charmonium production and $\gamma+\gamma$ to $\mu^+\mu^-$ in $p\bar{p}$ collisions at $\sqrt{s} = 1.96$ TeV". In: *Phys. Rev. Lett.* 102 (2009), p. 242001. DOI: 10.1103/PhysRevLett.102.242001. arXiv: 0902.1271 [hep-ex] (cit. on p. 40).

[85] M. G. Albrow. "Central exclusive production at the Tevatron". In: *AIP Conf. Proc.* 1105.1 (2009). Ed. by R. Fiore, I. Ivanov, A. Papa, and J. Soffer, pp. 3–6. DOI: 10.1063/1.3122222. arXiv: 0812.0612 [hep-ex] (cit. on p. 40).

[86] I. Abt et al. "The H1 detector at HERA". In: *Nucl. Instrum. Meth. A* 386 (1997), pp. 310–347. DOI: 10.1016/S0168-9002(96)00893-5 (cit. on p. 40).

[87] A. Wegner. "Elastic and inelastic production of J/ψ mesons at HERA". In: *AIP Conf. Proc.* 407.1 (1997). Ed. by José Repond and Daniel Krakauer, pp. 771–775. DOI: 10.1063/1.53665 (cit. on pp. 40–42).

[88] S. Chekanov et al. "Exclusive photoproduction of J/ψ mesons at HERA". In: *Eur. Phys. J. C* 24 (2002), pp. 345–360. DOI: 10.1007/s10052-002-0953-7. arXiv: hep-ex/0201043 (cit. on pp. 40, 42).

[89] R Aaij et al. "Exclusive J/ψ and ψ(2S) production in pp collisions at $\sqrt{s} = 7$ TeV". In: *J. Phys. G* 40 (2013), p. 045001. DOI: 10.1088/0954-3899/40/4/045001. arXiv: 1301.7084 [hep-ex] (cit. on pp. 41, 43).

[90] B. Abelev et al. "Exclusive J/ψ photoproduction off protons in ultra-peripheral p-Pb collisions at $\sqrt{s_{\mathrm{NN}}} = 5.02$ TeV". In: *Phys. Rev. Lett.* 113.23 (2014), p. 232504. DOI: 10.1103/PhysRevLett.113.232504. arXiv: 1406.7819 [nucl-ex] (cit. on pp. 42–44, 46).

[91] S. Afanasiev et al. "Photoproduction of J/ψ and of high mass e+e- in ultra-peripheral Au+Au collisions at s**(1/2) = 200-GeV". In: *Phys. Lett. B* 679 (2009), pp. 321–329. DOI: 10.1016/j.physletb.2009.07.061. arXiv: 0903.2041 [nucl-ex] (cit. on pp. 45, 46).

[92] B. Abelev et al. "Coherent J/ψ photoproduction in ultra-peripheral Pb-Pb collisions at $\sqrt{s_{\mathrm{NN}}} = 2.76$ TeV". In: *Phys. Lett. B* 718 (2013), pp. 1273–1283. DOI: 10.1016/j.physletb.2012.11.059. arXiv: 1209.3715 [nucl-ex] (cit. on pp. 46, 48).

[93] V. Khachatryan et al. "Coherent J/ψ photoproduction in ultra-peripheral PbPb collisions at $\sqrt{s_{\mathrm{NN}}} = 2.76$ TeV with the CMS experiment". In: *Phys. Lett. B* 772 (2017), pp. 489–511. DOI: 10.1016/j.physletb.2017.07.001. arXiv: 1605.06966 [nucl-ex] (cit. on pp. 46, 47).

[94] A. Adeluyi and C. Bertulani. "Gluon distributions in nuclei probed at the CERN Large Hadron Collider". In: *Phys. Rev. C* 84 (2011), p. 024916. DOI: 10.1103/PhysRevC.84.024916. arXiv: 1104.4287 [nucl-th] (cit. on p. 46).

[95] S. J. Brodsky, L. Frankfurt, J. F. Gunion, Alfred H. Mueller, and M. Strikman. "Diffractive leptoproduction of vector mesons in QCD". In: *Phys. Rev. D* 50 (1994), pp. 3134–3144. DOI: 10.1103/PhysRevD.50.3134. arXiv: hep-ph/9402283 (cit. on p. 47).

[96] M. L. Miller, K. Reygers, S. J. Sanders, and P. Steinberg. "Glauber modeling in high energy nuclear collisions". In: *Ann. Rev. Nucl. Part. Sci.* 57 (2007), pp. 205–243. DOI: 10.1146/annurev.nucl.57.090506.123020. arXiv: nucl-ex/0701025 (cit. on p. 47).

[97] K. J. Eskola, H. Paukkunen, and C. A. Salgado. "EPS09: A New Generation of NLO and LO Nuclear Parton Distribution Functions". In: *JHEP* 04 (2009), p. 065. DOI: 10.1088/1126-6708/2009/04/065. arXiv: 0902.4154 [hep-ph] (cit. on pp. 47, 48).

[98] V. Guzey, E. Kryshen, M. Strikman, and M. Zhalov. "Evidence for nuclear gluon shadowing from the ALICE measurements of PbPb ultra-peripheral exclusive J/ψ production". In: *Phys. Lett. B* 726 (2013), pp. 290–295. DOI: 10.1016/j.physletb.2013.08.043. arXiv: 1305.1724 [hep-ph] (cit. on p. 47).

[99] L. Frankfurt, V. Guzey, and M. Strikman. "Leading Twist Nuclear Shadowing Phenomena in Hard Processes with Nuclei". In: *Phys. Rept.* 512 (2012), pp. 255–393. DOI: 10.1016/j.physrep.2011.12.002. arXiv: 1106.2091 [hep-ph] (cit. on p. 47).

[100] E. Abbas et al. "Charmonium and e^+e^- pair photo-production at mid-rapidity in ultra-peripheral Pb-Pb collisions at $\sqrt{s_{\mathrm{NN}}} = 2.76$ TeV". In: *Eur. Phys. J. C* 73.11 (2013), p. 2617. DOI: 10.1140/epjc/s10052-013-2617-1. arXiv: 1305.1467 [nucl-ex] (cit. on p. 47).

[101] G. F. Chew and G.C. Wick. "The Impulse Approximation". In: *Phys. Rev.* 85.4 (1952), p. 636. DOI: 10.1103/PhysRev.85.636 (cit. on p. 49).

[102] S. R. Klein. "Ultra-peripheral collisions and hadronic structure". In: *Nucl. Phys. A* 967 (2017). Ed. by Ulrich Heinz, Olga Evdokimov, and Peter Jacobs, pp. 249–256. DOI: 10.1016/j.nuclphysa.2017.05.098. arXiv: 1704.04715 [nucl-ex] (cit. on p. 50).

[103] J. Adam et al. “Coherent $\psi(2S)$ photo-production in ultra-peripheral Pb Pb collisions at $\sqrt{s_{NN}} = 2.76$ TeV”. In: *Phys. Lett. B* 751 (2015), pp. 358–370. DOI: 10.1016/j.physletb.2015.10.040. arXiv: 1508.05076 [nucl-ex] (cit. on pp. 49–52).

3 ALICE experiment at the LHC

Alice laughed:"There's no use trying," she said;
"one can't believe impossible things."
"I daresay you haven't had much practice," said the Queen.
"When I was younger, I always did it for half an hour a day.
Why, sometimes I've believed as many as six
impossible things before breakfast."
Lewis Carroll (1831 – 1898)
"In Through the Looking-glass: And what Alice Found There"

Contents

SINCE their conception in the 1920s, the particle accelerators have grown in size and complexity, ranging from a few metres to tens of kilometres. The largest particle accelerator in the world, used in fundamental research, is the Large Hadron Collider (LHC) at CERN. It is a circular accelerator of around 27 km in circumference, itself composed by a whole series of linear and circular smaller accelerators injecting particles (protons (p) and lead ions (Pb) particularly).

This Chapter will describe the LHC, its physical objective and the various experiments that make it up. The emphasis will be on the ALICE experiment and its sub-detectors used during Run 2[1]. The major upgrades of ALICE for Runs 3 and 4 of LHC will be discussed in Chapter 6.

3.1 The Large Hadron Collider

3.1.1 The biggest particle accelerator on Earth

THE Large Hadron Collider (LHC) [104], located on the French-Swiss border, is the largest particle accelerator built to date that delivers the highest energy ever achieved by a collider (up to 13.6 TeV in the centre of mass in proton-proton (pp) collisions, world record

[1] At the LHC, a Run is a data taking period.

reached on July 5, 2022 [105]). The LHC is located at a depth ranging from 50 to 175 m underground in a concrete-lined tunnel, that was formerly used to house the Large Electron–Positron Collider (LEP) [106] during the period from 1989 to 2000. The collider tunnel features two-parallel beam pipes, each holding a beam that travels around the ring in opposing directions. Particle collisions happen at the four spots where the beams cross.

1232 dipole magnets, up to 15 m in size, bend the trajectory of the two particle beams circulating in opposite directions in tubes where a high vacuum prevails. These magnets are superconductors and generate a powerful magnetic field of 8.4 T. To achieve such performance, these magnets are cooled to a temperature of -271 °C, using liquid helium. 392 quadrupole magnets are also employed to concentrate the beams and optimise their trajectories. Figure 3.1 shows a 3D cut of an LHC dipole.

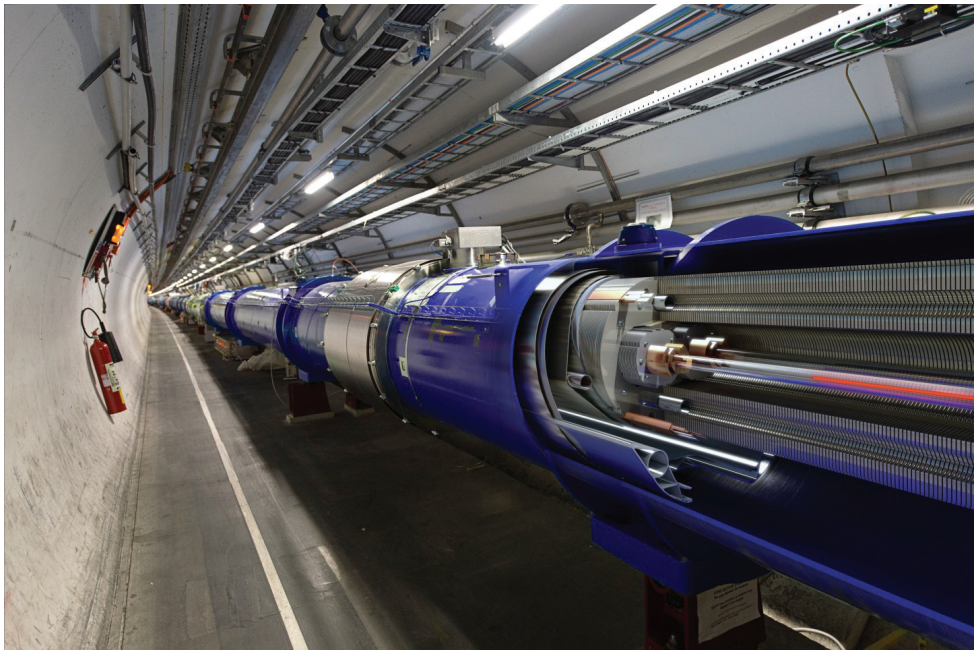

FIGURE 3.1. 3D cut of the LHC dipole, from [107].

The LHC was initially designed to provide pp collisions at the energy of $\sqrt{s} = 14$ TeV and Pb-Pb collisions at $\sqrt{s_{\mathrm{NN}}} = 5.5$ TeV. However, after a technical incident in 2008 [108] due to the quenching of a magnet, it was decided to gradually increase the energy and luminosity at each Run up to the High Luminosity Large Hadron Collider (HL-LHC) [109] during Run 4 scheduled to start in 2029.

Table 3.1 resumes all the important events of LHC until 2022.

All CERN facilities and the linear and circular accelerators are shown in Figure 3.2. The

Date	Event
	Run 1 (2008-2013)
	First day of data collection with 450 GeV per beam..
20 Nov 2009	With 1.18 TeV per beam, the LHC becomes the world's most pow-
30 Nov 2009	erful particle accelerator, beating the Tevatron's previous record of 0.98 TeV per beam, which had stood for eight years.
30 Mar 2010	At 13:06 CEST, the two beams hit each other in the LHC at an energy of 7 TeV (3.5 TeV per beam). This was the start of the LHC research program.
21 Apr 2011	With a peak luminosity of $4.67 \cdot 10^{32} \mathrm{cm}^{-2}\,\mathrm{s}^{-1}$, the LHC becomes the world's highest-luminosity hadron accelerator. It beats the Tevatron's previous record of $4 \cdot 10^{32} \mathrm{cm}^{-2}\,\mathrm{s}^{-1}$.
	Run 2 (2015-2018)
9 Apr 2015	A new record for the proton energy of 6.5 TeV was attained.
20 May 2015	In the LHC, protons collided with a record-breaking collision energy of 13 TeV.
During Nov 2015	The Pb-Pb ions beams reached an energy of $\sqrt{s_{\mathrm{NN}}} = 5.02$ TeV.
29 June 2016	The LHC achieves a luminosity of $1\cdot, 10^{34} \mathrm{cm}^{-2}\,\mathrm{s}^{-1}$.
	Run 3 (2022-2025)
5 July 2022	A new world record for proton energy of 13.6 TeV was reached.

TABLE 3.1. Some interesting events at the LHC.

most important facilities will be described in the following Sections. The three biggest rings (the magenta one represents the PS, the light blue one is the SPS and the dark blue one indicates the LHC) are the main accelerators at CERN. The straight lines represent the linear accelerators or the secondary beams. Finally, the four yellow dots are the four main experiments of the LHC.

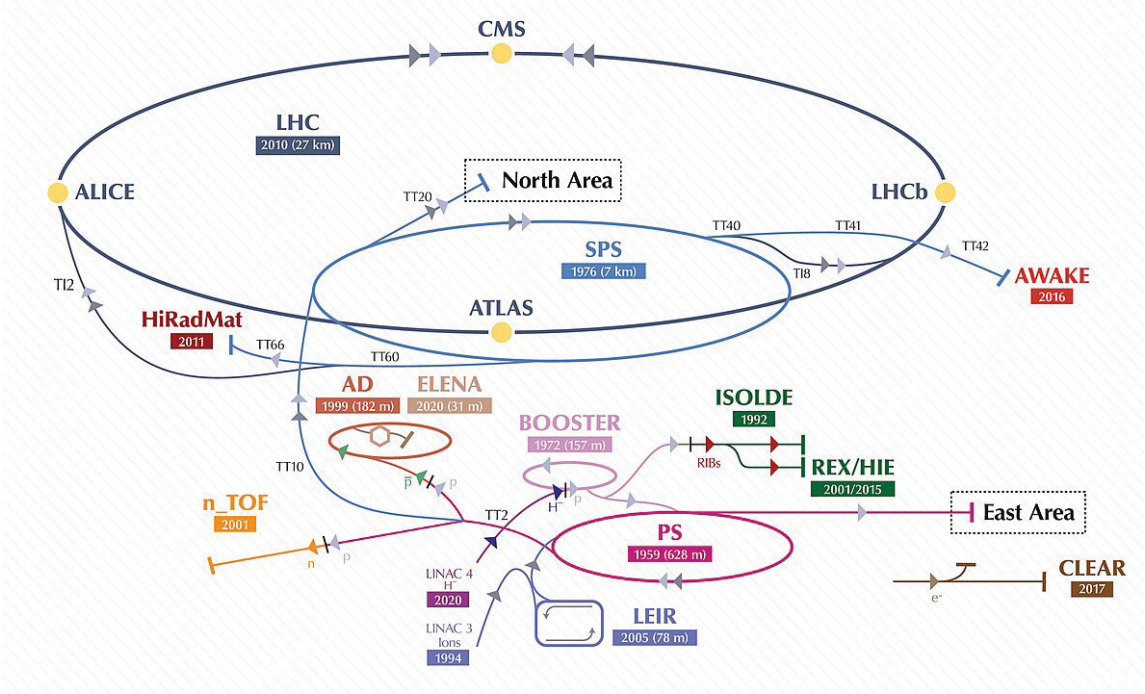

FIGURE 3.2. Diagram representing the CERN accelerator complex in 2019, from [110].

3.1.2 *pp* collisions at the LHC

EVERYTHING begins with a dihydrogen (H_2) tank when one wants to create pp collisions. Before the particles are injected into the collider, they are prepared by a succession of systems that incrementally enhance their energy. The first system is the Linear accelerator 4 (Linac4) [111], which produces 160 MeV negative hydrogen ions (H^-) and supplies the Proton Synchrotron Booster (PSB) [112]. There, all the electrons are removed from the hydrogen ions. After being accelerated to 2 GeV, protons are then fed into the Proton Synchroton (PS) [113], where they are accelerated to 26 GeV. The Super Proton Synchrotron (SPS) [114] is, then, used to raise the proton energy to 450 GeV. Further on, proton bunches are gathered, split and injected into the LHC. Within the LHC ring, the bunches circulating in both directions are accelerated to the nominal energy. After the acceleration, they enter in collision at the four interaction points, where ATLAS, CMS, LHCb and ALICE experiments are located.

3.1.3 Heavy-ions collisions at the LHC

THE LHC physics program is mostly focused on collisions between protons. Nonetheless, during shorter operating times, approximately one month each year, the schedule includes heavy-ions collisions. The particle source is a 3 cm lead cylinder, heated to approximately 500 °C to vaporise a small number of atoms that, after partly ionised by a high electric field, lose some electrons, becoming Pb^{29+}. These ions are accelerated in a linear device to strip off some of the remaining electrons, resulting in Pb^{54+} ions. In other words, the lead ions are initially accelerated using the Linear accelerator 3 (Linac3) [115]. Then they are stored and cooled *via* the Low Energy Ion Ring (LEIR) [116], in which all the electrons are ripped, obtaining Pb^{82+}. After this operation, ions are accelerated further by the PS and SPS before being injected into the LHC ring, where they reach energies greater than those attained by the Relativistic Heavy Ion Collider (RHIC)[2] [117]. It is important to notice that in the LHC, one can find also Xe-Xe collisions. The objective of the heavy-ion project is to examine the primordial QGP characteristics, as already explained in Section 1.4.

3.1.4 p-Pb collisions at the LHC

THE p-Pb collisions are similar to the preceding two systems, described in Sections 3.1.2 and 3.1.3. Nevertheless, one has to notice that the proton and Pb-ion beams moving in the opposite directions are exposed to the same electromagnetic field. As a result, they are accelerated up to difference energies. This causes the nucleon-nucleon center of mass system to move in the direction of the proton beam relative to the laboratory reference frame.

3.1.5 The four largest experiments at the LHC

THE four big experiments at the LHC are ATLAS, CMS, LHCb and ALICE, complemented by two smaller ones (TOTEM and LHCf).

A Toroidal LHC ApparatuS (ATLAS) [118] and Compact Muon Solenoid (CMS) [119] experiments are general-purpose detectors with numerous scientific goals, among which

[2]The RHIC is the first of only two heavy-ion colliders in operation. The only operational particle collider in the United States is located at Brookhaven National Laboratory (BNL) near Upton, New York, and is used by an international research teams. Its main experiments are STAR, PHENIX and the newest one, sPHENIX.

there are the searches and studies of the Higgs boson (as already cited in Section 1.1), the presence of extra dimensions, dark matter candidates and supersymmetry. The two experiments differ in their technical design decisions, notably at the level of superconducting magnets. To bend the track of the particles, ATLAS chose a toroidal field of 2 T, while CMS used a solenoidal field of 4 T.

The Large Hadron Collider beauty (LHCb) [120] experiment investigates matter-antimatter asymmetry in the b-quark sector. The LHCb collaboration has published various major results on the detection of uncommon decays of the B^0, B_s^0 and $\overline{B_s^0}$ mesons in multiple channels, as well as an excited state of the B_s^0 meson, $B_{s2}^*(5840)^0$ [121]. Among the important results obtained by the LHCb Collaboration, one has to also note the observation of tetraquark and pentaquark states.

The two small experiments, TOTal Elastic and diffractive cross section Measurement (TOTEM) [122], positioned near CMS, and Large Hadron Collider forward (LHCf) [123] are designed to explore physics at very small angles, which are inaccessible to general-purpose experiments. TOTEM focuses on the accurate measurement of the total cross-section of elastic and diffractive collision processes and the luminosity produced by the LHC. The goal of the LHCf experiment is to reproduce cosmic rays in the laboratory. In Figure 3.3, one can observe the LHC structure.

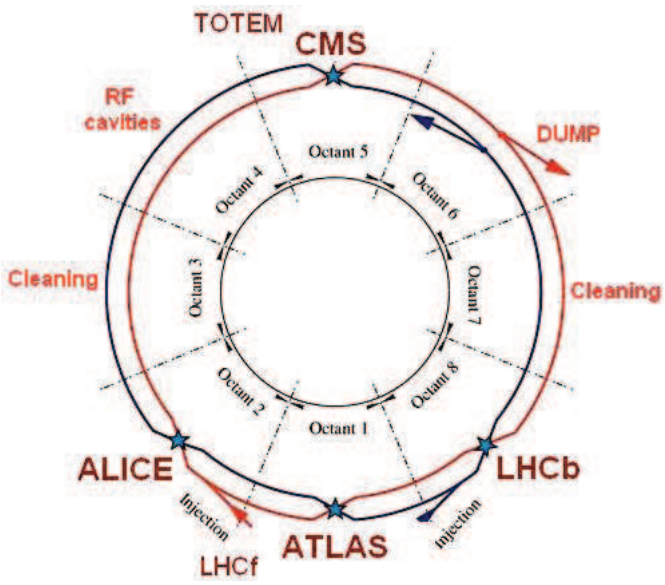

FIGURE 3.3. Diagram of the LHC and its experiments.

This Ph.D.'s work is based on the A Large Ion Collider Experiment (ALICE), an experiment that is specially designed for the study of the QGP.

3.2 A Large Ion Collider Experiment (ALICE)

ALICE [124, 125] brings together over 2000 researchers and 173 institutions from 40 countries. The experiment, which was approved in February 1997 [126], is primarily targetting the heavy-ion physics. Using these collisions, one explores the deconfined state of nuclear matter, known as Quark-Gluon Plasma (QGP). However, the ALICE physics program is not limited to heavy-ion collisions, pp and p-Pb measurements are also carried out, mainly to serve as a reference for the Pb-Pb collisions and to investigate cold nuclear effects, the QGP-like effects, the collectivity, respectively.

The detector is located in the French county of Saint Genis-Pouilly, at position P2 of the LHC ring (see Figure 3.2). It has a rather large size ($26 \times 16 \times 16$ m^3) and weighs around 10 000 tonnes. It is made up of a large number of sub-detectors, as illustrated in Figure 3.4. As it can be seen in this Figure, the ALICE detector can be roughly divided into two parts. The first one is contained inside the L3 solenoid magnet, which was used in the previous LEP experiment of which it inherits the name. The L3 magnet delivers a maximum magnetic field of 0.5 T and weighs roughly 8,000 tonnes (80% of the mass of the ALICE detector). It contains the ALICE subdetectors of the central barrel, covering the mid-rapidity range, as well as several detectors covering the forward rapidity range.

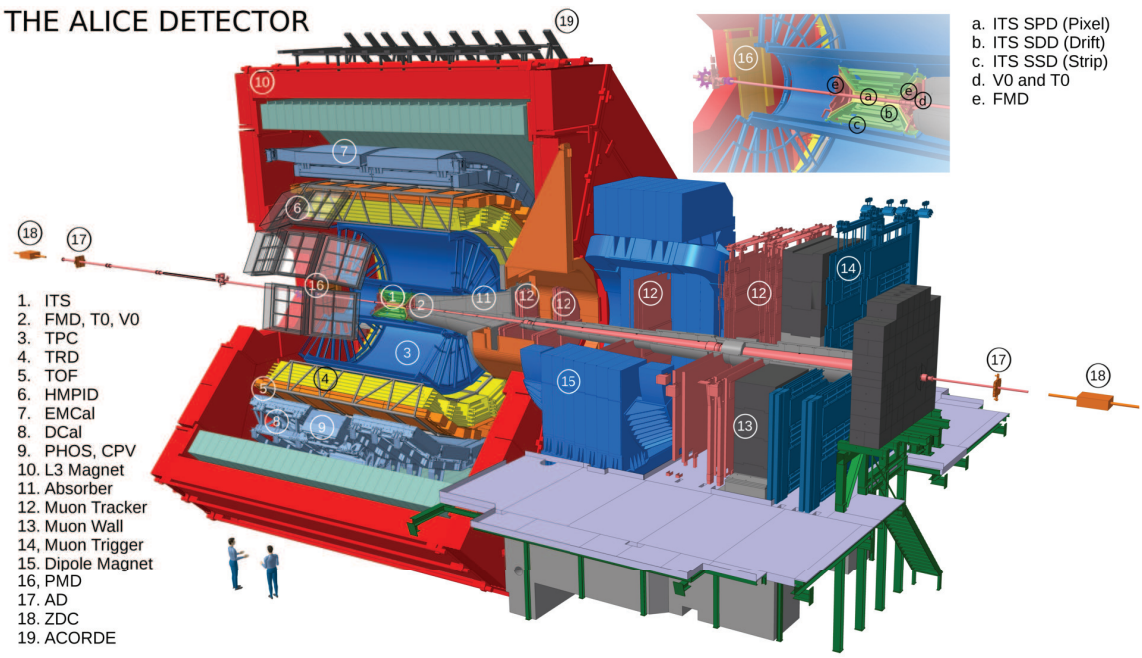

FIGURE 3.4. Schematic of the ALICE experiment and its detectors, numbered from 1 to 19.

The detectors of the central barrel ($|\eta| < 0.9$[3]) are arranged around the point of interaction and are responsible for the identification of hadrons, electrons and photons as well as reconstructing the corresponding charged-particle trajectories. Small-angle detectors, on the other hand, are employed for the interaction trigger and the characterisation of the recorded events.

The second important element of ALICE is the muon spectrometer ($-4.0 < \eta < -2.5$), which detects and reconstructs the trajectories of the charged particles emerging from the hadron absorber (mainly muons). The ALICE experiment also includes a cosmic ray detector, known as ACORDE [127], which is installed on top of the L3 magnet.

The Cartesian coordinate system of the experiment is defined to have the z-axis parallel to the beam axis and pointing in the opposite direction of the muon spectrometer (i.e. towards side A). The x-axis sits on the horizontal plane defined by the LHC ring, and points to the LHC center. Finally, the vertical y-axis is perpendicular to the previous two and point upwards. According to the collision system, the number of produced particles can vary from few units to few thousands. The various sub-detectors are designed to identify them and estimate their kinematics.

3.2.1 The central barrel

THE core of the ALICE detector is located inside the L3 magnet and the various detectors composing it are installed in coaxial layers around the beam axis. From the centre to the exterior of the detector, one finds the ITS, the TPC, the TRD, the TOF, HMPID, the two electromagnetic calorimeters (EmCal and PHOS) calorimeters.

3.2.1.1 ITS: Inner Tracker System

INSTALLED around the Interaction Point (IP), the Inner Tracker System (ITS) [128] is the vertex detector of the ALICE experiment, designed with a cylindrical geometry covering the pseudorapidity range $|\eta| < 0.9$. The reconstruction of primary vertices (and secondary for decay vertices located at more than 100 µm from the primary vertex) is achieved by tracking particles via six silicon layers divided into three sub-systems, as shown on Figure 3.6. The Silicon Pixel Detector (SPD) consists of the two innermost layers of ITS, the Silicon Drift Detector (SDD) of the two middle ones and the Silicon Strip Detector (SSD) of the two outermost. Table 3.2 provides the characteristics of ITS

[3] η is defined in Section 1.4.1.

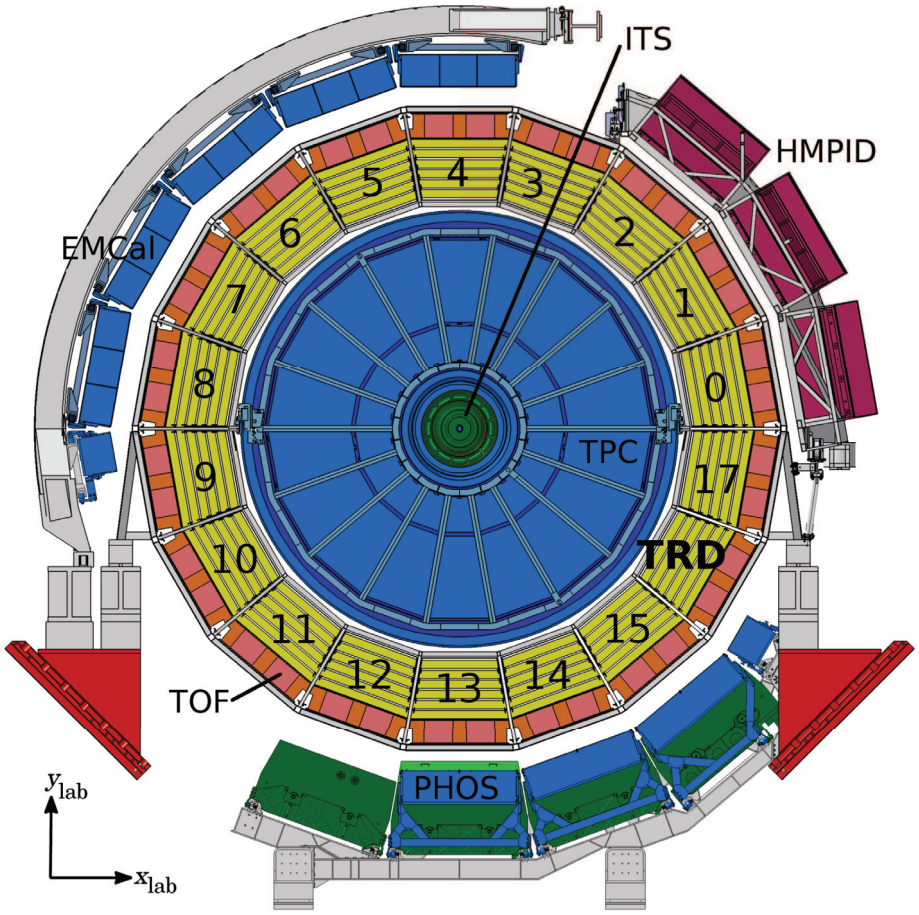

FIGURE 3.5. Schematic cross-section of the ALICE detector perpendicular to the LHC beam direction, during Run 2 of LHC. The central barrel detectors cover the pseudorapidity range $|\eta| < 0.9$ and are located inside the solenoid magnet, which provides a magnetic field with strength $B = 0.5\,\mathrm{T}$ along the beam direction.

layers.

Layer	Acceptance (η)	Position [m]	Dimensions [m^2]
1	$\|\eta\| < 2.0$	0.039	0.21
2	$\|\eta\| < 1.4$	0.076	
3	$\|\eta\| < 0.9$	0.150	1.31
4		0.239	
5	$\|\eta\| < 0.9$	0.380	5.00
6		0.430	

TABLE 3.2. ITS different layer characteristics.

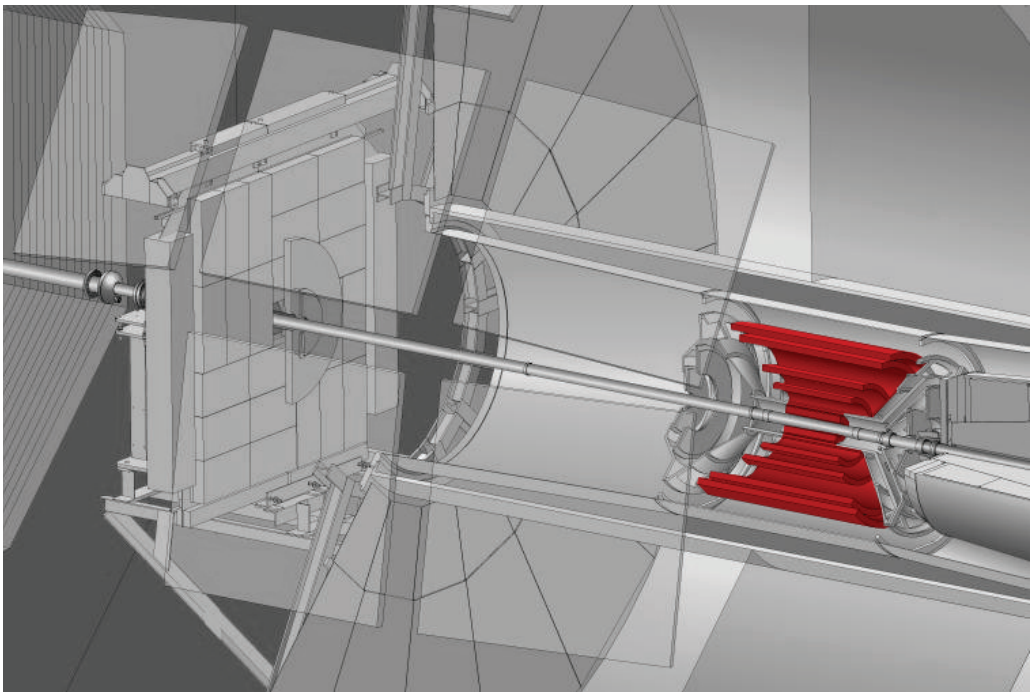

FIGURE 3.6. ITS detector inside ALICE experiment, from [129].

3.2.1.2 TPC: Time Projection Chamber

THE Time Projection Chamber (TPC) [130] is the main tracking and particle identification detector at mid-rapidity. The TPC is sounding outside the ITS (between $z = \pm 250$ cm) and consists of a cylinder filled with a Ne-CO_2 (90%–10%) gas mixture enabling accurate momentum and $\mathrm{d}E/\mathrm{d}x$ measurements of charged particles. On the end-caps, two readout planes read the ionization signal left by the charged particles traversing the gas volume. The active drift volume is divided by the central high-voltage electrode, which provides a 400 V/cm field.

As the ITS, the TPC covers a pseudo-rapidity range of $|\eta| < 0.9$ and it is shown in Figure 3.7.

3.2.1.3 TRD: Transition Radiation Detector

DIVIDED into 18 super-modules each one composed of 30 modules, grouped in 6 radial layers and 5 sectors along the beam direction, the Transition Radiation Detector (TRD) [131] has full azimuth coverage and pseudo-rapidity coverage of $|\eta| < 0.9$ and is completely surrounding the TPC. It detects the energy of the radiation released by high-

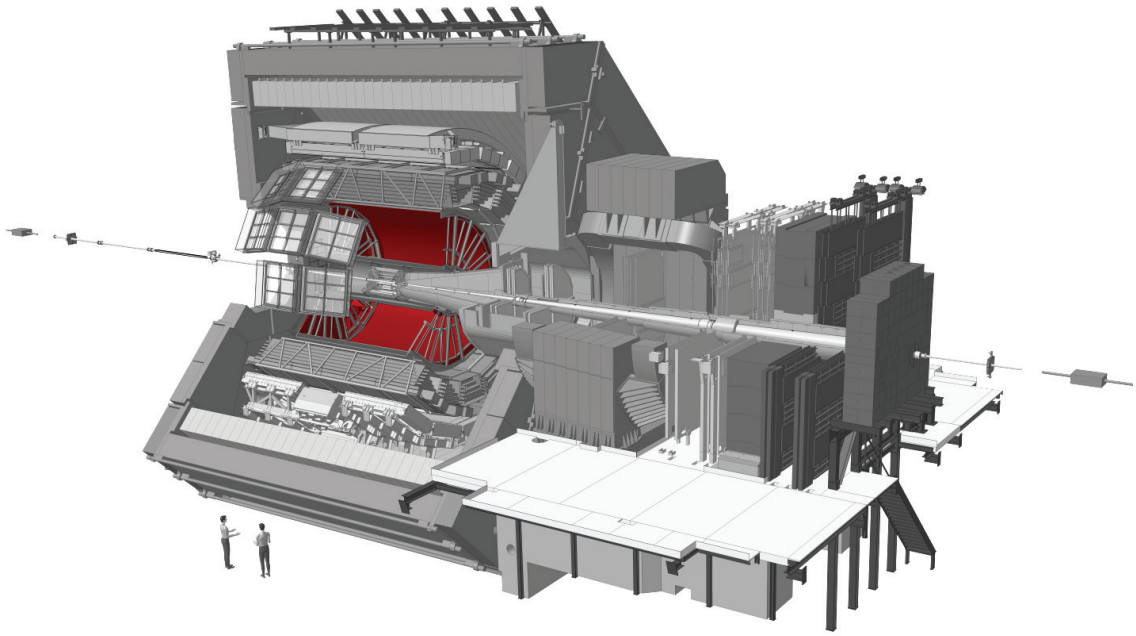

FIGURE 3.7. The TPC detector inside ALICE experiment, from [129].

energy charged particles and helps in reconstructing their track. The main purpose of the TRD is to identify charged particles: its performance are optimized to identify electrons with momentum higher than 1 GeV/c, rejecting 90% of pions.

3.2.1.4 TOF: Time Of Flight

THE Time Of Flight (TOF) [132] is a detector that measures the time of flight of the particles traversing it. It surrounds the TRD, and covers the same pseudorapidity range as the other detectors in the central barrel. It is structured according to a modular configuration with 18 sectors in azimuth and 5 modules along the beam axis. Figure 3.8 shows the location of TOF in the ALICE detector.

The time resolution of the TOF, the main parameter defining the particle identification performance of the detector, is around 50 ps, allowing for a 3σ separation of pions and kaons for momenta up to than 2.2 GeV/c, and of protons up to than 4 GeV/c.

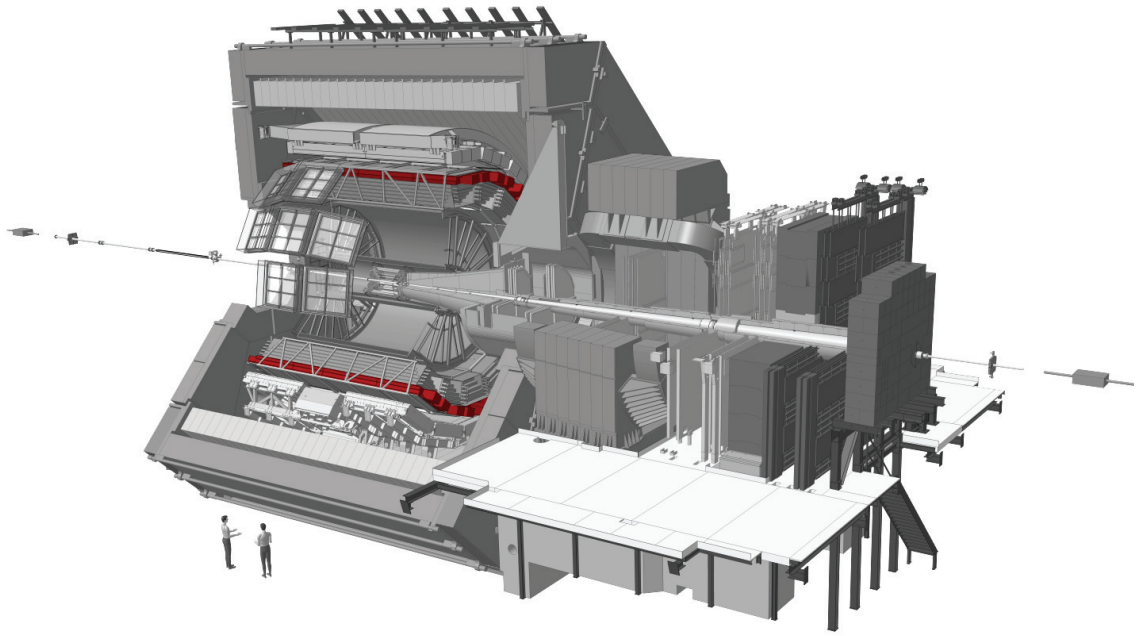

FIGURE 3.8. The TOF detector inside the ALICE experiment, from [129].

3.2.1.5 HMPID : High Momentum Particle Identification, EmCal : Electro Magnetic Calorimeter, and PHOS : PHOton Spectrometer

THE High Momentum Particle Identification (HMPID) [133] covers 57.6° in φ and $|\eta| < 0.6$, representing about 5% of the total acceptance of the central barrel. It is composed of 7 Ring Imaging CHerenkov (RICH) modules and is primarily designed to identify charged hadrons with transverse momentum above 1 GeV/c.

Composed of four modules, the PHOton Spectrometer (PHOS) [134] is a high-granularity electromagnetic calorimeter covering a pseudo-rapidity range of $|\eta| < 0.12$ and an azimuth angle of 100°. The excellent spatial and energy resolution of the PHOS is exploited for the detection of single photons with energies ranging from 0.5 to 10 GeV/c in p_{T} and photon pairs from light neutral mesons (η and π_0) of 1-2 to 10 GeV/c in p_{T}. This allows, in particular, for the analysis of direct photons, of jet-quenching by detecting the π_0 of high p_{T}, or even γ-jet correlations.

Finally, the coverage of the Electro Magnetic Calorimeter (EmCal) [135] is $|\eta| < 0.7$ in pseudo-rapidity and 107° in φ. It is composed of eleven supermodules, each one being segmented into 288 modules. Its primary goals are the investigation of jet-quenching, photon production, and γ-jet and hadron-jet correlations. Finally, there is the Di-jet Calorimeter (DCal) [136], which is an upgrade of the EmCal and extends the EMCAL's

physics capabilities by allowing back-to-back correlation measurements that are unattainable with the EMCAL alone but are required to provide a fuller view of the physics treated by the EMCAL.

3.2.2 Forward rapidity detectors

A group of detectors is installed at forward rapidity (the specific case of the Muon Spectrometer will be discussed in a dedicated Section) with the goal of measuring global observables, such as the multiplicity of photons or charged particles. The FMD, the T0, the PMD, the V0 and the AD play a crucial role in the characterization of heavy-ion collisions, estimating parameters such as the centrality and the reaction plane. The T0 and V0 are also used in the definition of the ALICE minimum-bias trigger conditions and they are important for determine the luminosity. Finally, the ZDC is the installed outside of the L3 magnet around 115 m from the interaction point and it measures the energy of spectator nucleons in A-A collisions to calculate the overlap zone.

3.2.2.1 FMD: Forward Multiplicity Detector and PMD : Photon Multiplicity Detector

Composed of 24 photon detection units, the Photon Multiplicity Detector (PMD) [137] is a high-granularity detector, able to characterize the detection plan and measure the specific global observables (multiplicity of photons and their spatial distribution, anisotropic flow, etc.).

The Forward Multiplicity Detector (FMD) [138] is segmented into 5 rings, each with 10,240 Silicon strips, and into 20 or 40 sectors in azimuth. The FMD main duty is to provide an accurate estimate of multiplicity in the pseudo-rapidity ranges listed in Table 3.3

Disc	Acceptance (η)	Position [m]	Dimensions [m^2]
1	$3.62 < \eta < 5.03$	inner : 3.20	
2	$1.70 < \eta < 3.68$	inner : 0.83 outer : 0.75	0.266
3	$-3.40 < \eta < -1.70$	inner : -0.63 outer : -0.75	

Table 3.3. FMD's different disks characteristics.

3.2.2.2 V0, T0 and AD detectors

Two arrays of scintillators, positioned perpendicular to the beam direction and asymmetrically on either side at $z = 340$ cm (V0-A) and $z = -90$ cm (V0-C) of the IP compose the V0 detector [138]. Both arrays consist of four rings of scientillators, each of them being further segmented into eight sectors. The V0 serves as a minimum-bias trigger, and provides rejection of beam-gas events by evaluating the time-of-flight difference between both parts. In addition, the detector can estimate the luminosity, the charged particle multiplicity, the collision centrality, and the direction of the event plane. Figure 3.9a shows the emplacement of the V0 in ALICE.

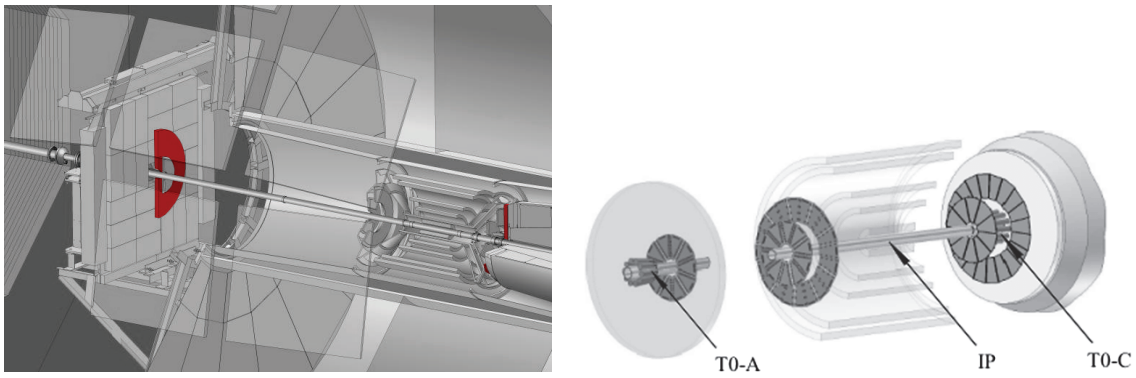

(A) V0 detector in ALICE experiment (B) Forward rapidity detectors : FMD, T0, V0

FIGURE 3.9. *Left side :* position of V0 detector in ALICE, from [129]. *Right side :* Location of T0 detector in the central region of ALICE. T0-A is on the extreme left, about 370 cm from IP, behind V0-A and the fifth ring of FMD. T0-C is about 70 cm from IP, surrounded by two rings of FMD and V0-C. Both T0-C and V0-C are attached directly to the front of the absorber.

The T0 detector [138], shown in Figure 3.9b, has a geometrical configuration similar to the one of the V0, as it consists of two arrays of detectors (T0A and T0C) installed on both sides of the IP, close to the V0 detectors ($z = 350$ cm and $z = -70$ cm). The arrays are composed of 24 Cherenkov counters with an excellent time resolution (better than 50 ps), which provide the collision time for the TOF, a precise determination of the vertex position (within 1.5 cm), an estimation of the particle multiplicity, and a minimum-bias trigger.

Finally, the ALICE Diffractive (AD) detector is composed of two arrays of eight scintillator tiles organised in two layers, covering the ranges $4.9 < \eta < 6.3$ (AD-A) and $-7.0 < \eta < -4.8$ (AD-C) and positioned at $z = 17$ m and $z = -19.5$ m from the interaction point, respectively. The AD detector is used to trigger and study the physics of diffractive and ultra-peripheral collisions, as well as for a variety of technical tasks like beam-gas background monitoring or as a luminometer.

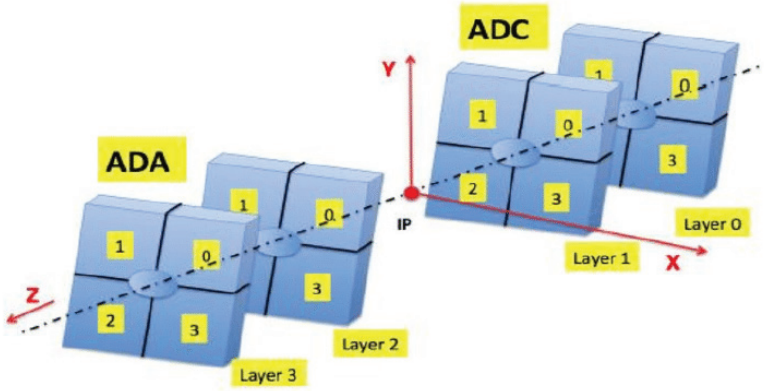

FIGURE 3.10. The AD-A and AD-C sub-detector. From [139].

3.2.2.3 ZDC: Zero-Degree Calorimeter

THE Zero Degree Calorimeter (ZDC) detector is composed into two distinct sets of quartz-fiber hadronic calorimeters, proton ZDC (ZP) and neutron ZDC (ZN). They are located on opposite sides of the IP at $z = \pm 112.5$ m, and measure the energy of spectator nucleons in heavy-ion collisions. The ZN is positioned between the two beam pipes at zero degrees with respect to the LHC axis, whereas the ZP is external to the outgoing beam pipe, as shown in Figure 3.11. They estimate the centrality of the A-A collisions by measuring the energy carried away by the spectator nucleons, which will have the same fixed energy as the beam nucleons.

Two electromagnetic calorimeters (ZEM), installed at forward rapidity at 7 m from the IP, provide further information for the identification of central and peripheral collisions, in the case where the number of spectators traversing the hadronic calorimeters may not be a reliable quantity due to the fragmentation of the colliding nuclei.

In Table 3.4, the η and φ ranges of V0, T0 and ZDC detectors are reported.

Disc	Acceptance (η) and (φ)	Position [m]	Dimensions [m^2]
	V0		
V0-A	$2.8 < \eta < 5.1$	3.40	0.548
V0-C	$-3.7 < \eta < -1.7$	–0.98	0.315
	T0		
T0A	$4.61 < \eta < 4.92$	3.75	0.0038
T0C	$-3.28 < \eta < -2.97$	0.73	
	ZDC		
ZP	$6.5 < \lvert\eta\rvert < 7.5$ $-9.7° < \varphi < 9.7°$	±116	2×0.027
ZN	$\lvert\eta\rvert < 8.8$		
ZEM	$4.8 < \eta < 5.7$ $-16° < \varphi < 16°$ $164° < \varphi < 196°$	7.25	2×0.0049

TABLE 3.4. V0, T0 and ZDC detectors and their characteristics.

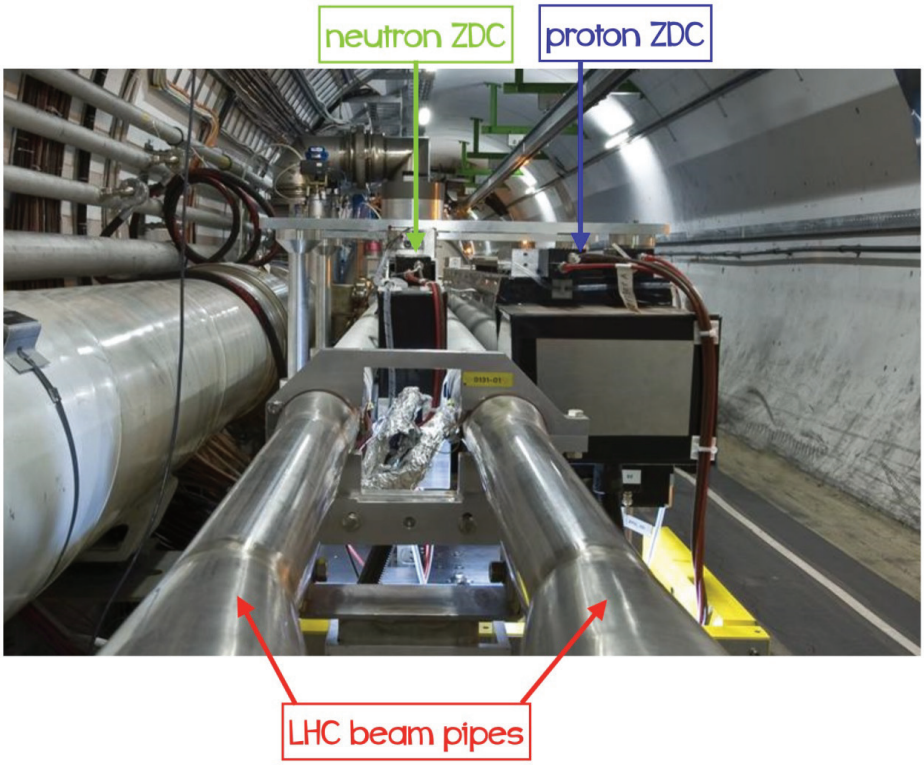

FIGURE 3.11. The ZDC detector composed by the ZP and the ZN.

3.2.3 The muon spectrometer

In high-energy particle physics, muons are the most penetrating charged particles that can be tracked in the detectors. The ALICE muon spectrometer [140, 141] angular acceptance ranges from 2° to 9°, corresponding to a pseudo-rapidity coverage of –4 $< \eta <$ –2.5. The spectrometer is made up of a hadron absorber, a dipole magnet, ten tracking chambers, a second absorber and four additional chambers for muon detection and triggering. A dedicated absorber surrounds the beam pipe, reducing background contamination from particles produced at small angles and interacting with the beam pipe. A layout of the ALICE muon spectrometer is shown in Figure 3.12, and its various elements are described in the following.

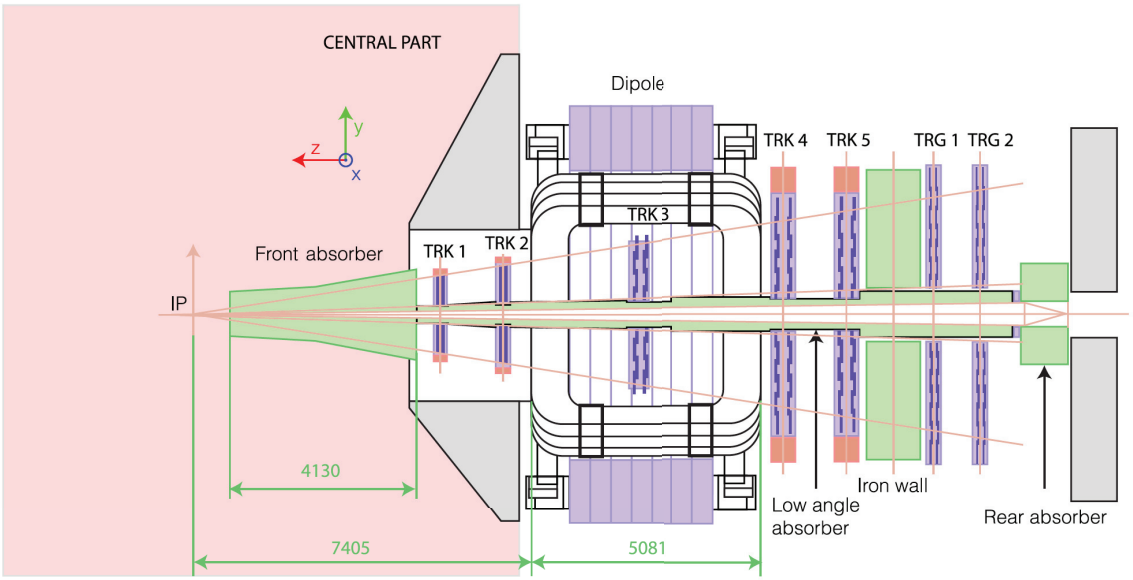

FIGURE 3.12. The ALICE muon spectrometer layout, from [142]. TRK stands for tracking chamber and TRG for trigger chamber. The distances, written in light green, are reported in mm.

3.2.3.1 The front absorber

Located 90 cm from the interaction point, behind the V0-C detector, the front absorber measures 4.13 m and its main role is to redece the significant amount of pions and kaons produced during the hadronic collisions, before they decay in the semi-muonic channel. The absorber also reduces the backscattering of charged and neutral particles towards the TPC. As a side effect, it also stops very low transverse momentum muons ($p_{\mathrm{T}} \lesssim 0.5$ GeV/c).

3.2.3.2 Tracking chambers

THE tracking system includes five stations, each composed of two chambers.

The first two stations are located between the front absorber (Section 3.2.3.1) and the dipole magnet (Section 3.2.3.3), the third station is situated inside the magnet, and the last two stations between the magnet and an iron wall screening the trigger stations (see below). The chambers within the same station are separated by 10 to 20 cm and are made up of Multi-Wire Proportional Chambers (MWPCs) with segmented cathodes or Cathode Pad Chamber (CPC). Figure 3.13 shows the position of the tracking stations (and also the trigger stations).

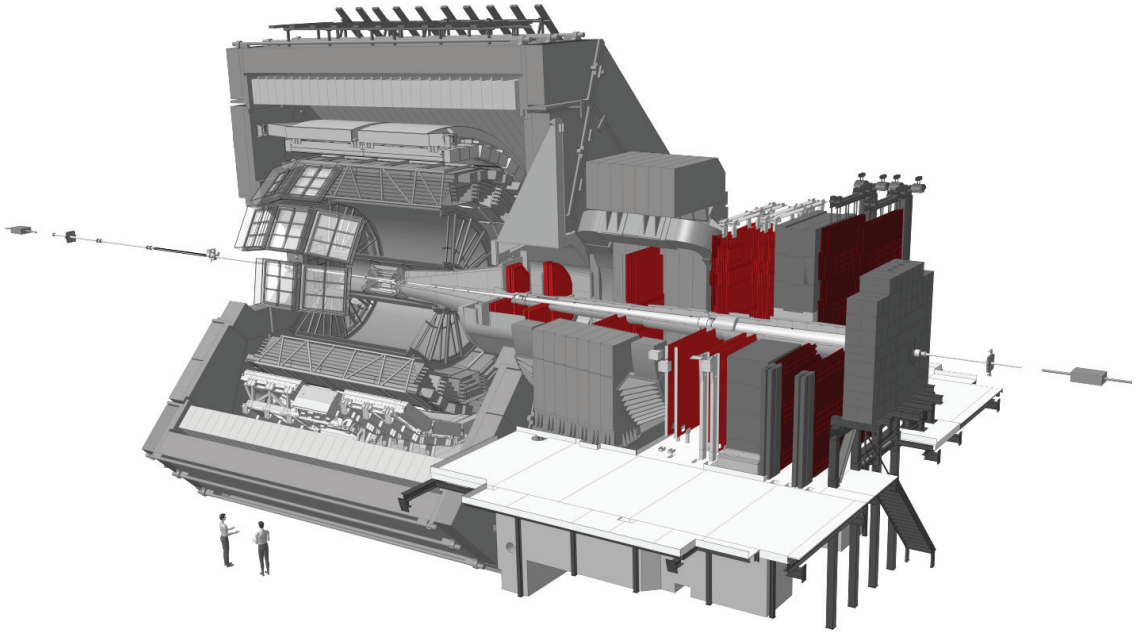

FIGURE 3.13. Tracking and trigger chambers, coloured in red, inside the ALICE detector, from [129].

3.2.3.3 Dipole magnet

A 4.97-m-long, 850-ton dipole magnet installed at 9.94 m from the interaction point provides an integrated field of 3 T.m. The direction of the magnetic field is aligned with the x-axis of the experiment. The dipole magnet deflects the path of the muons in order to perform an accurate measurement of their momentum, and hosts the spectrometer's third tracking chamber.

3.2.3.4 Trigger chambers

PLAYING a crucial role in data recorded, the muon trigger chambers stand 16 and 17 m from the interaction point. Indeed, the dimuon channel low branching ratios for the low-mass, J/ψ and Υ resonances and also for the single muons from b and c mesons imposes the a highly-selective trigger system. The two chambers are shielded by an iron filter that absorbs the residual hadrons emerging from the front absorber, as well as muons with low momentum.

The detection is performed by Resistive Plate Chambers (RPCs) with very good efficiency, and low neutron and gamma sensitivity. A hardware level-1 trigger, exploiting an approximate estimation of the transverse momentum of the tracks reaching the trigger stations, reduces the high rate of low-p_{T} muons mainly produced by the decays π and K.

3.2.4 Data acquisition in ALICE

TO record, process and calibrate the detectors, the ALICE experiment exploits three different systems: the ALICE Central Trigger, the Data AcQuisition (DAQ) and High Level Trigger (HLT) systems.

3.2.4.1 DAQ system

THE DAQ system of ALICE [124] ensures the continuous data-flow storage in the CERN servers. It is characterised by four steps.

1. At first, the signal from the Central Trigger Processor (CTP) is sent to the detector via the Local Trigger Unity (LTU). The detectors recorded signals are transferred to the DAQ ReadOut Receiver Cards (D-RORC) through the Detector Data Link (DDL). D-RORCs are PCI-X modules housed by Local Data Concentrator (LDC) computers, which are standard PCs, and each LDC may oversee many D-RORCs. The LDCs' goal is to rebuild the sub-events.

2. The HLT gets all pertinent data through DDLs and compresses it without causing any physical loss. The output data is subsequently sent to the HLT's LDC.

3. Sub-events created inside LDC are sent to the Global Data Collector (GDC). They

put together sub-events to form larger ones. The data is subsequently transferred to Transient Data Storage (TDS).

4. Finally, the data are reassembled and stored in the Permanent Data Storage (PDS). The PDS data are now accessible for reconstruction and physics analysis.

3.2.4.2 The main goal of the Central Trigger Processor

TRIGGER detectors have the main role to communicate to the CTP that a collision took place. If the required trigger criteria are fulfilled, the CTP records the event. These criteria are optimised for the ALICE physics program, the performance of the detectors, their readout electronics, the bandwidth of the DAQ and the raw data storage capacity.

Trigger classes are divided into two groups: Minimum Bias (MB) and rare triggers. In the CTP system, there are four levels of trigger.

- The fastest trigger level (650 ns delay) is Level Minus (LM) one, which was introduced in Run 2. It was just delivered as a pre-trigger to the Transition Radiation Detector (TRD).
- The Level 0 (L0) trigger as 900 ns latency. It profits from the information of V0, T0, SPD, TOF, EMCal and the muon triggers. The trigger classes for UPC triggers combine the L0 inputs of SPD, TOF, V0 and the muon trigger. Current UPC process triggers **exclusively** exploits the L0 trigger.
- The Level 1 (L1) trigger is based on the ZDC and TRD information, with a latency of 6.5 μ s.
- Finally, the Level 2 (L2) trigger is the slowest level (88 μ s of latency, which corresponds to the drift time of electrons in the TPC). This level provides the final decision to keep or reject an event.

To conclude, the LHC is a unique infrastructure to study the pp or A-A collisions at very high energy. The ALICE experiment, located in the LHC tunnel, is optimized to provide dedicated measurements of various observables allowing for the characterization of the QGP phase. In the following Chapters, the measurement of J/ψ in Pb-Pb ultra-peripheral collisions relevant for this Ph.D. thesis will be discussed.

References

[104] "LHC Machine". In: *JINST* 3 (2008). Ed. by L. Evans and P. Bryant, S08001. DOI: 10.1088/1748-0221/3/08/S08001 (cit. on p. 59).

[105] CERN. *The third run of the Large Hadron Collider has successfully started*. 2022. URL: https://home.cern/news/news/cern/third-run-large-hadron-collider-has-successfully-started (cit. on p. 60).

[106] S. Myers and E. Picasso. "The LEP collider". In: *Sci. Am.* 263N1 (1990), pp. 54–61. DOI: 10.1038/scientificamerican0790-54 (cit. on p. 60).

[107] CERN. *LHC run 3: Physics at record energy starts Tomorrow*. 2022. URL: https://home.cern/news/news/physics/lhc-run-3-physics-record-energy-starts-tomorrow (cit. on p. 60).

[108] M. Bajko et al. "Report of the task force on the incident of 19th September 2008 at the LHC". In: (Mar. 2009) (cit. on p. 60).

[109] G. Arduini et al. "High Luminosity LHC: challenges and plans". In: *JINST* 11.12 (2016). Ed. by P. Govoni, G. Lehmann, P.S Marrocchesi, F.-L. Navarria, M. Paganoni, A. Perrotta, and T. Rovelli, p. C12081. DOI: 10.1088/1748-0221/11/12/C12081 (cit. on p. 60).

[110] Paul Collier. *Status and Plans for the CERN Accelerator Complex*. 2019. DOI: 10.22323/1.367.0002 (cit. on p. 62).

[111] L. Arnaudon et al. "Linac4 technical design report". In: (Dec. 2006) (cit. on p. 62).

[112] K. H. Reich. "The CERN Proton Synchrotron Booster". In: *IEEE Trans. Nucl. Sci.* 16 (1969), pp. 959–961. DOI: 10.1109/TNS.1969.4325414 (cit. on p. 62).

[113] U. Mersits. "The Construction of the 28-GeV proton synchrotron and the first six years of its scientific exploitation". In: (1991), pp. 139–267 (cit. on p. 62).

[114] D. Banerjee et al. *The North Experimental Area at the Cern Super Proton Synchrotron*. Tech. rep. Dedicated to Giorgio Brianti on the 50th anniversary of his founding the SPS Experimental Areas Group of CERN-Lab II and hence initiating the present Enterprise. 2021. URL: https://cds.cern.ch/record/2774716 (cit. on p. 62).

[115] *Leading lead ions towards physics, first full acceleration of ions in the Lead Linac. Vers l'expérimentation, première pleine accélération des ions dans le linac à ions plomb*. 1994. URL: https://cds.cern.ch/record/1725520 (cit. on p. 63).

[116] M. Chanel. "LEIR: The low energy ion ring at CERN". In: *Nucl. Instrum. Meth. A* 532 (2004). Ed. by T. Katayama and T. Koseki, pp. 137–143. DOI: 10.1016/j.nima.2004.06.040 (cit. on p. 63).

[117] M. Harrison, Stephen G. Peggs, and T. Roser. "The RHIC accelerator". In: *Ann. Rev. Nucl. Part. Sci.* 52 (2002), pp. 425–469. DOI: 10.1146/annurev.nucl.52.050102.090650 (cit. on p. 63).

[118] G. Aad, T. Abajyan, et al. "ATLAS Collaboration". In: *Nuclear Physics A* 932 (2014). Hard Probes 2013, pp. 572–594. ISSN: 0375-9474. DOI: https://doi.org/10.1016/S0375-9474(14)00601-0. URL: https://www.sciencedirect.com/science/article/pii/S0375947414006010 (cit. on p. 63).

[119] S. Chatrchyan et al. "The CMS Experiment at the CERN LHC". In: *JINST* 3 (2008), S08004. DOI: 10.1088/1748-0221/3/08/S08004 (cit. on p. 63).

[120] A. A. Alves Jr. et al. "The LHCb Detector at the LHC". In: *JINST* 3 (2008), S08005. DOI: 10.1088/1748-0221/3/08/S08005 (cit. on p. 64).

[121] R. Aaij et al. "First Evidence for the Decay $B_s^0 \longrightarrow \mu^+\mu^-$". In: *Physical review letters* 110.2 (2013), p. 021801 (cit. on p. 64).

[122] G. Antchev et al. "The TOTEM detector at LHC". In: *Nucl. Instrum. Meth. A* 617 (2010). Ed. by Giorgio Chiarelli, Franco Cervelli, Francesco Forti, and Angelo Scribano, pp. 62–66. DOI: 10.1016/j.nima.2009.08.083 (cit. on p. 64).

[123] O. Adriani et al. "The LHCf detector at the CERN Large Hadron Collider". In: *JINST* 3 (2008), S08006. DOI: 10.1088/1748-0221/3/08/S08006 (cit. on p. 64).

[124] K. Aamodt et al. "The ALICE experiment at the CERN LHC". In: *JINST* 3 (2008), S08002. DOI: 10.1088/1748-0221/3/08/S08002 (cit. on pp. 65, 77).

[125] B. I. Abelev et al. "Performance of the ALICE Experiment at the CERN LHC". In: *Int. J. Mod. Phys. A* 29 (2014), p. 1430044. DOI: 10.1142/S0217751X14300440. arXiv: 1402.4476 [nucl-ex] (cit. on p. 65).

[126] CERN. *CERN accelerating science*. 1997. URL: https://timeline.web.cern.ch/alice-experiment-approved (cit. on p. 65).

[127] A. Fernández et al. "ACORDE a Cosmic Ray Detector for ALICE". In: *Nucl. Instrum. Meth. A* 572 (2007). Ed. by Franco Cervelli, Francesco Forti, Riccardo Paoletti, and Angelo Scribano, pp. 102–103. DOI: 10.1016/j.nima.2006.10.336. arXiv: physics/0606051 (cit. on p. 66).

[128] G. Dellacasa et al. "ALICE technical design report of the inner tracking system (ITS)". In: (June 1999) (cit. on p. 66).

[130] G. Dellacasa et al. "ALICE: Technical design report of the time projection chamber". In: (Jan. 2000) (cit. on p. 68).

[131] P. Cortese et al. *ALICE transition-radiation detector: Technical Design Report*. 2001 (cit. on p. 68).

[132] P. Cortese et al. "ALICE: Addendum to the technical design report of the time of flight system (TOF)". In: (Apr. 2002) (cit. on p. 69).

[133] P. Martinengo et al. "The ALICE high momentum particle identification system: An overview after the first Large Hadron Collider run". In: *Nucl. Instrum. Meth. A* 639 (2011). Ed. by R. Forty, G. Hallewell, W. Hofmann, E. Nappi, and B. Ratcliff, pp. 7–10. DOI: 10.1016/j.nima.2010.10.038 (cit. on p. 70).

[134] D. C. Zhou et al. "PHOS, the ALICE-PHOton Spectrometer". In: *J. Phys. G* 34 (2007). Ed. by Yu-Gang Ma, Zhi-Yuan Zhu, En-Ke Wang, Xu Cai, Huan-Zhong Huang, and Xin-Nian Wang, S719–S723. DOI: 10.1088/0954-3899/34/8/S81 (cit. on p. 70).

[135] P. Cortese et al. "ALICE electromagnetic calorimeter technical design report". In: (Sept. 2008) (cit. on p. 70).

[136] J. Allen et al. "ALICE DCal: An Addendum to the EMCal Technical Design Report Di-Jet and Hadron-Jet correlation measurements in ALICE". In: (June 2010) (cit. on p. 70).

[137] G. Dellacasa et al. "ALICE technical design report: Photon multiplicity detector (PMD)". In: (Sept. 1999) (cit. on p. 71).

[138] P Cortese et al. "ALICE technical design report on forward detectors: FMD, T0 and V0". In: (Sept. 2004) (cit. on pp. 71, 72).

[139] J.-C. Cabanillas-Noris, M. I. Martinez, and I. L. Monzon. "ALICE Diffractive Detector Control System for RUN-II in the ALICE Experiment". In: ed. by E. de la Cruz Burelo, A. Fernandez Tellez, and P. Roig. Vol. 761. 1. 2016, p. 012025. DOI: 10.1088/1742-6596/761/1/012025. arXiv: 1609.08056 [physics.ins-det] (cit. on p. 73).

[140] G. Martinez et al. "The Muon spectrometer of the ALICE experiment". In: *Nucl. Phys. A* 749 (2005). Ed. by D. Damova, A. Kugler, and P. Tlusty, pp. 313–319. DOI: 10.1016/j.nuclphysa.2004.12.059. arXiv: hep-ex/0410061 (cit. on p. 75).

[141] C. Finck. "The muon spectrometer of the ALICE". In: ed. by B. Sinha, J. Alam, and T. K. Nayak. Vol. 50. 2006, pp. 397–401. DOI: 10.1088/1742-6596/50/1/056 (cit. on p. 75).

[142] L. Bianchi. "Polarisation du J/ψ en collisions pp at $\sqrt{s}$ = 7 TeV avec le spectromètre à muons d'ALICE au LHC". PhD thesis. Université Paris Sud-Paris XI; Università degli studi (Torino, Italia), 2012 (cit. on p. 75).

4 Analysis of incoherent J/ψ polarisation in Pb–Pb UPC

We live in a highly polarised society.
We need to try to understand each other in respectful ways.
To that end, I believe that we should make room for both
spiritual atheists and thinking believers.
Alan Lightman (1948 –)

Contents

USING the Pb-Pb data collected by ALICE in the 2015 and 2018 data-taking periods, a study of polarisation of incoherent J/ψ production in UPC at $\sqrt{s_{\rm NN}}$ = 5.02 TeV at forward rapidity is performed and is described in this Chapter. The Chapter begins with the introduction of the formalism of the J/ψ polarisation and some theoretical aspects related to the measurements of the polarisation of photo-produced J/ψ. Further on, the entire procedure followed to extract the polarisation parameters is described. The results and the study of the uncertainty sources will be reported in Chapter 5.

4.1 Formalism of the J/ψ polarisation

THE degree of alignment of a particle's total angular momentum J with respect to a characteristic quantization axis z is referred to as polarisation. The particle is considered to be unpolarised if it has no favoured orientation. If, on the other side, the particle is most often seen in one of the eigenstates of J_z, it is said to be polarised.

For spin-1 particles, such as J/ψ, the quantum state in terms of angular momentum may be described as a superposition of the three J_z eigenstates:

$$|V\rangle = b_{+1}|{+1}\rangle + b_0|0\rangle + b_{-1}|{-1}\rangle\,. \tag{4.1}$$

Two extreme conditions can be identified: amplitudes b_{+1} (or b_{-1})=1 and $b_0 = 0$ correspond to *transverse* polarisation, whereas amplitudes $b_0 = 1$ and $b_{+1} = b_{-1} = 0$ correspond to *longitudinal* polarisation. Figure 4.1 shows the manifestation of the transverse and longitudinal polarisation of J/ψ in case of a dilepton decay. In such two-body decays, the angular distribution of decay particles in the rest frame of J/ψ will reflect a preferred spin alignment. An isotropic distribution will imply that quarkonium is not polarised while an anisotropic one might signal varying degrees of polarisation.

Figure 4.2 depicts the process J/$\psi \longrightarrow \ell^+\ell^-$, where the J/$\psi$ is in an initial state $|{\rm J}/\psi; 1, m\rangle$ and the dilepton system is in $|\ell^+\ell^- 1, l'\rangle$ state. Due to the helicity conservation of massless fermions in QED, the leptons, which are linked to a virtual photon in the process (J/$\psi \longrightarrow \gamma^* \longrightarrow \ell^+\ell^-$), should have spins parallel to their own momentum direction (z'[1]) in the quarkonium rest frame, hence the likely values for l' are ± 1. The amplitude

[1] z' axis is defined as the axis parallel to the momentum of the decay leptons in the quarkonium rest frame.

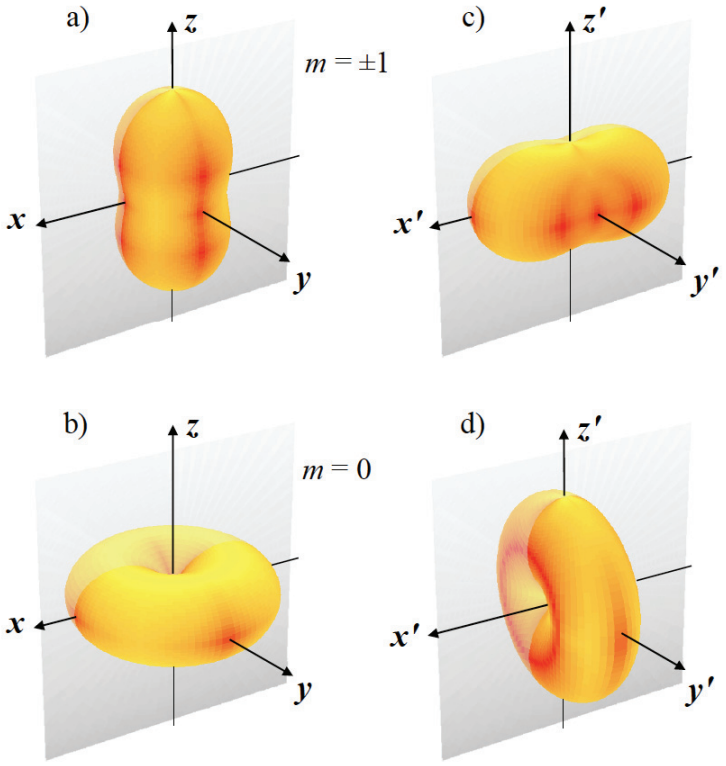

FIGURE 4.1. Transversely and longitudinally polarized quarkonium's dilepton decay distributions are shown graphically in the natural frame and in frames that have been rotated by 90 degrees, respectively, in the figures in (a-b) and (c-d). The probability of lepton emission in one direction is indicated by the distance of the relevant surface point from the origin, from [143].

of the process is given by

$$B_{ml'} = \langle \ell^+\ell^-; 1, l' | \mathscr{B} | \mathrm{J}/\psi; 1, m \rangle , \tag{4.2}$$

where $\mathscr{B}$ represents the transition operator that encodes the decay's dynamics.

If one wants to rotate the z-axis to coincide with z', the rotation is performed by $\mathscr{R}(\alpha,\beta,\gamma)$[2]. $|J, M'\rangle$ is then expressed as a superposition of $|J, M\rangle$ eigenstates.

$$|J, M'\rangle = \sum_{M=J}^{+J} \mathscr{D}^{J}_{MM'}(\alpha,\beta,\gamma)\,|J, M\rangle ,$$

where $\mathscr{D}^{J}_{MM'}(\alpha,\beta,\gamma)$ are the rotation matrix elements of the Wigner matrices [144]. To

[2] α, β and γ are the Euler angles.

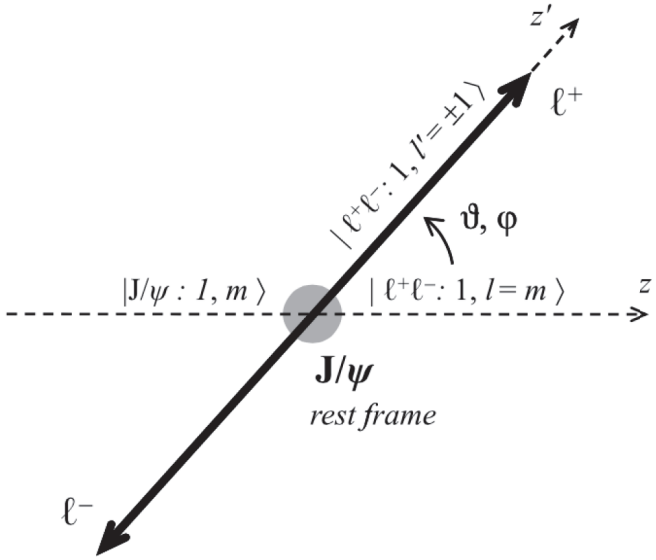

FIGURE 4.2. J/$\psi \longrightarrow \ell^+\ell^-$ process with notation of z and z' axes, the angles and the angular momentum states, from [143].

match the axes, α should be equal to φ, $\beta = \theta$[3] and $\gamma = \tilde{\varphi}$ with $\tilde{\varphi}$ defined as follows

$$\tilde{\varphi} = \begin{cases} \varphi - \dfrac{3\pi}{4} & \text{for } \cos\theta < 0, \\ \varphi - \dfrac{\pi}{4} & \text{for } \cos\theta > 0. \end{cases}$$

Due to the entire conservation of angular momentum ($l = m$), the transition operation takes the form $\langle \ell^+\ell^-; 1, l' | \mathscr{B} | \mathrm{J}/\psi; 1, m \rangle = B\mathscr{D}^*_{ml'}$ and the partial amplitude $B_{ml'}$ is equal to

$$B_{ml'} = \sum_{m=0,\pm1} B\mathscr{D}^{1*}_{ml'}(\varphi, \theta, \tilde{\varphi}). \tag{4.3}$$

Summing Equation 4.3 and defining $a_m = b_m B$ where b_m correspond to the amplitudes of the three J_z eigenstates, the angular distribution probability over all possible l' values is obtained as

$$W(\cos\theta, \varphi) \propto \sum_{l'=\pm1} |a_m \mathscr{D}^{1*}_{ml'}(\varphi, \theta, \tilde{\varphi})|^2 = |B_{l'}|^2.$$

[3] θ and φ are the polar and the azimuthal angles, respectively. Their definition is illustrated in Fig. 4.2.

Substituting $\mathscr{D}^{1*}_{ml'}(\varphi,\theta,\widetilde{\varphi})$ matrix elements, the $W(\cos\theta,\varphi)$ distribution becomes

$$W(\cos\theta,\varphi) \propto \frac{1}{3+\lambda_\theta}\left(1+\lambda_\theta\cos^2\theta+\lambda_\varphi\sin^2\theta\cos 2\varphi+\lambda_{\theta\varphi}\sin 2\theta\cos\varphi\right). \tag{4.4}$$

If the formula 4.4 is integrated over φ and $\cos\theta$ respectively, three one-dimensional angular distributions are obtained

$$\begin{cases} W(\cos\theta) \propto \dfrac{1}{3+\lambda_\theta}\left(1+\lambda_\theta\cos^2\theta\right), \\ W(\varphi) \propto 1+\dfrac{2\lambda_\varphi}{3+\lambda_\theta}\cos 2\varphi, \\ W(\widetilde{\varphi}) \propto 1+\dfrac{\sqrt{2}\lambda_{\theta\varphi}}{3+\lambda_\theta}\cos 2\widetilde{\varphi}, \end{cases} \tag{4.5}$$

where $\lambda_\theta,\lambda_\varphi$ and $\lambda_{\theta\varphi}$ are the *polarisation parameters* that correspond to various combinations of the elements of the spin density matrix of J/ψ. There are two particular polarisation cases

1. Transverse in case $\lambda_\theta,\lambda_\varphi,\lambda_{\theta\varphi}=(1,0,0)$;

2. Longitudinal in case $\lambda_\theta,\lambda_\varphi,\lambda_{\theta\varphi}=(-1,0,0)$.

The allowed domain of variation of the polarisation parameters $\lambda_\theta,\lambda_\varphi,\lambda_{\theta\varphi}$ are illustrated in Fig. 4.3.

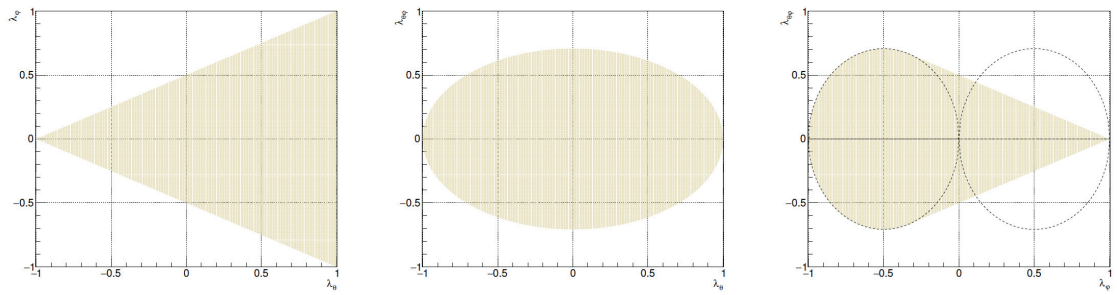

FIGURE 4.3. Left : $(\lambda_\theta,\lambda_\varphi)$ plane. Middle: $(\lambda_\theta,\lambda_{\theta\varphi})$ plane. Right: $(\lambda_\varphi,\lambda_{\theta\varphi})$ plane, from [145].

4.1.1 The reference frame definitions

THE definition of a reference frame is very important in any polarisation study. The frame is always selected to be the quarkonium rest frame with the y-axis perpendicular to the production plane which contains the momenta of the colliding beams and the quarkonium in the laboratory frame. Figure 4.4 describes the reference frame system of a two-body decay.

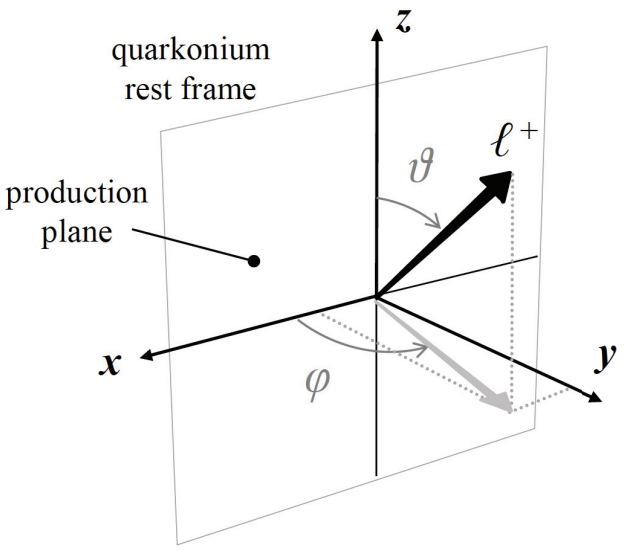

FIGURE 4.4. The angular distribution of a two-body decay measured in the quarkonium rest frame. The plane containing the momenta of the colliding beams is perpendicular to the y-axis, from [143].

There are several possible ways to select the orientation of the z axis. In the Gottfried-Jackson (GJ) frame, the z axis coincides with the direction of one of the colliding beams. In the Collins-Soper (CS) frame, the z axis is defined by the bisector of the angle between one beam's momentum and the opposite momentum of the other beam. Finally, the Helicity Frame (HX) is given by the direction of the J/ψ momentum in the centre of mass of the colliding beams. These three different definitions of the z axis are shown in Figure 4.5.

Maximum polar angular anisotropy corresponds to the axis of *natural polarisation*. Figure 4.6 depicts the decay angular distributions in case of natural longitudinal and transverse polarisation for various configuration of the CS and HX frames.

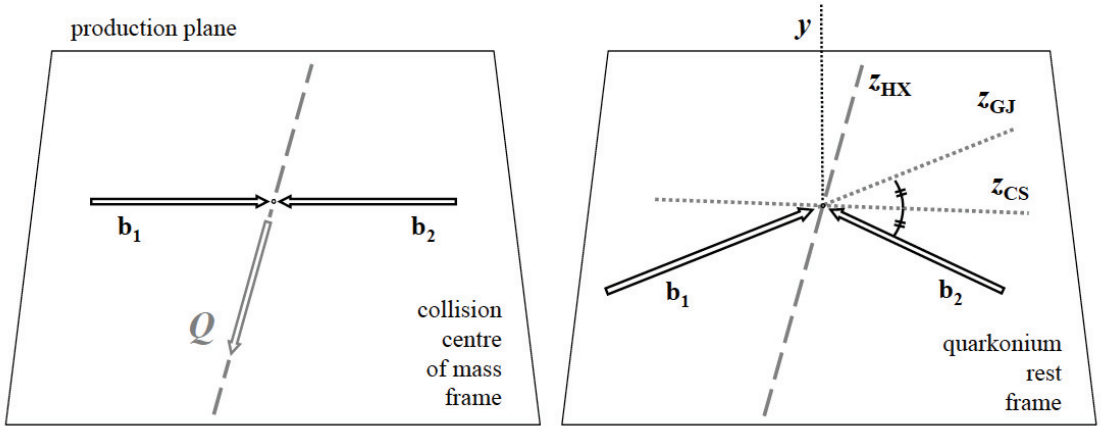

FIGURE 4.5. Three different definitions of the polarisation z axis (GJ, CS and HX) with regard to the directions of the colliding beams (b_1, b_2) and the quarkonium Q, from [143].

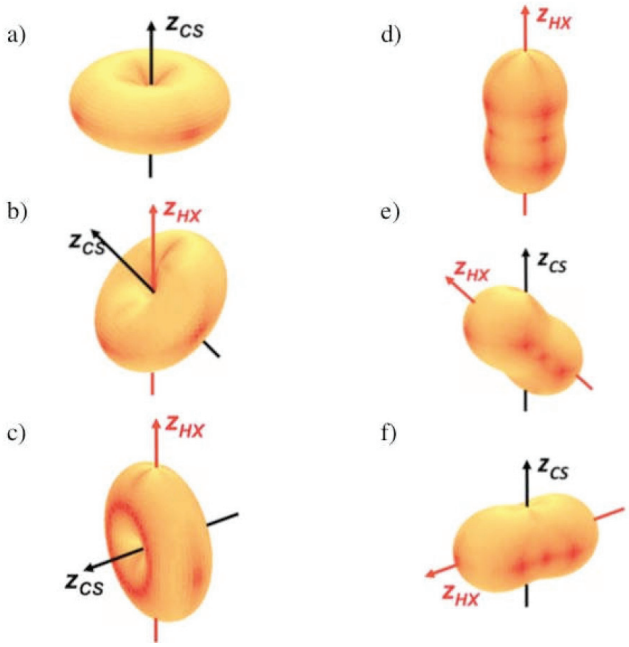

FIGURE 4.6. Decay-particle angular distribution shapes in case of fully longitudinal (left) and fully transverse (right) J/ψ polarisation, from [145].

4.1.2 Reference frame-invariant approach

A simple rotation around the y-axis is all that is needed to align one polarisation frame with another, since in all inclusive measurements the z-axis is defined to belong to the

production plane. This makes possible to define a frame-invariant polarisation parameter:

$$\lambda_{\text{inv}} = \frac{\lambda_\theta + 3\lambda_\varphi}{1 - \lambda_\varphi}, \tag{4.6}$$

which provides more information on the nature of the polarisation, for example transverse or longitudinal, of the production process, regardless of the direction of the spin alignment of the decaying particle. This parameter can be obtained using the polarisation parameters measured in a chosen reference frame.

4.2 The theoretical interest in the incoherent J/ψ analysis

As explained in Section 2.2.3, vector meson photoproduction is an important tool for probing nuclear structures at low Bjorken$-x$ [146, 147, 148]. Vector meson photoproduction occurs when an incident photon fluctuates into a $q\overline{q}$ dipole configuration, which then scatters elastically on the other nucleus (target), emerging as a real vector meson. The elastic scattering implied in this process may be thought of as occurring via the exchange of a colorless object with the same quantum numbers as the vacuum: the pomeron[4]. To the lowest order, the exchanged pomeron consists of two gluons, so the reaction probes the gluonic content of the target. Photoproduction may be either coherent or incoherent, as already explained in Section 2.2: in coherent production, the target nucleus remains intact, while in incoherent production, the target is excited or broken up.

High-energy photoproduction is mostly studied in Ultra-Peripheral Collisions (UPC) of relativistic ions, as detailed in Chapter 2. The intense electromagnetic fields associated with a Lorentz-boosted charged particle are, following the Weizsäcker-Williams method, quantized into a flux of nearly-real photons [149] (see Section 2.1). For Pb-Pb collisions at the LHC, the maximum photon-nucleon center of mass energy is about 700 GeV [149]. Because the photon flux scales with the nuclear charge Z as Z^2, the photon-nucleon luminosities are very high. This clears the way for precision studies of aspects of photoproduction, such as helicity conservation. The pomeron-exchange

[4]Well before the quark model became the general paradigm in particle physics, the notion of Regge poles [68] was the prevalent model for elementary particle scattering. The Regge pole theory fits scattering cross-sections using the complex plane and Regge trajectories, with the poles corresponding to resonances with particular spins near the resonance mass but arbitrary spins off. The exchange of Regge poles was fitted using scattering cross-section data (instead of single particles). At a period when it seemed that the Regge pole model would be the model for hadronic interactions, it was required to account for elastic scattering, i.e., when nothing else occurred than energy exchange. The pomeron trajectory was employed for this application of the Regge trajectory.

model predicts that the helicity of the vector meson should be the same as that of the incident photon [150]. This is a consequence of the fact that elastic scattering represents the absorptive part of the cross-section; absorption of some part of the wave function should not affect the polarisation of the produced vector meson. This is known as *s*-channel helicity conservation (SCHC) [151]. SCHC has been extensively verified in experiments, exploiting fixed-target photon-hadron interactions [152, 153], the electron-proton interactions at HERA, and UPCs at RHIC and LHC. The first polarisation measurement exploiting UPCs was performed by the STAR collaboration, focusing on ρ^0 photoproduction in Au–Au collisions [154], where the results were consistent with purely transverse polarisation. However, there are good reasons to search for violations of SCHC. A fraction of the production cross-section could be associated to a Reggeon exchange, which allows for the exchange of quantum numbers, including spin. Moreover, the Pomeron potential is not perfectly absorptive, and its real part could then also lead to a SCHC violation [155, 156].

Recently, ALICE has measured the polarisation of J/ψ mesons that are coherently photoproduced in Pb-Pb collisions, finding results that are consistent with SCHC [157]. These J/ψ mesons were produced with small transverse momenta, p_{T} <250 MeV/c. In this Chapter, one can find a complementary measurement of the polarisation of J/ψ mesons at higher p_{T} that are produced in incoherent photoproduction, in which the target nucleus does not remain intact.

In UPCs, the J/ψ p_{T} is the vector sum of the photon p_{T} and the pomeron p_{T}. The higher p_{T} range mostly corresponds to a larger momentum transfer between the target and the vector meson (the p_{T} of the photon with respect to the ion direction is a smaller contributor) [158], *i. e.* larger Mandelstam-$|t| \approx p_{\mathrm{T}}^2$, as briefly explained in Section 2.2.4.

The ZEUS Collaboration has measured the J/ψ polarization in the range 2<$|t|$<20 GeV^2 [159]. Their data was generally compatible with SCHC, but with a trend that Re(r_{10}^{04}) might be greater than zero, and with large uncertainties. Here, r is the spin-density matrix, and the real part of r_{10}^{04} is proportional to the single-spin flip amplitude. The H1 collaboration has also studied J/ψ production at large p_{T}, but their analysis selected events with large photon Q^2 [160], where increasing photon longitudinal polarization is expected as Q^2 rises, leading to a change in J/ψ polarization. The ZEUS collaboration has also studied polarization *vs* $|t|$ in ρ photoproduction, where the statistics are much higher [161]. They find a trend toward a decreasing r_{-11}^{04} with increasing $|t|$. The element r_{-11}^{04} is related to interference between the no-spin-flip and double-spin-flip amplitudes. This trend is particularly strong for proton-dissociative events, where the target proton breaks up. In these events for $|t|$ >2 GeV^2, r_{-11}^{04} is inconsistent with zero, and so rules out 100% transverse polarization.

Since incoherent production is visible at larger p_{T}, where coherent production is small, a change in polarization with increasing $|t|$ might be visible as a violation of SCHC for incoherent photoproduction, even if it holds for coherent photoproduction. Some theoretical work supports a change in J/ψ polarization with increasing $|t|$. Baranov, Lipatov and Zotov have predicted the polarization of J/ψ production at HERA using a k_T factorization approach [162]. They find that the polarization does depend on the J/ψ p_{T}. Unfortunately, their calculations include both direct and resolved photon components. Direct photons fluctuate to a $q\overline{q}$ dipole, while resolved photons are those that fluctuate to a $q\overline{q}$ dipole that radiates a gluon before interacting. In these non-exclusive J/ψ photoproduction events, the J/ψ has less energy than the incident photon. Some of the products of these radiation could be detected in ALICE, so a direct comparison is tricky.

4.3 Analysis strategy

QUARKONIUM polarisation is experimentally studied by extracting the angular distribution ($W(\cos\theta,\varphi)$) of its decay products. It is described in Section 4.1 and its expression is reported in Equation 4.4. The dimuonic channel decay[5] is used in this analysis. The analysis is done in the helicity polarisation frame, in which the polarisation axis is given by the flight direction of J/ψ in the centre-of-mass frame of the colliding nuclei. θ is the polar angle between the positive muon and the polarisation axis, and φ is its azimuthal angle with respect to the J/ψ production plane.

The analysis is performed following these steps :

1. select UPC event and apply muon track and dimuon selection;
2. define a binning for the angular variables;
3. separate the reconstructed dimuon events into the bins specified in the previous step and then plotting the invariant mass spectrum for each bin;
4. extract the number of J/ψ signal for each bin by a fit of the dimuon invariant mass spectra;
5. adjust the simulated p_{T} and y spectra to the spectra in the measured data;
6. use Equation 4.4 to fit the angular distribution and extract the polarisation parameters.

[5] J/$\psi \longrightarrow \mu^+\mu^-$.

Given the analysis procedure, the data sample is separated into bins of five variables: $\cos\theta$, φ, $\widetilde{\varphi}$, p_{T} and y . To perform reliable fits of the invariant mass distributions, the number of collected dimuon events in each studied bin must be sufficiently large.

4.3.1 Event, muon track and dimuon selection

THE data used in this analysis correspond to the data collected by the ALICE experiment in Pb-Pb collisions at $\sqrt{s_{\mathrm{NN}}}$ = 5.02 TeV in 2015 and 2018[6] periods during the LHC Run 2. The sample consists of 368 good runs passing the Quality Assurance (QA) selection during the first reconstruction production. The corresponding integrated luminosity is about 750 μb^{-1}.

Figure 4.7 shows the detectors used in the present analysis.

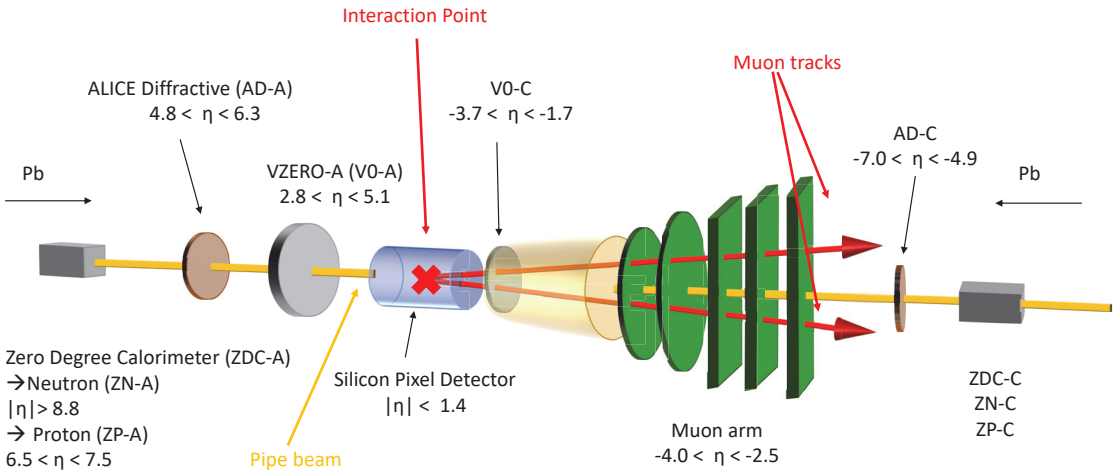

FIGURE 4.7. Schematic layout of the ALICE detector. The muon trigger is placed after the muon arm. The individual detectors are not in scale.

Events triggered by at least one of the following triggers are selected for theanalysis: for the 2018 data, three triggers have been employed `CMUP 10`, `CMUP 11` and `CMUP 26` and for 2015 data, `CMUP 13` and `CMUP 6` are used. In Table 4.1, the characteristics of each of these triggers are described.

[6]The 2015 (2018) period contains 139 (229) runs, the list of the numbers of the runs is in Appendix A.

Trigger name	Characteristics
2018	
CMUP11-B-NOPF-MUFAST (CMUP11)	OS dimuon low threshold, 0 signal in V0-A, in AD-A and in AD-C in BB window.
CMUP26-B-NOPF-MUFAST (CMUP26)	Same sign dimuon low threshold, 0 signal in V0-A, in AD-A and in AD-C in BB window.
CMUP6-B-NOPF-MUFAST (CMUP6)	OS dimuon low threshold, 0 signal in V0-A in BB window.
2015	
CMUP10	Single muon low threshold, 0 signal in V0-A, in AD-A and in AD-C in BB window.
CMUP13	OS dimuon low threshold, 0 signal in V0-A, in AD-A and in AD-C in BB window.

TABLE 4.1. Triggers used in this analysis to select the UPC events. The low muon p_{T} trigger threshold is set at 1 GeV/c.

The UPC events are further selected by requiring an absence of signal in the V0-A and AD detectors (described in Section 3.2.2.2). In addition, at most two hits compatible with beam-beam interactions are required in the V0-C detector which is positioned in front of the muon spectrometer.

In this analysis, standard cuts used in the J/ψ studies are employed for the single muon tracks and Opposite Sign (OS) dimuons, namely:

- single muon pseudo-rapidity in the range $-4 < \eta_{\mu} < -2.5$ to reject tracks at the edges of the Muon Spectrometer (MS);
- the radial transverse position of the muon tracks at the end of the absorber R_{abs} in the range $17.5 < R_{\mathrm{abs}} < 89.5$ cm, to remove tracks undergoing multiple Coulomb scatterings in the thicker parts of the absorber;
- application of $p \times DCA$ standard cut. It is based on the product of the particle momentum (p) and the distance at which the muon track makes its closest approach to the primary interaction vertex (DCA). To effectively eliminate muons that did not originate at the primary interaction vertex, such as those from beam-gas interactions, it is important to use an appropriate cut. In most of the UPC, there is no or little activity in the central barrel and therefore the primary vertex can not be reconstructed and is replaced by the nominal interaction point.
- both muon tracks reconstructed in the tracking chambers should match a trigger track reconstructed in the trigger system, above the single-muon low p_{T} trigger threshold;

- the rapidity of the dimuon in the range $-4 < y_{\mu\mu} < -2.5$, to cope with the MS acceptance;

- dimuons must be formed by the OS muons.

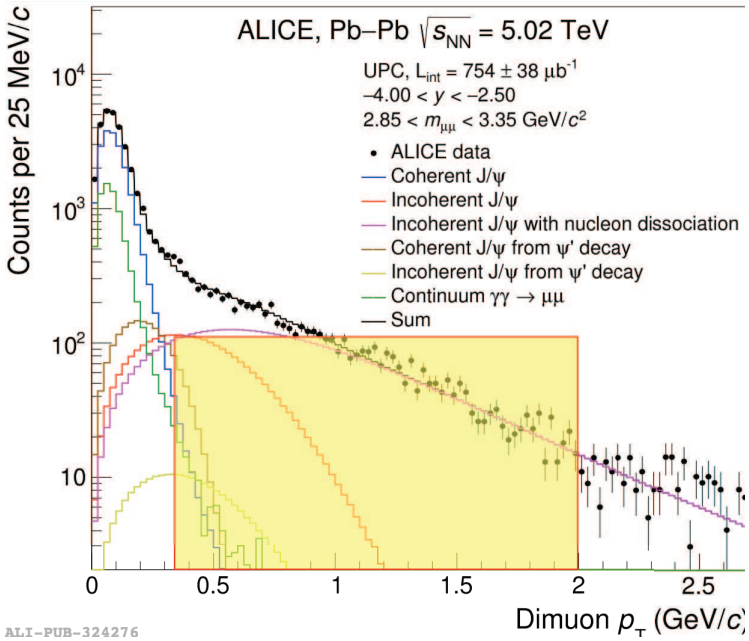

FIGURE 4.8. Transverse momentum distribution for muon pairs in the range $2.85 < m < 3.35$ GeV/c^2 (around the J/ψ mass), from [163]. Figure has been modified to highlight the studied p_T range.

The dimuon p_T is selected between 0.35 and 2 GeV/c, as shown using a yellow rectangle in Figure 4.8. The low p_T cut is chosen to avoid contamination from the coherent ψ (coherent ψ is dominant in $p_T < 0.25$ GeV/c [76]). The choice of the upper p_T cut is driven by the available statistics as there is a very small number of J/ψ candidates beyond this cut value.

The $|\cos\theta|$ in the HX frame is required to be smaller than 0.68. This selection requirement cuts the tails of the acceptance and removes only few J/ψ candidates. It is applied to guarantee the same number of entries in the $\cos\theta$, φ and $\tilde{\varphi}$ distributions (Section 4.5). Figure 4.9 shows the dimuon p_T as a function of the $\cos\theta$. One can observe that indeed the cut $|\cos\theta| < 0.68$ removes only the edges of the datector acceptance.

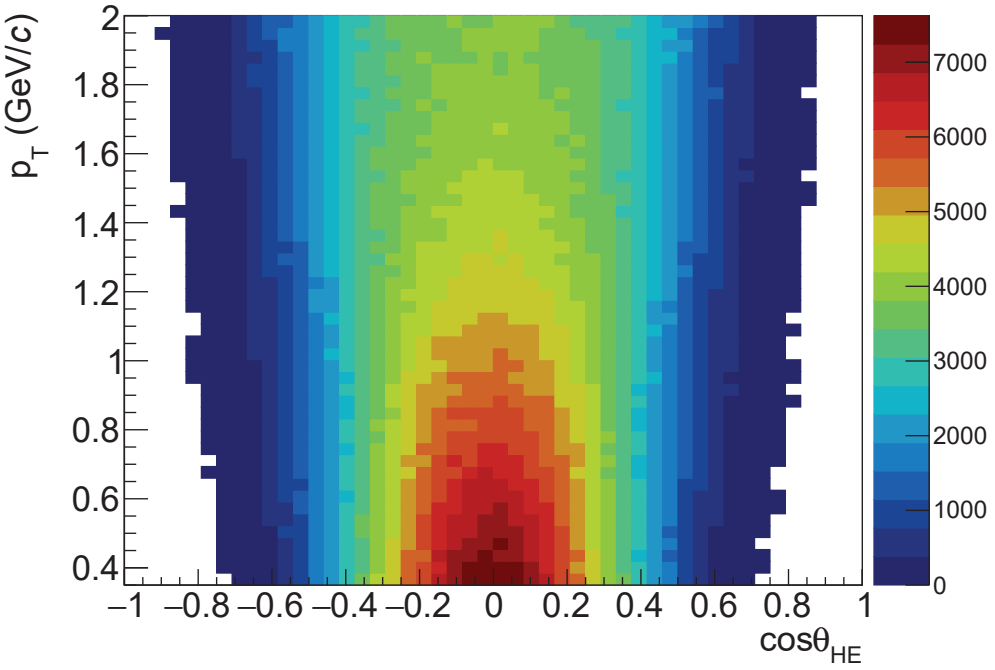

FIGURE 4.9. Two-dimensional p_T vs cosθ plot from the realistic MC simulation, created with the box generator, in the HX frame.

4.3.2 The MC production

To quantify the acceptance and the efficiency for such measurement and to understand the behavior of the reconstructed data, it is important to produce a Monte Carlo (MC) simulation capable to reproduce data.

`STARlight` is an MC generator, developed by Klein and Nystrand [164, 165], using a model that is based on the Generalized Vector meson Dominance Model (GVDM) [153], which relates the following processes :

$$\gamma + \mathrm{Pb} \longrightarrow V + \mathrm{Pb} \iff V + \mathrm{Pb} \longrightarrow V + \mathrm{Pb}$$

where V stands for the vector meson. `STARlight` uses an MC simulation of the two-photon and photon-pomeron interactions between relativistic nuclei and protons to determine the cross-section for a range of UPC final states. Despite `STARlight` usefulness in the study of coherent processes with $p_T < 0.25$ GeV/c, this generator poses problems in describing the contribution with nucleon break-up, represented with the magenta line in Figure 4.8. In addition, the steeply falling `STARlight` p_T spectrum re-

sults in very few J/ψ with p_{T} above 1-1.5 GeV/c and thus does not allow to study detector acceptance and efficiency in the p_{T} range used in this analysis.

For this reason, a new MC production created with a box generator, with a flat p_{T} between 0 and 2.5 GeV/c and $-4.2 < \eta < -2.3$ spectra, is used in this analysis as the default one. Furthermore, two STARlight-generated MCs are employed for comparisons and validation in Section 5.2.5. More information about the employment of these MC simulations and the reweighing procedure are reported in Section 4.4.

4.3.3 Signal extraction

After implementing the single muon and dimuon cuts outlined in Section 4.3.1, the invariant mass distributions are obtained and fitted to extract the J/ψ signal.

4.3.3.1 J/ψ and ψ' yields

The J/ψ yield is extracted through a fit of the dimuon invariant mass distribution: in each bin of $\cos\theta$, φ, $\widetilde{\varphi}$, p_{T} or y, the MC J/ψ invariant mass distribution is fitted with a double Crystal-Ball (CB2) function, described in Appendix B.1. The obtained CB2 tail parameters, the α_{low}, α_{high}, n_{low} and n_{high} parameters, are then used as fixed parameters in the corresponding fit of the invariant mass distribution in the data. Figure 4.10 shows the fit of J/ψ invariant mass distribution from the MC simulation, using the CB2 function.

J/ψ and ψ' are described by the same signal shapes: the same tail parameters of CB2 of J/ψ are also used for ψ'. The mass value of ψ' is given by:

$$m_{\psi'} = m^{\mathrm{Fit}}_{\mathrm{J}/\psi} + \Delta \mathrm{M}_{\mathrm{PDG}}$$

The $\sigma_{\psi'}$ value is determined by :

$$\sigma_{\psi'} = \frac{\sigma^{\mathrm{MC}}_{\psi'}}{\sigma^{\mathrm{MC}}_{\mathrm{J}/\psi}} \cdot \sigma^{\mathrm{Fit}}_{\mathrm{J}/\psi}$$

where the ratio $\sigma^{\mathrm{MC}}_{\psi'} / \sigma^{\mathrm{MC}}_{\mathrm{J}/\psi}$ is equal to 1.09 [157]. For the invariant mass fit in the data, only the normalisations of J/ψ and ψ' and the values of the J/ψ mass $m_{\mathrm{J}/\psi}$ and width $\sigma_{\mathrm{J}/\psi}$ are left free.

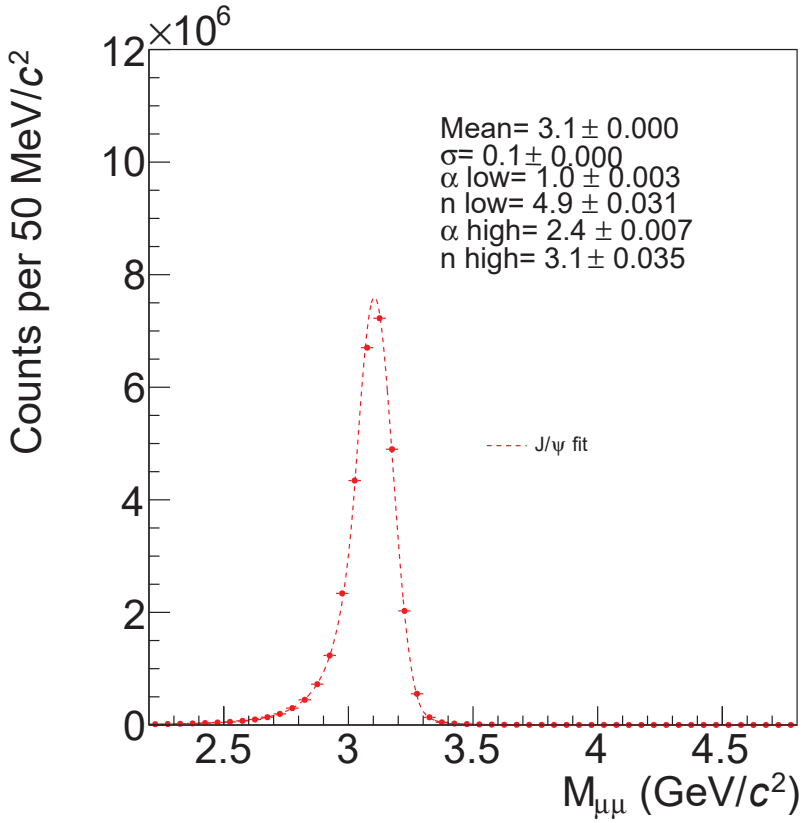

FIGURE 4.10. Fit of the J/ψ invariant mass distribution in the MC default simulation.

4.3.3.2 Background function description

IN the case of coherent J/ψ, the dimuon background source has been identified as $\gamma\gamma \longrightarrow \mu^+\mu^-$ continuum [163, 166]. It has been simulated with the `STARlight` event generator and used as a template in the dimuon invariant mass fit. In the case of incoherent J/ψ, the background sources have not been clearly identified, especially beyond 0.5 GeV/c (see Figure 4.8), and therefore the template method is not applicable. Instead different functions are tested. Each function used has four parameters and proved to properly describe the background shape in all the p_T, φ, y and $\cos\theta$ bins considered in this analysis. The first function is a Variable Width Gaussian (VWG), reported in Appendix B.2, the second function is a ratio of two polynomials of first and second orders (ratio of two polynomials of first and second orders (Pol1/Pol2)), described in Appendix B.3 and the last function is a product of second order polynomial and an exponential (product of a second order polynomial and an exponential (Pol2×Exp)), detailed in Appendix B.4.

4.3.3.3 J/ψ invariant mass fit

DUE to the limited number of entries in the dimuon invariant mass distributions, the maximum likelihood approach [167] is applied to all invariant mass fits.

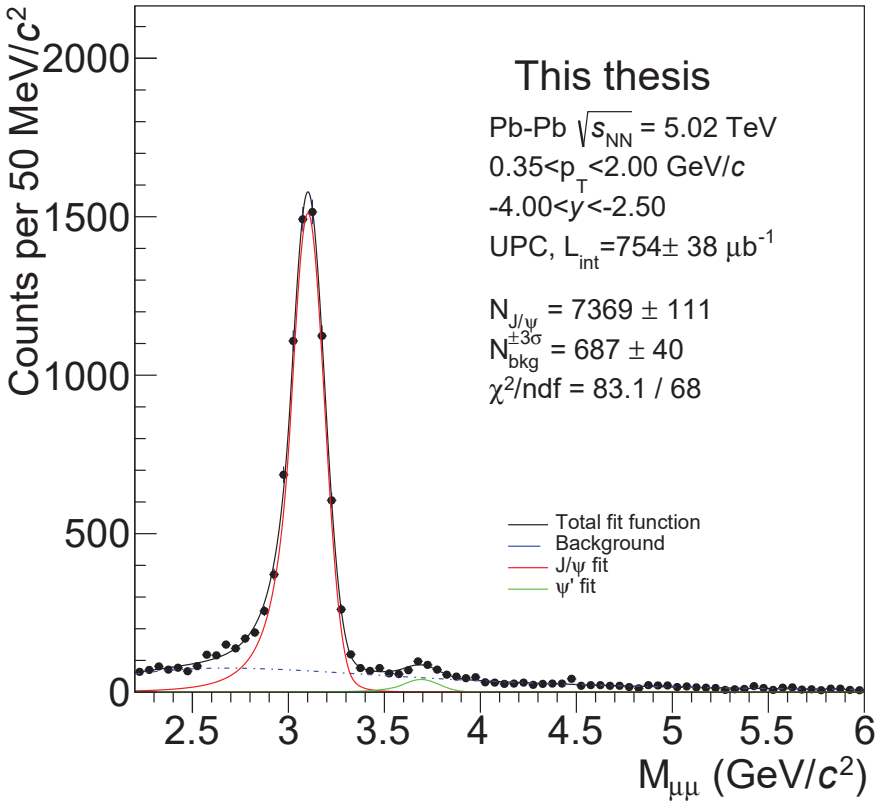

FIGURE 4.11. Dimuon invariant mass distribution. The data spectrum is integrated over p_T and y. The black distribution is fitted with a superpositon of two CB2 (red and green lines) functions and a VWG (blue line) for the background. The fit range is between 2.2 and 6.0 GeV/c^2.

The fits are performed in the mass ranges [2.2 – 6.0], [2.0 – 5.0] and [2.2 – 4.8] GeV/c to study the systematic uncertainties related to the choice of the fit range. Figure 4.11 shows the invariant mass fit in the MC and the data in the default p_T range between 0.35 and 2 GeV/c.

4.4 Adjusting of the MC p_{T} and y spectra

As mentioned in Section 4.3.2, the simulated p_{T} spectrum employing STARlight generator [168] has certain limitations since the incoherent production with nucleon break-up contribution (represented with the magenta line in Figure 4.13), which is the most essential contribution beyond 0.5 GeV/c, is not modelled.

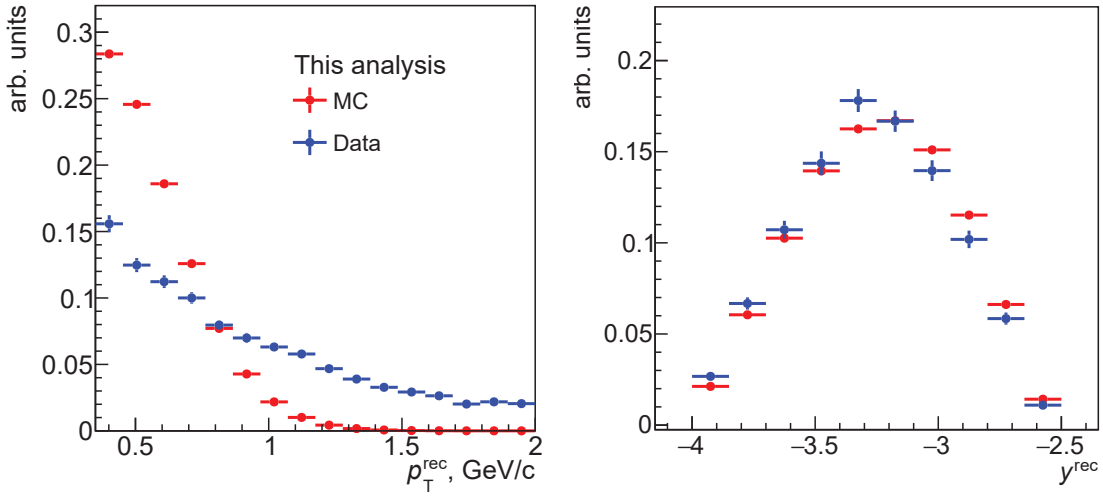

FIGURE 4.12. Reconstructed p_{T} (left panel) and y (right panel) spectra both for data (in blue) and MC (in red) produced with STARlight generator of incoherent J/ψ. The integrals of the data and MC spectra are both normalised to unity.

Indeed, the STARlight p_{T} spectrum, shown in the left panel in Figure 4.12, has practically a negligible amount of entries above 1.3 GeV/c, while the data extends to a larger p_{T} (more than 2.5 GeV/c, as Figure 4.8 shows). The reason of this discrepancy was identified to arise mainly from the missing contribution of nucleon break-up process in STARlight [163]. The contribution was parameterised with an *ad hoc* empirical function which was employed to reproduce the data spectra at higher p_{T}, with the template based on the H1 parametrisation of the J/ψ dissociative photoproduction [169]:

$$\frac{\mathrm{d}N}{\mathrm{d}p_{\mathrm{T}}} \sim p_{\mathrm{T}} \left(1 + \frac{b_{\mathrm{pd}}}{n_{\mathrm{pd}} p_{\mathrm{T}}^2}\right)^{-n_{\mathrm{pd}}}.$$

The H1 collaboration provided two sets of measurements corresponding to different photon–proton center-of-mass energy ranges: 25 GeV < $W_{\gamma\mathrm{p}}$ < 80 GeV (low-energy data set) and 40 GeV < $W_{\gamma\mathrm{p}}$ < 110 GeV (high-energy data set). More details can be found

in [76].

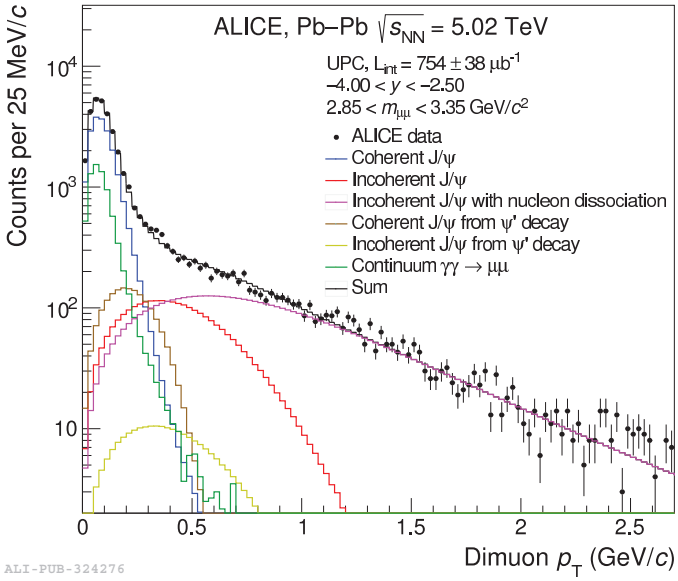

FIGURE 4.13. Transverse momentum distribution for muon pairs in the range 2.85 < m < 3.35 GeV/c^2 (around the J/ψ mass), from [76].

This issue with the `STARlight` MC generator necessitates not only adjusting its p_T spectrum to the data, but also limiting the analysis to p_T up to about 1.3 GeV/c due to inadequate MC statistics above this value. To mitigate this problem, a new uniform MC has been produced with the p_T and y spectra simulated in the ranges between 0 and 2.5 GeV/c and –4.2 and –2.3, respectively. The J/ψ decays to $\mu^+\mu^-$ are generated using EVTGEN package [170] assuming no polarisation, i.e. with polarisation parameters equal to zero.

Figure 4.14 shows the spectra of reconstructed p_T and y , using the generated flat p_T and y spectra in the MC box-generated production. Despite having enough statistics and reaching high enough p_T values, the MC spectra shapes do not match that of the data. This problem is solved by implementing an iterative MC re-weighting method.

The iterative method is characterised by the following steps :

- The reconstructed spectra of p_T and y are obtained both for data and MC, using the signal extraction procedure described in Section 4.3.1.
- The data/MC ratios is produced and fitted with appropriate arbitrary functions.
- The generated MC is then weighted at the generation level with the functions obtained in the previous step and the whole analysis is re-run.

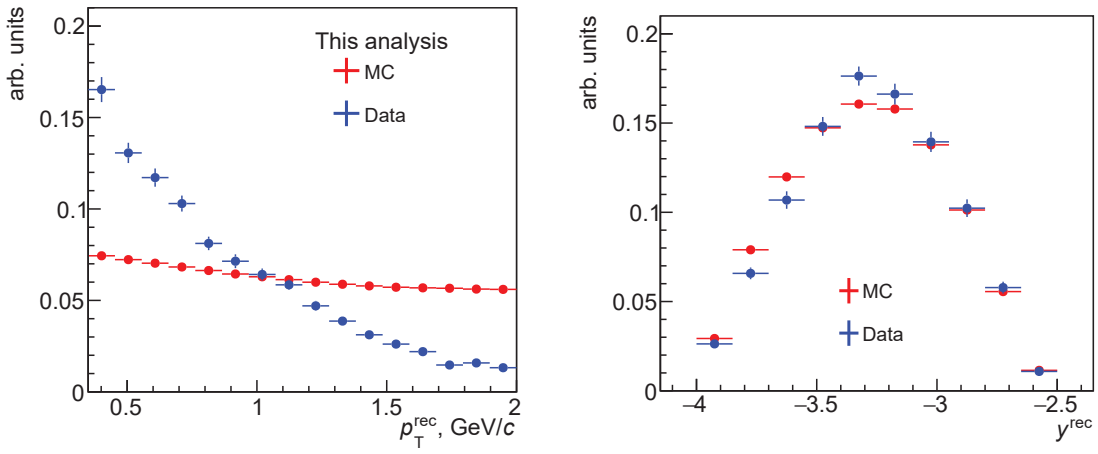

FIGURE 4.14. Reconstructed p_T (left panel) and y (right panel) spectra for both data and the box-generated MC production.

- The procedure is repeated until a satisfactory agreement between the reconstructed and the simulated p_T and y spectra is reached.

The functions used to fit the data/MC ratios of p_T and y spectra are the following:

$$\text{for the } p_T \ : \ p_1 \cdot \left(1 + p_2 \cdot (p_T - p_0) \cdot \exp\left\{\left(p_3 \cdot (p_T - p_0)^2\right)\right\}\right) \tag{4.7}$$

$$\text{for the } y \ : \ q_1 \cdot \left(1 + q_2 \cdot (y - q_0) + q_3 \cdot (y - q_0)^2\right) \tag{4.8}$$

where p_0, p_1, p_2, p_3 and q_0, q_1, q_2, q_3 are the fit parameters.

One can consider the results shown in Figure 4.14 as the first iteration of the p_T and y spectra re-weighting procedure. In general, three iterations of the method are required until the simulated spectra accurately reflect the data. In Figure 4.15, the data and the final re-weighted MC spectra are given: for improved visualisation, the data and MC spectra integrals are both normalised to unity.

To convince ourselves in the effectiveness of the re-weighting method, the data/MC ratios of p_T and y spectra are reported in Figure 4.16. As it can be seen the ratios can be fitted successfully with pol0 function and do not show discrepancies beyond the statistical fluctuations.

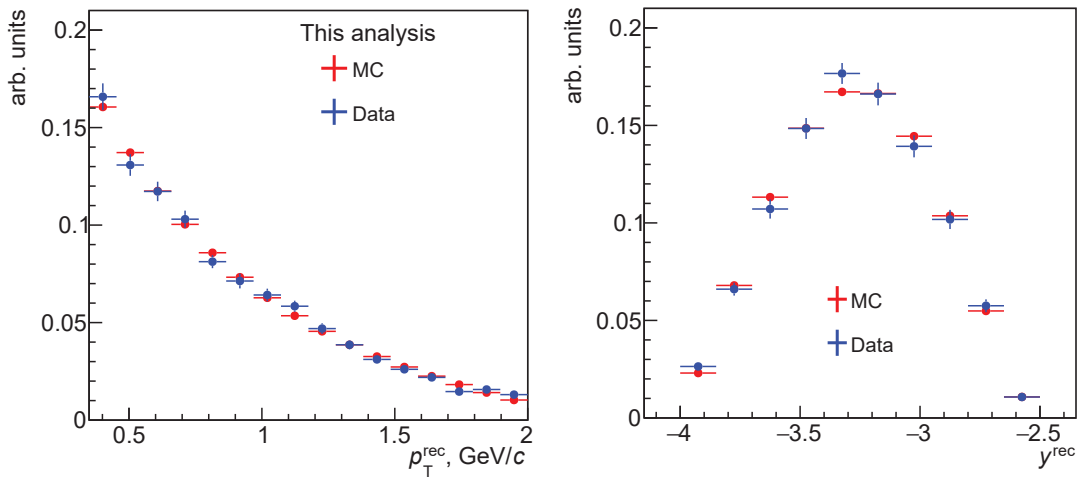

FIGURE 4.15. The reconstructed p_T (left panel) and y (right panel) spectra for both data and MC after three iterations of the MC re-weighting.

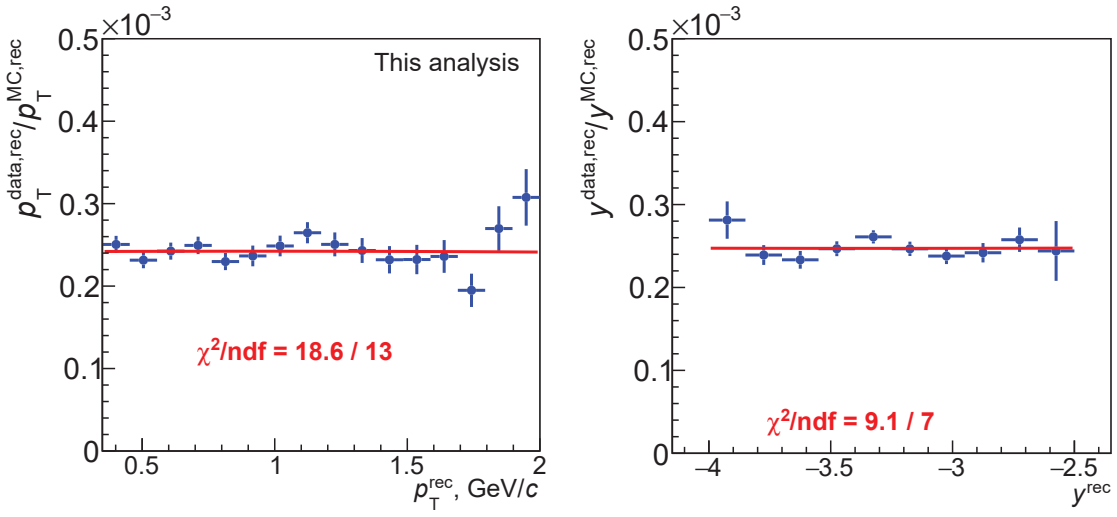

FIGURE 4.16. In this plot, the ratio between the reconstructed data and the reconstructed MC spectra both for p_T and y . The ratios are fitted with pol0 function. The plot is produced using invariant-mass fit range [2.2 – 6.0] GeV/c^2 and VWG as background function. The spectra are not normalised.

4.5 Extraction of polarisation parameters in the helicity frame

THE whole dataset is now prepared for the extraction of the polarisation parameters, as previously presented in Section 4.1. A 2D fit in $\cos\theta$, φ bins, by directly using the

Equation 4.4, cannot be performed since there are only a small number of incoherent J/ψ (about 7300, as seen in Figure 4.11). Using the three 1D angular distributions mentioned in Section 4.1 could be an alternative approach for the polarisation parameters determination. Two different methods are considered. They are described in Sections 4.5.1 and 4.5.2.

4.5.1 1st method (not used in this analysis)

USING the methods in [143] and keeping in mind what was explained in Section 4.1 to obtain Equation 4.5, it is feasible to perform three 1D fits for each angular distribution ($W(\cos\theta), W(\varphi), W(\widetilde{\varphi})$) to get the polarisation parameters ($\lambda_\theta, \lambda_\varphi, \lambda_{\theta\varphi}$). Here, the 1D distributions for each angle are reported anew:

$$\begin{cases} W(\cos\theta) = \dfrac{2\pi N_0}{3+\lambda_\theta}\left(1+\lambda_\theta\cos^2\theta\right) \\ W(\varphi) = \dfrac{2N_0}{3}\left(1+\dfrac{2\lambda_\varphi}{3+\lambda_\theta}\cos 2\varphi\right) \\ W(\widetilde{\varphi}) = \dfrac{2N_0}{3}\left(1+\dfrac{\sqrt{2}\lambda_{\theta\varphi}}{3+\lambda_\theta}\cos 2\widetilde{\varphi}\right) \end{cases}$$

These formulae hold true in the scenario of an ideal detector that provides a complete, uniform acceptance as well as a perfect response. However, as will be shown below, this is not the case in our study. The detector acceptance is in general a two-dimensional function of $\cos\theta$ and φ. In addition, the energy losses experienced by the muons in the absorber lead to significant and θ-dependent smearing and bias of the reconstructed φ angle. Because of this, the polarisation parameters are not extracted using this procedure.

4.5.2 2nd method : the *Template fit*

IN order to deal with the problems discussed in Section 4.5.1, the three 1D fits discussed there are combined into a single fit that takes properly into account the detector effects (acceptance and resolution). Since the polarisation parameters are calculated by fitting MC templates, the method is named as a "*template fit*".

The "*template fit*" is implemented as follows:

- Four MC templates are generated by applying weights using the true (generated) values of $\cos\theta$ and φ;
- After that, the angular distributions of reconstructed $\cos\theta, \varphi$ and $\tilde{\varphi}$ for each of the four templates are filled.

In this way, in total 4x3 distributions, one for each reconstructed $\cos\theta, \varphi, \tilde{\varphi}$ distribution and each of the four MC weight templates, are obtained separately. The four MC weight templates correspond to the four terms in Equation 4.4. They are defined as follows:

- 1st template is the const term with a weight equal to 1, ($w_{\text{const}} = 1$);
- 2nd template is the λ_θ term with a weight equal to $\cos^2\theta$, ($w_{\lambda_\theta} = \cos^2\theta$);
- 3rd template is the λ_φ term with the weight equal to $\sin^2\theta\cos 2\varphi$, ($w_{\lambda_\varphi} = \sin^2\theta\cos 2\varphi$);
- 4th template is the $\lambda_{\theta\varphi}$ term, with the weight equal to $\sin 2\theta\cos\varphi$, ($w_{\lambda\theta\varphi} = \sin 2\theta\cos\varphi$).

The three $\cos\theta, \varphi$ and $\tilde{\varphi}$ distributions in the data are then fitted using the superposition of these 4(x3) MC templates and the polarisation parameters λ_θ, λ_φ, $\lambda_{\theta\varphi}$ are extracted. A χ^2 fit is employed and the template integrals are used to correctly normalise the superposition.

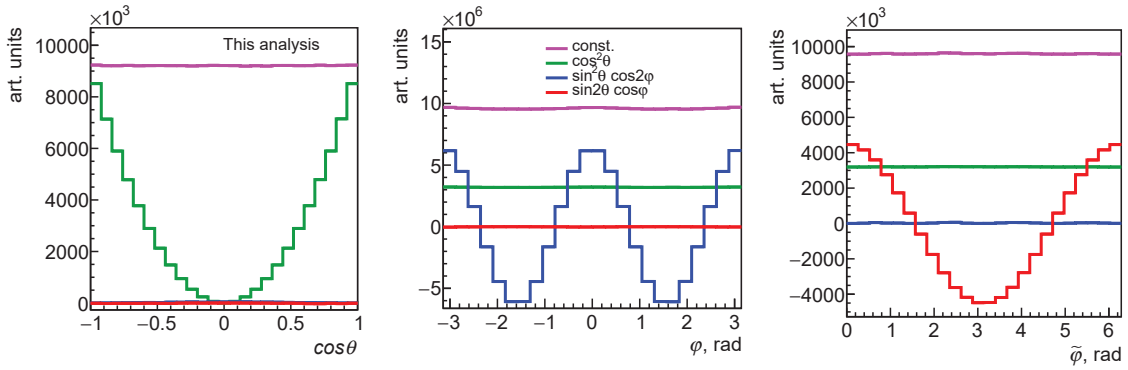

FIGURE 4.17. The four MC templates in case of ideal detector complete and uniform acceptance with a perfect response.

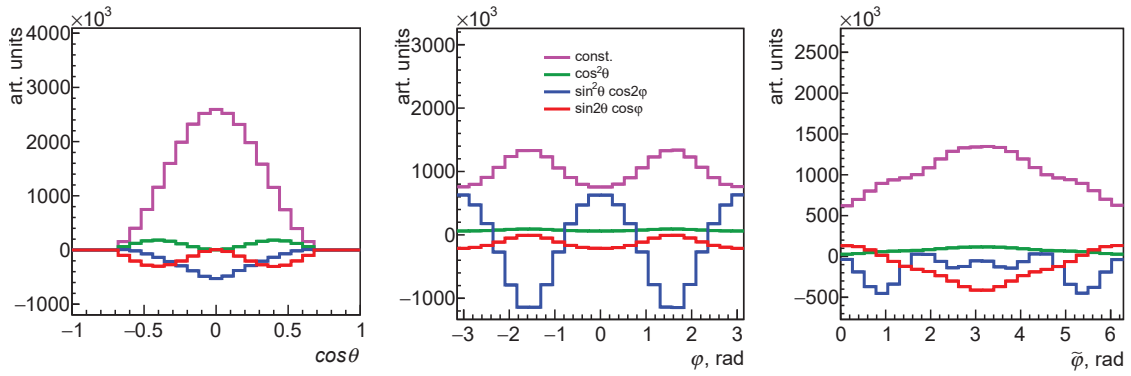

FIGURE 4.18. The fout MC templates in case of a real detector.

To demonstrate what has been described in Section 4.5.1 about the difference between an ideal and a real detector, and to elucidate the template fit procedure, a comparison between the templates created at the generator level(this is done by replacing the reconstructed $\cos\theta, \varphi$ and $\tilde{\varphi}$ by the true values at the generator level before any detector simulation) and reconstruction levels was done, in Figures 4.17 and 4.18.

At the generator level, Figure 4.17 shows the 4(x3) MC templates that correspond perfectly (by construction) to formulae introduced in Section 4.5.1. Naturally there is no mixing of various terms and their amplitudes correspond to the mentioned formulae.

When one turns to the reconstructed level, as seen in Figure 4.18, the picture changes. As can be observed, the detector acceptance and response impact not only the amplitudes of the different terms but also introduces mixing between various terms. For example, the $\sin^2\theta\cos 2\varphi$ term is not flat at 0 in the $\tilde{\varphi}$ distribution (right side of Figure 4.18). This is why the first approach presented in the Section 4.5.1 cannot be used. The second method provided here, on the other hand, takes into consideration the presence of the detector and allows for unbiased extraction of the polarisation parameters.

4.5.2.1 Validation of the template fit

MC simulation is used to validate the previously described template fit.

The first step in validation is to ensure that the uncertainties of the obtained λ polarisation parameters are correct. This is achieved using the *sub-sample* method:

- The MC is split into 100 sub-samples of equal size.

- In each one of them, the template fit is performed using templates created from the remaining MC sample.

The obtained distribution of the polarisation parameter values and their uncertainties are shown in Figure 4.19. The distributions of the parameter values are all centred at zero, and their means are also consistent with zero. The resulting standard deviations of the parameter values are totally consistent with the mean uncertainties as determined by the template fits.

Moreover, the distributions of the ratios between parameter values and their uncertainties are compatible with Gaussian distributions with a mean value of zero and σ of unity. These results prove that the uncertainties obtained with the template fit are correct.

In the sub-sample check above, the mean values of the obtained polarisation parameters are all consistent with zero, indicating that the template fit does not create biases since the employed MC sample has no polarisation (all λ's are equal to zero). The following method is used to check whether the fit introduces biases in the scenario of non-zero polarisation:

- A small fraction of the MC sample is taken and the template fit is applied constructing templates from the rest of the MC sample.
- Non-zero polarisation is introduced in the small sample at the generator level by picking randomly events according to Equation 4.4 for given polarisation parameter values.

The results of this check are shown in Figure 4.20. As observed, the fit reconstructs the true polarisation values within the uncertainties and does not induce biases. It is worth noting that the measured parameter values are (partially) correlated since they are based on the same tiny MC sample in which the random selection is applied.

The outcome of the performed checks demonstrate that the template fit does not bias the results and gives the proper parameter uncertainties.

Now that all the analysis procedures are described in detail, the next Chapter 5 is devoted to the results including the studies of the systematic uncertainties of the polarisation parameters.

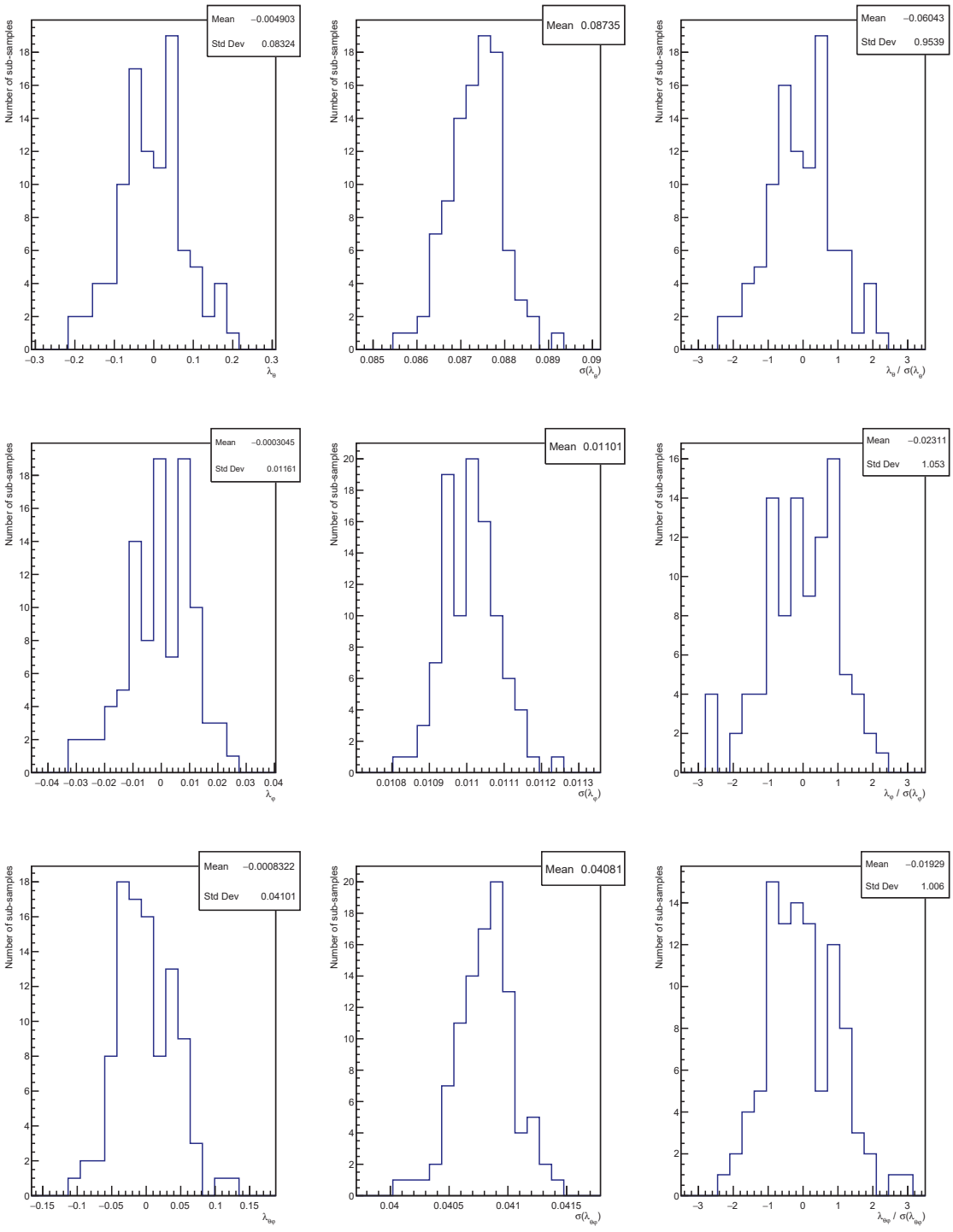

FIGURE 4.19. The distributions of the values (left), the uncertainties (middle) and their ratio (right) of λ polarisation parameters are measured in the 100 MC sub-samples.

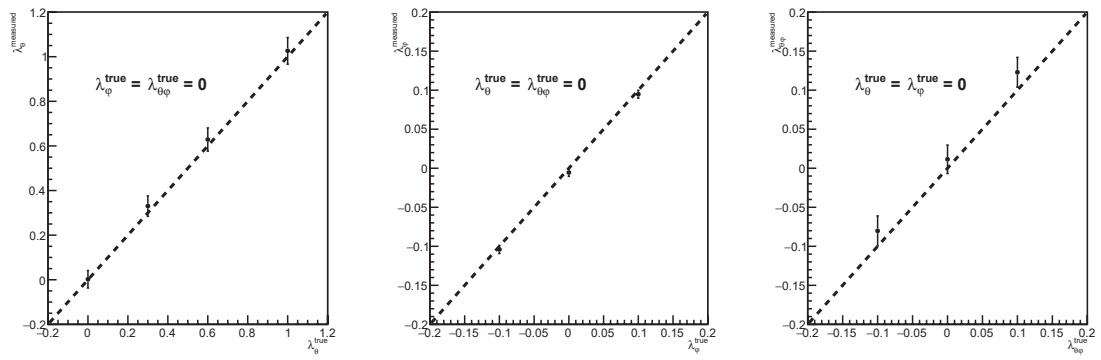

FIGURE 4.20. The measured vs true values of the polarisation parameters in MC (black points). The diagonals are plotted to guide the eye.

References

[143] P. Faccioli, C. Lourenco, J. Seixas, and H. K. Wohri. "Towards the experimental clarification of quarkonium polarization". In: *Eur. Phys. J. C* 69 (2010), pp. 657–673. DOI: 10.1140/epjc/s10052-010-1420-5. arXiv: 1006.2738 [hep-ph] (cit. on pp. 84, 85, 87, 88, 103).

[144] G B. Arous and A. Guionnet. "Wigner matrices". In: *The Oxford Handbook of Random Matrix Theory* (2011), pp. 433–451 (cit. on p. 84).

[145] A. Batista Camejo. "Study of J/ψ polarization in proton-proton collisions with the ALICE detector at the LHC". PhD thesis. U. Clermont Auvergne, 2017 (cit. on pp. 86, 88).

[146] A. J. Baltz. "The Physics of Ultraperipheral Collisions at the LHC". In: *Phys. Rept.* 458 (2008). Ed. by G. Baur et al., pp. 1–171. DOI: 10.1016/j.physrep.2007.12.001. arXiv: 0706.3356 [nucl-ex] (cit. on p. 89).

[147] S. R. Klein and H. Mäntysaari. "Imaging the nucleus with high-energy photons". In: *Nature Rev. Phys.* 1.11 (2019), pp. 662–674. DOI: 10.1038/s42254-019-0107-6. arXiv: 1910.10858 [hep-ex] (cit. on p. 89).

[148] J. G. Contreras and J. D. Tapia Takaki. "Ultra-peripheral heavy-ion collisions at the LHC". In: *Int. J. Mod. Phys. A* 30 (2015), p. 1542012. DOI: 10.1142/S0217751X15420129 (cit. on p. 89).

[149] S. R. Klein and P. Steinberg. "Photonuclear and Two-photon Interactions at High-Energy Nuclear Colliders". In: *Ann. Rev. Nucl. Part. Sci.* 70 (2020), pp. 323–354. DOI: 10.1146/annurev-nucl-030320-033923. arXiv: 2005.01872 [nucl-ex] (cit. on p. 89).

[150] H. Harari and Y. Zarmi. "Helicity conservation in diffraction scattering and duality". In: *Phys. Lett. B* 32 (1970), pp. 291–293. DOI: 10.1016/0370-2693(70)90530-7 (cit. on p. 90).

[151] F. J. Gilman, J. Pumplin, A. Schwimmer, and L. Stodolsky. "Helicity Conservation in Diffraction Scattering". In: *Phys. Lett. B* 31 (1970), pp. 387–390. DOI: 10.1016/0370-2693(70)90203-0 (cit. on p. 90).

[152] J. Ballam et al. "Conservation of s channel helicity in ρ^0 photoproduction". In: *Phys. Rev. Lett.* 24 (1970), pp. 960–963. DOI: 10.1103/PhysRevLett.24.960 (cit. on p. 90).

[153] T. H. Bauer, R. D. Spital, D. R. Yennie, and F. M. Pipkin. "The Hadronic Properties of the Photon in High-Energy Interactions". In: *Rev. Mod. Phys.* 50 (1978). [Erratum: Rev.Mod.Phys. 51, 407 (1979)], p. 261. DOI: 10.1103/RevModPhys.50.261 (cit. on pp. 90, 95).

[154] B. I. Abelev et al. "ρ^0 photoproduction in ultraperipheral relativistic heavy ion collisions at $\sqrt{s_{NN}}$ = 200 GeV". In: *Phys. Rev. C* 77 (2008), p. 034910. DOI: 10.1103/PhysRevC.77.034910. arXiv: 0712.3320 [nucl-ex] (cit. on p. 90).

[155] J. Dias de Deus. "On the Real Part of a Geometrical Pomeron". In: *Nuovo Cim. A* 28 (1975), p. 114. DOI: 10.1007/BF02730400 (cit. on p. 90).

[156] J. Pumplin and G. L. Kane. "Does the Pomeron Have Vacuum Quantum Numbers?" In: *Phys. Rev. D* 11 (1975), p. 1183. DOI: 10.1103/PhysRevD.11.1183 (cit. on p. 90).

[157] S. Acharya et al. "First measurement of coherent J/ψ polarisation in ultra-peripheral Pb-–Pb collisions at $\sqrt{s_{\mathrm{NN}}}$ = 5.02 TeV". In: *In ALICE review; to appear on the arXiv* (2023). URL: https://alice-publications.web.cern.ch/node/6342 (cit. on pp. 90, 96).

[158] S. R. Klein and J. Nystrand. "Interference in exclusive vector meson production in heavy ion collisions". In: *Phys. Rev. Lett.* 84 (2000), pp. 2330–2333. DOI: 10.1103/PhysRevLett.84.2330. arXiv: hep-ph/9909237 (cit. on p. 90).

[159] S. Chekanov et al. "Measurement of J/ψ photoproduction at large momentum transfer at HERA". In: *JHEP* 05 (2010), p. 085. DOI: 10.1007/JHEP05(2010)085. arXiv: 0910.1235 [hep-ex] (cit. on p. 90).

[160] C. Adloff et al. "Inelastic leptoproduction of J/ψ mesons at HERA". In: *Eur. Phys. J. C* 25 (2002), pp. 41–53. DOI: 10.1007/s10052-002-1014-y. arXiv: hep-ex/0205065 (cit. on p. 90).

[161] J. A. Crittenden et al. "Recent results from decay angle analyses of ρ^0 photoproduction at high momentum transfer from ZEUS". In: *Nucl. Phys. B Proc. Suppl.* 79 (1999). Ed. by J. Blumlein and T. Riemann, pp. 318–320. DOI: 10.1016/S0920-5632(99)00710-0. arXiv: hep-ex/9906005 (cit. on p. 90).

[162] S. P. Baranov, A. V. Lipatov, and N. P. Zotov. "Inclusive J/ψ photoproduction and polarization at HERA in the kt-factorization approach". In: *Eur. Phys. J. C* 71 (2011), p. 1631. DOI: 10.1140/epjc/s10052-011-1631-4. arXiv: 1012.3022 [hep-ph] (cit. on p. 91).

[163] S. Acharya et al. "Coherent J/ψ photoproduction at forward rapidity in ultra-peripheral Pb-Pb collisions at $\sqrt{s_{\mathrm{NN}}} = 5.02$ TeV". In: *Phys. Lett. B* 798 (2019), p. 134926. DOI: 10.1016/j.physletb.2019.134926. arXiv: 1904.06272 [nucl-ex] (cit. on pp. 94, 97, 99).

[164] S. R. Klein and J. Nystrand. "Exclusive vector meson production in relativistic heavy ion collisions". In: *Phys. Rev. C* 60 (1999), p. 014903. DOI: 10.1103/PhysRevC.60.014903. arXiv: hep-ph/9902259 (cit. on p. 95).

[165] S. R. Klein and J. Nystrand. "Photoproduction of quarkonium in proton proton and nucleus nucleus collisions". In: *Phys. Rev. Lett.* 92 (2004), p. 142003. DOI: 10.1103/PhysRevLett.92.142003. arXiv: hep-ph/0311164 (cit. on p. 95).

[166] ALICE Collaboration et al. *First measurement of coherent J/ψ polarisation in ultra-peripheral Pb-–Pb collisions at $\sqrt{s_{\mathrm{NN}}} = 5.02$ TeV*. 2022-2023. URL: https://alice-publications.web.cern.ch/node/6342 (cit. on pp. 97, 131).

[167] R. J. Rossi. *Mathematical statistics: an introduction to likelihood based inference*. John Wiley & Sons, 2018 (cit. on p. 98).

[168] S. R. Klein, J. Nystrand, J. Seger, Y. Gorbunov, and J. Butterworth. "STARlight: A Monte Carlo simulation program for ultra-peripheral collisions of relativistic ions". In: *Comput. Phys. Commun.* 212 (2017), pp. 258–268. DOI: 10.1016/j.cpc.2016.10.016. arXiv: 1607.03838 [hep-ph] (cit. on p. 99).

[169] C. Alexa et al. "Elastic and Proton-Dissociative Photoproduction of J/ψ Mesons at HERA". In: *Eur. Phys. J. C* 73.6 (2013), p. 2466. DOI: 10.1140/epjc/s10052-013-2466-y. arXiv: 1304.5162 [hep-ex] (cit. on p. 99).

[170] D. J. Lange. "The EvtGen particle decay simulation package". In: *Nucl. Instrum. Meth. A* 462 (2001). Ed. by S. Erhan, P. Schlein, and Y. Rozen, pp. 152–155. DOI: 10.1016/S0168-9002(01)00089-4 (cit. on p. 100).

5 Results of the analysis of the incoherent J/ψ polarisation in Pb–Pb UPC

Success is a science;
if you have the conditions, you get the result.
Oscar Wilde (1854 – 1900)

Contents

THE time has come to find out the results obtained during this analysis, whose procedure has been described in Chapter 4. In this Chapter, the polarisation parameters $(\lambda_\theta, \lambda_\varphi, \lambda_{\theta\varphi})$ results will be presented, including all the studies done to determine the systematic uncertainties and the background sources. A comparison between `STARlight` generator MC and the one created especially for this analysis with flat p_T and y spectra (presented in Section 4.4) will also be given for completeness.

5.1 Example of the template fit results

IN Section 4.5.2, the method to extract the polarisation parameters using the so-called template fit is described in detail. Let us now present results obtained using the template fit method. These results correspond to one particular case, in which the dimuon invariant mass distributions are fitted in 2.2 – 6.0 GeV/c^2 and the VWG function is used for the description of the background (Figure 5.1).

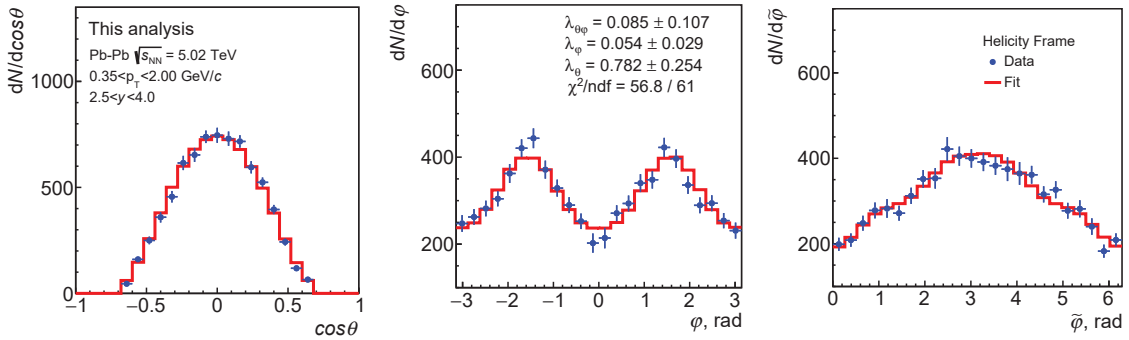

FIGURE 5.1. Data distribution functions $\cos\theta$, φ and $\tilde{\varphi}$, represented by the blue crosses, and the fitted superposition of the MC templates, represented by the dashed red lines. The obtained λ_θ, λ_φ and $\lambda_{\theta\varphi}$ parameter values are also reported. The fit is performed using the VWG function for the background in the mass region $2.2 < M_{\mu^+\mu^-} < 6.0$ GeV/c^2.

In Figures 5.2 and 5.3, the contour plots of the extracted polarisation parameters are shown. Given the way the MC templates are normalised in the template fit, the normalisation parameter N shown in Fig. 5.3 corresponds to the total number of J/ψ measured. As it can be seen from the figure, there is no sizable correlation between the λ's and N. This proves that the correctness of the chosen normalisation.

On the other hand, one can notice in Figure 5.2 that the values of the extracted λ's are correlated.

Given the example results presented above, it is possible to conclude that the template

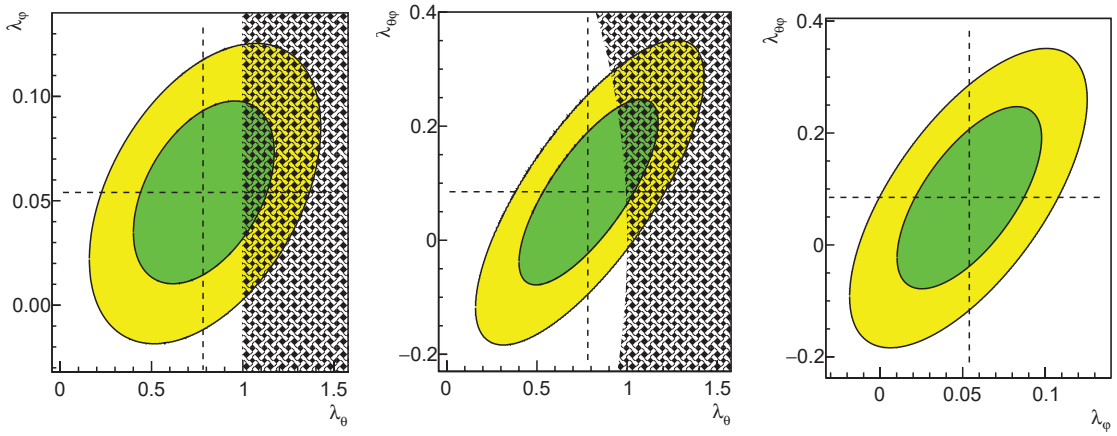

FIGURE 5.2. Correlations between polarisation parameters. Green zones indicate 1σ (68% CL) and yellow zones 2σ (95% CL) contours, respectively.

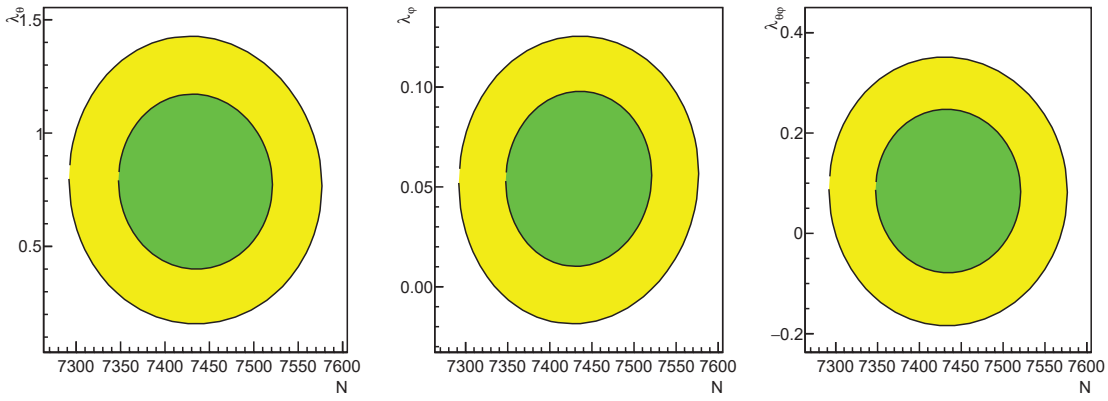

FIGURE 5.3. Correlations between polarisation parameters and the normalisation parameter N. Green zones indicate 1σ (68% CL) and yellow zones 2σ (95% CL) contours, respectively.

fit method performs quite satisfactory. The final values of the polarisation parameters are obtained by averaging the results using various invariant mass fit ranges and dimuon background functions, that will be discussed in Section 5.2.1.

5.2 Systematic uncertainties

THE following sources of systematic uncertainties are considered:

- Signal extraction;

- Trigger efficiency;
- MC p_{T} and y spectra adjustment;
- Influence of polarisation in MC.

The listed above systematic uncertainties are considered uncorrelated and therefore the total systematic uncertainties of the polarisation parameters are obtained as quadratic sums of the individual uncertainties.

5.2.1 Signal extraction

THE J/ψ yields are determined via invariant mass fits in which the dimuon background is described with various functions. As already mentioned in Section 4.3.3.2, three different background functions are used in this analysis. They are reported in the following list:

- VWG, described in Appendix B.1;
- Pol1/Pol2, described in Appendix B.3;
- Pol2×Exp, described in Appendix B.4.

In addition, it has been noted that the fit results are dependent on the fit range. Hence, the following three fit ranges are used:

- From 2.2 to 6.0 GeV/c^2;
- From 2.0 to 5.0 GeV/c^2;
- From 2.2 to 4.8 GeV/c^2.

The choice of these ranges is driven by the requirement to have sufficient and balanced background side-bands around the J/ψ peak and in general to preserve the fit stability.

The systematic uncertainty is derived by varying the background function and fit range used for signal extraction and analyzing the standard deviation of the acquired polarisation parameter values.

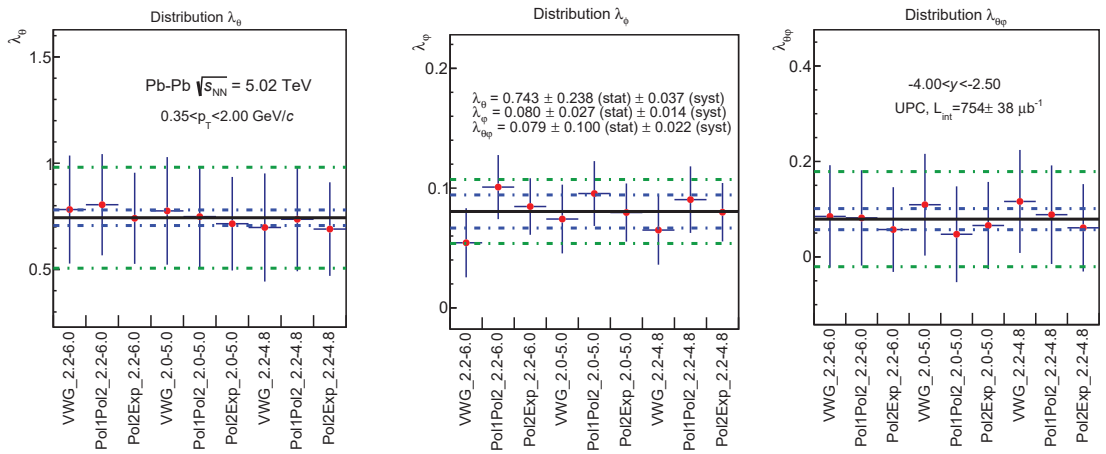

FIGURE 5.4. The values of the polarisation parameters ($\lambda_\theta, \lambda_\varphi, \lambda_{\theta\varphi}$) (red dots) depending on the fit range and background functions. The solid black line represents the mean values. The dotted blue lines represent the systematic uncertainty. Dotted green lines show the average statistical uncertainty.

This results in 9 tests/fits {(3 fit ranges)⊗(3 background functions)}. The averages of these 9 tests/fits are used to determine the central values of the parameters. The statistical uncertainties of the polarisation parameters are calculated as the averages of the statistical uncertainties of the 9 tests/fits. The systematic uncertainties of the polarisation parameters are defined as the standard deviations of the parameter values acquired in the 9 tests/fits (Figure 5.4). In Table 5.1, the average of the polarisation parameters ($\overline{\lambda_\theta}, \overline{\lambda_\varphi}, \overline{\lambda_{\theta\varphi}}$) and their statistical and systematic uncertainties are given.

	Polarisation parameter	Statistical uncertainty	Systematic uncertainty
$\overline{\lambda_\theta}$	0.743	±0.238	±0.037
$\overline{\lambda_\varphi}$	0.080	±0.027	±0.014
$\overline{\lambda_{\theta\varphi}}$	0.079	±0.100	±0.022

TABLE 5.1. Summary of the polarisation parameters determined by averaging the results using different fit ranges and the dimuon background functions. The systematic uncertainties are determined using the standard deviations of the parameters.

5.2.2 Trigger response function

ANOTHER source of systematic uncertainty is related to the limited accuracy of the simulation of the muon trigger response.

The trigger response function (Trigger Response Function (TRF)) is defined as the ratio of muon tracks passing the low-p_{T} cut trigger condition (referred to as "Lp_{T}" and corresponding to $p_{\mathrm{T}} > 1\,\mathrm{GeV}/c$) to the entire number of muon tracks (the "Ap_{T}" sample, with "A" representing the all-p_{T} condition). The same run list, reported in Appendix A, as for the polarisation analysis is exploited to generate a "Lp_{T}/Ap_{T}" distribution to have a data sample reflecting the same detector setup. The generation is done using trigger class that does not contain any muon trigger input since the objective is to assess the muon trigger response function. This procedure is described in Ref. [171]. It is used to estimate the systematic effect associated with the MC description of the TRF of the MS to single muons. The corresponding uncertainty is derived using the difference between the TRF in the data and the MC simulation.

In terms of the single muon transverse momentum, the TRF exhibits a sharp rise up to p_{T} 2 GeV/c followed by a plateau corresponding to a ~100% efficiency. The function considered to describe and fit the TRF is defined as follows:

- if the single muon p_{T} is higher than p_6 (where p_6 is forced to be < 2 GeV/c) the TRF is equal to:

$$\mathrm{TRF}(p_T > p_6) = p_7 + p_0 \cdot \mathrm{erf}\left(\frac{\max(p_T, p_6) - p_1}{\sqrt{2}p_2} - 1\right)$$

- if the p_{T} of the single muon is lower than p_6, RF is equal to the previous equation plus one additional term :

$$\mathrm{TRF}(p_T < p_6) = \mathrm{TRF}(p_T > p_6) + p_3 \cdot \mathrm{erf}\left(\frac{-\max(p_T, p_6) - p_4}{\sqrt{2}p_5} - \mathrm{erf}\left(\frac{-p_6 - p_4}{\sqrt{2}p_5}\right)\right)$$

- if p_{T} is larger than 2 GeV/c, TRF is :

$$\mathrm{TRF}(p_T > 2\,\mathrm{GeV}/c) = p_8 + \frac{p_9}{1 + \exp\{(-p_{10}(p_T - p_{11}))\}}$$

The TRF function parameters obtained in Ref.[171] are reported in Table 5.2 :

The obtained TRF in the data and the MC simulations are presented in Figure 5.5. The fits using the function described above are also shown.

The ratio of the TRF fit functions in the data and the MC is shown in the top panel of Figure 5.6. The bottom panel of the figure displays the p_{T} spectrum of single muons in the 'flat' MC used in this analysis (see Section 4.3.2). The corresponding spectrum in

	Data	MC
p_0	0.486	0.479
p_1	1.050	1.070
p_2	0.326	0.335
p_3	0.117	0.445
p_4	-0.305	-0.350
p_5	0.0844	0.271
p_6	0.650	0.293
p_7	0.995	0.999
p_8	0.123	0.123
p_9	0.877	0.877
p_{10}	1.970	2.720
p_{11}	-0.570	-0.0399

TABLE 5.2. List of parameters of TRF as obtained in [171].

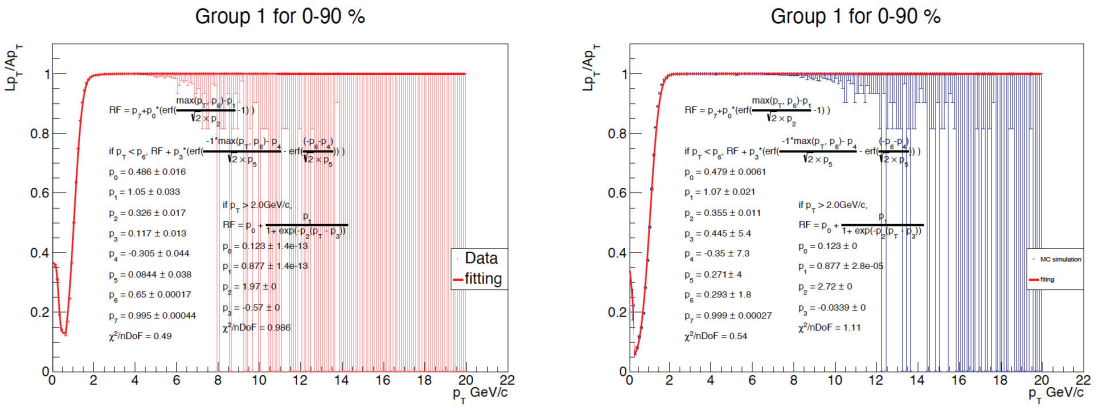

FIGURE 5.5. The TRF in the data (left panel) and in the MC (right panel). The fits using the function described in the text are also shown. The figure is taken from Ref.[171].

which the MC is weighted using the ratio of the TRF fit functions is also presented. As it can be seen, the two spectra differ significantly only at low where anyway the absolute yields are small. Therefore, the possible influence of the inaccurate TRF description in the MC is not expected to have a large impact.

The following procedure is conducted to determine the impact of the imperfect TRF description in the MC on the results for the polarisation parameters. The MC is re-weighted, with the dimuon weight being defined as the product of the single muon weights described above. The whole analysis is then rerun using this reweighted MC. The difference between the obtained in this way values of the polarisation parameters and the values obtained using the MC without weighting are taken as systematic

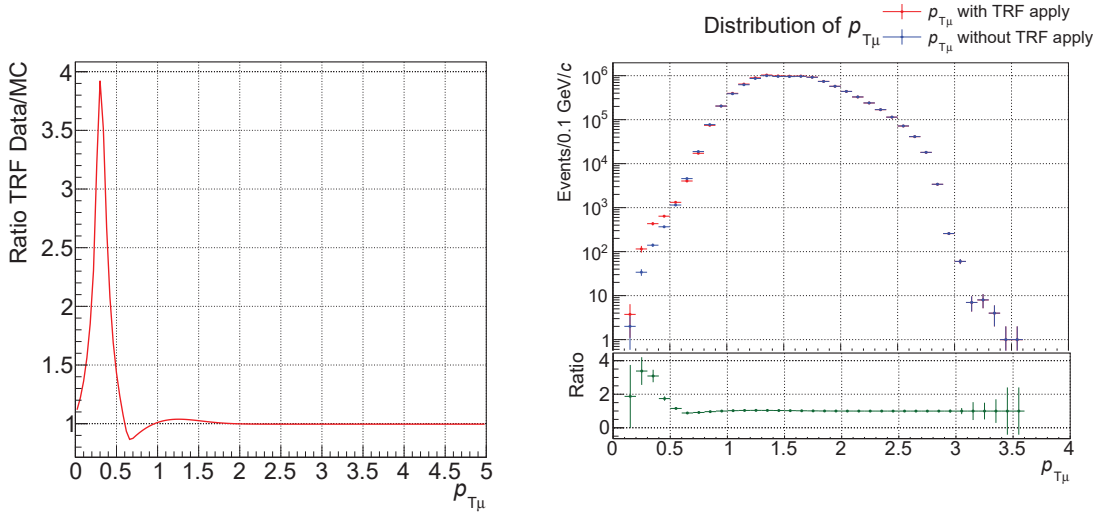

(A) RATIO TRF DATA/MC (B) p_T DISTRIBUTIONS

FIGURE 5.6. In the left panel, the ratio between the TRF fit functions in data and MC. In the right panel, the p_T of single muons in the MC. The blue points correspond to the case of no weights, and the red points to the case in which the weights using the ratio of TRF fit functions are applied.

uncertainties. It is important to mention that the analysis with the reweighted MC is performed using the three invariant mass fit ranges and the three dimuon background functions in the same way as it is done for the case of MC without weights. The results of the MC re-weighting are shown in Figure 5.7 and reported in Table 5.1.

	polarisation parameter	Statistical uncertainty	Systematic uncertainty
$\lambda_{\theta\,\mathrm{TRF}}$	0.762	$\pm$0.238	$\pm$0.019
$\lambda_{\varphi\,\mathrm{TRF}}$	0.084	$\pm$0.027	$\pm$0.004
$\lambda_{\theta\varphi\,\mathrm{TRF}}$	0.091	$\pm$0.100	$\pm$0.012

TABLE 5.3. Summary of the polarisation parameters obtained with the reweighted MC. The assigned systematic uncertainties related to the imperfect description of the muon trigger response in the MC are also quoted.

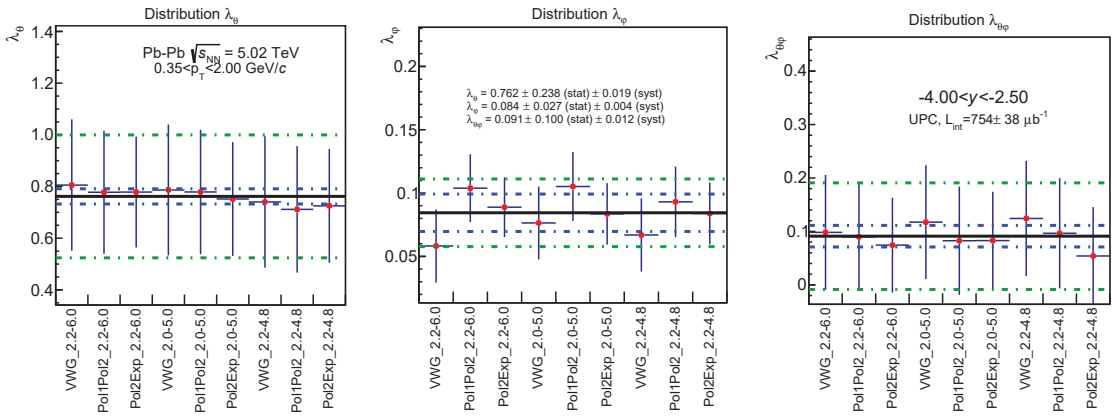

FIGURE 5.7. Polarisation parameters ($\lambda_\theta, \lambda_\varphi, \lambda_{\theta\varphi}$) as function of the invariant mass fit range and the dimuon background functions in case of the reweighted MC. The black solid line indicates the average values. Dotted blue lines indicate the attributed systematic uncertainties (using the differences between the average λ values with and without the re-weighting). Dotted green lines show the statistical errors.

5.2.3 MC p_T and y spectra adjustment

THE p_T and y spectra in the MC are adjusted using the procedure outlined in Section 4.4.

The adjustment has a limited accuracy due to the poor statistics in the data, which might affect the results for the polarisation parameters. To assess this, the parameters acquired during the last adjustment iteration from the fits of the p_T and y ratios data/MC (see Equations 4.7 and 4.8) are varied within their statistical uncertainties.

The following variations are performed:

- ***x* Up** meaning that the fit parameters are increased by 1σ;
- ***x* Default** meaning that the fit parameters are left unchanged;
- ***x* Low** meaning that the fit parameters are decreased by 1σ,

where x denotes the p_T or y variables. In Table 5.4, the nomenclature of the nine (3×3) fit parameter variations is reported. The effect of the variations of the fit parameters on are illustrated in Figure 5.8, where the corresponding variations of the fit functions are compared to the ratios data/MC of p_T and y spectra. As it can be seen the variations enclose well the statistical fluctuations seen in the ratios.

p_{T} value	y value
p_{T} Up	y Up
p_{T} Low	y Low
p_{T} Default	y Up
p_{T} Default	y Low
p_{T} Up	y Low
p_{T} Low	y Up
p_{T} Up	y Default
p_{T} Low	y Default
p_{T} Default	y Default

TABLE 5.4. Variations of p_{T} and y spectra in the MC used to evaluate the influence of the fit parameter uncertainties obtained during the adjustment of p_{T} and y spectra in the MC.

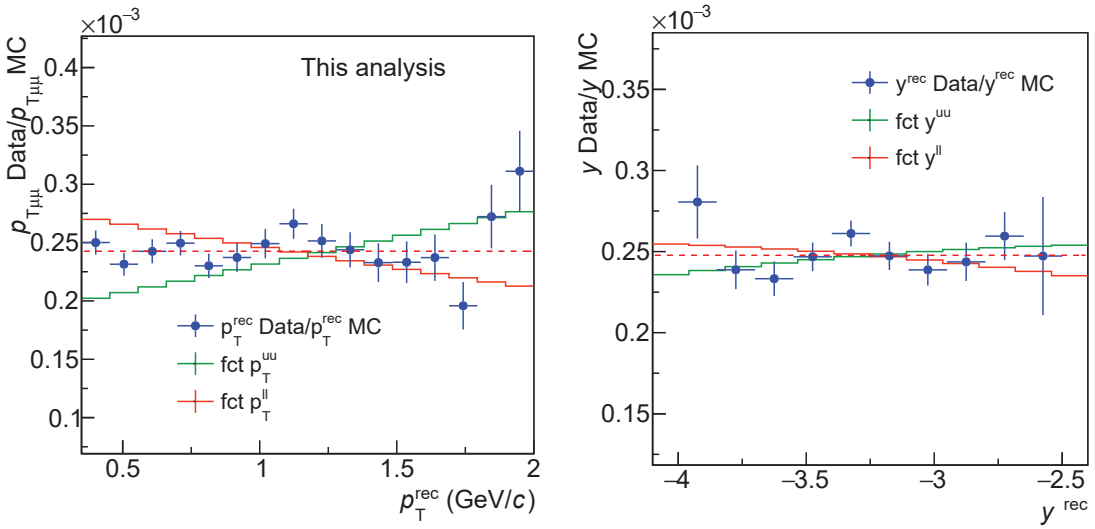

FIGURE 5.8. p_{T} Low, p_{T} Up and y Low, y Up variations compared to the ratios of data/MC p_{T} (left) and y (right) spectra, respectively.

The entire analysis is repeated for each of these 9 variations including the invariant mass fits with different fit ranges and dimuon background functions. The corresponding results for the λ parameters are shown in Figure 5.9. The method for assigning systematic uncertainties is the same as in the case of systematic uncertainties related to the signal extraction (see Section 5.2.1), i.e. the standard deviation of the obtained polarisation parameters are taken as systematic uncertainties. The obtained results are also summarised in Table 5.5.

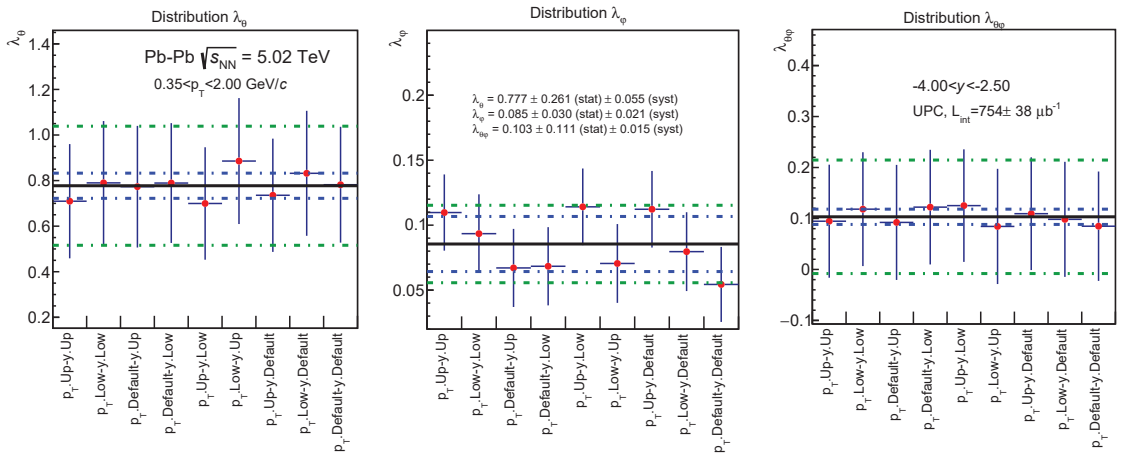

FIGURE 5.9. Polarisation parameters ($\lambda_\theta, \lambda_\varphi, \lambda_{\theta\varphi}$) as a function of the MC p_T and y spectra variations. The black solid line indicates the average values. Dotted blue lines indicate the attributed systematic uncertainties. Dotted green lines show the average statistical uncertainties.

	polarisation parameter	Statistical uncertainty	Systematic uncertainty
λ_θ MC adj	0.738	±0.237	±0.079
λ_φ MC adj	0.086	±0.027	±0.011
$\lambda_{\theta\varphi}$ MC adj	0.091	±0.100	±0.023

TABLE 5.5. Summary of the resulting polarisation parameters calculated by averaging the values obtained with the variations of the MC p_T and y spectra. The systematic uncertainties are determined using the corresponding standard deviations as explained in the text.

5.2.4 Influence of polarised MC

THE template fit method, employed here and described in Section 4.5.2, is by construction insensitive to polarisation in the MC. Nevertheless, the 'flat' MC employed in this analysis (see Section 4.3.2) is performed without polarisation, while an eventual presence of a polarisation may affect the reconstructed p_T and y spectra through the detector acceptance (for example the acceptance as a function of p_T in general depends on cos$_\theta$ as illustrated in Figure 4.9). Therefore, the polarisation in MC can alter the MC spectra adjustment and hence result in a systematic effect on the extracted values of the polarisation parameters. Given that the polarisation is *a priori* unknown, the systematic effect is estimated by introducing full transverse polarisation in the MC. This is done by re-weighting the MC. The corresponding weight is defined as:

$$w = \frac{1 + \lambda_\theta \times \cos(\theta)^2}{3 + \lambda_\theta}, \tag{5.1}$$

with $\lambda_\theta = 1$. The re-weighting is applied at the MC generator level.

Figure 5.10 shows the results of this MC re-weighting. As in the case of the other systematic uncertainties, the entire analysis is repeated including the invariant mass fits with different fit ranges and dimuon background functions. The difference of the obtained

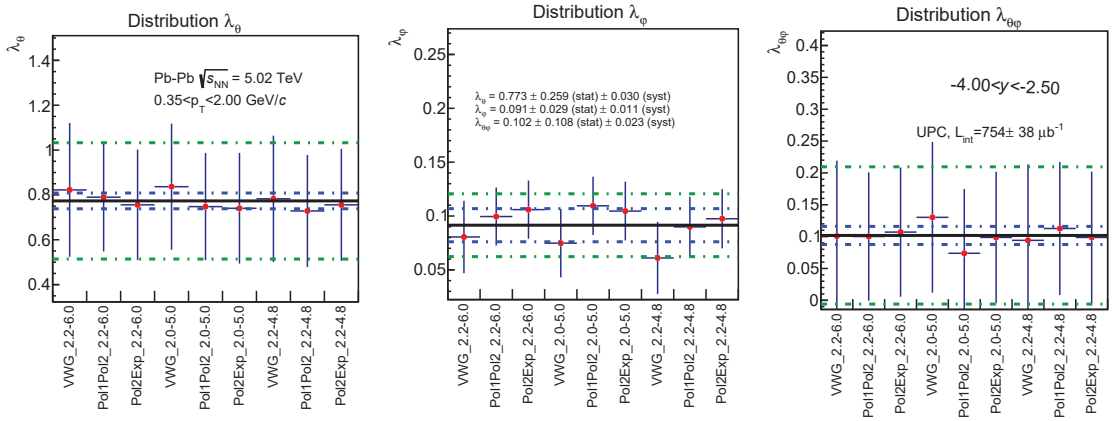

FIGURE 5.10. Polarisation parameters ($\lambda_\theta, \lambda_\varphi, \lambda_{\theta\varphi}$) obtained by introducing full transverse polarisation in the MC. The black solid line indicates the average values. Dotted blue lines indicate the attributed systematic uncertainties calculated using the differences with respect to the nominal values of polarisation parameters. The dotted green lines show the average statistical uncertainties.

parameter values with respect to the nominal ones (using the default MC without polarisation) are taken as systematic uncertainties. The results of this systematic check are summarized in Table 5.6.

	polarisation parameter	Statistical uncertainty	Systematic uncertainty
λ_θ Pol	0.773	±0.259	±0.030
λ_φ Pol	0.091	±0.029	±0.011
$\lambda_{\theta\varphi}$ Pol	0.102	±0.108	±0.023

TABLE 5.6. Summary of the polarisation parameters determined introducing full transverse polarisation in the MC. The systematic uncertainties are determined using the difference between the average λ values and the nominal ones from Table 5.1.

5.2.5 Comparison with `STARlight` generator

IN addition to the systematic checks described above, one further study related to the usage of the 'flat' MC is performed. As explained in Section 4.3.2, the `STARlight` generator MC is replaced by a MC simulation with flat p_T and y spectra. Below, a comparison

between the results obtained with the two MC simulation is presented in order to assess the performance of the 'flat' MC used by default in the analysis.

Results with STARlight and 'flat' MC simulations are shown in Figures 5.11 and 5.12 for the p_{T} range between 0.35 and 1.35 GeV/c. The upper p_{T} limit is chosen to allow the usage of the STARlight generator as explained in Section 4.3.2. One can notice

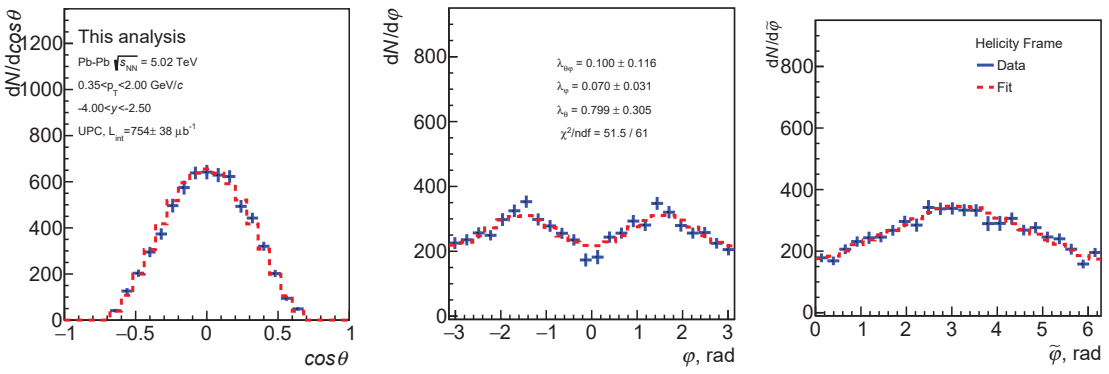

FIGURE 5.11. The polarisation parameters $(\lambda_\theta, \lambda_\varphi, \lambda_{\theta\varphi})$ for p_{T} between 0.35 and 1.35 GeV/c obtained using STARlight MC.

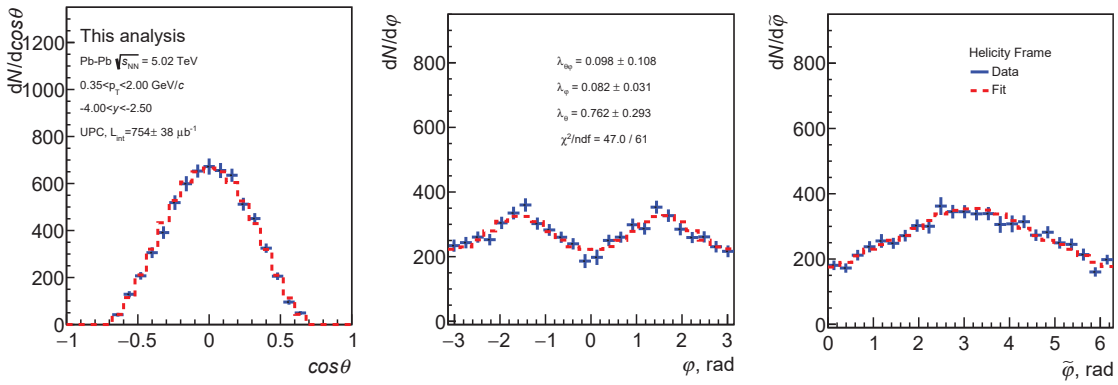

FIGURE 5.12. The polarisation parameters $(\lambda_\theta, \lambda_\varphi, \lambda_{\theta\varphi})$ for p_{T} between 0.35 and 1.35 GeV/c obtained using the 'flat' MC.

that the results are very close. The most sizeable difference is observed for λ_θ. Here it is worth noting that the STARlight MC contains pure transverse polarisation, while by default the 'flat' MC does not. Therefore, the observed difference should be compared to the systematic uncertainty related to the presence of polarisation in MC (see Section 5.2.4). As can be seen the λ_θ difference is about 0.036 which is comparable to the associated systematic uncertainty of 0.030 (see Table 5.6). Unfortunately, one

can not perform more strict comparisons between the STARlight and 'flat' MCs, because the polarisation in STARlight is implemented in the γ-pomeron rest frame and the data stored in the MC is insufficient to "undo" precisely enough (for example via re-weighting) the implemented polarisation.

A final point regarding the comparison of the two MCs is that the drastic differences in their p_{T} spectra (Figures 4.12 and 4.14 in Section 4.4) can eventually result in residual differences in the adjusted MC p_{T} spectra, which however are well covered by the systematic uncertainties discussed in Section 5.2.3.

5.2.6 Summary of statistical and systematic uncertainties

PUTTING together all the data presented in Tables 5.1, 5.2, 5.5 and 5.6, Table 5.7 summarises the statistical and systematic uncertainties of the polarisation parameters (λ_θ ,λ_φ ,$\lambda_{\theta\varphi}$) obtained in this analysis. The uncertainties are considered uncorrelated, each statistical errors from each test is summed in quadrature with the other ones.

Uncertainties	λ_θ	λ_φ	$\lambda_{\theta\varphi}$
Statistical	0.238	0.027	0.100
Signal extraction	0.037	0.014	0.022
Trigger response	0.019	0.004	0.012
MC spectra adjustment	0.079	0.011	0.023
Polarised MC	0.030	0.011	0.023
Total systematic	0.094	0.021	0.041

TABLE 5.7. Summary of statistical and systematic uncertainties.

5.3 J/ψ background studies

IN Section 4.3.3.2, the sources of the dimuon background under the J/ψ peak were briefly discussed. In addition to this background, there are also J/ψ not originating from incoherent photo-production. These have to be considered as background in this analysis. Their study will be presented in this Section.

5.3.1 Background from hadronic interactions

CONSIDERING that the analysis goes up to a relatively high p_{T} of 2 GeV/c, a substantial amount of background from hadronically produced J/ψ may arise. Two studies are performed to elucidate the amount of this kind of background. The first study uses same-sign (Same Sign (SS)) dimuons and an extrapolation of J/ψ yields in 0-90% collision centrality (Section 5.3.1.1). The second study employs the SPD tracklet distribution in the UPC data sample (Section 5.3.1.2).

5.3.1.1 The same-sign dimuons and the extrapolation of J/ψ yields in 0-90% centrality

THE first performed check relies on the same-sign dimuons. The rest of the event, track and dimuon selection is kept the same. The opposite-sign and same-sign dimuon invariant mass distributions are compared in Figure 5.13. These distributions correspond

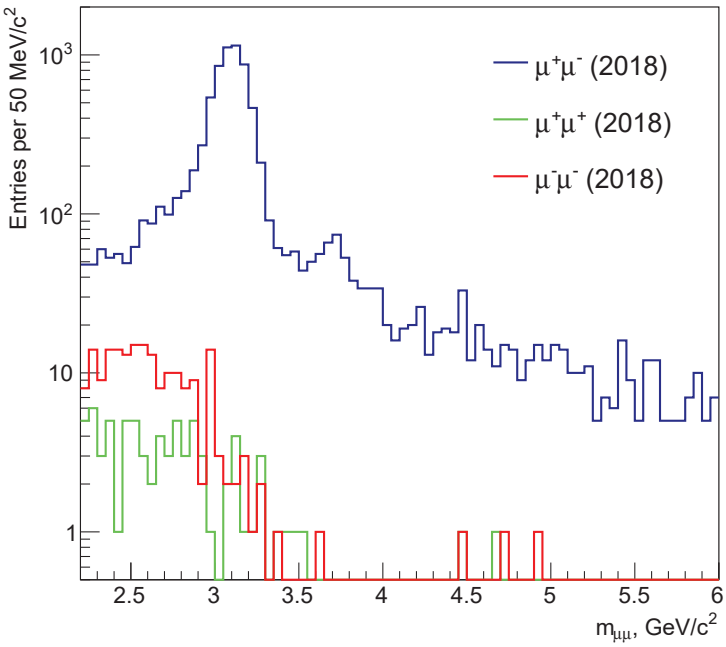

FIGURE 5.13. Invariant mass distribution for same-sign and opposite-sign dimuons for p_{T} between 0.35 and 2 GeV/c in the 2018 data sample.

only to the 2018 data sample. The reason to use only 2018 data is that, in 2015, the CMUP10 trigger (based on single trigger input, described in Table 4.1) was only employed

for a small portion of the data and there was no dedicated same-sign dimuon trigger. On the other hand, in 2018, same-sign dimuon CMUP26 trigger was used during the entire data taking. It is worth noting that the 2018 data sample is 75% of the all data sample and hence comprises about 5500 J/ψ in $0.35 < p_{\mathrm{T}} < 2.00$ GeV/c.

In the mass range between 2.5 and 3.7 GeV/c^2, 168 $\mu^-\mu^-$ and $\mu^+\mu^+$ couples are found. The J/ψ and dimuon yields in hadronic collisions as a function of centrality are studied to determine whether these dimuons arise from hadronic collisions and, if so, what is the corresponding level of the hadronically produced J/ψ. The muon track and dimuon selections remain unchanged. The event selection requires CMUL7[1] or CMLL7[2] triggers to be fired. The analysis is done with and without applying the physics selection[3]. The events in which only CMLL7 trigger is fired are weighted with the inverse of the CMLL7 downscaling factor. This factor is obtained from the CTP scalers and is calculated run-by-run.

Three dimon invariant mass regions are defined :

- $2.5 < m_{\mu\mu} < 2.9$ GeV/c^2, the left side band background;
- $2.9 < m_{\mu\mu} < 3.3$ GeV/c^2, the J/ψ signal region;
- $3.3 < m_{\mu\mu} < 3.7$ GeV/c^2, the right side band background.

The J/ψ yields are obtained by subtracting the yields in side band regions from the signal region. This simplified approach is adapted instead of an invariant mass fit because the present study does require very high precision. In Figure 5.14, the obtained number of J/ψ, together with Opposite Sign (OS) and Same Sign (SS) dimuon background vs average event multiplicity in numerous centrality bins, is provided. The event multiplicity values are taken from Ref. [172]. The distributions of the signal and the SS dimuon background are fitted using power-law functions. The OS background is fitted using the sum of two power-law functions, with the power-law exponents fixed to the signal and SS dimuon background values. The power-law exponent of the signal, represented by the red dots in Figure 5.14, is found to be close to 1, which agrees with the linear multiplicity dependence seen in p-p collisions [173]. The SS dimuon background, represented by the blue dots, has a power-law coefficient of 2, indicating that this background is combinatorial. Finally, the OS dimuon background represented by the green

[1] CMUL7-B-NOPF-MUFAST (CMUL7) is OS dimuon trigger, which is a coincidence of 0MUL (OS dimuon with low p_{T} threshold), V0A and V0C triggers.

[2] CMLL7-B-NOPF-MUFAST (CMULL7), SS dimuon trigger, which is a coincidence of 0MLL (SS dimuon with low p_{T} threshold), V0A and V0C triggers.

[3] The physics selection denotes a standard offline selection of hadronic collisions. Its main part is the requirement of signals compatible with beam-beam interactions in both V0A and V0C detectors.

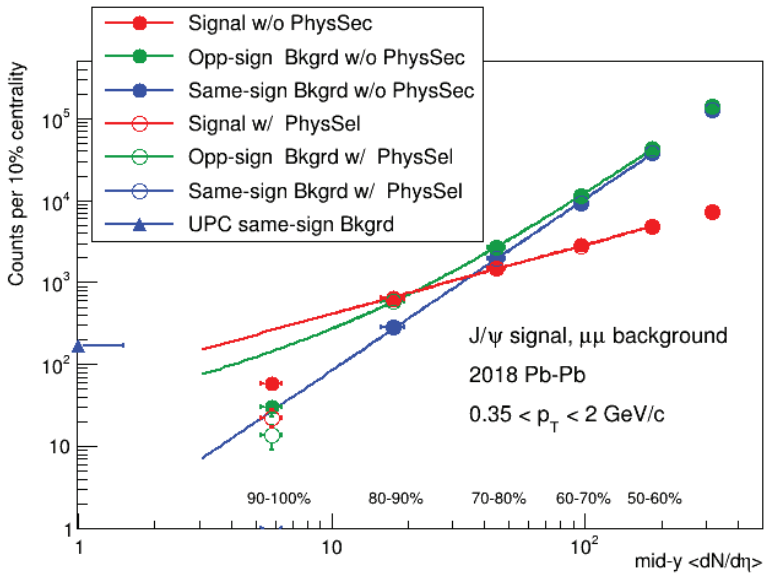

FIGURE 5.14. The number of J/ψ, OS and SS background dimuons vs average mid-rapidity event multiplicity in several centrality bins of hadronic Pb-Pb collisions. The power-law fits are performed excluding 90-100% centrality bin because the CMUL7 and CMLL7 triggers are fully efficient only for 0-90% centrality.

dots, which is a superposition of two power-law functions, contains both correlated (mostly from the correlated creation of $c\bar{c}$ quarks) and combinatorial components.

As can be seen from Figure 5.14, the amount of SS dimuons observed in the UPC dataset greatly exceeds the predicted quantity from hadronic collisions in the 90–100% centrality bin. Given that the UPC data sample can be contaminated only by hadronic collisions with 90-100% centrality [4], the origin of the SS dimuon in the UPC data sample can not come from hadronic collisions. Their origin is likely from beam-gas events.
As can be seen from Figure 5.14, the expected number of hadronic J/ψ in the 90-100% bin is approximately 260 out of which about 60 are observed. This means that about 200 J/ψ might still end up in the UPC sample. This represents around 3.5% of the total number of observed J/ψ in the UPC data sample. This estimate is very conservative, because of the assumption that all hadronic collisions for which the V0 trigger is inefficient satisfy the V0A, AD-A and AD-C trigger vetoes used in the present UPC analysis.

[4] The UPC trigger requirements are such that they exclude coincidence of signals in the V0A and V0C detectors and this coincidence is fully efficient for hadronic collisions with 0-90% centrality.

5.3.1.2 The SPD tracklets study

To further investigate the possibility of a hadronic background, the distribution of the number of SPD tracklets in the UPC data sample is examined in Figure 5.15. This distribution is expected to be sensitive possible presence of hadronic background, because the hadronic collisions produce sizable charged-particle activity at midrapidity and this will results in the presence of one or several reconstructed SPD tracklets.

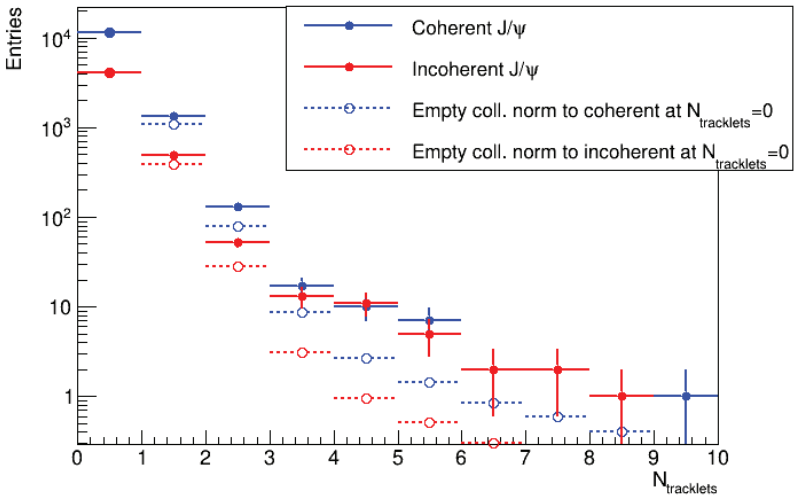

FIGURE 5.15. The distribution of the number of SPD tracklets for coherent and incoherent J/ψ. The distributions correspond to the 2018 data taking period. The plot is taken from the analysis presented in Ref. [76].

The "empty" distributions in Figure 5.15 have been produced using a special trigger which required LHC beams bunch crossing in ALICE and absence of signals in the V0 and AD detectors. These distributions demonstrate the contribution from e^+e^- pair pile-up [76]. This contribution is characterised by the fraction of 9.3% (with negligible uncertainty) of the "empty" events having at least one tracklet. The corresponding fraction of events in case of incoherent and coherent J/ψ is slightly higher, namely 12.5±0.5% for the incoherent J/ψ and 11.6±0.3% for the coherent J/ψ. This suggests that the upper limits of the contamination from hadronic collisions are 3.2±0.5% and 2.3±0.3%, respectively. From Table 4.2 in [171], also reported in Appendix C, the shape of the hadronic J/ψ spectrum is such that the number of J/ψ at $p_{\mathrm{T}} < 0.3$ GeV/c is about 20 times smaller than at $0.3 < p_{\mathrm{T}} < 2$ GeV/c. In addition, the number of coherent J/ψ is about 3 times larger than the number of incoherent J/ψ. This implies that the hadronic contamination is insignificant for coherent J/ψ and is at most (3.2±0.5)% - (2.3±0.3)% = 0.9±0.6% for incoherent J/ψ.

Finally, to evaluate the influence of any possible hadronic contamination, the entire polarisation analysis is performed with an extra event-selection constraint of having no SPD tracklets. The resulting dimuon invariant mass distribution is presented in Figure 5.16. One can notice that the number of incoherent J/ψ is reduced by 13.7±0.4%[5]

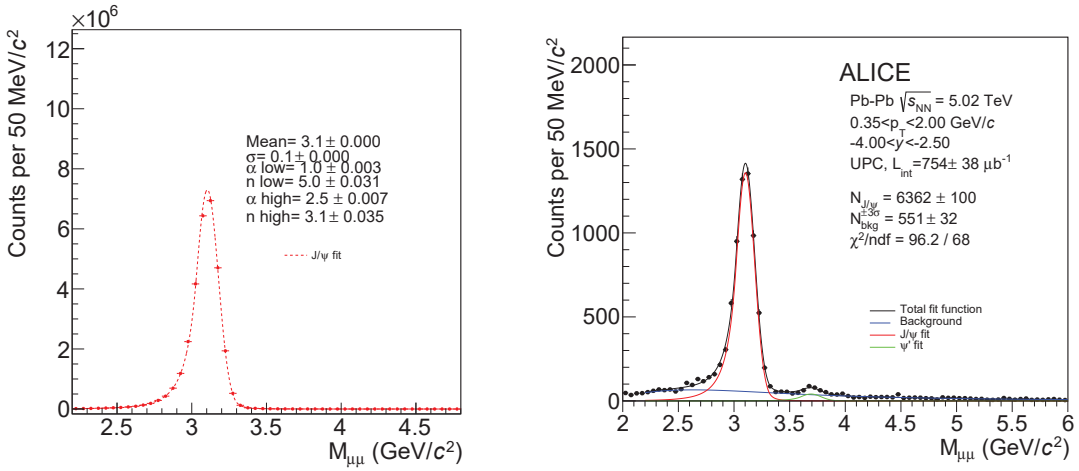

FIGURE 5.16. Dimuon invariant mass in $0.35 < p_{\mathrm{T}} < 2$ GeV/c applying the cut on the number of SPD tracklets. To be compared with Figure 4.11.

and background by 19.8±1.5%. The p_{T} and y spectra of incoherent J/ψ with and without the tracklet cut are compared in Figure 5.17. As it can be seen, no sizable modifications in the spectra shapes are observed. Given that the hadronic contibution is expected to increase with increasing p_{T}, this observation further corroborates the hypothesis of a very limited probability of hadronic contamination.

Figure 5.18 summarises the obtained values for the polarisation parameters in case the tracklet cut is applied. Applying the Barlow criterion [174], no statistically significant modification of the results is identified. Although the statistical uncertainties are larger due to the decreased sample size, the systematic uncertainties associated with the invariant mass fit range and the dimuon background fit function are considerably reduced. This is presumably owing to the decreased background around the J/ψ peak.

[5]This number is slightly different from the fraction of incoherent J/ψ events in 2018 data sample with at least one SPD cluster discussed at the beginning of this Section. The most probable reason for this is the different beam conditions in 2015 and 2018.

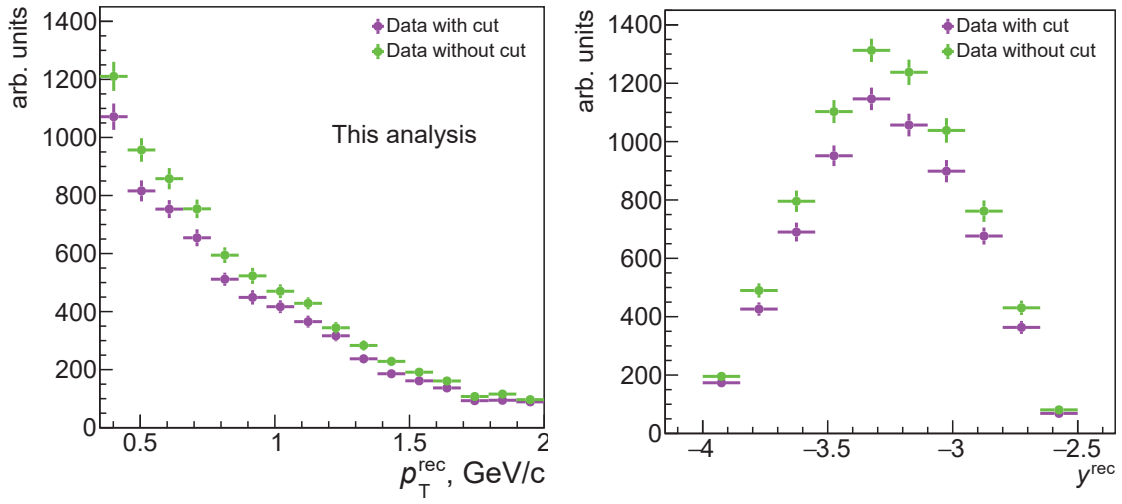

FIGURE 5.17. Incoherent J/ψ p_T and y spectra with (in green) and without (in purple) tracklet cut applied.

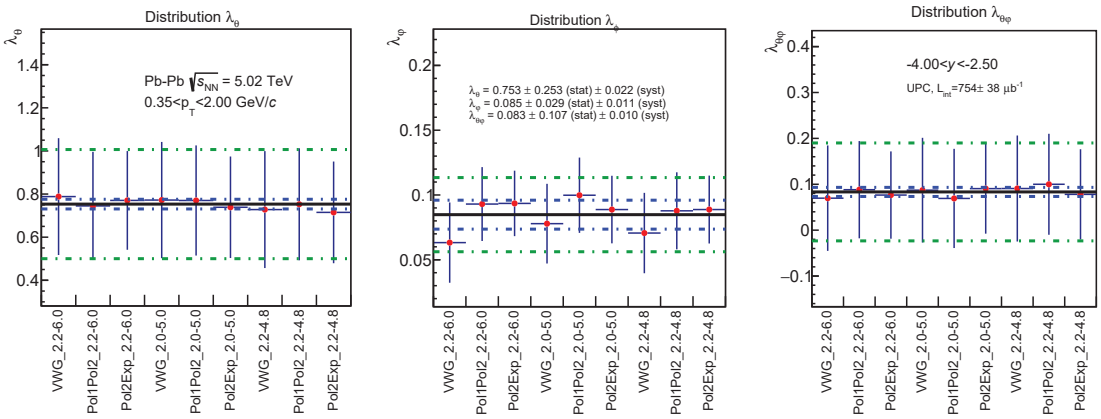

FIGURE 5.18. Results for the polarisation parameters in case the tracklet cut is applied. The red solid line indicates the average values. Dotted blue lines indicate the attributed systematic uncertainties related to the invariant mass fit range and the dimuon background function. The dotted magenta lines show the average statistical uncertainties.

5.3.2 Background from coherent J/ψ and J/ψ from coherent ψ' decays

To determine the contamination level from the coherent J/ψ and coherent ψ' decays, the results obtained by the ALICE Collaboration [76] are used (see also Figure 4.8). In the p_T range between 0.35 and 2 GeV/c the following values are obtained: 1.2% of background from coherent J/ψ and 3% of background from J/ψ from coherent ψ' decays.

Given that the extracted values of polarisation parameters for incoherent J/ψ presented in this Section and the corresponding results for coherent J/ψ in Ref.[166] are very similar, the net effect of these backgrounds is expected to be negligible. A more conservative approach would be to consider *a priori* unknown polarisation of coherent ψ and assign systematic uncertainties varying their λ parameters within the physically allowed ranges. Such systematic uncertainties will be anyway sub-dominant with respect to the other uncertainties considered in this analysis.

5.4 Conclusions

In this Chapter, the polarisation parameter results for the incoherent J/ψ polarisation in UPC data at $\sqrt{s_{\mathrm{NN}}} = 5.02$ TeV as well as the studies on all the systematic uncertainties and the background sources were presented. The analysis is carried out using the angular distributions of the muons from J/$\psi \to \mu^+\mu^-$ decays in the helicity reference frame.

The obtained results for the polarisation parameters are

$$\begin{cases} \lambda_\theta = 0.743 \pm 0.238 \pm 0.094 \\ \lambda_\varphi = 0.089 \pm 0.027 \pm 0.021 \\ \lambda_{\theta\varphi} = 0.079 \pm 0.100 \pm 0.041 \\ \lambda_{\mathrm{inv}} = 1.109 \pm 0.333 \pm 0.140, \end{cases}$$

where the first uncertainties are statistical and the second uncertainties are systematic.

The value of the frame-invariant λ_{inv} is obtained using Equation 4.6. Its statistical uncertainty is calculated taking into account the correlation between the polarisation parameters illustrated in Fig. 5.2, while its systematic uncertainty is calculated assuming that the systematic uncertainties of the polarisation parameters are uncorrelated.

The presented results are compatible with pure transverse polarisation of incoherent J/ψ in the kinematic range $0.35 < p_{\mathrm{T}} < 2$ GeV/c and $2.5 < y < 4.0$, corroborating the SCHC scenario discussed in Section 4.2. The results are also consistent with the corresponding results for coherent J/ψ within the uncertainties of the measurements [166]. Even though this consistency hints an absence of sizeable $|t|$-dependence of the photoproduced J/ψ, such a dependence can not be excluded due to the significant experimental uncertainties, especially of λ_θ and λ_{inv} parameters. Future data to be collected during the LHC Runs 3 and 4 will allow to perform more precise measurements and

thus to draw more firm conclusions [175].

References

[171] C. L. Huang. "Inclusive J/ψ production in pp and Pb-Pb collisions at forward rapidity at $\sqrt{s_{\mathrm{NN}}}$ = 5.02 TeV in ALICE at the LHC". PhD thesis. U. Paris-Saclay, AIM, Saclay, 2020 (cit. on pp. 116, 117, 128, XIV).

[172] J. Adam et al. "Centrality Dependence of the Charged-Particle Multiplicity Density at Midrapidity in Pb-Pb Collisions at $\sqrt{s_{\mathrm{NN}}}$ = 5.02 TeV". In: *Phys. Rev. Lett.* 116.22 (2016), p. 222302. DOI: 10.1103/PhysRevLett.116.222302. arXiv: 1512.06104 [nucl-ex] (cit. on p. 126).

[173] S. Acharya et al. "Forward rapidity J/ψ production as a function of charged-particle multiplicity in pp collisions at $\sqrt{s}$ = 5.02 and 13 TeV". In: *JHEP* 06 (2022), p. 015. DOI: 10.1007/JHEP06(2022)015. arXiv: 2112.09433 [nucl-ex] (cit. on p. 126).

[174] R. Barlow. "Systematic errors: Facts and fictions". In: (July 2002), pp. 134–144. arXiv: hep-ex/0207026 (cit. on p. 129).

[175] Z. Citron et al. "Report from Working Group 5: Future physics opportunities for high-density QCD at the LHC with heavy-ion and proton beams". In: *CERN Yellow Rep. Monogr.* 7 (2019), pp. 1159–1410. DOI: 10.23731/CYRM-2019-007.1159. arXiv: 1812.06772 [hep-ph] (cit. on p. 132).

6 The ALICE future: the new upgrades for LHC Runs 3 and 4

Let me upgrade you
Flip a new page
Introduce you to some new things, and upgrade you
I can (up), can I? (Up), let me, upgrade you
Beyoncé (1981 –)

Contents

DURING the period from late 2018 to early 2022, the LHC was shut down and this time-lapse is known by the name of Long Shutdown 2 (LS2). Taking advantage from this period, the detectors of the four large experiments described in Chapter 3 have been upgraded.

In particular, ALICE exploited the LS2 to boost its physics capabilities and fully benefit from a higher luminosity in Run 3. The ITS, described in Section 3.2.1.1, has been updated with a new silicon tracker based on MAPS technology and a new tracking device, called MFT, in front of the MS has been installed to provide vertexing capabilities at forward rapidity. New GEM detectors have been installed on the end-caps of the TPC in place of the multi-wire proportional chambers exploited in Run 1 and 2, see Section 3.2.1.2, in order to reduce ion backflow in the active volume, and enable continuous data collection. Furthermore, a new detector array designed for quick triggering has been installed. On the software side, a new framework has been developed, specifically designed to manage the online data flow under the continuous acquisition paradigm, and the offline reconstruction and analysis stages.

All these upgrades will be presented in this Chapter. In particular, the scientific program with the MFT detector and the expected improvements in terms of physics program with respect to the current MS will be discussed. All the results of the qualification tests of this new detector will be presented in Chapter 7.

6.1 What made new detectors needed for the ALICE experiment?

DESPITE the remarkable results achieved by the ALICE experiment during LHC Runs 1 and 2, the Collaboration has chosen to schedule a series of improvements [176] to the apparatus to develop studies of hadrons, electrons, muons, heavy flavors, photons and jets produced in heavy-ion collisions on a wide kinematics range. It is important to notice that this hadron study development aims to better understand and know new proprieties of the QGP.

Since the ALICE experiment mainly focus on untriggerable probes (especially at very

low-p_{T}), the ALICE Collaboration has decided to adopt a minimum-bias data-taking approach raising the event readout rate for Pb-Pb interactions from 1 kHz to 50 kHz [177]. This required upgrading the DAQ systems for the readout for all of the ALICE detectors, while a large hardware upgrade was also undertaken for the TPC to enable continuous readout.

In addition to that, three new detectors has also been installed (that will be described in the next Sections):

- the new ITS (ITS2) improving the vertexing resolution at mid-rapidity with respect to the detector exploited in Runs 1 and 2;
- the MFT, installed in front of the MS, providing vertexing capabilities at forward rapidity;
- the new FIT detection system, installed at forward and backward rapidity on both sides of the Interaction Point (IP).

The new O^2 data processing is needed to handle the huge data flow caused by the new continuous readout paradigm, compressing the quantity of stored data by a factor of 30 in comparison to the input data flow.

ALICE is also actively working to further improve its detector during Long Shutdown 3 (LS3) in preparation for Run 4, expected to start in 2029. This new upgrade phase, however, will not be covered in this document.

6.2 ITS2: the new Inner Tracking System

As mentioned in Section 3.2.1.1, the Inner Tracker System (ITS) is the core of the ALICE experiment. The so-called ITS2 [178], which employs a CMOS Monolithic Active Pixel Sensor (MAPS) technology, has been built and installed in its predecessor's place to increase impact parameter resolution and tracking efficiency, particularly for particles with low-p_{T}, as well as the readout-rate capabilities. It is composed, like the "old" ITS, of several layers of increasing radii and length. In particular, it is composed of seven cylindrical layers of silicon pixel sensors, installed coaxially to the beam pipe and centred on the IP, as shown in Figure 6.1. The innermost layer radius is as small as 22 mm, reducing by almost a factor of 2 the radius of the innermost layer of the previous version (39 mm).

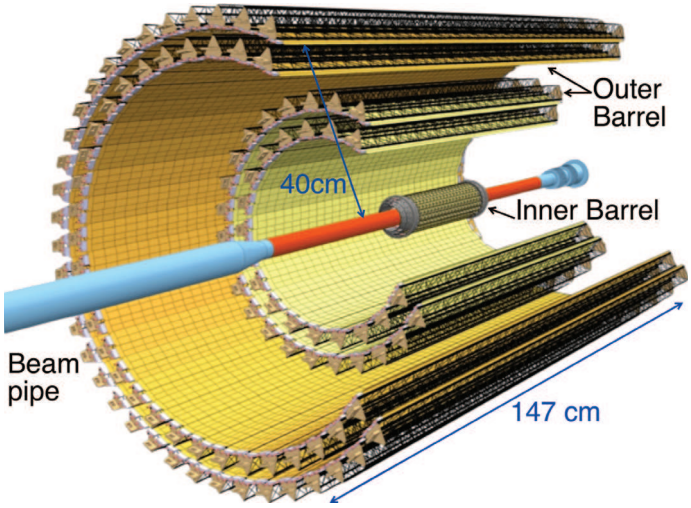

FIGURE 6.1. Detector overview of the ALICE ITS2, from [179].

The ALice PIxel DEtector (ALPIDE) sensor, which will be described in Section 6.6.4, on which the ITS2 is based, carries out in-pixel amplification, shaping, discrimination, and multi-event buffering while consuming less than 40 mW cm^{-2} of specific power. It can endure a particle rate of 100 MHz cm^{-2} without pile up and has a pixel pitch of 27 × 29 µm^2 and detection effectiveness of >99%.

Thanks to the employment of these new chip sensors, the impact parameter resolution for low-p_{T} tracks ($p_{\mathrm{T}} \sim 0.5$ GeV/c) will be improved by a factor of 3 and 5 in the $r\varphi$ and z coordinates, respectively, thanks to the reduction of the material budget of the inner layers to 0.35% X/X_0 compared to 1.14% X/X_0 of its predecessor.

Finally, the maximum readout rate will be increased to 1 MHz for pp collisions and 100 kHz for Pb-Pb collisions.

The concentric layers have radii that vary from 23 mm to 400 mm, divided into a total of 192 staves covering a 10 m^2 active silicon area with 12.5×10^9 pixels. The detector will cover the pseudo-rapidity range $|\eta| < 1.22$ and is divided into two main sections:

- The Inner Barrel (IB), corresponding to the three innermost layers, each of them composed of 48 staves measuring 27 cm in length.
- The Outer Barrel (OB), corresponding to the Middle Layers (MLs) and Outer Layers (OLs), composed of 54 and 90 staves of 84 cm and 150 cm, respectively.

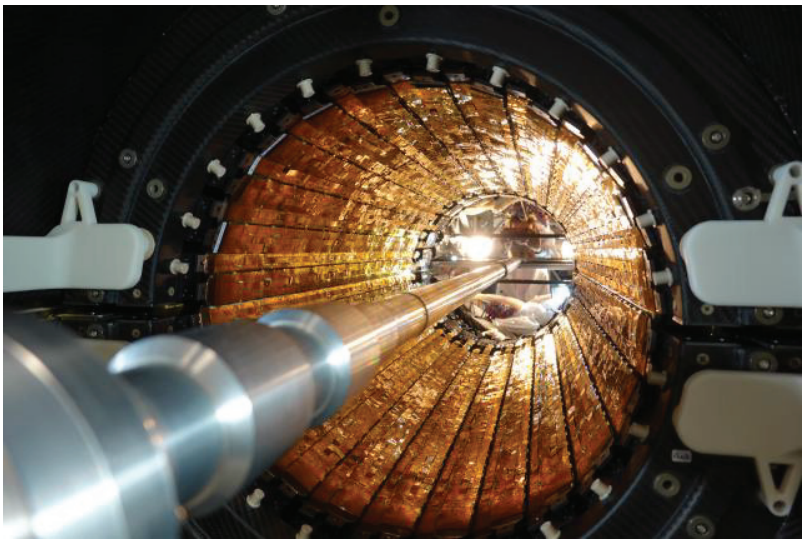

FIGURE 6.2. Picture of the ITS2 inside view, from [180].

6.3 TPC: the Time Projection Chamber upgrade

THE gaseous ALICE Time Projection Chamber (TPC), the largest of its kind in the world (see Section 3.2.1.2), has also undergone a major upgrade [181]. During Run 1 and 2, the electrons created within the TPC active volume were read out using Multi-Wire Proportional Chambers (MWPCs), which restricted the readout rate to a few kHz due to the need to reduce ion backflow into the TPC with a wire gating grid.

The goal of the TPC upgrade was to provide continuous readout while taking into account that the TPC Ne-CO_2-N_2 gas combination required a gain of 2000, that the ion backflow had to be limited to less than 1%, and that the dE/dx performance had to be preserved. The solution was identified by swapping out the gated MWPC for a quadruple Gas Electron Multiplier (GEM) stack, where the two internal ones are made out of big hole pitch (280 µm) GEM foils, and the externals are made out of normal hole pitch (140 µm) GEM foils.

The signal charge is handled by the newly developed front-end ASIC SAMPA [182, 183], manufactured using 130 nm TSMC CMOS technology, equipped with 32 channels, a preamplifier, a shaper, and a 10-bit ADC. The FECs (3276 FECs in total) receive and collect the output of 5 SAMPA chips in continuous sampling mode at 5 MHz. The data output expected for 50 kHz Pb-Pb collisions is 3.3 Tbyte/s; it is clear from this number that data filtering and compression are required before storage.

The TPC was raised to the surface in 2019; GEM module installation began in May of

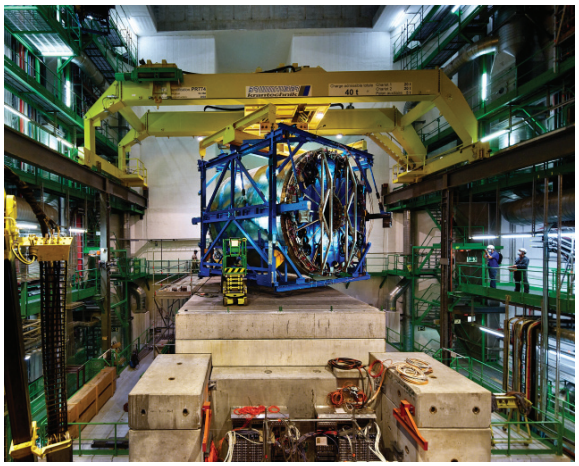

FIGURE 6.3. The TPC is lowered down the shaft to the experimental cavern, from [184].

that year, pre-commissioning began in November and the final installation in the L3 magnet was completed in December 2020, as shown in Figure 6.3.

6.4 FIT: the Fast Interaction Trigger detector

THE Fast Interaction Trigger (FIT) [185] has been installed in place of some of the trigger detectors exploited in Runs 1 and 2 (in replaces in particular the V0 detector, described in Section 3.2.2.2, whose life had come to an end by the end of Run 2). The composite detector system FIT plays a crucial role in the functioning of the ALICE experiment, providing a fundamental input for the selection of the events and the monitoring of the luminosity delivered by the LHC to the ALICE experiment.

The FIT is composed of three subsystems, shown in Figure 6.4, described below.

- A disk-shaped scintillator detector, FV0, is read out by optical fibers. It is located 3.5 m away from the IP on the side opposite to the MS, and covers the rapidity interval $2.2 < \eta < 5.0$. It monitors the multiplicity, centrality and event plane of ion collisions and contributes to the 425 ns latency minimum bias and centrality events triggers used for online vertex calculation, selection and rejection of beam-gas events [177].
- Two quartz Cherenkov radiators, called FT0-A and FT0-C, are arrayed in squares with sides of about 20 cm, read out by microchannel plate-based photomultipliers, and positioned on opposite sides relative to the IP. Between the MFT and the MS, at 80 cm from the IP, FT0-C is positioned 80 cm behind FV0. The pri-

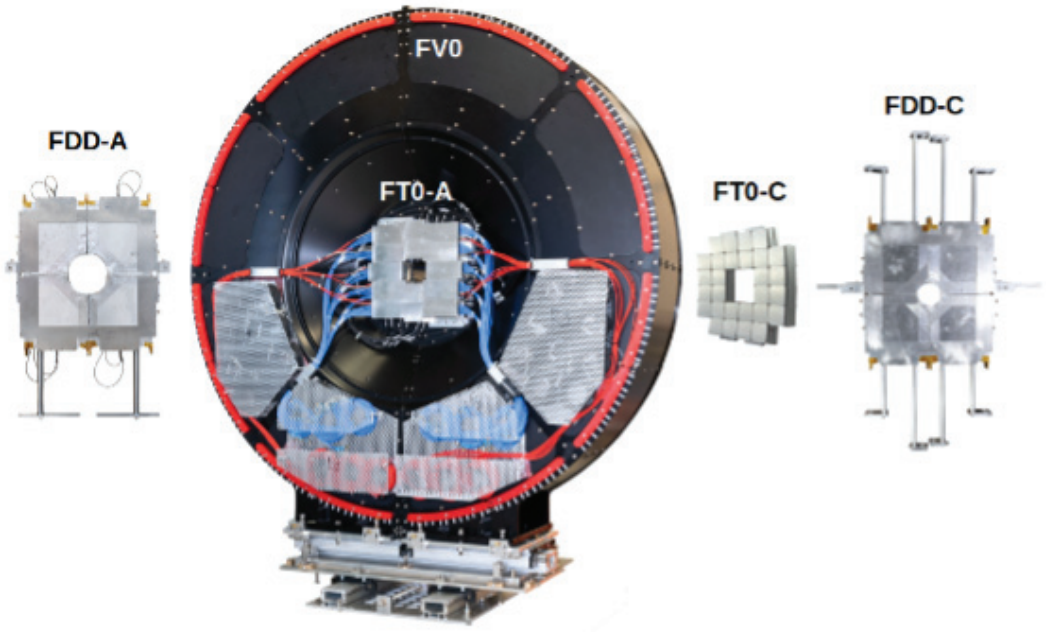

FIGURE 6.4. Pictures of the FIT subdetectors, which are situated at 17.5 (FFD-A), 3.2 (FT0-A and FV0), -0.8 (FT0-C), and 19.5 m (FDD-C) from the IP, from [186].

mary function of FT0 is to determine the collision time, which is utilized in TOF-based particle identification, and to generate the aforementioned selection triggers with FV0.

- Last but not least, FDD-A and FDD-C are located on each side of the IP, respectively at a distance of 17 m and 19.5 m, with pseudo-rapidity acceptance reaching a maximum of $\eta = 6.9$. They are composed of plastic scintillator pads, wavelength-shifting bars, and readout optic fibres. They provide measurements of the diffractive cross-sections, a tag for diffractive events, used for UPC physics.

6.5 O^2: the Online-Offline processing

To manage the 3 TByte/s of dataflow that will be produced by the ALICE detector, and to reduce its storage output while maintaining physics and tracking information, the foreseen reconstruction approach is divided into two phases: a first synchronous online reconstruction step during data collection that allows detector calibration, and a second calibrated asynchronous reconstruction stage. This synchronous-asynchronous structure is implemented by the online-offline framework called Online-Offline (O^2) [187, 188].

The hardware infrastructure of the O^2 system is composed of First Level Processors (FLPs), which take raw data from detectors and split the continuous data flow into time frames of 10-20 ms each. These are routed to the Event Processing Nodes (EPN), which reduce the flow to a tolerable 0.1 TByte/s and send it to disk storage.

The Central Trigger Processor (CTP) supplies the common clock, the synchronisation signals (including triggers to detectors not implementing continuous readout) and the timing data required for the proper construction of the sub-events, controlling the whole process.

6.6 MFT: the Muon Forward Tracker

A new high-resolution silicon tracker, named Muon Forward Tracker (MFT) [189], operates since the beginning of Run 3 covering the pseudo-rapidity range of $-2.5 < \eta < -3.6$. The MFT is installed in front of the MS front absorber, mentioned in Section 3.2.3.1 and by matching the muon tracks downstream of the absorber with the so-called MFT standalone tracks (tracks reconstructed using the information of the 5 disks composing the MFT), it will provide vertexing information for the Muon Tracking system.

In the following Sections, the main characteristics of the MFT will be described. Chapter 7 will focus on all qualifying tests performed before the installation of the detector in the ALICE cavern to calibrate the detector, a work which has been done during this Ph.D. thesis.

6.6.1 MFT physics motivations

THE installation of a vertex telescope is the best approach for improving the MS performance, and the silicon pixel technology was quickly identified as the best option for the new detector.

The physics of quarkonia and open heavy flavors, in particular, as described in Section 1.5.2, is directly connected to the investigation of the QGP phase and the measurement of its fundamental parameters (temperature, energy density, transport coefficients, etc.). The presence of the massive hadron absorber, needed to reduce the hadron flux arriving the chambers of the Muon Spectrometer as discussed in Section 3.2.3.1, degraded the vertex resolution measurement for the quarkonia reconstructed in the MS, a limitation which will be overcome by matching the information

coming from the MS with the one coming from the MFT.

The most significant contributions of the MFT to the ALICE experiment are listed below.

- Thanks to the expected MFT performances, the measurement of secondary vertices corresponding to the decay of B mesons into $J/\psi + X$, requiring a vertex resolution of the order of ~ 100 µm, will finally be possible with ALICE at forward rapidity, opening the way to beauty measurements at forward rapidity.
- At the same time, the possibility of identifying prompt J/ψ production is interesting in its own, since promptly-produced J/ψ are among the most valuable QGP probes, being sensitive to the effects of dense matter created in heavy ion collisions, as discussed in Section 1.5.2. Quarkonia physics, in particular the study of the dissociation and recombination mechanisms, need extremely precise measurements, including the possibility to separate direct charmonia production (*prompt* J/ψ) from contributions from B meson disintegration (*non-prompt* or *displaced* J/ψ), which account for 20% of J/ψ and 40% of ψ'. The MFT will give a crucial contribution in this direction.
- Finally, an accurate measurement of the open heavy flavors can be made in the single-muon channel, providing a further input to the characterisation of the mechanisms determining the interaction of heavy quarks for the medium.

6.6.1.1 Improvements in specific measurements

THE possibility of measuring beauty production in the non-prompt J/ψ channel concerns the B^0, B^+, B_s^0 and Λ_b^0 hadrons[1], which have a decay length ranging from 420 to 490 µm, see Table 6.1[2]. Since the J/ψ partners in these kinds of decays will not be detected at forward rapidity, the beauty cross-section will be calculated using the inclusive branching ratio for the $J/\psi + X$ decays shown in Figure 6.5, which can be predicted using phenomenological models like PYTHIA. One has to notice that other b baryons can decay into a single muon channel, detectable with the MFT detector.

Because the prompt *vs* displaced tagging cannot be applied on the single J/ψ candidates, prompt and displaced J/ψ samples must be statistically separated, based on the shape of their L distributions, the distance between the primary vertex and the production vertex of the J/ψ, which coincides with the primary vertex of the collision when

[1] B^0 mesons are $d\bar{b}$ mesons, B^+ are $u\bar{b}$ mesons, B_s^0 are $s\bar{b}$ mesons and Λ_b^0 are udb baryons [190].
[2] Beauty hadrons $\longrightarrow$ J/ψ + X, where X represents the remaining decay products.

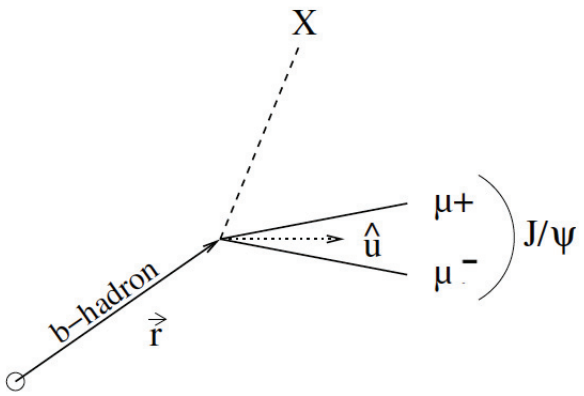

FIGURE 6.5. Schematic representation of a b-hadron decay into J/ψ, where $\hat{u}$ is the unit vector in the direction of the J/ψ.

the J/ψ is produced as a prompt particle, due to the short decay time of the meson. The most probable transverse decay length of the b-hadron, in the laboratory frame, is calculated as

$$L_{xy} = \frac{\hat{u}^T S^{-1} \vec{r}}{\hat{u}^T S^{-1} \hat{u}} \simeq \frac{\hat{u}^T \vec{r}}{\hat{u}^T \cdot \hat{u}},$$

where $\hat{u}$ is the unit vector in the direction of the J/ψ and S^1 is the inverse of the sum of the primary and secondary vertex covariance matrices.

Ideally, correcting L_{xy}/c by the γ factor of the b-hadron, an estimation of the proper decay time of the hadron could be obtained. However, since the γ factor of the beauty hadron can only be approximated to the one of the daughter J/ψ, the resulting in the so-called pseudo-proper decay time t_z, exploited for instance by the LHCb Collaboration in [191]:

$$t_z = \frac{|z_{J/\psi} - z_0| \cdot M_{J/\psi}}{p}, \tag{6.1}$$

where $z_{J/\psi}$ and z_0 are the longitudinal positions of the secondary and primary vertices[3] respectively, and p is the total momentum of the J/ψ. With the installation of the MFT, it will be possible to measure this quantity at forward rapidity in ALICE, as already done in ALICE, ATLAS and CMS [192] at mid-rapidity, and in LHCb at forward rapidity.

Furthermore, the improvement in the () for the measurement of quarkonia will make the ψ' measurement possible even in central Pb-Pb collisions, a crucial asset to improve our understanding of the dissociation and recombination mechanisms of quarkonia.

Another measurement that the MFT installation will enhance is the Distance of Closest

[3] J/ψ vertex and collision vertex.

Approach (DCA) evaluation for single muons, which will lead to a better understanding of the single-muon production, allowing for a proper separation between single muons from charm and beauty mesons, and background sources mainly corresponding to muon from pion and kaon decays. The accurate measurement of the open charm production, in particular, provides a crucial input for the investigation of the early-state creation of $c\overline{c}$ pairs, and contribute to our understanding of the gluon shadowing [193] and possible saturation effects in p-A collisions.

Particle	$c\tau$
$\pi^{\pm}$	7.8 m
$K^{\pm}$	3.7 m
$D^{\pm}/D^{0}$	311.8 µm/122.9 µm
$B^{\pm}/B^{0}$	419.1 µm/455.4 µm
J/ψ	2150 fm
Υ	3704 fm

TABLE 6.1. Time of flight of some particles, from [194]

More generally, the possibility to reject muons from π and K decays based on the measurement of the single-track offset at the primary vertex (distance of closest approach, DCA), will result in higher () ratio throughout the whole mass spectrum for prompt dimuon production, including at masses below than the J/ψ where the sensitivity to the measurement of thermal dimuons will be improved, as well as the separation of low mass vector mesons (ϕ, ρ and ω) due to the better mass resolution.

6.6.1.2 Improvements in photoproduction measurements in UPC

IN Chapters 4 and 5, it was thoroughly described the relevance of UPC and how to measure photoproduced J/ψ polarisation. The physics of small x-Bjorken created at very low-p_{T} is critical to probe the nuclear gluon distribution, described in Section 2.2.4.

In comparison to Run 2, the integrated luminosity of the LHC Run 3 and Run 4 will rise by a factor of 13, improving the available statistical sample for multi-differential measurements [195]. As the MFT will give a more accurate measurement of J/ψ production, all its characteristics, even its polarisation, will be better understood.

At very low-p_{T}, the ALICE upgrade program will guarantee a higher precision as a function of centrality [196]. Totally new measurements will be available, such as the detection of interference effects [197] between the two source-target configurations of the

heavy-ions and Υ[4] photoproduction [198], which happens on a scale ten times greater than the J/ψ.

6.6.1.3 Improvements in bottom mesons and light flavor mesons measurements

THE MFT insertion in the ALICE experiment will not only have an effect on charmonia: the separation between the open-charm and open-bottom mesons, separation of the multiple excited state of Υ as well as a better separation of low mass vector mesons (ϕ, ρ and ω) will finally be possible.

At low mass and hence low-p_{T}, the ALICE apparatus[5] particle tracking, during LHC Run 2, was degraded by the multiple scattering but the MFT installation will improve the measurements. In this sense, the analysis of the ρ spectrum function to restore chiral[6] symmetry [200] is a strong physical reason to justify the MFT installation, giving an original measure in the LHC experimental program.

For what concerns open flavors, in the single muon decay channel, the Distance of Closest Approach (DCA) measurement also allows for the separation of open charm and open beauty contributions. Even while the MFT will not help ALICE perform better for detecting Υ resonances, its contribution will be essential for determining the open beauty reference via the $B \longrightarrow \mathrm{J}/\psi + X$ channel. The measurements of the total cross-sections of the charm and beauty may therefore be carried out, allowing for the identification of a potential increase in charm or beauty production.

The accurate measurement of the open charm also provides for a better comprehension of the early state creation of $c\overline{c}$ pairs. Simple heavy quark measurements compared to quarkonia measurements can help to better understand gluon shadowing [193] and the consequences of saturations in p-A collisions.

[4] The most known bottomonium ($b\overline{b}$) state is the Υ meson.

[5] Described in Section 3.2.

[6] In 1904, Lord Kelvin proposed the idea of chiral symmetry: "*I call any geometrical figure, or group of points, chiral, and say it has chirality, if its image in a plane mirror, ideally realised, cannot be brought to coincide with itself*" [199]. Helicity is the spin projection in the direction of flight of a moving particle having a spin. Two helicity states-left and right-states are attainable for particles with a spin of 1/2. For massless particles, chirality and helicity may be confounded. In the sector of light quarks, the chiral symmetry becomes an exact symmetry of the Lagrangian. This is the symmetry $SU(n_f)_L \times SU(n_f)_R$, where n_f is the number of flavours.

6.6.2 Comparison of the MS-only and the MS+MFT performance

TABLE 6.2 presents two scenarios for the MS with and without the MFT detector in central Pb–Pb collisions, assuming an integrated luminosity of 10 nb^{-1} [201].

Observable	Muon Spectrometer Only		Muon Spectrometer+MFT	
	p_T^{min} GeV/c	uncertainty	p_T^{min} GeV/c	uncertainty
Inclusive J/ψ R_{AA}	0	5% at 1 GeV/c	0	5% at 1 GeV/c
ψ' R_{AA}	0	30% at 1 GeV/c	0	10% at 1 GeV/c
Prompt J/ψ		not accessible	0	10% at 1 GeV/c
J/ψ from B mesons		not accessible	0	10% at 1 GeV/c
Open charm in single μ			1	7% at 1 GeV/c
Open beauty in single μ			3	10% at 1 GeV/c
Open HF in single μ no c/b separation	4	30% at 4 GeV/c		
Low mass spectral func. and QGP radiation		not accessible	1–2	20% at 1 GeV/c

TABLE 6.2. Comparison of physics reach for the two scenarios without and with the MFT (Muon Spectrometer only /Muon Spectrometer + MFT) assuming an integrated luminosity of 10 nb^{-1} in central Pb–Pb collisions. p_T^{min} gives the minimum accessible p_T for the different observables. The quoted uncertainties include both statistical and systematic uncertainties, from [201].

An important variable that can be improved thanks to the MFT installation is the determination of the elliptic flow v_2[7], which is a strong signature of the QGP presence. In Chapter 1, some results of the ALICE Collaboration are shown. With the MFT, new measurements will be finally possible [189].

During the MFT design phase, a fast MC simulation tool was used to determine the performance of the detector, allowing to investigate the impact on characteristics such as chip size, chip overlap and disk shape. These investigations were also used to determine the MFT geometrical configuration, described in Section 6.6.3.

6.6.2.1 Example of performance expected from the MFT for the meson ψ'

THE MFT TDR [189] includes a long review of the MFT performances, with a focus on the impact of the detector on the ALICE physics program. All of the mechanisms outlined

[7] The elliptic flow is a measure of how the flow is not uniform in all directions when viewed along the beam-line, due to the pancake shape of nuclei.

in Section 6.6.1 have been simulated [189, 201]. Here, one example of a simulation physical processes is reported.

The MFT tracking capabilities enable a large decrease in the combinatorial background caused by semi-muonic decay of light hadrons, primarily π and K, as well as non-prompt correlated sources such as open charm and open beauty processes [189]. This background reduction is especially relevant for the ψ' investigation[8] in central Pb–Pb collisions, where the S/B ratio is improved by a factor of up to ten, depending on the p_{T} range, as shown in Figure 6.6.

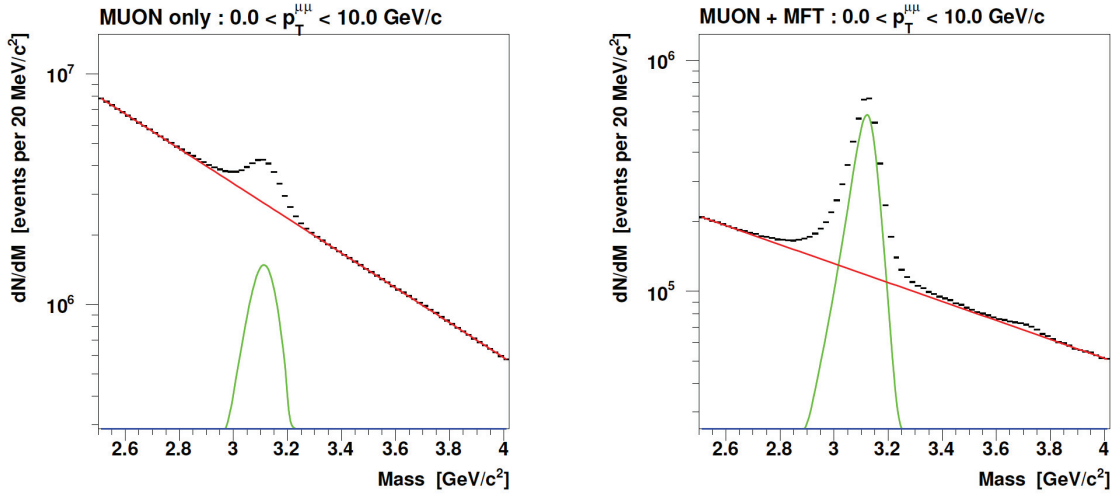

FIGURE 6.6. Dimuon mass distribution in the charmonium region integrated in p_{T}, for 0-10% Pb-Pb collisions at $\sqrt{s_{\mathrm{NN}}} = 5.02$ TeV normalized to the expected statistics in a 10 nb^{-1} integrated luminosity scenario without the MFT (left) and with the MFT (right), from [201].

In Table 6.3, the expected yields, S/B, significance and statistical and systematical uncertainties for inclusive J/ψ production in the scenarios without (top) and with (bottom) the MFT is reported.

6.6.3 Detector description

THE MFT has been installed in the ALICE cavern in December 2020, between the IP and the front absorber of the MS, around the beam pipe [202].

The detector is made of two Half-MFT cones, called Bottom MFT (H0) and Top MFT (H1). As shown in Figure 6.8, each Half-MFT cone consists of five Half-Disks (H-Ds)

[8] The improvement on ψ' measurement is described in Section 6.6.1.1.

p_T [GeV/c]	Signal [$\times 10^3$]		S$\sqrt{\text{S+B}}$	Stat. Err. [%]	Sys. Err [%]
Inclusive J/ψ (2.80 < $M_{\mu\mu}$ < 3.30 GeV/c^2), R_{AA} = 0.7, without the MFT					
0−1	1710	0.15	470	0.20	5
1−2	3320	0.14	650	0.14	5
2−3	2784	0.16	610	0.16	5
3−4	1750	0.16	490	0.19	5
4−5	1055	0.18	400	0.25	5
0−10	12040	0.15	1300	0.08	5
Inclusive J/ψ (2.80 < $M_{\mu\mu}$ < 3.30 GeV/c^2), R_{AA} = 0.7, with the MFT					
0−1	531.6	0.50	420	0.23	7
1−2	851.9	0.92	640	0.15	7
2−3	715.3	1.28	630	0.15	7
3−4	544.0	2.03	600	0.17	7
4−5	382.2	3.25	540	0.18	7
0−10	3664	1.15	1400	0.07	7

TABLE 6.3. Some expected values for inclusive J/ψ production in the scenarios without (top) and with (bottom) the MFT, from [201].

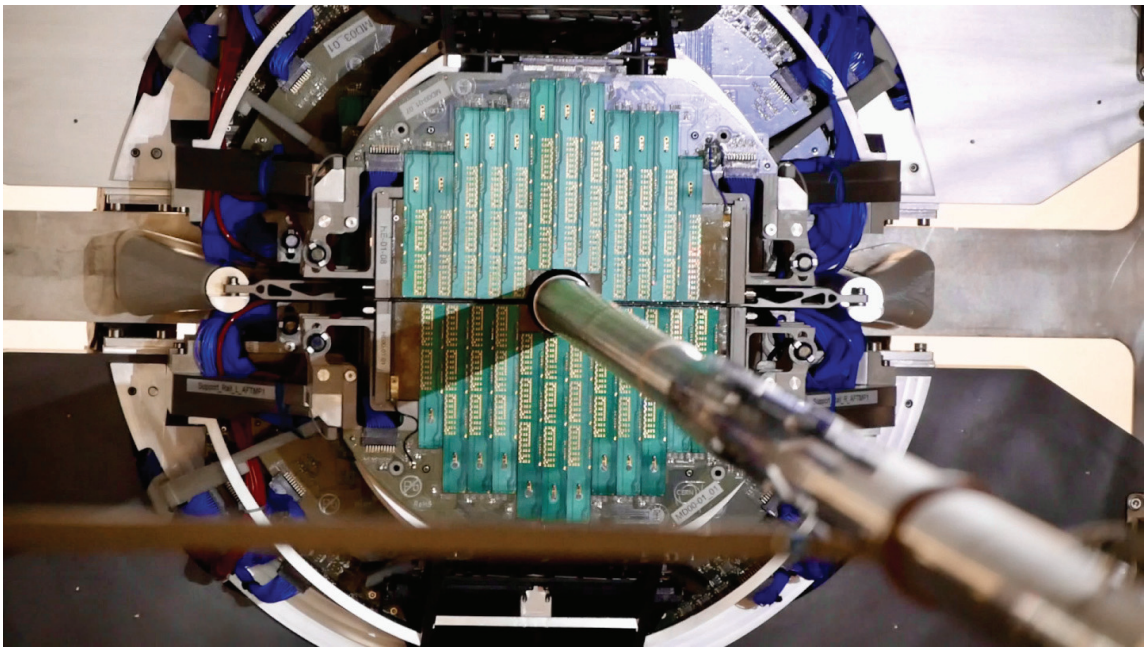

FIGURE 6.7. The MFT detector around the beam pipe inside the ALICE experiment, from [202].

arranged along the beam axis in the direction of the MS, with the first H-D positioned at $z = -46$ cm from the nominal IP.

The first two H-Ds (H-D 0 and H-D 1) are identical, whereas the following three H-Ds (H-D 2 to H-D 4) have larger sizes. Table 6.4 summarizes the geometrical properties of

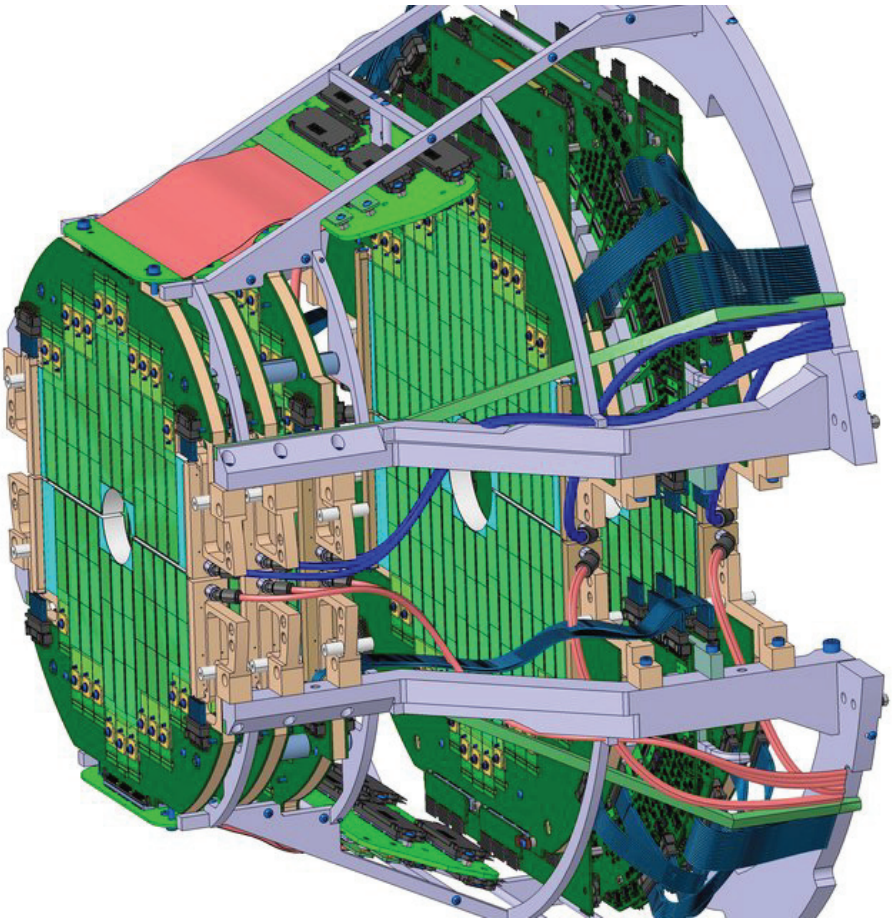

FIGURE 6.8. Schematic of MFT detector in its two half-cones structure. Notice that between H-D 3 and H-D 4 in each half-cone MFT there is the Power Supply Unit (PSU), from [203].

each H-D.

Half-Disk	0	1	2	3	4
Inner radius (mm)	25.0	25.0	25.0	38.2	39.2
Outer radius (mm)	98.0	98.0	104.3	130.1	143.5
z position (mm)	−460	−493	−531	−687	−768

TABLE 6.4. Geometrical variables of the MFT.

The MFT basic detecting element is a silicon pixel sensor based on the MAPS technology: it is the same chip equipping the ITS2, called ALPIDE, and is described in Section 6.6.4.

Sensor ladders are made up of two, three, four or five silicon pixel sensors that are powered through Flex Printed Circuit (FPC) using aluminium strips. The ladders' production will be described in the following. The ladders are glued on both faces of the H-Ds

with a pitch of 17 mm (the ladder width itself is 16 mm), which optimises the detector acceptance around the beam-pipe and increases the detector overlap: 50% of charged particles will pass through both the H-D planes of a disk.

Selected ladders are glued to the mechanical structure of the H-D, composed of a disk spacer, a disk support, two Printed Circuit Boards (PCBs) located outside the detector acceptance – equipped with connectors for the ladder connection and the signal cables – and a cooling systems. More details on the H-Ds production will be given in Section 6.6.6.

To ensure a good contact with the mechanical structure, the ladders are screwed on one edge and glued to the H-D spacer along both sides of H-D. To maintain the ladders cool, water polyimide pipes run on the surface of the H-D spacer.

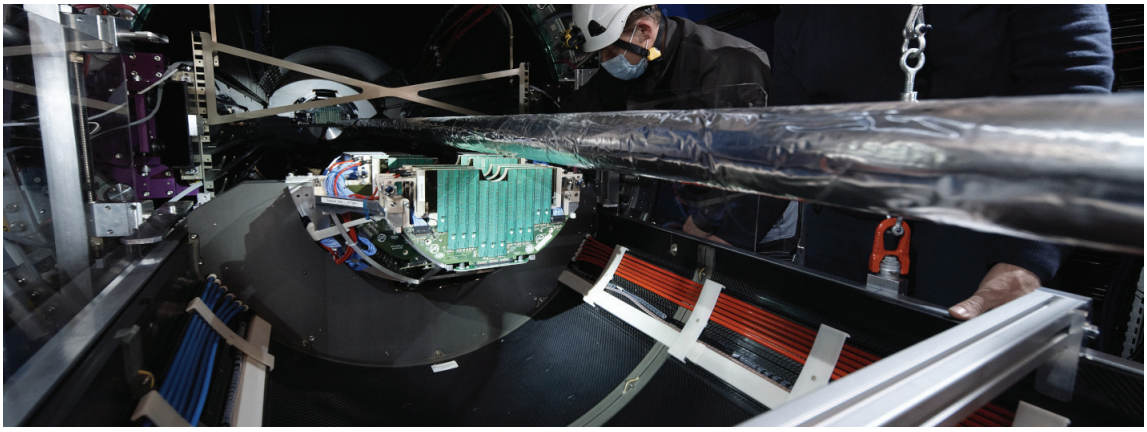

FIGURE 6.9. MFT and FIT installation inside the ALICE magnet, from [204].

6.6.4 ALPIDE: pixel sensor

ALPIDE [205, 206] chips are based on a Complementary Metal-Oxide Semiconductor (CMOS) Monolithic Active Pixel Sensor (MAPS) system technology developed for the ALICE ITS2 and MFT: The CMOS technology offers excellent performance in terms of granularity, material thickness, read-out speed, power consumption and radiation hardness [207].

ALPIDE chips combine the active volume and read-out electronics into a single detecting device. The primary benefit of CMOS pixels over conventional hybrid technology is a cheaper material budget and power usage [208]. The estimated values of heat production and current for each H-D are reported in Table 6.5.

H-D	Heat production [W]	Current [A]
0	193	107.2
1	193	107.2
2	227	126.1
3	251	139.4
4	276	153.3
Total	1140	633.2

TABLE 6.5. Estimate of the power consumption of the MFT sensors, from [201].

The ALPIDE sensors cover a total surface area of $0.4\,m^2$ for the MFT, and around $10\,m^2$ for the ITS2. Table 6.6 summarises the ALPIDE sensor chracteristics.

Parameter	Value
Spatial resolution	$\sim 5\,\mu m$
Pixel pitch	$\sim 26\,\mu m$
Detection efficiency	$> 99.5\%$
Integration time	$< 20\,\mu m$
Sensor thickness	$5050\,\mu m$
Binary output	1-bit
Power dissipation	$< 150\,mW\,cm^{-2}$
Radiation tolerance	$\sim O(10^{13})\,n_{eq}/cm^2$
(10-years operation)	$\sim O(10^{13})$ krad

TABLE 6.6. The essential characteristics for MFT CMOS sensors, from [189].

Each ALPIDE chip measures $30 \times 15\,mm^2$ and includes a 512×1024 matrix of sensitive silicon pixels. The chip structure, the analog and digital supply lines and the soldering pads used to connect the chip to the FPC are shown in Figure 6.10. Each pixel measures $29.24 \times 26.88\,\mu m^2$ and features an epitaxial[9] layer, having a thickness of $25\,\mu m$, (type *p*) with a high resistivity ($> 1\,k\Omega\,cm$), which improves charge collection and increases the radiation tolerance by allowing the collection diode to be reverse-biased, as explained in Appendix D, expanding the substrate depletion volume.

Figure 6.11 illustrates a schematic view of the pixel's well-structure, highlighting the epitaxial layer, the diode and the transistors.

- The prefixes *n* and *p* denote the kind of semiconductor component used in the pixels and both *n*MOS and *p*MOS transistors are deployed in the active pixel region.

[9] Epitaxy is the process of forming a crystal layer on the crystal base of another mineral in such a way that the crystalline orientation of the layer is the same as the crystalline orientation of the substrate.

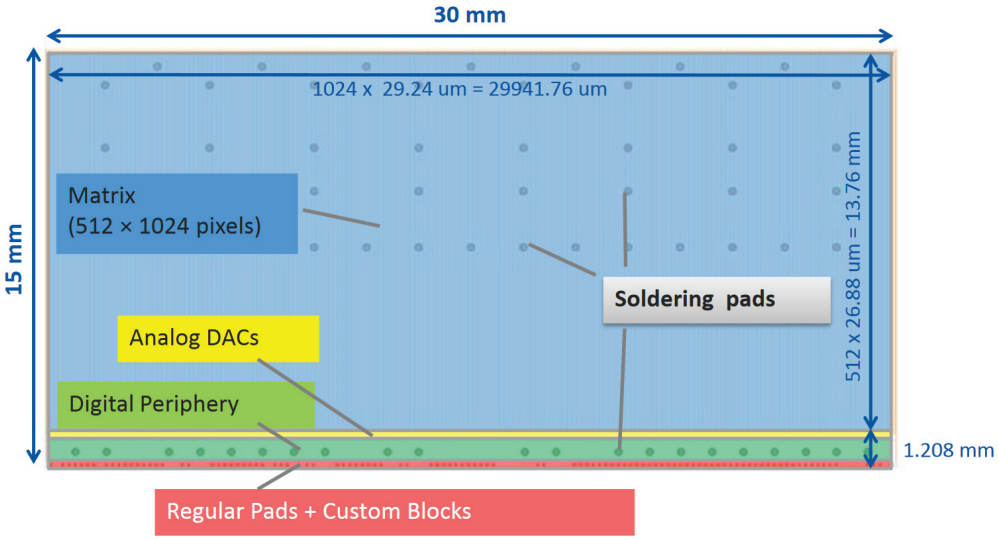

FIGURE 6.10. ALPIDE sensor is shown in schematic form (top view).

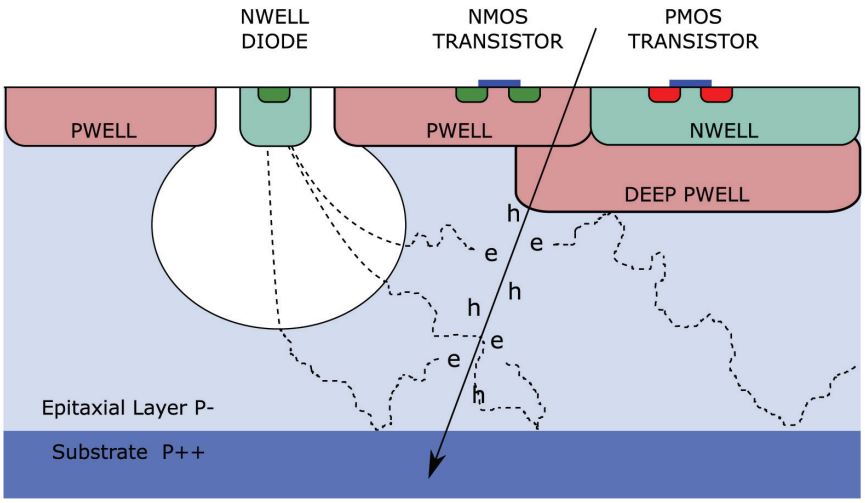

FIGURE 6.11. ALPIDE chip is shown in cross-section. After crossing the sensitive volume (the high-resistivity epitaxial layer between the substrate and the layer with CMOS transistors), a charged particle generates free charge carriers, which then diffuse across the epitaxial layer until they reach the drift region of an n-well diode, where they are captured and stored, from [209].

- The collection diode (noted $n-$well in Figure 6.11) with a low capacitance results in a greater collection efficiency [206].

- The deep p-wells shielding pMOS[10] transistors together with the six metal layers enable the integration of the front-end circuitry at a very low power consumption ($40\,\mathrm{mW\,cm^{-2}}$).

[10] Additional information on p-well transistor technology is available here: [210].

In addition to the active volume and the front-end electronics, each ALPIDE pixel also incorporates the back-end electronics: charge collection, signal amplification and discrimination are all handled by the electronics, which also writes binary hit information to an event buffer.

8-bit Digital to Analog Converters (DACs) are located around the perimeter of the chip and their primary function is to control both the voltage and currents in the front-end circuits of pixels [211]. The voltage `VCASN` and current `ITHR`, which determine the charge threshold, are the most significant `DACs` for the work discussed in Section 7.2.4.2.

6.6.4.1 Electronic circuitry in ALPIDE sensors

FIGURE 6.12 shows the three components of the ALPIDE chips: a collection diode, a pixel analog Front-end and a Multi Event Buffer (MEB). In this Section, the integrated circuits inside the sensors are described. On a single chip, there are 512 copies of the circuit, with one circuit every two-pixel columns.

Both analog and digital parts are included in the matrix.

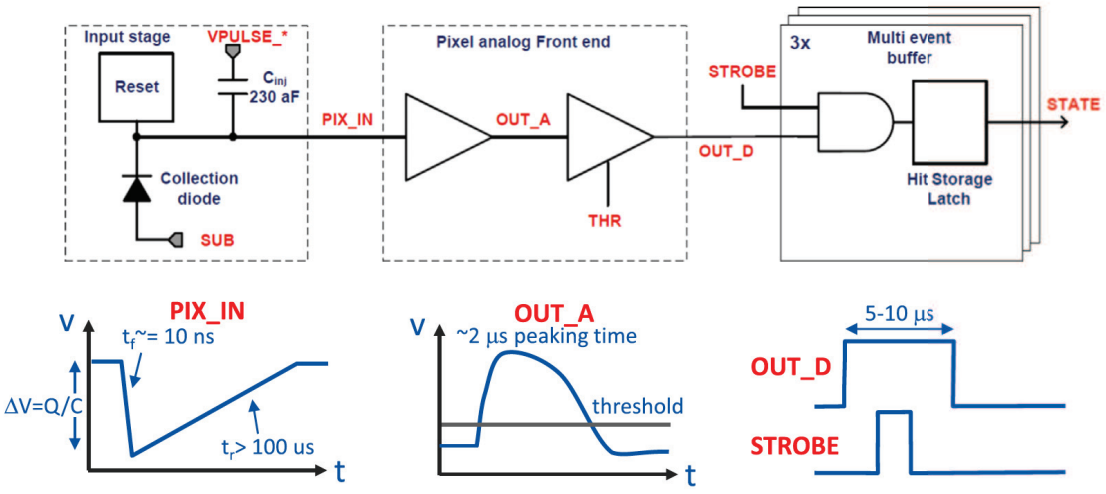

FIGURE 6.12. ALPIDE pixel cell block diagram.

Digital components

- Three hits storage registers (MEB),
- a pixel masking register
- and a pulsing logic technology.

Analog components

- The front-end circuit
- and the discriminator,

using a total of 40 nW [212].

A common threshold level in all the pixels can be performed using a STROBE signal, as shown on the right side of Figure 6.12. To this end, each pixel has a pulse injection capacitor for injecting a test charge into the Front-end, needed to the qualification tests described in Chapter 7.

The pixel hit data readout from the matrix is based on a circuit name Priority Encoder (PE) [213] and the sensor readout calibration is performed during one hit transfer cycle. The cycle is repeated until all pixels' addresses have been transmitted. The matrix readout is organized in 32 regions (512×32 regions), called RRU (Region Readout Units), each one executing the readout of a submatrix.

The 32 Region Readout Units (RRUs) are able to read out the matrix. The ALPIDE chips also contain specific control interfaces responsible for transmitting signals, such as trigger messages [214].

A series of on-chip 8-bit DACs generates all of the analog signals necessary by the Front-ends, as said in Section 6.6.4. The outputs of the internal DACs may be monitored using the analog monitoring pads that are provided.

Finally, in each ALPIDE chip, there are three dataflow lines: slow control, clock and data lines.

- The slow control interface serves two purposes: first, providing write and read access to internal registers, commands, configuration and memories; second, distributing trigger commands or other broadcast synchronous signals.
- The clock is needed to synchronize the data based on the 40.08 MHz LHC clock.
- The data lines collect the electronic signals resulting from the passage of charged particles through the active volume.

6.6.5 Ladder production

As said before, the ladders are composed of two to five silicon pixel sensors that are glued to an FPC using aluminium strips. The assembly of the ALPIDE chips took place at CERN at the Department Silicon Facility (DSF), in a clean room environment. Chips were delivered to DSF as wafers, undergoing a visual check before being cleaned and submitted to an electrical test. The following criteria were considered to select high-quality chips:

- chips have to be intact and thinned down to 50 µm;
- chips have to be aligned to FPCs with a precision better than 10 mm;
- chips have to be clean, so it is important to avoid dust particles deposition.

Once sensors are chosen, a ladder could be assembled by mounting chips on an FPC with around 70 connections per chip. The key assembly requirement is that chips have to be positioned accurately within 5µm.

ALice Integrated Circuit Inspection and Assembly machine (ALICIA), shown in Figure 6.13, was used to provide an automated inspection and assembly method. Some

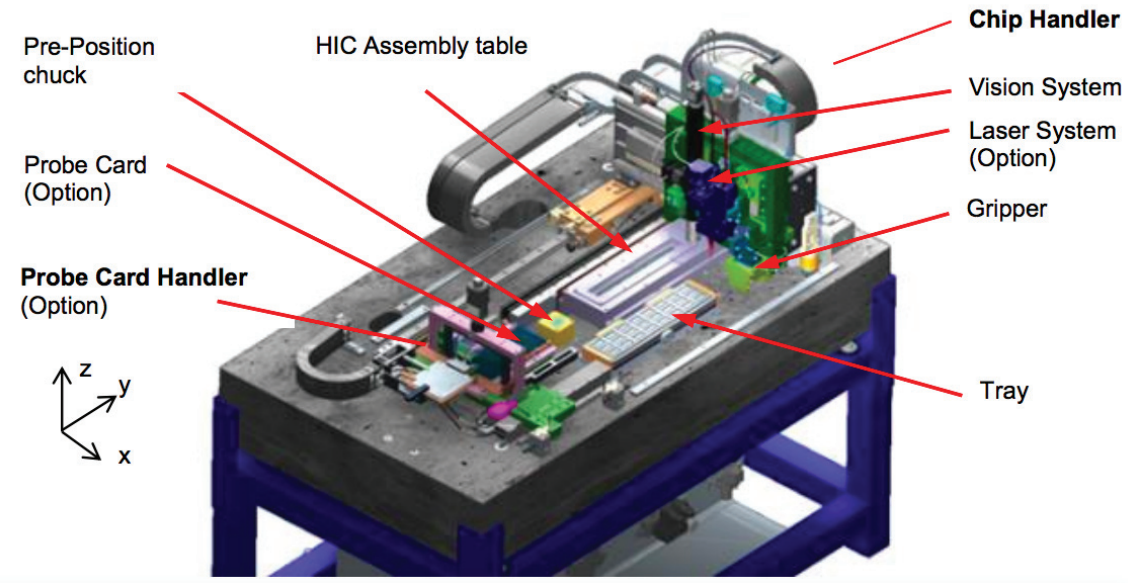

FIGURE 6.13. Main components of ALICIA robot.

features of the ALICIA ladder assembling procedure are reported in Appendix E.

The sensors were glued to the FPC: after 4 hours the glue had polymerised, and the ladders were ready to be fed to the MFT wire bonding machine, where the electrical connection between the chips and the FPC was established by ultrasonic wire bonding technology.

6.6.6 Mechanical Half-Disks production

To build the mechanical part of a Half-Disk (H-D), different components are needed. A team from SUBATECH in Nantes designed the H-D plastic supports, as well as the heat

exchangers, shown in Figure 6.14 and all of their associated components. The heart of the heat exchanger is a foam volume with grooves hosting the pipes for the water-cooling system; on the faces of this volume are glued two cold plates, and on the sides two water pipe connectors are installed, allowing water to flow.

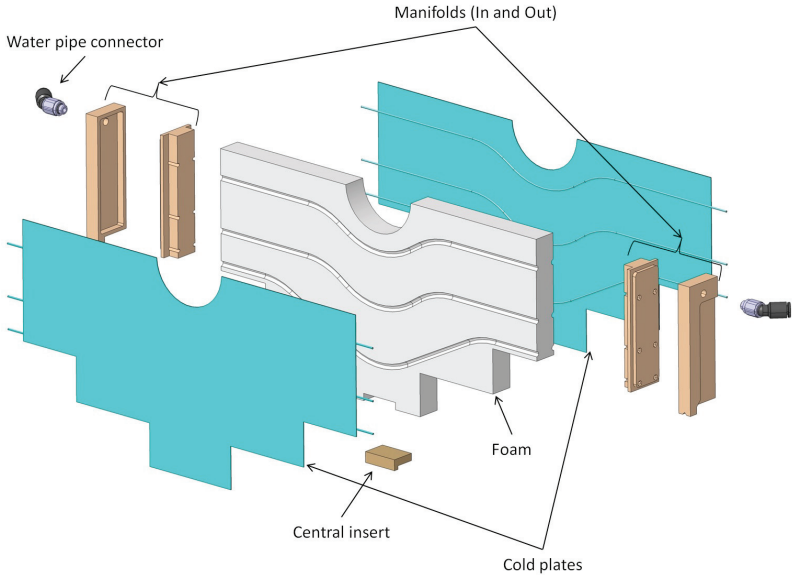

FIGURE 6.14. Schematics view of a heat exchanger for the smaller H-Ds.

The PCB, which is manufactured in China, is the other component that goes into the mechanical assembly of the H-D. It provides power to the chips, transports data and allows the connection with the ladders and other devices. It is important to notice that the ground of each H-D is the same for all the ladders. In addition, on PCBs, there are also temperature and humidity sensors.

The assembling of ladders on a mechanical H-D was done at the IP2I Lyon lab. Using a robot, the glue was applied in a spiral shape, as shown in Figure 6.15.

After gluing the ladders on both sides of the heat exchanger, the H-D is ready to be tested and qualified for the commissioning. Figure 6.16 shows an example of a H-D, with the ladders glued on the heat exchanger and connected to the PCB.

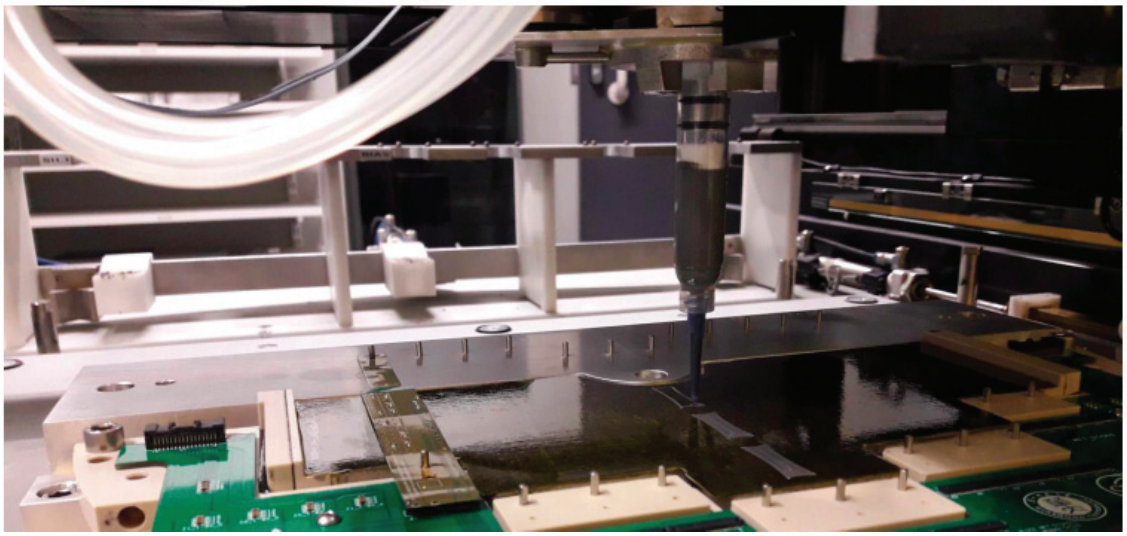

FIGURE 6.15. The glue dispensing is performed with a needle moved by a robot 500µm above the heat exchanger.

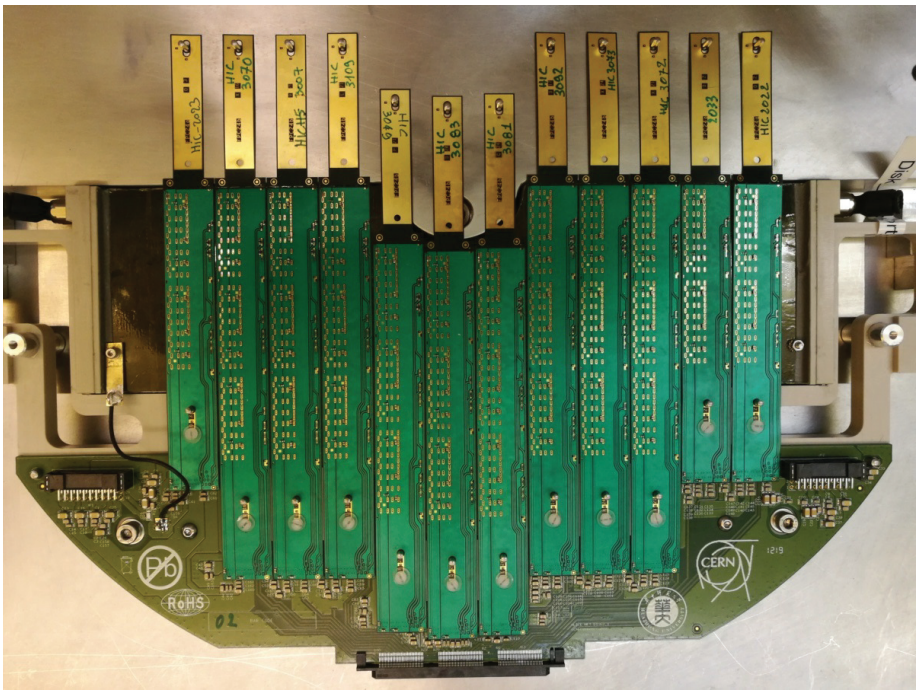

FIGURE 6.16. Picture of a face of one H-D produced in Lyon.

References

[176] W. H. Trzaska et al. “New ALICE detectors for Run 3 and 4 at the CERN LHC”. In: *Nucl. Instrum. Meth. A* 958 (2020). Ed. by M. Krammer, T. Bergauer, M. Dragice-

vic, M. Friedl, M. Jeitler, J. Schieck, and C. Schwanda, p. 162116. DOI: 10.1016/j.nima.2019.04.070 (cit. on p. 134).

[177] A. Ferretti et al. "The ALICE Experiment Upgrades". In: (Jan. 2022). arXiv: 2201.08871 [physics.ins-det] (cit. on pp. 135, 138).

[178] Felix Reidt. "Upgrade of the ALICE ITS detector". In: *Nucl. Instrum. Meth. A* 1032 (2022), p. 166632. DOI: 10.1016/j.nima.2022.166632. arXiv: 2111.08301 [physics.ins-det] (cit. on p. 135).

[179] D. Andreou. "Heavy-flavour Measurements in Pb–Pb Collisions with the Upgraded ALICE Inner Tracking System". In: *Acta Phys. Polon. Supp.* 14 (2021). Ed. by P. Bicudo, R. Höllwieser, J. Jovicevic, R. Kaminski, and M. Krstic Marinkovic, p. 29. DOI: 10.5506/APhysPolBSupp.14.29. arXiv: 2004.14877 [nucl-ex] (cit. on p. 136).

[180] Luciano Musa and Stefania Boelé. *Alice tracks new territory*. 2021. URL: https://cerncourier.com/a/alice-tracks-new-territory/ (cit. on p. 137).

[181] J. Adolfsson et al. "The upgrade of the ALICE TPC with GEMs and continuous readout". In: *JINST* 16.03 (2021), P03022. DOI: 10.1088/1748-0221/16/03/P03022. arXiv: 2012.09518 [physics.ins-det] (cit. on p. 137).

[182] S. H. I. Barboza et al. "SAMPA chip: a new ASIC for the ALICE TPC and MCH upgrades". In: *JINST* 11.02 (2016), p. C02088. DOI: 10.1088/1748-0221/11/02/C02088 (cit. on p. 137).

[183] J. Adolfsson et al. "SAMPA Chip: the New 32 Channels ASIC for the ALICE TPC and MCH Upgrades". In: *JINST* 12.04 (2017), p. C04008. DOI: 10.1088/1748-0221/12/04/C04008 (cit. on p. 137).

[184] ALICE Collaboration. *The Alice TPC is upgraded*. 2020. URL: https://home.cern/news/news/experiments/alice-tpc-upgraded (cit. on p. 138).

[185] "Upgrade of the ALICE Readout & Trigger System". In: (2013). Ed. by P. Antonioli, A. Kluge, and W. Riegler (cit. on p. 138).

[186] Solangel Rojas Torres. *Status of the Fast Interaction Trigger detector for the ALICE upgrade*. 2022. DOI: 10.22323/1.398.0795 (cit. on p. 139).

[187] P. Buncic, M. Krzewicki, and P. Vande Vyvre. "Technical Design Report for the Upgrade of the Online-Offline Computing System". In: (Apr. 2015) (cit. on p. 139).

[188] D. Rohr. "The ALICE Run 3 online/offline processing". In: *Nucl. Instrum. Meth. A* 1038 (2022), p. 166954. DOI: 10.1016/j.nima.2022.166954. arXiv: 2208.07412 [physics.ins-det] (cit. on p. 139).

[189] ALICE Collaboration. *Technical Design Report for the Muon Forward Tracker*. Tech. rep. 2015. URL: https://cds.cern.ch/record/1981898 (cit. on pp. 140, 145, 146, 150).

[190] R. L. Workman et al. "Review of Particle Physics". In: *PTEP* 2022 (2022), p. 083C01. DOI: 10.1093/ptep/ptac097 (cit. on p. 141).

[191] R. Aaij et al. "Measurement of J/ψ production in pp collisions at $\sqrt{s}$ = 7 TeV". In: *Eur. Phys. J. C* 71 (2011), p. 1645. DOI: 10.1140/epjc/s10052-011-1645-y. arXiv: 1103.0423 [hep-ex] (cit. on p. 142).

[192] A. M Sirunyan et al. "Measurement of prompt and nonprompt J/ψ production in pp and p-Pb collisions at $\sqrt{s_{\mathrm{NN}}}$ = 5.02 TeV". In: *Eur. Phys. J. C* 77.4 (2017), p. 269. DOI: 10.1140/epjc/s10052-017-4828-3. arXiv: 1702.01462 [nucl-ex] (cit. on p. 142).

[193] B. Z. Kopeliovich and A. V. Tarasov. "Gluon shadowing and heavy flavor production off nuclei". In: *Nucl. Phys. A* 710 (2002), pp. 180–217. DOI: 10.1016/S0375-9474(02)01124-7. arXiv: hep-ph/0205151 (cit. on pp. 143, 144).

[194] P.A. Zyla et al. "Review of Particle Physics". In: *PTEP* 2020.8 (2020, 10.1093/ptep/ptaa104), p. 083C01. URL: 10.1093/ptep/ptaa104 (cit. on p. 143).

[196] B Abelev et al. "Upgrade of the ALICE Experiment: Letter Of Intent". In: *J. Phys. G* 41 (2014), p. 087001. DOI: 10.1088/0954-3899/41/8/087001 (cit. on p. 143).

[197] S. R. Klein and J. Nystrand. "Interference in exclusive vector meson production in heavy ion collisions". In: *Phys. Rev. Lett.* 84 (2000), pp. 2330–2333. DOI: 10.1103/PhysRevLett.84.2330. arXiv: hep-ph/9909237 (cit. on p. 143).

[198] T. Herman. "Latest ALICE results on J/ψ photoproduction in ultra-peripheral collisions at the LHC". In: *SciPost Phys. Proc.* 8 (2022), p. 106. DOI: 10.21468/SciPostPhysProc.8.106. arXiv: 2107.13284 [nucl-ex] (cit. on p. 144).

[199] W. T. Kelvin. *The molecular tactics of a crystal*. Clarendon Press, 1894 (cit. on p. 144).

[200] L Ya Glozman. "Restoration of chiral symmetry in excited hadrons". In: *arXiv preprint hep-ph/0410194* (2004) (cit. on p. 144).

[201] ALICE Collaboration. *Addendum of the Letter of Intent for the upgrade of the ALICE experiment : The Muon Forward Tracker*. Tech. rep. Final submission of the present LoI addendum is scheduled for September 7th. Geneva: CERN, 2013. URL: https://cds.cern.ch/record/1592659 (cit. on pp. 145–147, 150).

[202] CERN. *ALICE takes leap forward with major new installation*. 2021 (cit. on pp. 146, 147, 195).

[203] K. Yamakawa, A. Augustinus, G. Batigne, P. Chochula, M. Oya, S. Panebianco, O. Pinazza, K. Shigaki, R. Tieulent, and Y. Yamaguchi. "Design and Implementation of Detector Control System for Muon Forward Tracker at ALICE". In: *JINST* 15.10 (2020), T10002. DOI: 10.1088/1748-0221/15/10/T10002. arXiv: 2006.07224 [physics.ins-det] (cit. on p. 148).

[204] M. Brice. *ALICE images gallery*. 2020. URL: https://home.cern/resources/image/experiments/alice-images-gallery (cit. on p. 149).

[205] G. Aglieri Rinella et al. "The ALPIDE pixel sensor chip for the upgrade of the ALICE Inner Tracking System". In: *Nucl. Instrum. Meth. A* 845 (2017). Ed. by G. Badurek, T. Bergauer, M. Dragicevic, M. Friedl, M. Jeitler, M. Krammer, J. Schieck, and C. Schwanda, pp. 583–587. DOI: 10.1016/j.nima.2016.05.016 (cit. on p. 149).

[208] A. Francisco. "Measurement of the elliptic flow in Pb-Pb collisions at $\sqrt{s_{\mathrm{NN}}} = 5.02$ TeV with the muon spectrometer of ALICE at the LHC". PhD thesis. SUBATECH, Nantes, 2018 (cit. on p. 149).

[209] B. Abelev et al. "Technical Design Report for the Upgrade of the ALICE Inner Tracking System". In: *J. Phys. G* 41 (2014), p. 087002. DOI: 10.1088/0954-3899/41/8/087002 (cit. on p. 151).

[210] Basic Electronics Tutorials. *p-well Process*. 2018, https://www.electronics-tutorial.net/CMOS-Processing-Technology/p-well-Process/ (cit. on p. 151).

[211] G. Aglieri et al. "Monolithic active pixel sensor development for the upgrade of the ALICE inner tracking system". In: *JINST* 8 (2013), p. C12041. DOI: 10.1088/1748-0221/8/12/C12041 (cit. on p. 152).

[212] Arts, L. "ALPIDE Testing Software for the upgraded Inner Tracking System of the ALICE experiment". PhD thesis. 2016 (cit. on p. 152).

[213] ALICE ITS ALPIDE development team. *ALPIDE Operations Manual*. 2017 (cit. on pp. 153, XXIII).

[214] M. Aquilina. *ALPIDE Visualiser*. Tech. rep. 2017. URL: https://cds.cern.ch/record/2283978 (cit. on p. 153).

7 MFT calibration and qualification during the commissioning on surface

The only calibration that counts is how much heart people invest,
how much they ignore their fears of being hurt or caught out or humiliated.
And the only thing people regret is that they didn't live boldly enough,
that they didn't invest enough heart, didn't love enough.
Nothing else really counts at all.
Ted Hughes (1930 – 1998)

Contents

As described in Chapter 6, the ALICE Collaboration installed, qualified and calibrated various new sub-detectors during LS2 to increase the experiment performance and be able to collect data at higher interaction rates. The foreseen interaction rate will be as high as 50 kHz in Pb-Pb collisions – corresponding to an instantaneous luminosity of $\mathscr{L} = 6 \times 10^{34}\,\mathrm{cm}^{-2}\,\mathrm{s}^{-1}$ – and will reach 200 kHz in p-p and p-Pb collisions.

The MFT, a novel silicon pixel tracker developed to provide vertexing capabilities to the MS, has been described in Section 6.6; this Chapter will focus on the qualifying tests performed on the detector before its installation in the ALICE cavern. After an explanation of the tests performed to provide a general qualification on this detector, the analysis of the results obtained will be presented.

7.1 The main reasons to qualify and calibrate a particle physics detector

Before describing all of the tests performed to qualify the MFT performance, it is reasonable to question what the detector calibration and qualification are, and why this is a crucial step in view of the analysis of the collected data.

- **What are the detector's calibration and qualifications?**

When designing a detector, simulations and calculations are performed under ideal conditions, focusing on the goals for which it is built and the way it will be exploited. Unfortunately, the detectors are not ideal.

Qualification and calibration mean quantifying the behaviour of the detector, to include these defects in MC simulations and select the reconstructed data in the best possible way.

- **Why is it important to qualify and calibrate a detector?**

Qualifying and calibrating sensors (*e.g.* ALPIDE chips) and complex detectors (*e.g.* all the upgrades installed in the ALICE cavern during LS2) are needed to check the accuracy and the repeatability of their output. They are a critical need in order the data collected by the detectors to be validated by the quality assurance procedures.

- **How have the MFT calibration and qualification been performed?**

As it will be discussed in Section 7.2, two test benches had been configured to perform a series of five tests to qualify the behaviour of single ladders and H-D, respectively, see Sections 7.1.1 and 7.1.2[1]. The qualification and calibration work performed during this Ph.D. thesis focused on the ALPIDE sensors; the H-D mechanical structures and cabling employed to power and operate the detector had been validated in a previous step[2], and for this reason they will not be described here.

7.1.1 1st test bench : single ladder test bench

THE test bench developed for the qualification of the single ladders, installed at IP2I, is shown in Figure 7.1, in a configuration with no back-bias applied (V_{BB}0 V). For the back-bias configuration, the 0 Ω resistor in the ICM_F board, represented by the dark yellow square in Figures 7.1 and 7.2, is replaced by a negative potential provided by the laboratory power supply ($V_{BB} = -3$ V)[3], as shown in Figure 7.2.

[1]Both for ladder and H-D qualification, the software (C++, ROOT© and Qt5© based) used to perform the tests is available on the MFT CERN GitLab repository. With a few clicks on a simple Graphical User Interface (GUI), the user may navigate the test sequence, conduct the tests, and see the grade received at each stage.

[2]In SUBATECH, lab in Nantes, France, all the components that constitute the H-Ds have been tested, starting from the heat-exchanger, all the electrical devices and the water connectors.

[3]The reverse bias technology is explained in Section D.1.

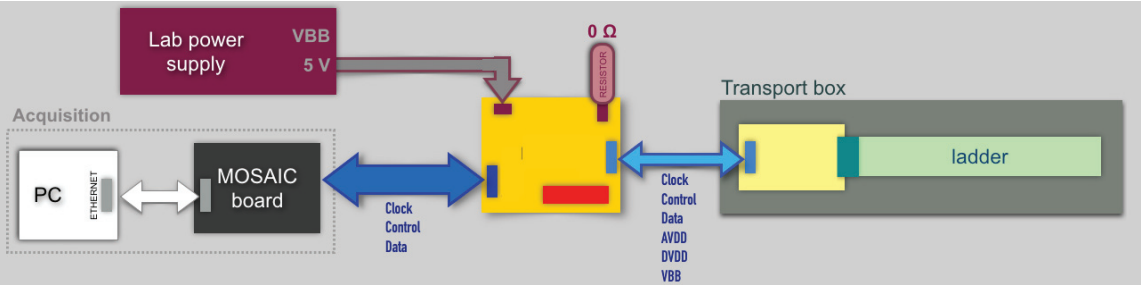

FIGURE 7.1. Overview of the hardware of test bench for ladders qualification without back-bias.

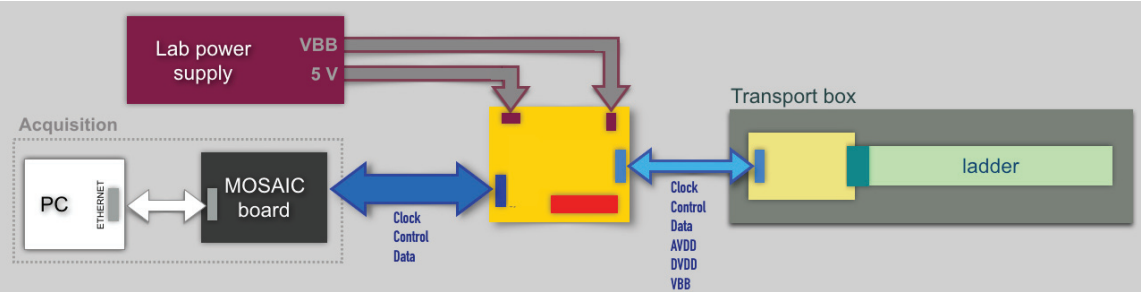

FIGURE 7.2. Overview of the hardware of test bench for ladders qualification with back-bias $-3V$.

The laboratory power supply provides 5 V for analog and digital voltage, and a stable −3 V for back-bias. The ICL, shown in Figures 7.1 and 7.2 in light yellow, ensures the connection between the sensors and the acquisition system, and the MOdular System for Acquisition Infrastructure and Control (MOSAIC), in black, is the ALPIDE interpreter connected with the computer. The MOSAIC board is equipped with a trigger and pulse system which transmits fundamental commands to the ALPIDEs [215].

In short, the MOSAIC board [216] performs the measurements on the sensors, driven by the computer's command. Unlike the final acquisition board used in ALICE cavern, able to "speak" with several ladders at the same time, it can only deal with a single ladder and can send the clock[4], set/read its configuration (*via* the bi-directional slow control line) and perform its readout (*via* the high-speed data lines) to five chips at most, at the same time.

7.1.2 2nd test bench : H-D test bench

THE hardware components of the test bench used to qualify the Half-Disks (H-Ds) behaviour with the MOSAIC board are shown in Figure 7.3. As it can be noticed, the test

[4]The nominal clock at 40.08 MHz corresponds to the LHC clock.

bench can test and characterize only one face of the H-D at a time.

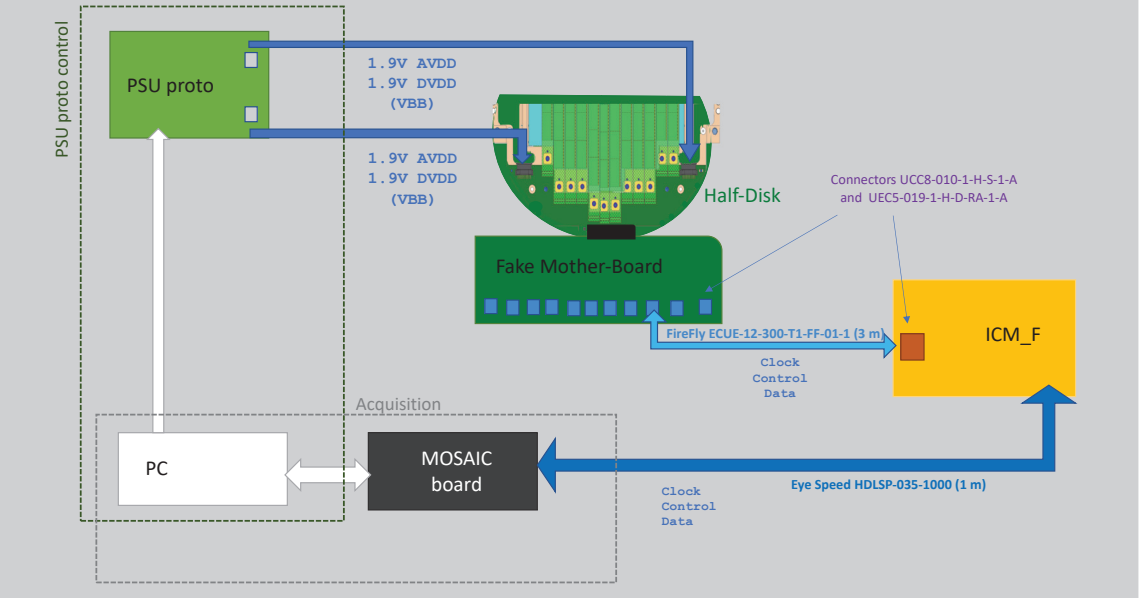

FIGURE 7.3. Overview of the hardware components of the test bench for an H-D characterization.

With the Power Supply Unit (PSU) proto board, it is possible to power up to 2 zones[5] of the H-D, at the same time.

The PSU proto [217] board is connected to the computer through a micro-controller board. The computer controls the PSU proto [217] board using a custom-made *LabVIEW*© GUI. Four tensions of ±8 V are provided to the PSU:

- 8 V to power the digital DC-DC converter,
- 8 V to power the analog DC-DC converter,
- 8 V and −8 V to power the operational amplifiers.

The voltage provided to the amplifiers is used to control the latch-up and to produce and send the following voltages to the H-D:

- 1.9 V for AVDD,

[5]Each H-D face has 4 four zones, composed of at least 3 ladders. All ladders of the same zone are powered at the same time. An example of the division of a H-D in zones is shown in Appendix F.

- 1.9 V for DVDD,
- and down to −3 V for the V_{BB}.

The H-D is connected to a Fake Mother-Board (FMB), represented by the dark green rectangle in Figure 7.3, on which a connector exists for each of the possible ladder positions on one face of the H-D. This is implies that:

(i) there are 4 types of FMB;

(ii) it is necessary to use the specific connector that corresponds to the ladder position that will be tested, to ensure that the test is successful.

Data, clock and slow-control are monitored, as for the ladder test bench (Section 7.1.1), by the MOSAIC board.

7.1.3 The current consumption of the chips throughout the qualification tests

EXAMINING the detector's current consumption is the first step in determining whether or not its calibration and qualification are accurate. This Section will focus on the characterisation of the how the increase of the absorbed current with the chip usage, and how this increase is monitored.

As the test sequence progresses, the trend of the ALPIDEs' total current consumption (analog + digital) is monitored using as a reference the three following current levels:

- *Level A* represents the chips' current consumption immediately after they are switched on, in the absence of a clock, *i.e.* without performing any functional tests (Total *Level A* ≃ 100 mA per face per H-D);
- *Level B* denotes the increased current consumption caused by the clock when it is sent to the chips. Total current consumption of 50 to 60 mA per sensor is expected in this case;
- *Level C* refers to the current consumption when the clock is enabled in addition to various other chip operations (for *e.g.* pulsing a row on the chip matrix at a given frequency and sending the corresponding data off-chip). The *level C* amounts to a total current consumption of 100 to 110 mA per sensor.

The increase from *level A* to *level B* is purely attributable to the addition of the **digital** component to the system. Consequently, if *level A* and *level B* values are the same (no or too little rise), it means that the clock cannot be effectively received by the chip(s).

The further increase from *level B* to *level C* is also strongly dominated by the digital part, because the **analog** current remains more or less constant at all consumption levels.

7.2 Functional tests

THE functional tests [218, 219] performed on chips on H-Ds are as follows:

- Read-back test;
- FIFO scan;
- Digital scan;
- Threshold scan;
- Noise occupancy scan;
- Eye Measurement scan.

With each scan comes a corresponding classification, which is used to assess the overall chip quality on the ladder under test. Apart from the Read-back test, the total grade awarded to the whole ladder is the same as the grade assigned to the chip with the worst result. In the following Sections, each functional test will be described with some results obtained and analyzed during the Ph.D. thesis.

7.2.1 Read-back test

THE first stage in the validation procedure is relatively simple and is referred to as the *Read-back test*. For each expected chip ID, as shown in Figure 7.4a, the MOSAIC writes an arbitrary value in a particular register and attempts to read back it.

The test is declared successful *if and only if* the Read-back value is rigorously **equal** to the written one. This is possible only when both the clock and slow control lines are working properly[6] in the test. When the chip cannot even be configured, it is consid-

[6]Most of the time, a failure in the Read-back test was rather traced to a broken clock or slow control lines towards the chip than to a broken chip itself.

ered non-conformal (or Not-Conf).

The Read-back test is automatically done by the test bench software, before any more complex functional test. This test is made chip by chip and takes less than a second to complete. As soon as a chip on the ladder fails the Read-back test, the GUI window instantly prevents the user. During this step, the expected chip current consumption corresponds to *level A*,as described in Section 7.1.3.

All ladders with at least a chip having a Read-back problem have been discarded, and they are not used in any H-D assembly. It should be noted, however, that such an issue is not necessarily related to a problem in the chips: it could also happen because of a lock or slow control lines damage occurring during the H-D assembly procedure, despite all the caution and the assembly operators' skills. Regrettably, after the glue has polymerized, it is impossible to intervene on H-Ds, which means that ladders with non-conforming chips cannot be changed.

Nonetheless, only 6 chips out of the 936 composing the whole MFT detector (0.64%) failed the Read-back test.

7.2.2 FIFO scan

AFTER the Read-back test, the qualification procedure sequence continues with another basic test, the *First In, First Out (FIFO) scan*, where the oldest (first) entry – or "head" of the queue – is processed first.

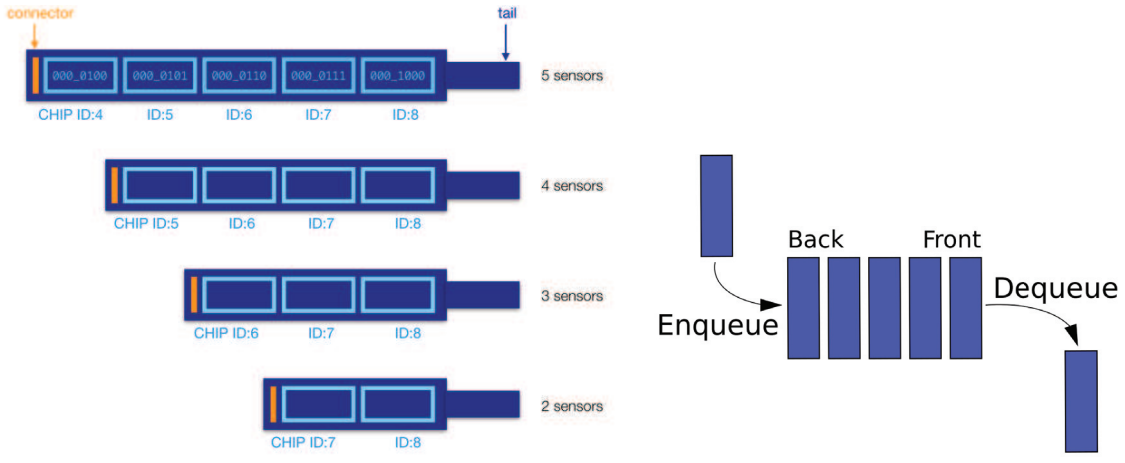

(A) READOUT (B) FIFO SCAN

FIGURE 7.4. **(a)** Schematic view of ALPIDE chips showing the corresponding Chip ID on ladders of various lengths; **(b)** graphical representation of a FIFO scan.

A schematic representation of the FIFO scan is presented in Figure 7.4b. This test begins by setting each enabled chip in the *configuration mode* [220]. During the FIFO scan, four-bit patterns are written into the DPRAM[7], then read and compared to the written pattern. The DPRAMs can be accessed *via* FIFO RRUs, hence the name of the scan.

The FIFO scan is considered successful if **all write/read operations** for all bit patterns in all chip regions were good and each read pattern is **equal** to the written one.

This scan is done chip by chip and takes around 10 seconds to complete, and the MOSAIC board assigns one of two potential grades to each evaluated chip: Gold if zero errors in the bit pattern are found, Red in any other case. Communication issues, as well as physical faults in the area DPRAMs, might be the primary cause of a Red test result.

7.2.3 Digital scan

7.2.3.1 The ALPIDE functional blocks involved during the Digital scan

THE *Digital scan* is the third stage of the validation procedure. It also begins by putting each chip into the slow-control configuration. In particular, the chips will be operated in the *triggered mode* [220][8] and the in-pixel analog front-end is used to inject a known charge – simulating a particle hit – on each pixel, as shown in Figure 7.5.

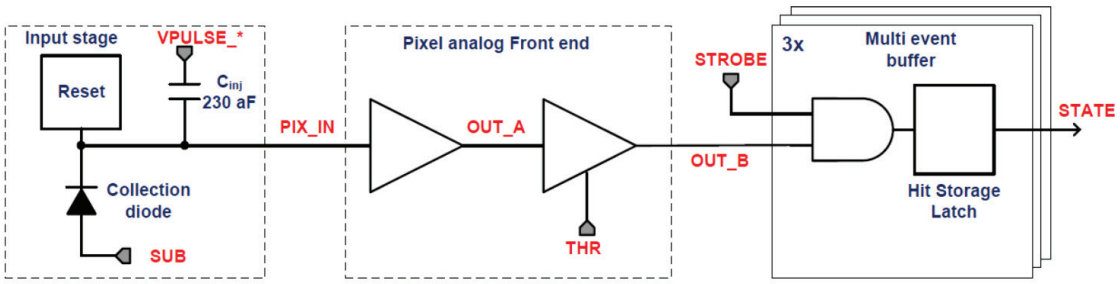

FIGURE 7.5. Simplified block diagram of the ALPIDE in-pixel circuitry, from [220].

This procedure only tests the pixel digital functional block and the entire pixel matrix

[7] (i) with only zeroes, (ii) with only ones, (iii) with a succession of zero and one, (iv) with a succession of one and zero [220].

[8] "*In triggered mode, the chip prioritizes events that are already stored in the matrix over new incoming triggers. [...] A trigger command received when the matrix buffers are all full will not generate a new strobing interval. The trigger command will still be acknowledged in the data stream with an empty chip data packet.*" [from [220] page 58].

readout, resulting in a significant digital circuitry deployment on the chip's periphery during testing. The following Sections give a concise summary; more information may be found in [220].

The digital part ensures the binary "hit" information stored in a Multi Event Buffer (MEB), equipped with a set-reset latch mechanism. The pixel matrix readout involves several functional blocks. The first task is to collect the "hit" pixels addresses , via the mechanism provided by the Priority Encoders (PEs), locally reading each double-column[9]. The PEs then send these addresses to the DPRAMs of each RRU formatting data. The formatted data undergo the serialization in the Data Transmission Unit (DTU), operating at the highest possible speed allowed by the ALPIDE, (1.2 Gbit/s in the case of the MFT ladders). In Appendices G and H, the possible issue during the Digital scan and the DTU operations are described.

7.2.3.2 Current consumption during the Digital scan

BECAUSE of the high solicitation of the functional blocks of the digital periphery[10], the current consumption reaches its maximum (*level C*, explained in Section 7.1.3) during this scan[11].

The chips are all scanned at the same time. Unless there are some defects in the pixel matrix, the Digital scan is normally not affected whenever $V_{BB} = -3\,V$ is also provided to the chips.

7.2.3.3 The outcome of the Digital scan

THIS test allows to identify and list the coordinates of the **not working pixels** ($n_{\text{bad pixels}}$) *i.e.* dead, inefficient or noisy pixels on the matrix of each chip. To do this, each pixel is pulsed a total of $N = 50$ times, allowing for the identification of the $n_{\text{bad pixels}}$ categories:

- Pixels that do not respond at all, are considered ***dead***.
- If a pixel answers at least once but less than N[12] times, it is considered ***inefficient***.

[9] "*Looking at the chip with the digital periphery on the bottom, the leftmost region is region 0 and the right-most region is region 31. Each region contains 16 double columns. Double column 0 is the leftmost and double column 15 is the rightmost.*" [from [220]]

[10] A full rolling row of pixels is unmasked and they endure $N = 50$ consecutive "digital pulses".

[11] This is due in particular to the DTU which is very demanding in power.

[12] In our case, $N = 50$.

- If a pixel responds more than N times, it is considered ***hot*** or ***noisy***.

Finally, thanks to a ROOT© macro the response of the Digital scan pixel matrices is analysed and produces maps, identifying the position of the bad pixels for each chip tested. An example of these maps can be found in Figure 7.6.

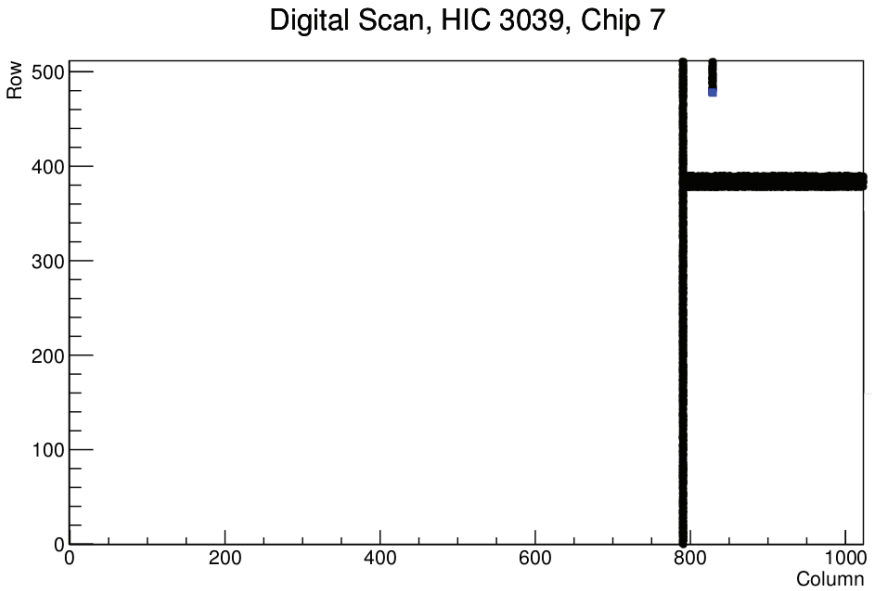

FIGURE 7.6. Digital map example of chip 7 on ladder 3039. Black dots represent the dead pixels and the blue one is an inefficient pixel. This ALPIDE chip has a dead column.

7.2.3.4 The grades system for the qualification of ALPIDE chips

WHEN performed on a ladder, this test is done simultaneously on all chips and lasts about 6 seconds. It can assign four different grades – Gold, Silver, Bronze or Red – to each tested chip, depending on the number of $n_{\text{bad pixels}}$ found for the chip.

- If $n_{\text{bad pixels}} < 51$[13], the chip is Gold;
- if $51 \leq n_{\text{bad pixels}} < 2101$, the chip is Silver;
- if $2101 \leq n_{\text{bad pixels}} < 5244$ the chip is Bronze;
- otherwise, the chip is Red.

All 930 conformal chips glued on the 10 H-Ds – selected to be installed in ALICE cavern – have less than 5244 bad pixels per chip, i.e. none of them is Red.

[13] Just for the remainder, the ALPIDE pixel matrix has 512×1024 columns, for a total of 524,888 pixels.

7.2.4 Threshold scan

BOTH the analog and digital components of the ALPIDE chips are checked using the *Threshold scan* , as described in Figure 7.5.

Choosing an appropriate threshold level is very important: in particular, decreasing the threshold value would boost the detection effectiveness but also increases the fake-hit rate. It is, therefore, necessary to find the "good" threshold level. In practice, the Threshold scan is realized by sending "analog pulses" to each in-pixel analog front-end, shown in Figure 7.5, *i.e.* by injecting many times a test charge q_{inj}, which simulates the particle charge deposited in the pixel. The number of times the pixel fires allows to measure the corresponding hit-detection probability.

The variation of q_{inj} is obtained by applying a range of step-by-step increasing values of the voltage[14] V_{Pulse} on the known in-pixel injection capacitor[15] C_{inj} expressed as:

$$q_{\text{inj}} = C_{\text{inj}} \cdot V_{\text{Pulse}} \tag{7.1}$$

where V_{Pulse} is common to the whole sensor matrix.

Since V_{Pulse} is set on the chip in DAC units, q_{inj} is also set in DAC units. Two ingredients are used to compute the DAC-to-electron conversion factor, which is estimated to be 10 electrons per DAC unit.

During the Threshold scan:

- the number of steps in V_{Pulse} (and hence in q_{inj}) is chosen to be $N_{\text{steps}} = 50$;
- the number of injections for each value of q_{inj} is taken to be $N_{\text{inj}} = 50$ [221].

7.2.4.1 The threshold *S-curve*

FIGURE 7.7 illustrates the evolution of the single pixel response as a function of the charge injected number into the pixel: this kind of plot is called *S-curve*.

[14] This is done by configuring two 8-bit on-chip registers in DAC units, namely $V_{\text{Pulse}}^{\text{high}}$ and $V_{\text{Pulse}}^{\text{low}}$, to get $V_{\text{Pulse}} = V_{\text{Pulse}}^{\text{high}} - V_{\text{Pulse}}^{\text{low}}$. In the Threshold scan algorithm, the choice was to fix $V_{\text{Pulse}}^{\text{high}}$ and vary $V_{\text{Pulse}}^{\text{low}}$ to change the value of V_{Pulse}.

[15] The value of this capacitor was not measured, neither its spread, pixel by pixel nor chip by chip. Only the design value [220] is known *i.e.* $C_{\text{inj}} = 230\,\text{aF}$.

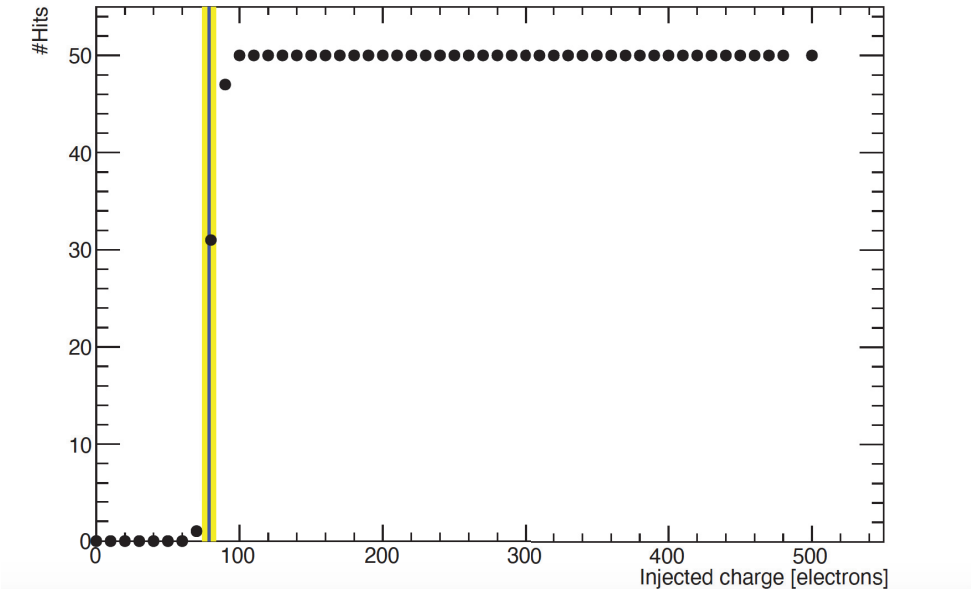

FIGURE 7.7. (Solid black circles) The number of hits digitized as a function of the injected charge for a single pixel (located at row 0, column 0) on chip 7 of ladder 3032. The parameters of the fitted S-curve are also represented, the threshold q_{thr} as a vertical blue line and the temporal noise σ as a yellow vertical band.

In an *ideal* situation, the pixel response to a given injected charge value should always be the same. In particular, for charges right below the threshold, the hits number should always be *strictly zero*. And right above the threshold, it should always be *strictly equal to the number of injections*. So ideally, the pixel response should be a step function.

In reality, as seen in Figure 7.7, the pixel response slightly below the threshold is non-zero and, slightly above, the threshold is not yet at its maximum. This smearing is caused by the pixel's *temporal* noise (also known as random noise), which fluctuates separately from pixel to pixel. The variation of the temporal pixel response under a constant (injected) charge value is due to several noise sources [222] and quantization effects. The latter are related to the small input transistors size, used in the circuitry[16]. In a CMOS sensor, the temporal noise can have contributions from the thermal and $1/f$ noise, originating from the pixel reset mechanism, the transistors switch and the double-column in-pixel circuitry.

Thanks to different tests [223, 224], in particular performed on the most recent ALPIDE prototypes [225], it was possible to conclude that, at low illumination, the dominant noise source is the pixel reset and readout transistors. At high illumination, the domi-

[16]The ALPIDE is built with the 0.18 µm CMOS technology.

nant noise source is created by the collection diode shot noise, which is essentially the leakage current manifestation in the $p-n$ junction. To prevent an increase in the collection diode shot noise, a *black box* is used to shield the ALPIDEs from the (sun) light to avoid it contributing to the leakage current.

Assuming a Gaussian distribution for the temporal noise, the S-curve can be fitted with the following Gaussian-based error function:

$$f(q_{\text{inj}}) = \frac{1}{2} N_{\text{inj}} \left[1 + \text{Erf}\left(\frac{q_{\text{inj}} - q_{\text{thr}}}{\sqrt{2} \cdot \sigma} \right) \right], \tag{7.2}$$

where q_{thr} is the charge at which the selected pixel fires with a probability of 50% and defines the *threshold*; σ is the pixel *temporal noise* and describes the slope, *i.e.* first derivative of the rising part of the S-curve.

To allow the fit to converge, the fit range must include a part of the *plateau* both at the left and the right of q_{thr}, as shown in Figure 7.7. From this test one can conclude that:

- At the S-curve lower left, the injected charge is too tiny and the pixel will never fire;
- at the S-curve upper right corner, the injected charge is enough to cause the pixel to always fire.

The pixel-by-pixel threshold q_{thr} values and temporal noise σ are collected into histograms per chip. The threshold distribution **average** is defined as the **chip threshold**.

The RMS of each distribution, Δq_{thr}[17] and $\Delta\sigma$, will be used to assess the uniformity of the pixel response over the chip matrix.

7.2.4.2 How to adjust the pixel threshold?

SEVERAL test beams have been considered to determine the chip detection efficacy as a function of the threshold. The requirement is to operate the sensors with a detection efficiency > 99% and a fake-hit rate < 10^{-6} per pixel per event. According to an early study performed on a limited sample of ALPIDE sensors, this criterion may be met by setting the sensors to an effective threshold in the range (80, 180) electrons [226]. The

[17] The RMS Δq_{thr} mainly originates from the transistor mismatch in the circuitry, leading to a variability in the pixel response to the same V_{Pulse} stimulus throughout the matrix, in a spatial pattern that will be stable over time. This corresponds to the so-called Fixed-Pattern Noise (FPN).

chips will be operated at the target threshold value of **100 electrons** (or equivalently 10 DAC units), for both the settings of the back-bias V_{BB} mentioned above.

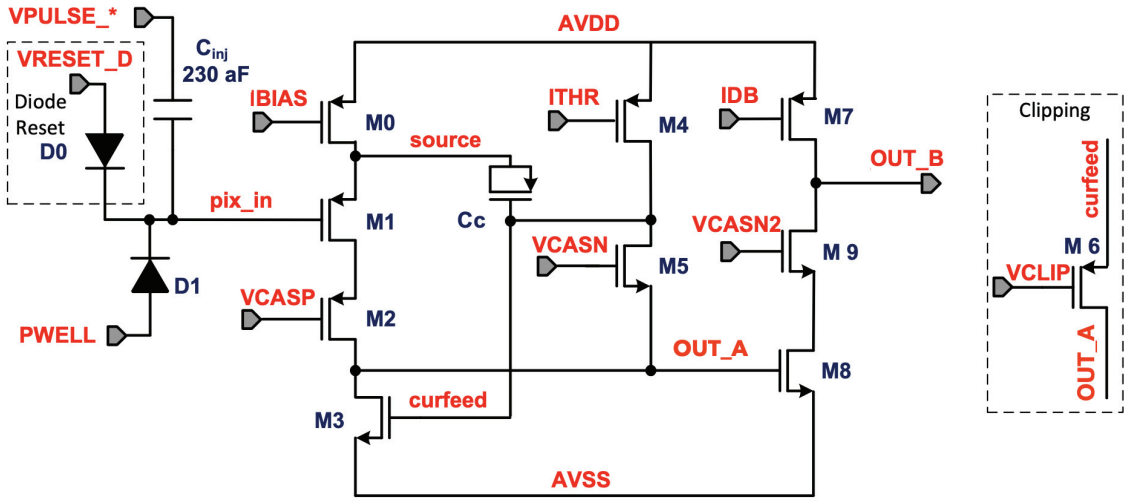

FIGURE 7.8. ALPIDE in-pixel analog front-end, from [220].

There is not a specific on-chip register to quickly adjust the desired charge threshold. The chip analog front-end, on the other hand, is created with several configurable on-board bias DACs [18], as can be seen in Figure 7.8. The in-pixel amplifier, shaper and discriminator circuits are contained in the circuit as described in Section 6.6.4.1.The ALPIDE in-pixel analog front-end can be described as follows:

- The injected charge is sent as `PIX_IN` to the front-end circuitry. It is first used to produce the amplified analog pulse `OUT_A` during the gain and shaper stage.
- The output of the discrimination stage is the signal `OUT_B`.
- `IBIAS` is the first stage bias current.
- `ITHR` and `VCASN` define `OUT_A` baseline voltage, `ITHR` defines the return to the baseline and decreases the effective threshold. `VCASN` increases the effective threshold.
- `VCASN2` has less impact than `VCASN` and therefore it is always defined as `VCASN2`=`VCASN`+12 to reduce the bias parameters numbersetting the effective charge threshold.

[18] All bias parameters are supplied chip-wide and therefore are common to all the pixels in the matrix.

- VCLIP is used to set the clipping point above which the head of the very high input charge peaks will be "cut" and ignored by the circuitry, thus reducing the time needed by OUT_B to return to the baseline.

Any reverse substrate bias voltage V_{BB} externally applied to the sensor will be connected to *p*-well[19].

Some of the transistors shown in Figure 7.8 are nMOS transistors and they are housed in a *p*-well. Therefore, the V_{BB} application will lower the nMOS transistor's bulk voltage and will result in its threshold voltage increase. This has to be compensated for by increasing VCASN, to obtain a similar situation as without V_{BB}.

The target threshold value of 100 electrons can be approached with the bias parameter settings [20,21] summarized in Table 7.1.

	$\mathbf{V_{BB}} = 0\,\mathrm{V}$	$\mathbf{V_{BB}} = -3\,\mathrm{V}$
IBIAS	64	64
IDB	29	29
ITHR	51	51
VCASN	50	105
VCASN2	62	117
VCASP	86	86
VCLIP	0	60

TABLE 7.1. Values of the bias parameters (in DAC units) used to operate the sensors at a threshold value close to 100 electrons, in two cases *i.e.* without or with back-bias voltage externally applied to the sensor.

7.2.4.3 The implemented method of Threshold tuning

DURING physics data taking, it is very useful to have a detector response as uniform as possible, *i.e.* to have approximately the same detection efficiency in all the MFT ALPIDE sensors. To this end, the operating point of each chip has been set, in such a way that

[19] (whereas *n*-wells are connected to the supply voltage AVDD).

[20] Note that the higher value of VCLIP used in the case with non-zero V_{BB} does not influence the value of the threshold. It is given for completeness. This higher value of VCLIP only anticipates the fact that the collection of the charge deposited by a particle hitting the pixel will be more efficient when the reverse substrate back-bias is applied. Therefore, higher input charge peaks can often be reached in this mode and they need to be clipped sooner.

[21] The value of VRESETD used by the reset mechanism of the pixel is not indicated in the Table as it does not affect the effective charge threshold. It is set to 117 DAC.

its average threshold would still be close to 100 electrons but with the smallest possible threshold RMS. This operation is called *Threshold tuning*, and was developed specifically during this Ph.D. work.

The Threshold tuning procedure can be described as follows:

1. For each chip, quick Threshold scans are performed on a small part of the matrix (126 out of 512 rows, *i.e.* 24.6% of each chip).
2. After this step, VCANS[22] is varied, increasing by a DAC unit, starting with the smallest value for a fixed value of ITHR. 126 rows are tested and this tuning step lasts approximately 30 seconds.
3. Thereafter, ITHR is tested between 30 to 100 DAC units values with and without back-bias application for a fixed value of VCASN. As for VCASN, values are increased one by one and 126 rows are tested. This step lasts approximately 45 seconds.
4. By quadratic interpolation, the best value of (ITHR, VCASN) is deduced. The final values of the average threshold, threshold RMS, average temporal noise and temporal noise RMS for each chip are obtained from a full matrix Threshold scan done with the best value of (ITHR, VCASN) determined for each chip.[23]

7.2.4.4 Current and grades system for the Threshold scan

THE Threshold scan incorporates all the steps involved in the Digital scan, as described in Section 7.2.3: as a result, the current consumption reaches the *level C*.

All of the enabled chips are scanned at the same time, with one row at a time being unmasked and pulsed. The first Threshold scan, involving only 126 rows, lasts about ~30 seconds; the second one, involving a full matrix, lasts about ~5 minutes, including the phase of injection of the charges and data analysis. All tested chips must be protected from light for the entire time of the Threshold scan, due to the well-known sensitivity of the sensors. This is necessary to avoid any bias in the recovered threshold and noise distribution of the pixels.

Such as the Digital scan grade system, explained in Section 7.2.3.4, the grading system is based on the number of pixels that do not respond appropriately to the dif-

[22] VCASN values vary between 40 and 62 DAC units without back-bias application and these cover a range from 80 to 130 DACs with the negative voltage of −3 V.

[23] The Threshold tuning must be done twice for each sensor, *i.e.* with and without reverse substrate bias voltage and will result in two different operating points (ITHR, VCASN) for each setting in V_{BB}.

ferent test steps: there are *pixels without hits*, *pixels without threshold* and *hot pixels*, *i.e.* $n_{\text{bad pixels}} = n_{\text{pixels without hits}} + n_{\text{pixels without threshold}} + n_{\text{hot pixels}}$. In particular:

- If the sum of these three contributions $n_{\text{bad pixels}}$ is less than 51, the chip is Gold.
- The chip is Silver when $51 \leq n_{\text{bad pixels}} \leq 2100$;
- It is Bronze, if $2101 \leq n_{\text{bad pixels}} \leq 5243$).
- Otherwise, the chip is considered Red ($n_{\text{bad pixels}} > 5243$).

7.2.5 Noise occupancy scan

WITH the *Noise occupancy scan*, the aim is to find the fraction of the data taken by the pixel matrix that is due to the so-called "noisy" pixels, *i.e.* the pixels firing in the absence of any ionizing particles.

Why is the noisy pixel identification so important?

1. On one side, these unwanted data – heavily dominated by mono-pixel clusters – can degrade the tracking performance, either by reducing the average cluster size and thus deteriorating the spatial resolution or by increasing the combinatorics to be treated by the track reconstruction algorithm.

2. On the other side, namely the readout chain, these unwanted data can also consume part of the bandwidth. Too many noisy pixels can eventually saturate the readout chain. As such, they will introduce inefficiency as only a small fraction of the readout data would be related to some actual signal left by real particles hitting the sensors.

It is therefore crucial to identify and mask the noisy pixels to preserve both aspects.

The *fake-hit rate* is the quantity estimated during the Noise Occupancy scan. In practice, the output of the sensor is collected during a fixed amount of time[24] where no external input is sent[25]: the number of recorded hits N_{hit} will then correspond, by construction, to the number of fake hits.

[24] – or equivalently a fixed number of random triggers or events –

[25] No external input means no beam, no light, no radioactive source, no charge injection. Unfortunately, cosmic rays can not be avoided but they have a known and steady rate.

The requirement for an ALPIDE standard operation is to have a fake-hit rate lower than 10^{-5} hit/event/pixel. To gather enough statistics to reach this sensitivity, the measurement is done with the number of triggers $N_{\text{trg}} = 10^6$. The fake-hit rate O_{noise} is then given by

$$O_{\text{noise}} = \frac{N_{\text{hit}}}{N_{\text{pix}} \cdot N_{\text{trg}}} \tag{7.3}$$

where N_{pix} is the number of pixels in the sensor, N_{trg} is the triggers' number and N_{hit} is the number of collected hits.

The fake-hit rate has a dependence on the threshold at which the chip operates: a threshold reduction will automatically increase the fake-hit rate, and vice-versa. Therefore, *the fake-hit rate will always be measured for sensors operating at a tuned threshold of 100 electrons*[26].

The **noisy pixels** are defined as pixels fired strictly more than **10 times** after one million triggers, during the scan. These pixels might be referred to as "hot" pixels since they have a higher chance of obtaining a hit. The coordinates of each noisy pixel is put in a list, together with the corresponding number of fake hits.

Based on this list, the choice may be made whether or not to mask the noisiest pixels – if this is necessary – to decrease the fake-hit rate below the maximum fake-hit rate requirement. The system of grades is based on the number of noisy pixels and is the same as the one described in Section 7.2.3.4, but based on the noisy pixels' number.

7.2.6 Eye Measurement scan

THE so-called eye diagram is a general-purpose tool for analyzing the serial digital signal transmission quality throughout the data line from the source – the sensor – to the receiver – in this case, the MOSAIC board.

When done with an oscilloscope[27], the eye diagram is obtained from a digital waveform by folding the parts of the waveform corresponding to each bit into a single graph with signal amplitude (in Volts) on the vertical axis and time on the horizontal axis. By repeating this construction over many waveform samples, the resulting graph will represent the statistically-averaged shape of the signal, and will resemble an eye. During this measurement, the sensor is put in a specific test mode, the PRBS mode *i.e.* its DTU

[26] (or equivalently 10 DAC units)

[27] In that case, the probes connected to the oscilloscope will sample the digital signal at a point of the data lines before the receiver, *i.e.* the MOSAIC board.

will send off-chip a pseudo-random sequence of bits.

The eye-opening corresponds to one-bit period. An ideal digital waveform with sharp rise, fall edges and constant amplitude will have an eye diagram similar to what Figure 7.9a shows. Real-world high-speed digital signals suffer significant problems including attenuation, noise, crosstalk, clock jitter, etc. A real eye diagram shape is shown in Figure 7.10b, which resembles the shape of an eye.

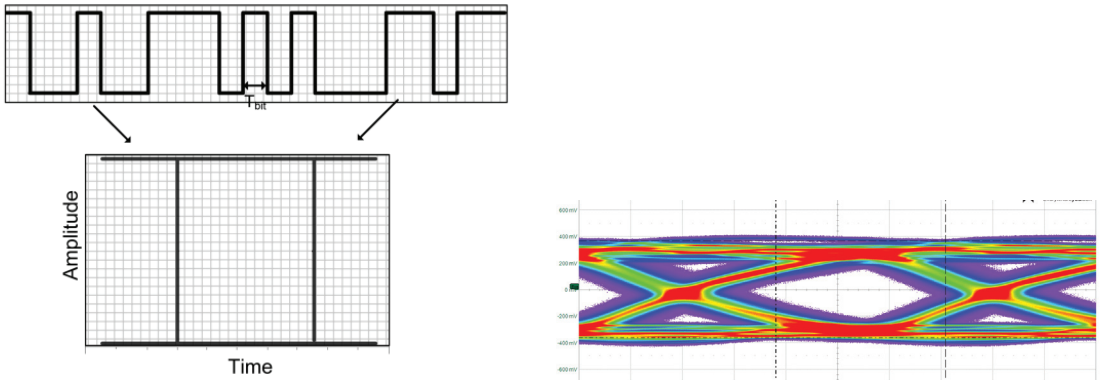

(A) IDEAL EYE DIAGRAM (B) REAL EYE DIAGRAM

FIGURE 7.9. **(a)** Ideal high-speed digital signal with eye diagram (from [227]); **(b)** real oscilloscope-made eye diagram.

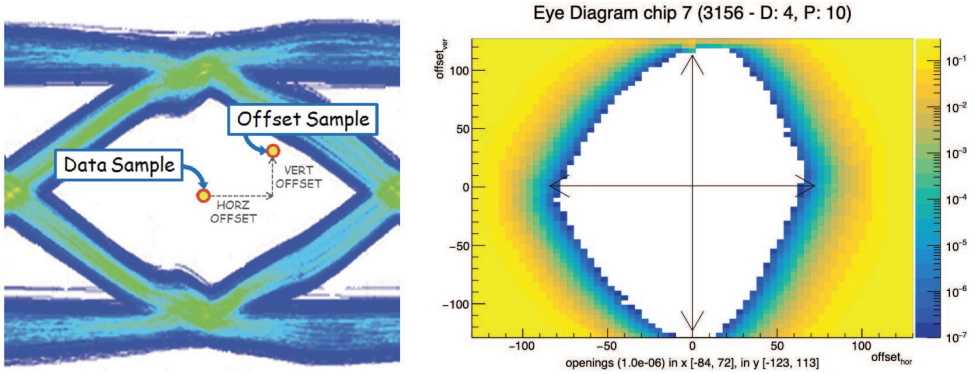

(A) OSCILLOSCOPE-MADE EYE DIAGRAM (B) MOSAIC-MADE EYE DIAGRAM

FIGURE 7.10. **(a)** Example showing, on an oscilloscope-made eye diagram, how are chosen the samples used by the MOSAIC board FPGA to build the statistical eye diagram (from [228]). **(b)** Example showing, an eyediagram done with MOSAIC algorithm (Ladder 3156 - chip 7).

In our case, the *Eye measurement scan* is performed by the MOSAIC board Xilinx FPGA [228], which can realize a *statistical* eye diagram.

Any eye scan functionality is based on the comparison between the Data Sample in the nominal eye center and the Offset Sample, at a programmable horizontal and vertical offset, from the nominal eye center, as shown in Figure 7.10a).

A bit error is defined as a mismatch between these two samples and the Bit Error Rate (BER) is defined as the bit errors ratio to the data-to-offset-sample comparisons total number : calculating BER at each point of an array of horizontal and vertical offsets provides the data for a statistical eye.

Based on the documentation of the MOSAIC board FPGA (Table 4-20 in [228]), it is possible to estimate the absolute horizontal time unit. It is 1/256 of the UI *i.e.* $1/(1.2 \times 10^9 \times 256) \approx 3.255\,\text{ps}$. Unfortunately, the FPGA literature does not provide sufficient information to identify the vertical axis's absolute unit[28].

Each chip is analyzed individually and the test lasts more or less 20 minutes for a ladder with three chips.

7.2.6.1 The Eye Measurement scan grades system

THE Eye diagram qualification system is different compared to the other tests. The vertical and the horizontal parameters, whose evaluation is based on the Bit Error Rate (BER), are the $X_{Opening}$ and $Y_{Opening}$ – which could be converted to a time and a voltage. The Eye Measurement scan grades are assigned on the basis of the measurement of both the X and the Y openings, evaluated in the same moment, where the algorithm chooses between the two opening results the one with the worst grade.

Possible grades for the X_{Opening} :

- If $X_{\text{Opening}} > 80$, the chip is Gold;
- if $80 \geq X_{\text{Opening}} > 60$, the chip is Silver;
- if $60 \geq X_{\text{Opening}} > 40$ is Bronze otherwise the chip is Red.

All the tested chips have a Gold X_{Opening}, so the final grade comes out of the Y_{Opening} evaluation.

[28] This is quite annoying, as we know the minimal size of the vertical opening (±70 mV for the up and down directions) requested by the electronic board – the Readout Unit – that will read the sensors during the real operation of the detector and that could be used as an easy criterion to veto a ladder with a too small eye on any sensor.

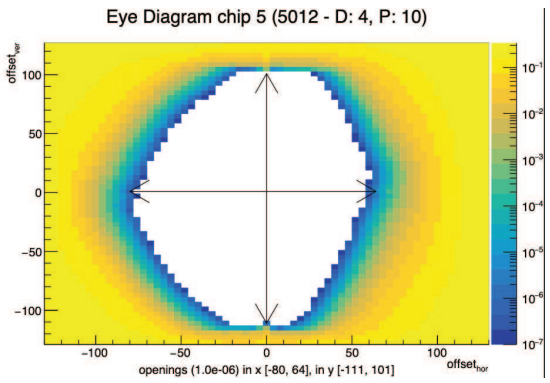

(A) GOLD EYE DIAGRAM

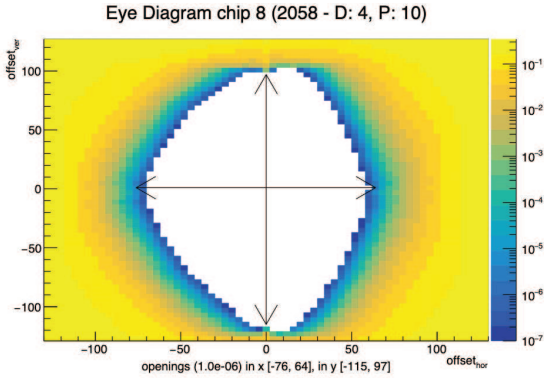

(B) SILVER EYE DIAGRAM

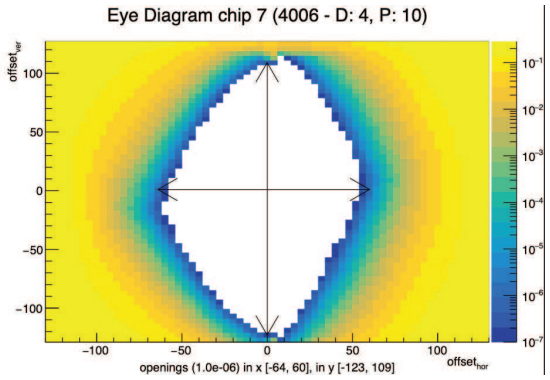

(C) BRONZE EYE DIAGRAM

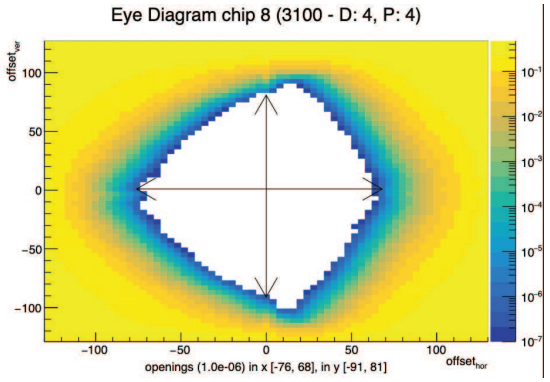

(D) RED EYE DIAGRAM

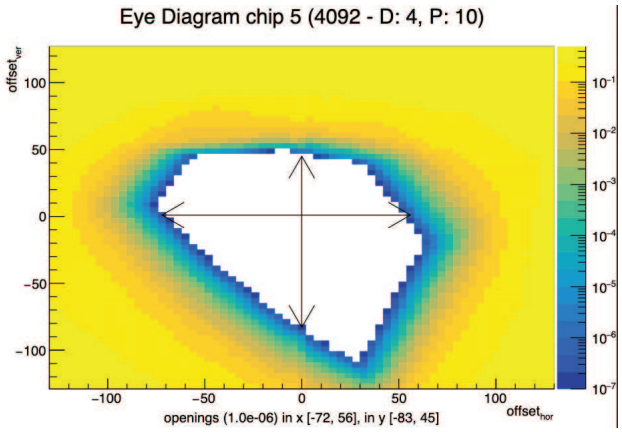

(E) RED EYE DIAGRAM

FIGURE 7.11. **(a)** Gold eye diagram: H0 D4 MD04_02 ladder 5012 chip 5; **(b)** Silver eye diagram: H0 D1 MD00–01_06 ladder 2058 chip 8.; **(c)** Bronze eye diagram: H0 D4 MD04_02 ladder 4006 chip 7; **(d)** Red eye diagram: H0 D0 MD00–01_01 ladder 3100 chip 8; **(e)** Red eye diagram: H0 D3 MD03_03 ladder 4092 chip 5.

Possible grades for the Y_{Opening} :

- If $Y_{\text{Opening}} > 230$, the chip is Gold;
- if $230 \geq Y_{\text{Opening}} > 200$, the chip is Silver;
- if $200 \geq Y_{\text{Opening}} > 170$ is Bronze otherwise the chip is Red.

Let's observe some examples, reported in Figure 7.11. Even if the Gold chip eye diagram (Figure 7.11a) has an asymmetrical shape, it is less tapered than the Silver one (Figure 7.11b). The more the eye diagram is closed, the more this tapered shape is visible, as Figures 7.11c and 7.11d show. The Bronze eye diagram is very close to the "cat eye" shape. Only two chips in the whole MFT detector were found to have a Red eye diagram. The first Red chip is shown in Figure 7.11d, tested with D4P4–CP8 configuration: its shape is more rectangular and less symmetrical than the others. Using the D4P10–CP10 configuration, its shape will resemble the others. The second one is shown in Figure 7.11e, tested with D4P10–CP10 configuration: this asymmetrical diamond shape is representative of a physical defect.

7.3 Some interesting results collected during the commissioning on the surface

THE 10 H-Ds composing the MFT detector have been assembled and installed together on the two half-MFT cones at CERN, and are listed below:

Bottom MFT – H0

- H-D 0: MD00–01_01
- H-D 1: MD00–01_06
- H-D 2: MD02_02
- H-D 3: MD03_03
- H-D 4: MD04_02

Top MFT – H1

- H-D 0: MD00–01_07
- H-D 1: MD00–01_04
- H-D 2: MD02_03
- H-D 3: MD03_01
- H-D 4: MD04_01

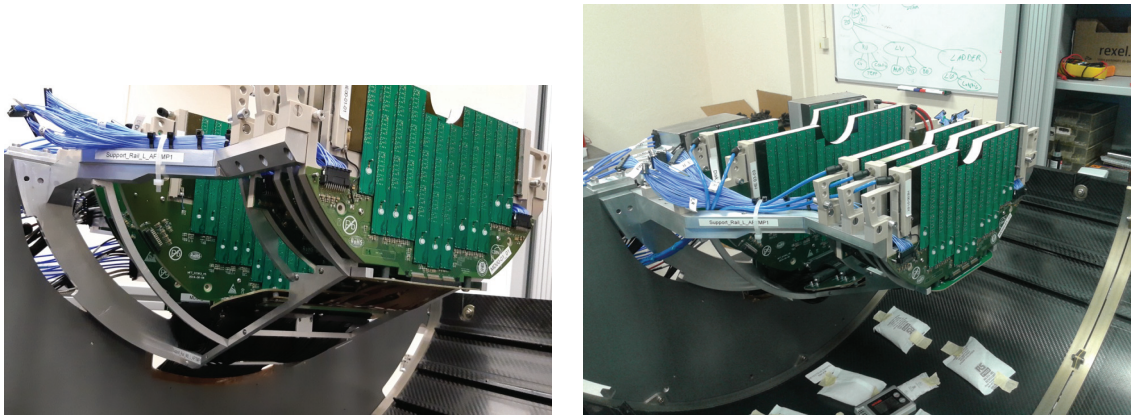

(A) BOTTOM MFT (B) TOP MFT

FIGURE 7.12. Pictures of the two half-cones assembled at CERN Building 581.

In what follows, the most important results from the commissioning, obtained during this Ph.D. work, are presented.

7.3.1 General overview of the results

EACH half-MFT cone is completely assembled with the gluing of 140 ladders: 16 ladders with 2 chips, 68 with 3 chips, 48 with 4 chips and 8 with 5 chips, for a total of 468 ALPIDE chips. During assembly operations, only 13 ladders were damaged on the whole MFT

detector, representing 4.64% of the chosen ladders. After gluing, they are submitted to the functional tests discussed in Section 7.2: FIFO, Digital, Threshold, Noise Occupancy and Eye Measurement scans.

FIFO, Digital, Threshold, Noise Occupancy scans results

Each chip qualification grade occurrence, resulting from the first four tests, is plotted in Figures 7.13a and 7.13b. Even if it is customary to give a single grade to the whole ladder based on the worst sensor, in these Figures each chip grade is taken into account with and without back-bias voltage use.

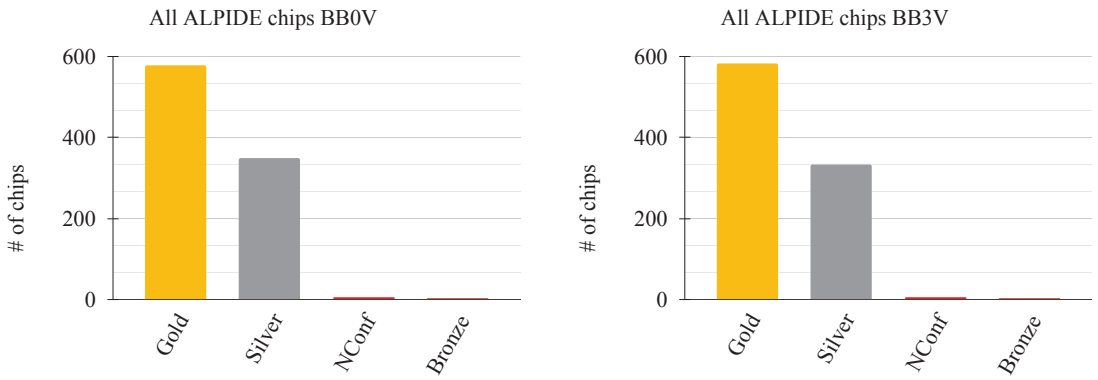

(A) Without V_{BB} (B) With V_{BB}

FIGURE 7.13. The population of chips for each qualification grade was obtained with the four tests (FIFO, Digital, Threshold and Noise scans) on the 10 H-Ds of the MFT. (*left :*)The results are obtained without back-bias voltage application. *right :* The results are obtained with back-bias voltage application.

All the results from the first four functional tests, corresponding to $V_{BB} = 0\,V$ and $V_{BB} = -3\,V$, are reported in Table 7.2.

One can see that, on Bottom MFT (H0), there is only 6 not-conformal failing the Read-back test, as described in Section 7.2.1. On Top MFT (H1), five chips are not-conformal, from two different ladders. Despite the presence of these defective chips, more than 99% of the active surface of the MFT detector is covered by the gold (~61%) and silver (~37%) sensors.

Eye Measurement scans results

Concerning the Eye Measurement scan, all tests are done without the reverse back-bias voltage applied to the sensors. Indeed, the Eye Measurement only involves the digital block of the ALPIDE and therefore is not sensitive to any change in the analog block.

Bottom MFT		
Qualification grades	$V_{BB} = 0V$	$V_{BB} = -3V$
Gold	314 chips (67.10%)	314 chips (67.10%)
Silver	152 chips (32.48%)	152 chips (32.48%)
Bronze	1 chip (0.21%)	1 chip (0.21%)
Non-Conformal	1 chip (0.21%)	1 chip (0.21%)
Top MFT		
Qualification grades	$V_{BB} = 0V$	$V_{BB} = -3V$
Gold	264 chips (56.76%)	269 chips (57.84%)
Silver	197 chips (41.73%)	192 chips (40.65%)
Bronze	2 chips (0.43%)	2 chips (0.43%)
Non-Conformal	5 chips (1.08%)	5 chips (1.08%)

TABLE 7.2. Results from the first four functional tests of the whole MFT, with and without back-bias voltage application.

The H-D MD00–01_01, chosen as H0 H-D 0, was tested with D4P4–CP8 parameters, *i.e.* with the same set used to test the ladders in their boxes and the remaining nine H-Ds were scanned with D4P10–CP10. As expected, the comparison between Figures 7.14a and 7.14b shows that the configuration D4P10–CP10 gives much better results as this set was specifically optimized to the hardware used in the test of the H-Ds, as explained in Section 7.2.6,. The H-D 0 has been retested, using the Readout Unit – the final board using the operations –, with this configuration to improve the quality of the high-speed data signals at the receiver, during the surface commissioning giving coherent results as the other H-Ds.

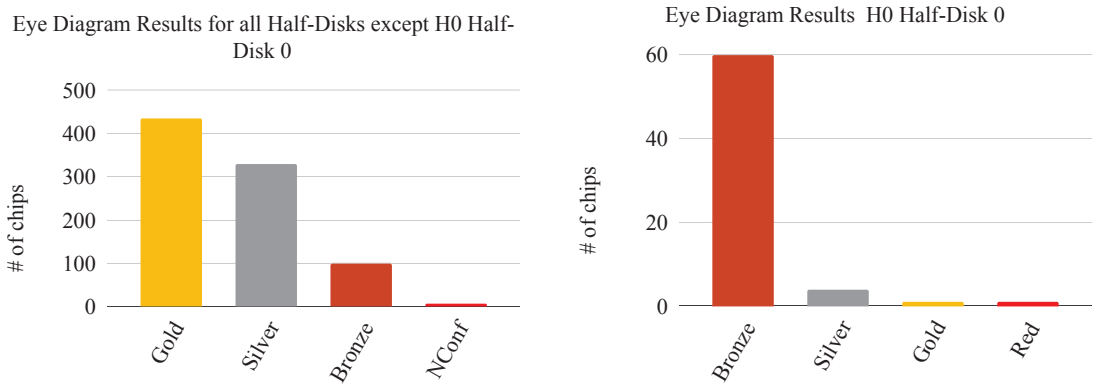

(A) Results with D4P10–CP10

(B) Results with D4P4–CP8

FIGURE 7.14. (*left :*) Population of chips for the whole MFT Eye Diagrams: results of all H-Ds, except H0 H-D 0, tested with parameters D4P10–CP10. *right :* Population of chips for the Bottom MFT Eye Diagrams: results of H-D 0 tested with parameters D4P4–CP8.

In Table 7.3, the chip number for each grade of the Eye Measurement scan is reported. Most chips glued are Gold (~45%) or Silver (~36%).

	Bottom MFT		**Top MFT**
Eye diagram grades	H0 H-D 0	Other H0 H-Ds	All H1 H-Ds
Gold	1 chip (1.51%)	184 chips (45.77%)	251 chips (53.63%)
Silver	4 chips (6.07%)	129 chips (32.09%)	201 chips (42.95%)
Bronze	60 chips (90.91%)	88 chips (21.64%)	11 chips (2.35%)
Red	1 chip (1.51%)	/	/
Non-Conformal	/	1 chip (0.25%)	5 chips (1.07%)

TABLE 7.3. Results of eye diagrams for all chips glued.

7.3.2 Digital scan results

TABLES 7.4 and 7.5 summarize the Digital scan results on the ALPIDE chips chosen for the MFT, in particular the number of chips with 0 bad pixels but also the number of those with one bad row, one bad column and two bad columns. These Tables show that the biggest contribution in the bad pixels comes from the dead pixels. The bad and stuck pixels represent only ~0.07% and ~0.05% of whole H1 and H0 surfaces, respectively. While the dead pixels are "intrinsically" masked, the others – the inefficient, noisy and stuck pixels – shall be configured to be masked during the acquisition. For this reason, they are all grouped as pixels to mask in Tables 7.4 and 7.5.

Digital scan H0		
	$V_{BB} = 0\,V$	$V_{BB} = -3\,V$
Chips with 0 bad pixel	250 (53.53%)	224 (47.97%)
Chips with 512 bad pixels (one bad row)	21 (4.50%)	20 (4.28%)
Chips with 1024 bad pixels (one bad column)	35 (7.49%)	34 (7.28%)
Chips with 2048 bad pixels (two bad columns)	5 (1.70%)	4 (0.86%)
Total number of stuck pixels per H-D	140	198
Total number of dead pixels per H-D	123 279	121 747
Total number of inefficient pixels per H-D	7 355	9 379
Total number of noisy pixels per H-D	19	12
Total number of pixels to mask	7 514 (0.0031%)	9 589 (0.0039%)

TABLE 7.4. Results corresponding to the front and back side of all Bottom MFT H-Ds for the Digital scan.

Digital scan H1		
	$V_{BB} = 0\,V$	$V_{BB} = -3\,V$
Chips with 0 bad pixel	210 (45.36%)	210 (45.36%)
Chips with 512 bad pixels (one bad row)	13 (2.81%)	16 (3.46%)
Chips with 1024 bad pixels (one bad column)	38 (8.21%)	36 (7.78%)
Chips with 2048 bad pixels (two bad columns)	3 (0.65%)	3 (0.65%)
Total number of stuck pixels per H-D	1 940	1 626
Total number of dead pixels per H-D	158 841	157 880
Total number of inefficient pixels per H-D	10 423	9 429
Total number of noisy pixels per H-D	542	540
Total number of pixels to mask	12 906 (0.0053%)	11 595 (0.0048%)

TABLE 7.5. Results corresponding to the front and back side of all Top MFT H-Ds for the Digital scan.

7.3.3 Threshold scan results

FOR what concerns the combined study of the (analog+digital) parts of the ALPIDE chips, we are showing here a small selection of the results obtained during this Ph.D. thesis,namely the ones corresponding to Bottom MFT (H0). Figures 7.15 and 7.16 show the behaviour of four variables relevant for the threshold scan: *Average Threshold, RMS Threshold, Average Noise* and *RMS Noise*, see Section 7.2.4.

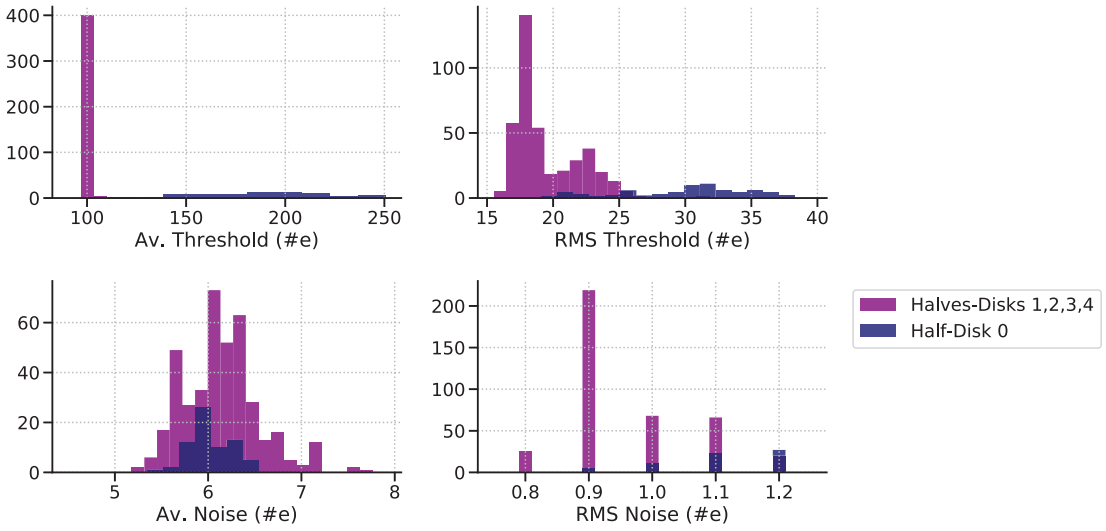

FIGURE 7.15. Results from H0 threshold scan without back bias applied: **top left**, average threshold distribution; **top right**, RMS Threshold one; **bottom left**, the Noise distribution and **bottom right**, the RMS Noise one.

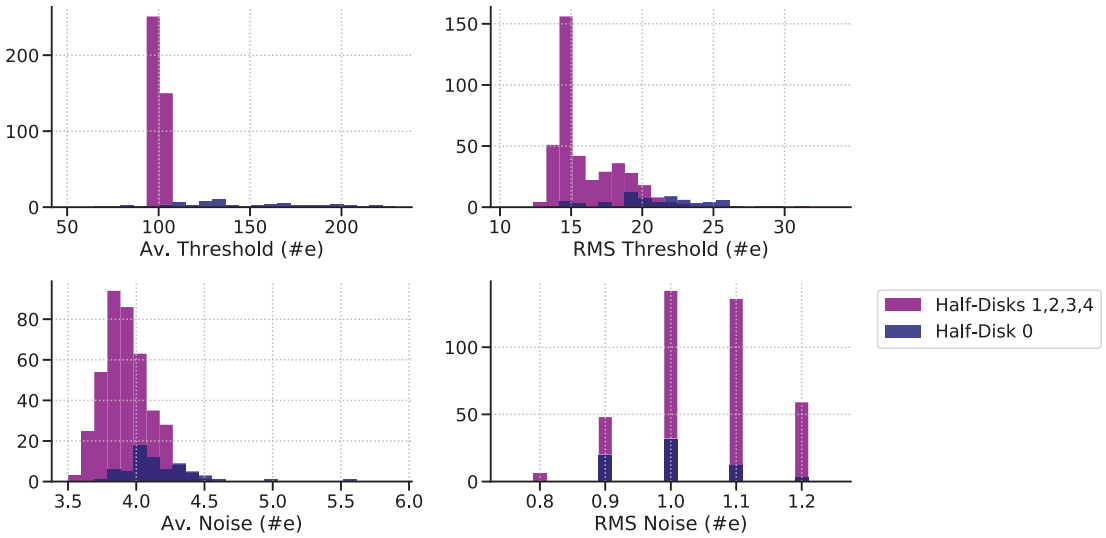

FIGURE 7.16. Results from H0 threshold scan with back bias applied: **top left**, average threshold distribution; **top right**, RMS Threshold one; **bottom left**, the Noise distribution and **bottom right**, the RMS Noise one.

The Threshold tuning procedure, explained in Section 7.2.4.3, was developed after the qualification of H-D 0 of H0. As one can see in the histograms (purple profile) in Figures 7.15 and 7.16, the Average Thresholds vary between 99.1 and 105.4 (±0.8) electrons for the H-D other than H0, thanks to the tuning of ITHR and VCASN parameters. However, for the 66 chips of H-D 0, plotted separately into Figures 7.15 and 7.16 as dark-blue histograms, the Average Threshold values vary between 121.4 and 249.7 (±31.6) electrons, because the H0 H-D 0 was not tested to ITHR and VCASN tuning.

	H0 H-D 0 $V_{BB} = 0$ V	**H0 H-Ds 1, 2, 3, 4** $V_{BB} = 0$ V
Av.(Min; Max) Threshold [#e]	188±32 (121;250)	101±1 (99;105)
Av.(Min; Max) Threshold RMS [#e]	30±5 (20;38)	19±2 (16;32)
Av.(Min; Max) Noise [#e]	6.0±0.2 (5.4;6.5)	6.1±0.4 (5.2;7.7)
Av.(Min; Max) Noise RMS [#e]	1.1±0.1 (0.9;1.6)	1±0.1(0.8;1.4)
VCASN (Min; Max) [#DAC]	50 (Std value)	53±2 (49;57)
ITHR (Min; Max) [#DAC]	51 (Std value)	53±1 (50;55)

TABLE 7.6. Results corresponding to the front and back side for Threshold scan of Bottom MFT without back-bias.

Finally, Figures 7.17 and 7.18 show the ITHR and VCASN behaviours after the tuning has been performed on all the H-Ds of H0. The distributions are centered around ~ 52 DACs for both ITHR and VCASN with $V_{BB} = 0$ V. They are around ~ 53 and ~ 102 ITHR

	H0 H-D 0 $V_{BB} = -3$V	**H0 H-Ds 1, 2, 3, 4** $V_{BB} = -3$V
Av.(Min; Max) Threshold [#e]	146±39 (68;228)	100±1 (99;102)
Av.(Min; Max) Threshold RMS [#e]	21±4 (14;29)	16±2 (13;31)
Av.(Min; Max) Noise [#e]	4.1±0.3 (3.7;5.6)	3.9±0.2 (3.5;4.5)
Av.(Min; Max) Noise RMS [#e]	1±0.1±(0.9;1.5)	1.1±0.1(0.8;1.4)
VCASN (Min; Max) [#DAC]	117 (Std value)	103±3 (97;111)
ITHR (Min; Max) [#DAC]	51 (Std value)	53±3 (48;62)

TABLE 7.7. Results corresponding to the front and back side for Threshold scan of Bottom MFT with back-bias.

and VCASN, respectively wihout and with the back-bias application ($V_{BB} = 3$V).

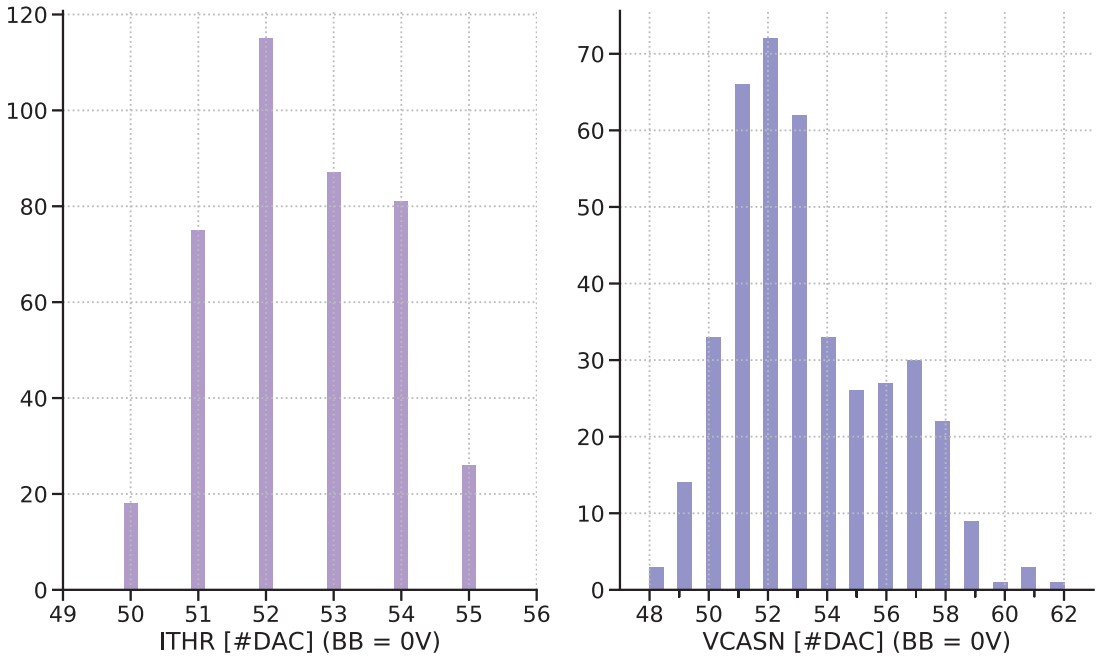

FIGURE 7.17. Distribution of (**left**) ITHR and (**right**) VCASN parameters without back-bias for H0 sensors – without H-D0. Both sides of each H-D are included (401 chips).

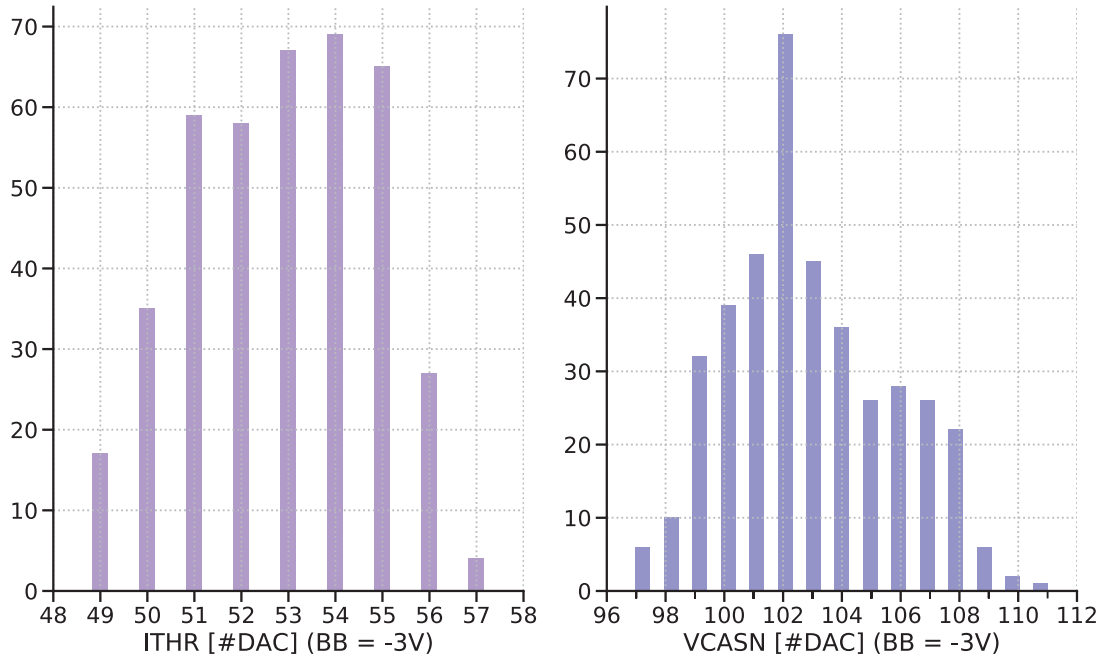

FIGURE 7.18. Distribution of (**left**) `ITHR` and (**right**) `VCASN` parameters with back-bias for H0 sensors – without H-D0. Both sides of each H-D are included (401 chips).

7.3.4 Noise Occupancy scan results

THE noise occupancy or fake-hit rate (O_{noise}) is measured by sending several triggers (N_{trg} fixed at 1×10^6) to the chip without providing any external input, as explained in Section 7.2.5. A pixel is considered noisy when it fires more than 10 times for 1×10^6 triggers. Since the fake-hit rate can be influenced by the threshold setting of the sensors, it is measured for sensors operating at a tuned threshold of 100 electrons. For the Noise scan, the results from Top MFT (H1) are reported.

Figure 7.19 shows that, with back-bias, the chips glued on the disks have a very low noise rate: 74.5% of chips with back-bias have a noise occupancy equal to zero for 1×10^6 triggers. The maximum fake-hit rate overall H1 H-Ds is equal to 2.95×10^{-11} evt^{-1} pixel^{-1} without the application of back-bias voltage. The value is reduced at 1.05×10^{-12} evt^{-1} pixel^{-1} with the back-bias voltage application. Tables 7.8 and 7.9 report some results on the Noise Occupancy scan.

Applying the back-bias voltage drastically reduces the noisy pixels' number, as shown in Figure 7.20. This is expected: the back-bias voltage increases the depleted volume around the collection diode, consequently improving the S/ B ratio. Without back-bias

$V_{BB} = 0$ V	H1 D0	H1 D1	H1 D2	H1 D3	H1 D4
Number noisy pixels/disk	300	736	700	1234	2105
Max fake-hit rate [10^{-11} evt^{-1} pixel^{-1}]	0.867	2.30	1.63	1.99	2.95
Chips < 51 noisy pixels (Gold)	66	60	80	117	131
Chips ≥ 51 noisy pixels (Silver)	0	1	2	1	5

TABLE 7.8. Noise Occupancy scan results for the Top MFT without back-bias voltage application.

$V_{BB} = -3$ V	H1 D0	H1 D1	H1 D2	H1 D3	H1 D4
Number noisy pixels/disk	25	15	45	42	40
Max fake-hit rate [10^{-13} evt^{-1} pixel^{-1}]	7.23	4.69	10.5	6.79	5.61
Chips < 51 noisy pixels (Gold)	66	61	82	118	136
Chips ≥51 noisy pixels (Silver)	0	0	0	0	0

TABLE 7.9. Noise Occupancy scan results for the top MFT with back-bias voltage application.

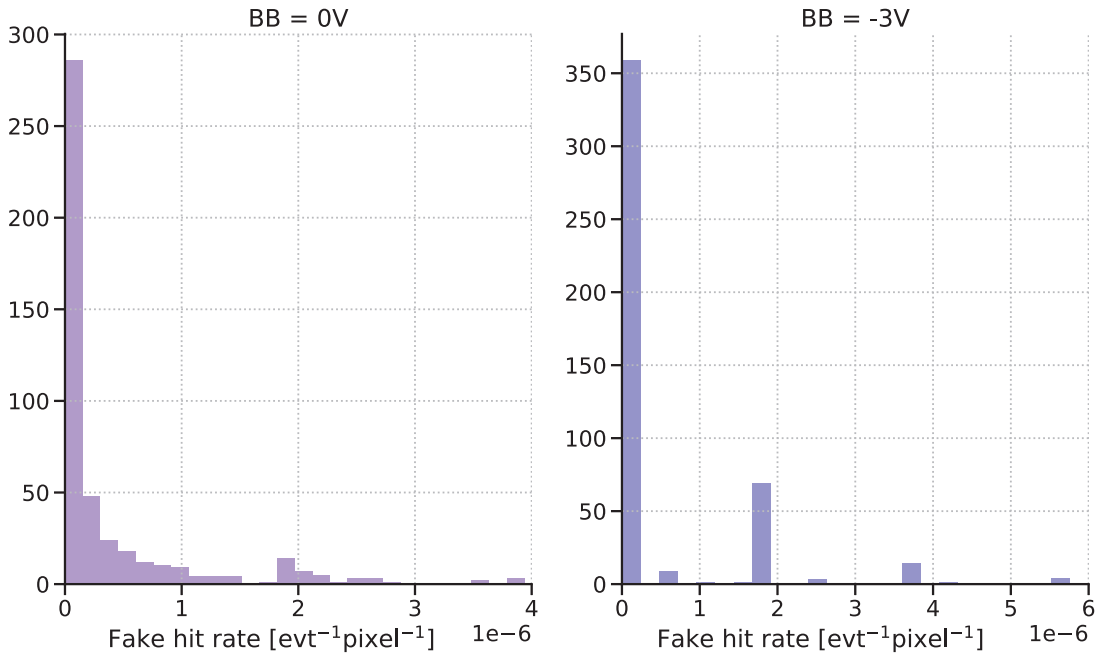

FIGURE 7.19. Noisy occupancy distribution per chip with and without back-bias for H1. 463 chips are plotted and 5 non-conformal chips are missing.

voltage application, the noisy pixels' largest number is 136 per chip. With back-bias, this number is reduced to 6. This is consistent with the Threshold scan results, presented in Section 7.3.3, where the Average Noise is lowered with the back-bias voltage

application.

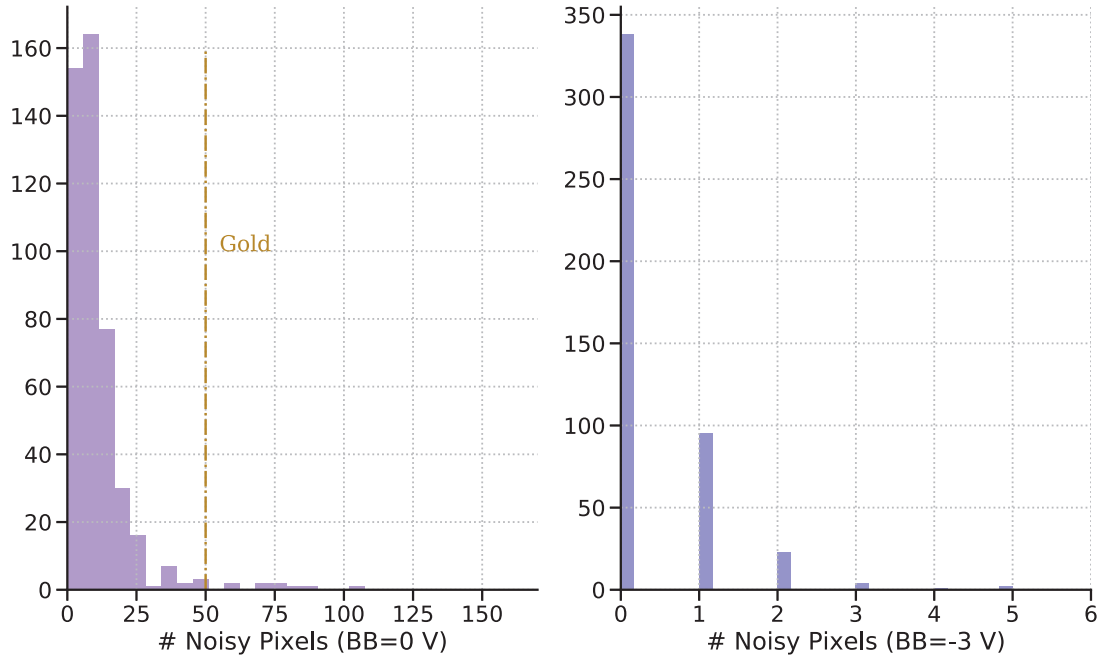

FIGURE 7.20. Number of noisy pixels per chip for H1. 463 chips are plotted, 5 non-conformal chips are missing. The gold dotted line divides gold and silver grades.

Figures 7.21 and 7.22 show how the noise occupancy for H1 decreases when the noisy pixels are masked. In these fake-hit rate distributions, the noisy pixels are classified starting from the noisiest ones, *i.e.* the ones that respond to almost every trigger (> 99% of the triggers) down to the quietest pixels (only a single response out of all the triggers sent). The noisy pixels number considered in these plots is larger than the quantities shown earlier in Tables 7.8 and 7.9 since in Figures 7.22 and 7.21 all the "hot" pixels are considered, even those that responded only once during the triggering time.

If it is decided to run the MFT detector at a fake-hit rate below 10^{-10} evt^{-1} pixel^{-1} (*i.e.* much lower than the design requirement for the per sensor noise occupancy), this appears to be easily feasible with the back-bias voltage application. Figure 7.21 shows that 120 pixels out of 2.4×10^8 pixels present on the 463 chips of the Top MFT (H1) send hits during almost all the triggering time, and 19 other pixels respond between 10% and 99% to the triggers. If these 139 pixels – that constitute only the 5.73×10^{-5} % of all the pixels on this half-MFT – are masked, the noise occupancy will decrease by several orders of magnitude *i.e.* from 5.32×10^{-7} evt^{-1} pixel^{-1} to 1.1×10^{-10} evt^{-1} pixel^{-1}.

When the back-bias voltage is not applied, the situation is a bit different, as Figure 7.22 shows. Even if reaching a fake-hit rate below 10^{-10} evt^{-1} pixel^{-1} is still possible, the

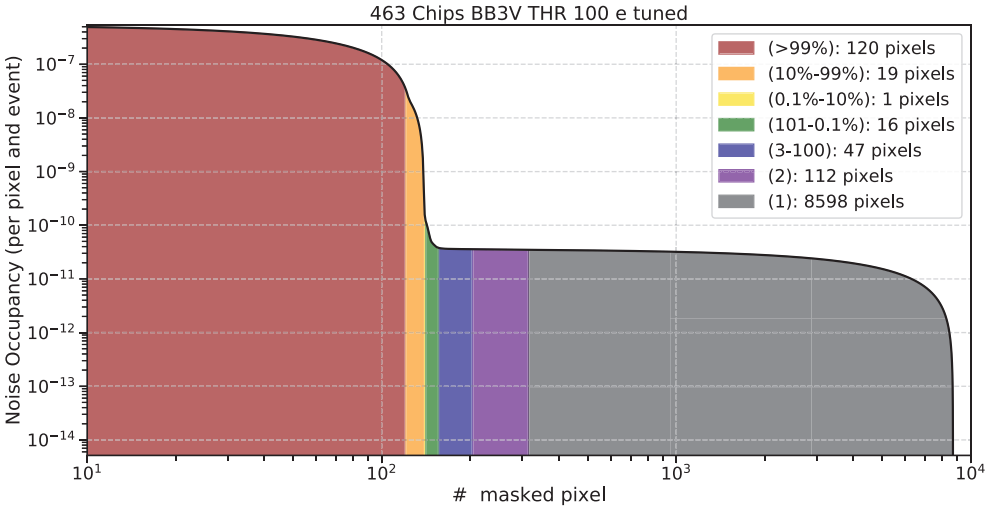

FIGURE 7.21. Evolution of the fake-hit rate for H1 with the back-bias applied ($V_{BB} = -3$V) as a function of the number of noisy pixels being masked, starting from the noisiest ones.

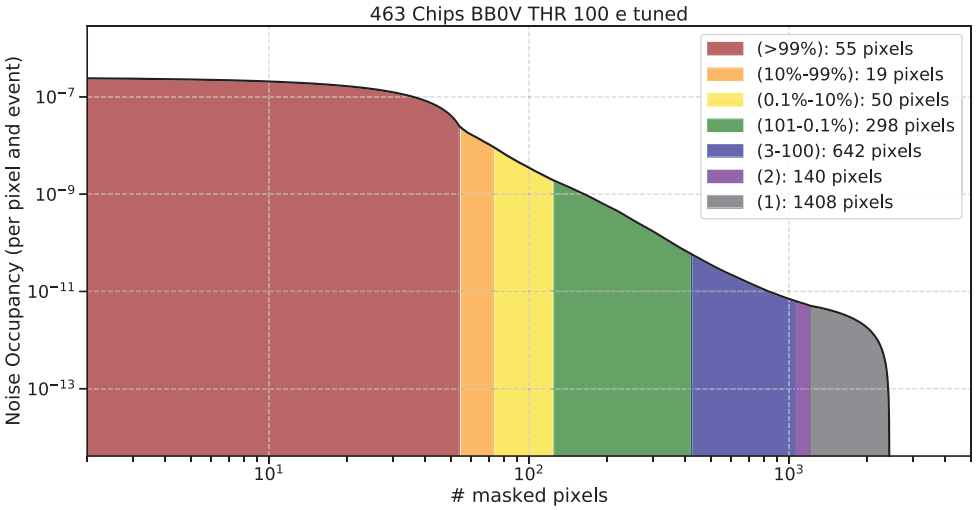

FIGURE 7.22. Evolution of the fake-hit rate for H1 without any back-bias applied ($V_{BB} = 0$V) as a function of the number of noisy pixels being masked, starting from the noisiest ones.

number of pixels to be masked is significantly higher: it would be necessary to mask between 400 to 450 pixels on the Top MFT (H1) – that corresponds to $\sim 1.74 \times 10^{-4}$ % of the total number of pixels – to decrease the noise occupancy down to the target value.

7.4 Conclusions and perspectives

THE results obtained with the MOSAIC board tests were presented in the previous Section 7.3 for the two half-MFT. The functioning quality of the ALPIDE sensors' digital and analog parts was studied in detail.

Considering the results obtained in this Ph.D. work, it is fair to say that the MFT detector is a "gold detector with silver areas". Only 3 chips have been classified as bronze and 6 chips show problems on the slow control lines. As much as 99% of the pixels' surface is operational: this implies that there are good chances that the detector will fulfil the design goals providing precision measurements for study of secondary vertices in the forward rapidity region, as described in Section 6.6.1. During the period from June to December 2020, some spare H-Ds have also been produced.

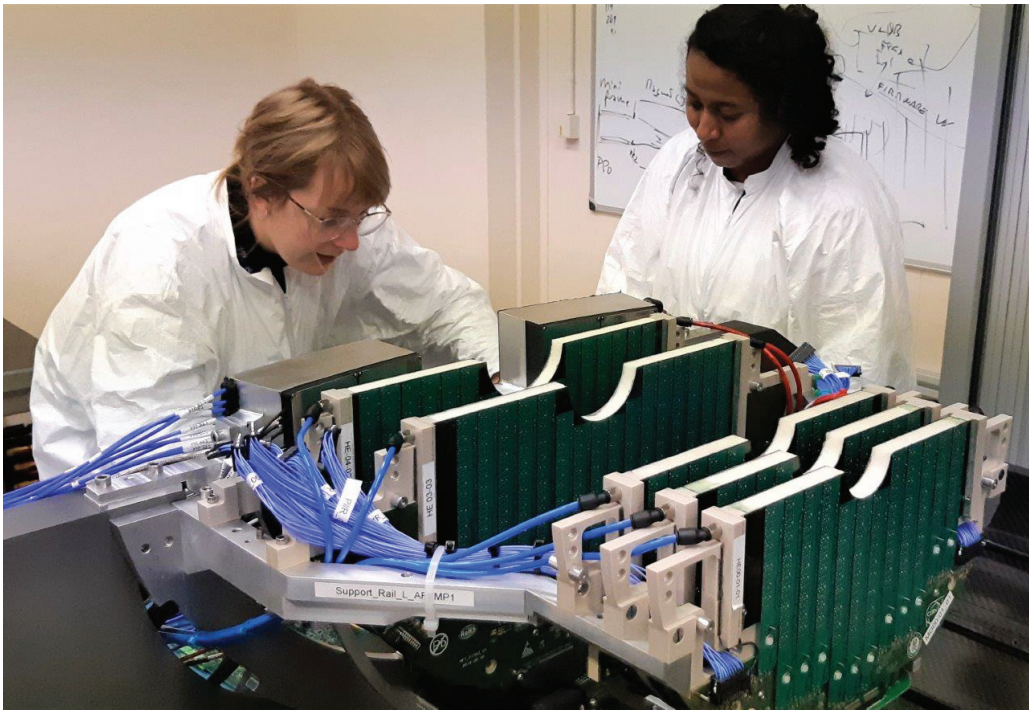

FIGURE 7.23. Picture of Andry Rakotozafindrabe, CEA permanent researcher, and myself, during the surface commissioning at CERN, in February 2020.

As for the bad pixels present on conformal chips, only ~0.007% of them will have to be masked. This small percentage implies that the number of inefficient, noisy or stuck pixels is negligible over the whole detector. For the eye diagram, the results obtained with the MOSAIC using the D4P10–CP10 parameters are promising: in most cases the signal is excellent. Using the final readout chain with the Readout-Unit boards, it will be

possible to look for a new set of these parameters to further improve the eye-opening, especially for the chips with the most closed eyes, to achieve the best possible data signal transmission between the ALPIDE chips and the acquisition boards.

Thanks to the possibility of adjusting the values of `ITRH` and `VCASN` for each chip, it has been shown that the MFT detector can run with a nearly uniform threshold. The resulting noise and threshold values are also very satisfactory: with a threshold of 100 electrons, the noise never exceeds 10 electrons.

Following the successful return of the TPC, as cited in Section 6.3, inside the ALICE L3 magnet during the year 2020, the ALICE collaboration successfully installed the MFT detector in the experimental cavern. The two MFT barrels were hauled to the ALICE site and dropped into the 60 m-deep tunnel during the first week of December 2020 [229]. The detector was then precisely positioned to a hundredth of a millimetre within a carbon composite cage at the TPC's heart – a delicate and challenging task. This accomplishment is the culmination of more than five years of design, building and qualification testing by a dozen research institutions in Europe, Asia and South America.

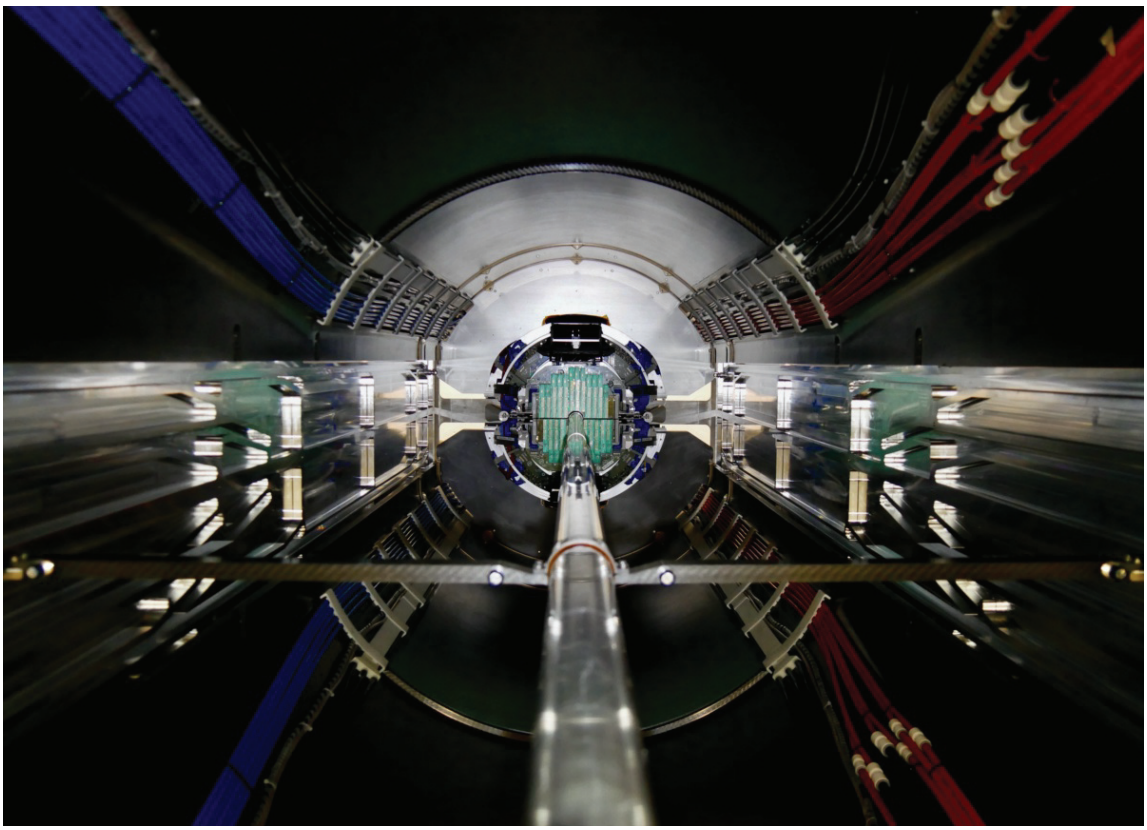

FIGURE 7.24. Inside the ALICE experiment, the MFT detector is in its final position around the beam pipe [202].

References

[215] INFN. *ALICE Pixel IT Barrel MOSAIC Test System* (cit. on p. 163).

[216] ALICE Collaboration. *MOSAIC board: Schematics, manual, and utilities on the MFT Twiki*. 2016 (cit. on p. 163).

[217] ALICE MFT Collaboration. *PSU prototype operation*. 2020 (cit. on p. 164).

[218] Migliorin, L. C. *Évaluation expérimentale de la performance du détecteur MFT développé pour les Runs 3 et 4 du LHC*. 2019 (cit. on p. 166).

[219] Arts, L. "ALPIDE Testing Software for the upgraded Inner Tracking System of the ALICE experiment". PhD thesis. 2016 (cit. on p. 166).

[220] ALICE ITS ALPIDE development team. *ALPIDE Operations Manual*. 2017 (cit. on pp. 168, 169, 171, 174).

[221] P. Karczmarczyk. *Characterization of the pALPIDE chip for the Muon Forward Tracker detector* (cit. on p. 171).

[222] L.K.J. Vandamme. "Noise as a diagnostic tool for quality and reliability of electronic devices". In: *IEEE Transactions on Electron Devices* 41.11 (1994), pp. 2176–2187. DOI: 10.1109/16.333839 (cit. on p. 172).

[223] T. Lazareva. "Analysis of test beam data of ALPIDE, the Monolithic Active Pixel Sensor (MAPS) for the ALICE ITS upgrade". In: 2017. URL: https://cds.cern.ch/record/2290779 (cit. on p. 172).

[224] G. Tambave et al. "Characterization of monolithic CMOS pixel sensor chip with ion beams for application in particle computed tomography". In: *Nucl. Instrum. Methods Phys. Res., A* 958 (2020), p. 162626. DOI: 10.1016/j.nima.2019.162626. URL: https://cds.cern.ch/record/2713712 (cit. on p. 172).

[225] J. W. van Hoorn. "Study and Development of a novel Silicon Pixel Detector for the Upgrade of the ALICE Inner Tracking System". TU Vienna, Oct. 2015 (cit. on p. 172).

[226] M. Suljic. "Study of Monolithic Active Pixel Sensors for the Upgrade of the ALICE Inner Tracking System". Presented 02 Feb 2018. Trieste University, 2018 (cit. on p. 173).

[227] ON Semiconductor. "Understanding data eye diagram methodology for analyzing high speed digital signals". In: *Application Note.[Online]* (2015) (cit. on p. 179).

[228] Xilinx. *7 Series FPGAs GTP Transceivers, User Guide*. 2016 (cit. on pp. 179, 180).

[229] CERN. *ALICE takes leap forward with major new installation*. 2021 (cit. on p. 195).

[230] S.M. Sze and K. K. Ng. *Physics of semiconductor devices*. John wiley & sons, 2006. ISBN: 9781119429135 (cit. on p. XV).

[231] Mikronierk. *ALICE Powered by ALICIA*. 2016 (cit. on p. XVIII).

[232] I. Collins. *Phase-Locked Loop (PLL) Fundamentals*. 2018 (cit. on p. XXIV).

[233] J. S. Pattavina. *Charge-Pump Phase-Locked Loop–A Tutorial–Part I*. 2011 (cit. on p. XXV).

Conclusions

THE present document reported on the research work accomplished during the three years of my Ph.D. thesis. The document is organised into two parts: the first focuses on the analysis of Ultra-Peripheral Collisions Pb–Pb data at $\sqrt{s_{\mathrm{NN}}} = 5.02$ TeV collected during Run 2 of the LHC in 2015 and 2018.

The analysis reported in the first part, corresponding to Chapter 1 to 5, focuses on the measurement of the polarisation of J/ψ mesons produced in incoherent processes in ultra-peripheral Pb-Pb collisions (UPC) at $\sqrt{s_{\mathrm{NN}}} = 5.02$ TeV, and the extraction of the corresponding polarisation parameters. In particular, Chapter 1 introduces the basic concepts of heavy-ion physics, while the second one shortly reviews the physics underlying the photoproduction of vector mesons such as the J/ψ. The third Chapter presents the ALICE experimental apparatus and its performances in Run 2, while chapter 4 focuses on the analysis strategy employed in the measurement of the polarisation of incoherently-produced J/ψ. Chapter 5, finally, shows the obtained results for the polarisation parameters, and details the estimation of the corresponding systematic uncertainties. The main goal of the measurement, performed in the dimuon channel exploiting the data collected by the ALICE Muon Spectrometer, is to achieve a better understanding of the mechanisms behind incoherent photoproducted J/ψ polarization . The analysis was conceived and developed in the ALICE group at IP2I, Lyon. It was reviewed in detail by the UPC Physics Working Group of the ALICE Collaboration, whose members are coming from various laboratories in Europe and North America, such as Czech Technical University in Prague, Joint Institute for Nuclear Research in Dubna or University of Kansas in Lawrence, Kansas. It is important to notice that this analysis is the first analysis on incoherent photoproducted J/ψ polarization what makes this analysis a novelty uniquely limited by statistics.

The second part of the manuscript, corresponding to Chapter 6 and 7, focused on the work accomplished for the characterisation and validation of the hardware components of the Muon Forward Tracker detector, a new vertex tracker covering the accep-

tance of the ALICE Muon Spectrometer, installed in the experimental cavern in December 2020, during the LHC Long Shutdown 2. A significant part of the characterisation activity was carried at IP2I-Lyon, with the support of the ALICE groups at CEA of Saclay, SUBATECH in Nantes and CERN. Thanks to the installation of the MFT in front of the absorber of the Muon Spectrometer, the detail of the vertex region can be accessed at forward rapidity, and in particular for the muon tracks reconstructed in the Muon Spectrometer. This will allow, starting of Run 3, for the statistical separation of prompt and displaced J/ψ in the dimuon channel, and to reject a significant fraction of the dimuon combinatorial background. This possibility, together with the significantly larger data sample expected to be collected in the LHC Runs 3 and 4, will result in smaller statistical and systematic uncertainties for several analyses, improving the significance of the results.

Acronyms

$p \times$ ***DCA*** Momentum times Distance of Closest Approach. 93

***n*MOS** n-channel Metal Oxide Semiconductor. 150

***p*MOS** p-channel Metal Oxide Semiconductor. 150

AD ALICE Diffractive. 72

ADC Analog-to-Digital Converter. 137

AGS Alternating Gradient Synchrotron. 13

ALICE A Large Ion Collider Experiment. 2, 62–64, 83, 134

ALICIA ALice Integrated Circuit Inspection and Assembly machine. XVIII, 154

ALPIDE ALice PIxel DEtector. 136, 148

ASIC Application-Specific Integrated Circuit. 137

ATLAS A Toroidal LHC ApparatuS. 2, 62, 63

AVDD Analog Voltage Drain-to-Drain. 164

BER Bit Error Rate. 180

BNL Brookhaven National Laboratory. 63

CB2 double Crystal-Ball. 96

CDF Collider Detector at Fermilab. 40

CMOS Complementary Metal-Oxide Semiconductor. 135, 149, 172

CMS Compact Muon Solenoid. 2, 62, 63

CP PLL Charge-Pump. XXII–XXIV, 185, 194

CPC Cathode Pad Chamber. 76

CS Collins-Soper. 87, 88

CTP Central Trigger Processor. 77, 140

D DTU Driver. XXII–XXIV, 185, 194

D-RORC DAQ ReadOut Receiver Cards. 77

DACs Digital to Analog Converters. 152

DAQ Data AcQuisition. 77, 135

DC-DC Direct Current to Direct Current. 164

DCA Distance of Closest Approach. 142–144

DCal Di-jet Calorimeter. 70

DDL Detector Data Link. 77

DIS Deep Inelastic Scattering. 10

DL Driver Logics. XXIV

DPRAM Dual Ported Random Access Memory. 168

DSF Department Silicon Facility. 153

DTU Data Transmission Unit. XXIII, XXIV, 169, 178

DVDD Digital Voltage Drain-to-Drain. XXI, 165

EmCal Electro Magnetic Calorimeter. 66, 70

EPN Event Processing Nodes. 140

FECs ront-End Cards. 137

FIFO First In, First Out. 167

FIT Fast Interaction Trigger. 135, 138

FLPs First Level Processors. 140

FMB Fake Mother-Board. 165

FMD Forward Multiplicity Detector. 71

FPC Flex Printed Circuit. 148, 153

FPGA Field-Programmable Gate Array. 179

FPN Fixed-Pattern Noise. 173

GDC Global Data Collector. 77

GEM Gas Electron Multiplier. 134, 137

GJ Gottfried-Jackson. 87, 88

GSI GSI Helmholtz Centre for Heavy Ion Research. 13

GUI Graphical User Interface. 162, 164

GVDM Generalized Vector meson Dominance Model. 95

H-D Half-Disk. 148, 154, 162

H-Ds Half-Disks. 146, 163

H0 Bottom MFT. 146, 184–187

H1 Top MFT. 146, 184, 186, 190, 192, 193

HERA Hadron-Electron Ring Accelerator. 37, 40

HIC-AT HIC Assembly Table. XVIII

HL-LHC High Luminosity Large Hadron Collider. 60

HLT High Level Trigger. 77

HMPID High Momentum Particle Identification. 66, 70

HX Helicity Frame. 87, 88, 94

IB Inner Barrel. 136

ICL Intermediate Card to Ladder. 163

ICM_F Intermediate Card for MOSAIC, version with Firefly connector. 162

IP Interaction Point. 66, 135

IP2I Institut de Physique des 2 Infinis. 155, 162

ITS Inner Tracker System. 66, 134, 135

ITS2 new Inner Tracking System. 135, 148

L0 Level 0. 78

L1 Level 1. 78

L2 Level 2. 78

LDC Local Data Concentrator. 77

LEIR Low Energy Ion Ring. 63

LEP Large Electron–Positron Collider. 60

LHC Large Hadron Collider. 2, 13, 29, 59, 134, 163

LHCb Large Hadron Collider beauty. 62–64

LHCf Large Hadron Collider forward. 63, 64

Linac3 Linear accelerator 3. 63

Linac4 Linear accelerator 4. 62

LM Level Minus. 78

LS2 Long Shutdown 2. 134, 161, 162

LS3 Long Shutdown 3. 135

LTU Local Trigger Unity. 77

MAPS Monolithic Active Pixel Sensor. 134, 135, 148, 149

MB Minimum Bias. 78

MC Monte Carlo. 95, 122, 145

MEB Multi Event Buffer. 152, 169

MFT Muon Forward Tracker. I, 134, 140, 161

MLs Middle Layers. 136

MOSAIC MOdular System for Acquisition Infrastructure and Control. 163

MS Muon Spectrometer. 93, 116, 134

MWPCs Multi-Wire Proportional Chambers. 76, 137

N^{3}LO next-to-NNLO. 8

NLO next-to-leading order. 8

NNLO next-to-next-to leading order. 8

O^2 Online-Offline. 135, 139

OB Outer Barrel. 136

OLs Outer Layers. 136

OS Opposite Sign. XXXII, 93, 126, 127

P DTU Pre-Emphasis. XXII–XXIV, 185, 194

PCBs Printed Circuit Boards. 149

PDFs Parton Distribution Functions. 10, 37

PDS Permanent Data Storage. 78

PE Priority Encoder. 153

PEs Priority Encoders. 169

PFD Phase-Frequency Detector. XXIV

PHENIX Pioneering High Energy Nuclear Interaction eXperiment. 22, 45, 63

PHOS PHOton Spectrometer. 66, 70

PLL Phase Lock Loop. XXII, XXIV

PMD Photon Multiplicity Detector. 71

Pol1/Pol2 ratio of two polynomials of first and second orders. 97, 114

Pol2×Exp product of a second order polynomial and an exponential. 97, 114

PPC Pre-Position Chuck. XVIII

PRBS PseudoRandom Binary Sequence. 178

PS Proton Synchroton. 61, 62

PSB Proton Synchrotron Booster. 62

PSU Power Supply Unit. XXI, 148, 164

QA Quality Assurance. 92

QCD Quantum-Chromo-Dynamics. 4, 5, 37

QED Quantum-Electro-Dynamics. 7, 83

QGP Quark-Gluon Plasma. 2, 5, 10, 65, G

res. NNLO NNLO matched with resummed next-to-leading logs. 8

RHIC Relativistic Heavy Ion Collider. 13, 63

RICH Ring Imaging CHerenkov. 70

RMS Root Mean Square. 173

RPCs Resistive Plate Chambers. 77

RRUs Region Readout Units. 153, 168

S/ B Signal-to-Background. 190

SCHC *s*-channel helicity conservation. 90

SDD Silicon Drift Detector. 66

SM Standard Model. 2

SPD Silicon Pixel Detector. 66, 128

SPS Super Proton Synchrotron. 13, 61, 62

SS Same Sign. XXXII, 125–127

SSD Silicon Strip Detector. 66

STAR Solenoidal Tracker At RHIC. 39, 63

TDS Transient Data Storage. 78

TOF Time Of Flight. 66, 69, 139

TOTEM TOTal Elastic and diffractive cross section Measurement. 63, 64

TPC Time Projection Chamber. 66, 68, 134, 137, 195

TRD Transition Radiation Detector. 66, 68, 78

TRF Trigger Response Function. 116

TSMC Taiwan Semiconductor Manufacturing Company. 137

UI User Interval. 180

UPC Ultra-Peripheral Collisions. I, 29, 30, 78, 83, 89, 139, 143, G

VCO Voltage Controlled Oscillator. XXIV

VMD Vector Meson Dominance. 35

VWG Variable Width Gaussian. 97, 112, 114

ZDC Zero Degree Calorimeter. 71, 73

ZN neutron ZDC. 73

ZP proton ZDC. 73

A Runs selection

A.1 2018q

295585, 295586, 295587, 295588, 295589, 295612, 295615, 295665, 295666, 295667, 295668, 295671, 295673, 295675, 295676, 295677, 295714, 295716, 295717, 295718, 295719, 295723, 295725, 295753, 295754, 295755, 295758, 295759, 295762, 295763, 295786, 295788, 295791, 295816, 295818, 295819, 295822, 295825, 295826, 295829, 295831, 295854, 295855, 295856, 295859, 295860, 295861, 295863, 295881, 295908, 295909, 295910, 295913, 295936, 295937, 295941, 295942, 295943, 295945, 295947, 296061, 296062, 296063, 296065, 296066, 296068, 296123, 296128, 296132, 296133, 296134, 296135, 296142, 296143, 296191, 296192, 296194, 296195, 296196, 296197, 296198, 296241, 296242, 296243, 296244, 296246, 296247, 296269, 296270, 296273, 296279, 296280, 296303, 296304, 296307, 296309, 296312, 296377, 296378, 296379, 296380, 296381, 296383, 296414, 296419, 296420, 296423, 296424, 296433, 296472, 296509, 296510, 296511, 296514, 296516, 296547, 296548, 296549, 296550, 296551, 296552, 296553, 296615, 296616, 296618, 296619, 296622, 296623.

A.2 2018r

296690, 296691, 296694, 296749, 296750, 296781, 296784, 296785, 296786, 296787, 296791, 296793, 296794, 296799, 296836, 296838, 296839, 296848, 296849, 296850, 296851, 296852, 296890, 296894, 296899, 296900, 296903, 296930, 296931, 296932, 296934, 296935, 296938, 296941, 296966, 296967, 296968, 296969, 296971, 296975, 296976, 296979, 297029, 297031, 297035, 297085, 297117, 297118, 297119, 297123, 297124, 297128, 297129, 297132, 297133, 297193, 297194, 297196, 297218, 297219, 297221, 297222, 297278, 297310, 297312, 297315, 297317, 297363, 297366, 297367, 297372, 297379, 297380, 297405, 297408, 297413, 297414, 297415, 297441, 297442, 297446, 297450, 297451, 297452, 297479, 297481, 297483, 297512, 297537, 297540, 297541, 297542, 297544, 297558, 297588, 297590, 297595.

A.3 2015o

244980, 244982, 244983, 245064, 245066, 245068, 245145, 245146, 245151, 245152, 245231, 245232, 245233, 245253, 245259, 245343, 245345, 245346, 245347, 245353, 245401, 245407, 245409, 245410, 245446, 245450, 245496, 245501, 245504, 245505, 245507, 245535, 245540, 245542, 245543, 245554, 245683, 245692, 245700, 245705, 245729, 245731, 245738, 245752, 245759, 245766, 245775, 245785, 245793, 245829, 245831, 245833, 245949, 245952, 245954, 245963, 245996, 246001, 246003, 246012, 246036, 246037, 246042, 246048, 246049, 246053, 246087, 246089, 246113, 246115, 246148, 246151, 246152, 246153, 246178, 246181, 246182, 246217, 246220, 246222, 246225, 246272, 246275, 246276, 246390, 246391, 246392, 246424, 246428, 246431, 246433, 246434, 246487, 246488, 246493, 246495, 246675, 246676, 246750, 246751, 246755, 246757, 246758, 246759, 246760, 246763, 246765, 246804, 246805, 246806, 246807, 246808, 246809, 246844, 246845, 246846, 246847, 246851, 246855, 246859, 246864, 246865, 246867, 246871, 246930, 246937, 246942, 246945, 246948, 246949, 246980, 246982, 246984, 246989, 246991, 246994.

B Fit functions

B.1 Crystal Ball

This function has a normalization factor N, two Gaussian core parameters ($\overline{x}$ and σ) and four tail parameters (α_{low}, n_{low}, α_{high} and n_{high}). It is defined as

$$f(x) = N \cdot \begin{cases} \exp\left\{\left(\dfrac{-(x-\overline{x})^2}{2\sigma^2}\right)\right\} & \text{if } -\alpha_{\text{low}} \geq \dfrac{x-\overline{x}}{\sigma} \geq \alpha_{\text{high}} \\ A \cdot \left(B - \dfrac{x-\overline{x}}{\sigma}\right)^{-n_{\text{low}}} & \text{if } \dfrac{x-\overline{x}}{\sigma} \leq -\alpha_{\text{low}} \\ C \cdot \left(D + \dfrac{x-\overline{x}}{\sigma}\right)^{-n_{\text{high}}} & \text{if } \dfrac{x-\overline{x}}{\sigma} \geq -\alpha_{\text{high}} \end{cases}$$

with

$$\begin{cases} A = \left(\dfrac{n_{\text{low}}}{|\alpha_{\text{low}}|}\right)^{n_{\text{low}}} \cdot \exp\left(\dfrac{-|\alpha_{\text{low}}|^2}{2}\right) \quad , \quad B = \dfrac{n_{\text{low}}}{|\alpha_{\text{low}}|} - |\alpha_{\text{low}}| \\ C = \left(\dfrac{n_{\text{high}}}{|\alpha_{\text{high}}|}\right)^{n_{\text{high}}} \cdot \exp\left(\dfrac{-|\alpha_{\text{high}}|^2}{2}\right) \quad , \quad D = \dfrac{n_{\text{high}}}{|\alpha_{\text{high}}|} - |\alpha_{\text{high}}| \end{cases}$$

B.2 Variable Width Gaussian (VWG) function

This function has a normalization factor N, and four parameters ($\overline{x}$, α, β, γ) and it is defined as

$$f(x) = N \cdot \exp\left(\frac{-(x-\overline{x})^2}{2\sigma^2}\right) \quad \text{where } \sigma = \alpha + \beta\left(\frac{x-\overline{x}}{\overline{x}}\right) + \gamma\left(\frac{x-\overline{x}}{\overline{x}}\right)^2$$

B.3 Ratio Pol1/Pol2 function

This function is a ratio between two polynomials, with a normalization factor N and three parameters ($p1$, $p2$, $p3$) and it is defined as

$$f(x) = N \cdot \frac{(1 + p1 \cdot x)}{(1 + p2 \cdot x + p3 \cdot x^2)}$$

B.4 Pol2×Exp function

This function has a normalization factor N and three parameters ($p1$, $p2$, $p3$) and it is defined as

$$f(x) = \begin{cases} N \cdot \exp(p1 \cdot x) \cdot (1 + p2 \cdot (x - x_{ch})^2 + p3 \cdot (x - x_{ch})^3) & \text{if } x \leq x_{ch}; \\ N \cdot \exp(p1 \cdot x) & \text{if } x > x_{ch}; \end{cases}$$

with $x_{ch} = 4.0\,\mathrm{GeV/c^2}$.

C Raw number of J/ψ in p_{T} intervals for $2.5 < y < 4$

p_{T} (GeV/c)	$<N_{\mathrm{raw}}^{\mathrm{J}/\psi}>\pm$ stat.$\pm$ syst.
0.0 – 0.3	1731 ±59 ±77
0.3 – 1.0	14788 ±186 ±574
0.0 – 1.0	16519 ±195 ±579
1.0 – 2.0	29693 ±262 ±927
2.0 – 3.0	22189 ±215 ±591
3.0 – 4.0	13985 ±165 ±367
4.0 – 5.0	8110 ±120 ±207
5.0 – 6.0	4711 ±87 ±111
6.0 – 7.0	2730 ±67 ±61
7.0 – 8.0	1479 ±50 ±37
8.0 – 9.0	841 ±37 ±16
9.0 – 10.0	510 ±30 ±12
10.0 – 11.0	294 ±21 ±6
11.0 – 12.0	183 ±19 ±8
10.0 – 12.0	477 ±28 ±10
12.0 – 15.0	261 ±21 ±6
15.0 – 20.0	82 ±12 ±2
4.0 – 12.0	18808 ±186 ±526
0.0 – 12.0 (direct fit)	101136 ±459 ±2936
0.0 – 12.0 (sum of p_{T} bins)	101244 ±461 ±1319
0.0 – 20.0 (direct fit)	101285 ±452 ±3012
0.0 – 20.0 (sum of p_{T} bins)	101587 ±461 ±1319

TABLE C.1. Raw number of J/ψ in some p_{T} intervals observed in an analysis of pp collisions, from [171].

D ALPIDE technology addendum

D.1 Reverse bias technology

ELECTRONS have just discrete energy levels, unlike other particles. The atomic layers of solid matter combine to form energy bands when they are cold. According to Figure D.1, the conduction and valence bands in metals are overlapping, however, in insulators and semiconductors, these levels are separated by an energy gap (*band gap*).

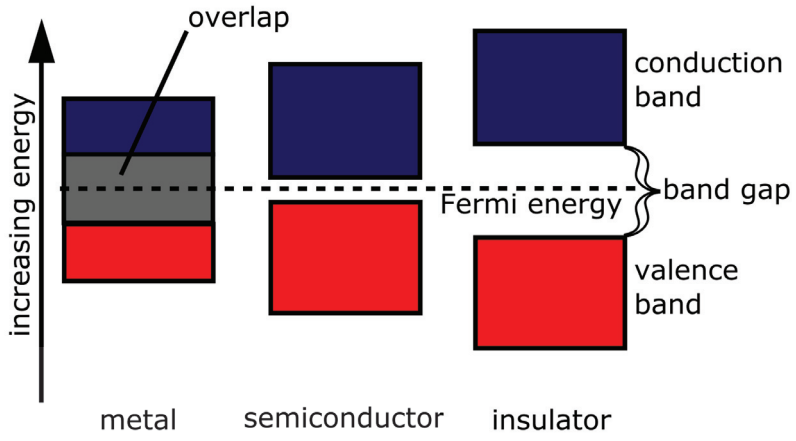

FIGURE D.1. The valence and conduction bands of insulators, metals and semiconductors are shown in this figure. The Fermi energy E_f is the designation given to the electron orbital with the greatest energy filled at absolute zero temperature.

This split created in the gap band is much more pronounced in insulators. Because of the tiny band gap present in semiconductors such as silicon [230], electrons already inhabit the conduction band at room temperature and electrons from the conduction band may recombine with holes when the temperature is raised. To achieve a thermal equilibrium between excitation and recombination, the charged carrier concentration

($n_e = n_h = n_i$[1]) can be expressed by the following formula :

$$n_i = \sqrt{N_c \cdot N_v} \cdot \exp\left\{\left(-\frac{E_g}{2kT}\right)\right\} \propto T^{\frac{3}{2}} \cdot \exp\left\{\left(-\frac{E_g}{2kT}\right)\right\},$$

where N_c and N_v are the effective density states as the conduction and valence bands edge, k the Boltzmann constant, E_g the gap energy and T the temperature.

When an $n-p$ junction is produced, in Fermi levels a carries surplus is created establishing a thermal equilibrium. The stable space charge area, also known as the *depletion zone*, is free of charge carriers. Electrons and holes are replenished into the depletion zone by applying an external voltage V while connecting the cathode and anode to p and n, respectively, causing a forward bias phenomenon. If one wants to operate the inverse operation, the reverse bias technology is obtained. In Table D.1, the most important differences between the forward and the reverse bias are reported.

Forward bias	Reverse bias
The depletion zone is very thin.	The depletion zone is thick.
$p-n$ junction offers very low resistance.	$p-n$ junction offers very high resistance.
An ideal diode has zero resistance.	An ideal diode has infinite resistance.
The cathode is connected to p-side of a $p-n$ junction and the anode with the n.	The cathode is connected to n-side of a $p-n$ junction and the anode with the p.

TABLE D.1. Difference between forward bias and reverse bias of semiconductor diode.

Notice that ALPIDE chips work with the application of a reverse bias, whose technology is depicted in Figure D.2.

When an external voltage V is applied with the anode connected to p and the cathode connected to n, electrons and holes are recreated becoming the depletion zone more compact. The potential barrier decreases in size by a few electron volts, making diffusion across the junction faster.

The current flowing through the connection dramatically rises. Thus, with $p-n$ junction reverse bias direction, the semiconductor detectors perform much better than a radiation detector. Charged particles that pass through the epitaxial layer produce electron-hole pairs as they go through many scattering processes in the material.

[1] n_e defines the number of electrons produced, n_h the number of holes and n_i the number of either holes or electrons.

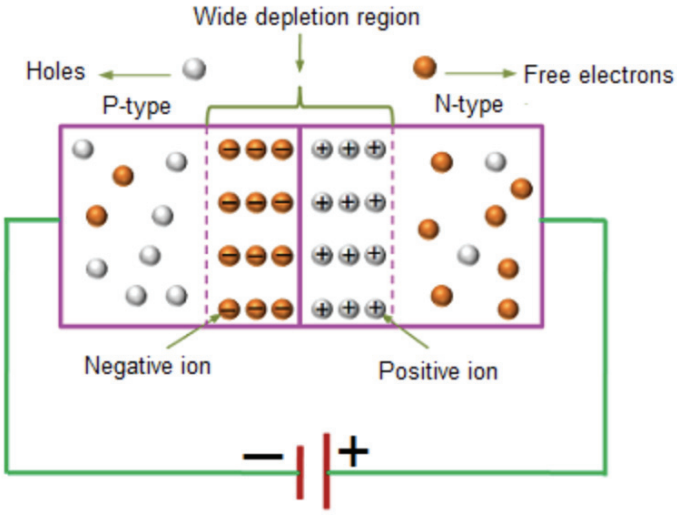

FIGURE D.2. Schematic of the reverse bias.

In the case of charged particles that are heaver than the electron, the Bethe-Bloch[2] formula is used to predict how much energy they lose on average.

To characterize the ALPIDE chips' quality, qualification tests are conducted with two alternative back-bias configurations: V_{BB} = 0 V and V_{BB} = – 3 V and their results will be presented in Chapter 7.

[2]The relativistic version of the formula is $-\frac{dE}{dx} = \frac{4\pi}{m_e \cdot c^2} \cdot \frac{n_z^2}{\beta^2} \cdot \left(\frac{e^2}{4\pi\epsilon_0}\right) \cdot \left[\ln\left(\frac{2m_e \cdot c^2\beta^2}{I \cdot (1-\beta^2)}\right) - \beta^2\right]$, where c is the speed of light and ϵ_0 the vacuum permittivity, $\beta = \frac{v}{c}$, e and m_e the electron charge and rest mass respectively.

E Ladder production

E.1 ALICIA and its characteristics

HERE the main characteristics of ALice Integrated Circuit Inspection and Assembly machine (ALICIA) and its components are reported. In Figure 6.13, one can observe all the components and their position.

- A high-resolution vision system was employed to determine the placement of the chips. The vision system determined the location of markings on the chips and on the two vacuum chucks that hold them:
  1. a Pre-Position Chuck (PPC) for testing and initial alignment of chips;
  2. a HIC Assembly Table (HIC-AT) for final ladder assembly [231].
- A vacuum gripper has been added to manipulate the chips.
- This three-axis high precision movement frame was called the Chip Handler and it included the vision system, the gripper and the laser system.
- A tray containing several chips was placed into the machine. Chips were removed from the tray and put on the PPC with the assistance of the gripper. The orientation of the chip was measured here and the quality of the chip was evaluated by the vision system.
- Following that, chips of the good standard were put on the HIC-AT with the help of the gripper. Chips of lower quality were discarded and put back into the tray of chips.

- Finally, sensors were glued to FPC using a non-conductive adhesive to complete the assembly.

F A example of a Half-Disk face divided in four zones

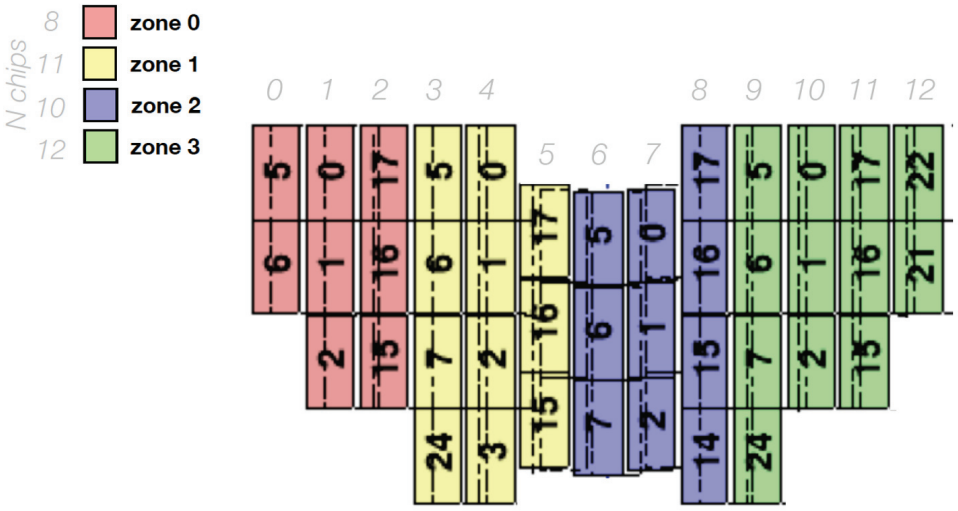

FIGURE F.1. Example of a H-D 2 front face. There are four zones and each is indicated with a color. Both zones and ladders are enumerated starting with 0, from left to right. The number written on the chips is the chip name chosen on the hardware side. The front face is the face closest to the IP.

G Possible issues during the Digital scan and their causes

DURING the Digital scan, an issues number, which can interfere with the extraction of individual pixel, responses or the complete chip response might arise.

The latch mechanism, contained in each in-pixel digital functional block, can be defective and when this happens the pixel will be never latched and it is called a “stuck” pixel.

While **PE errors** are rare, they can create spurious double-column addresses, not correlated to the real addresses, making it impossible to determine their true locations on the matrix. These errors might be caused by faults in the chip digital circuitry, that have been spread across the matrix.

At the other end of the high-speed data link, **8b10b errors**[1] can arise preventing us to extract the responding pixels coordinates which were carried in this corrupted part. They are frequently a symptom that the chip is not being used in the best possible way to ensure reliable data transmission to the MOSAIC board. As a result, certain of its settings or operational conditions may need to be changed. Typically:

- The DVDD voltage, applied to the H-D PCB and down to the chip, should be extremely clean (low noise), highly stable and high enough for the chip DTU to operate properly. In particular, a DVDD voltage value $\geq 1.83\,V$ allows to recover of the most fragile DTU, which would otherwise provoke 8b10b errors. As a logical result, the DVDD voltage, supplied by the PSU proto, must be set in such a manner, that it reaches at least the chip target value, taking into account voltage attenuation along the way.

[1] 8b10b errors are data encoding errors.

- The LHC clock periods number required to read the entire chip matrix can be enhanced to smooth out current consumption fluctuations, which can have an impact on the power stability. A similar effect may be seen, if all of the pixels are simultaneously asserted with the signals (pulsing, reset, and configuration) that are identical to the whole matrix. This has a impairing effect on the digital voltage stability. It is, therefore, preferable to distribute these global signals to smaller matrix parts and use several LHC clocks to cover the whole matrix.

- Similar to the previous point, the occupancy (*i.e.* the proportion of the pixel matrix that is pulsed concurrently) and pulse frequency should be regulated. The Digital scan, in particular, pulses **one row at a time**.

- The DTU internal parameters, detailed below, should be tuned. These must be empirically optimized, due to H-D-specific traits, namely the total length of the high-speed data cables. The test used to assess the impact of the chosen values of the DTU parameters will be detailed in the Section 7.2.6.

  (i) The DTU Driver (D) is used to improve the overall high-speed data transmission strength.

  (ii) The DTU Pre-Emphasis (P) allows to compensate for the attenuation of the rising – or falling – edge of the bits composing the high-speed data signal.

  (iii) Tuning the PLL Charge-Pump (CP) enables reduction of the jitter on the clock generated by the PLL inside the DTU and to serialize the data.

H The DTU structure

FIGURE H.1 shows the architecture of the DTU in ALPIDE chips, which are responsible for the data serialisation. It will also program the serial port rate at the highest possible value allowed by the ALPIDE (1.2 Gbit/s). It finally intervenes to improve the data off-chip signal transporting quality *via* the high-speed data links. Three parameters are involved in the same functional block, namely the PLL Charge-Pump (CP), the DTU Driver (D) and the DTU Pre-Emphasis (P). Therefore, they affect the eye diagram result influencing the jitter, the shape and the high-speed data signal strength sent off-chip.

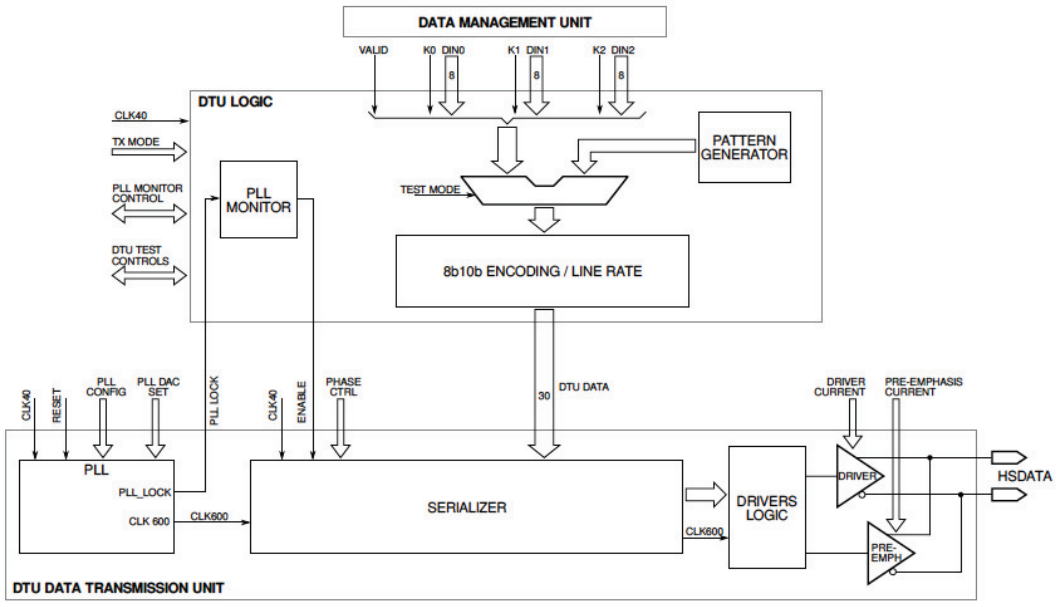

FIGURE H.1. Functional block diagram of the Data Transmission Unit and the related digital module DTU LOGIC (from [213]).

The Phase Lock Loop (PLL) system [232] is widely used in wireless frequency synthesis, clock data recovery and clock generation. On ALPIDE chips, it comprehends a Phase-Frequency Detector (PFD), a charge-pump component, a loop filter and a Voltage Controlled Oscillator (VCO). A PLL is a feedback system, as depicted in Figure H.2, locking the output clock phase to the input clock phase. The locked condition is satisfied when the input and output signals are at the same frequency *i.e.* they have no phase difference (or a constant phase difference) over time (steady state). Let's observe the different components :

- The input signal is the LHC 40 MHz clock (named "CLK 40" in Figure H.1).
- The feedback signal is made out of the output signal with the help of a frequency divider (labelled "1/n" in Figure H.2), in such a way that it has the same frequency as the input signal.
- The output signal is the 600 MHz clock needed by the DTU serializer (noted "CLK 600" on Figure H.1).
- The output phase is compared to the input phase in the PFD and, thanks to the Voltage Controlled Oscillator (VCO), the output frequency will be proportional to the input phase difference. The phase difference between the input signal and the feedback signal is translated in two control signals used to steer current into or out of a capacitor causing the voltage across the capacitor to increase or decrease.

In each cycle, the charge delivered is dependent on the phase difference and the addition of CP[1] between the PFD and loop-filter, as shown in Figure H.2, can convert the voltage fluctuation in the phase detector to the corresponding current signal thereby reducing the static error. Therefore, an optimized value of the CP enables to reduce of the jitter on the clock generated by the PLL inside the DTU and is used to serialize the data before it is shipped off-chip.

The high-frequency clock generated at the PLL stage is used by the serializer to put the data into its final format, as proved in Figure H.1. Before sending this data stream off-chip, it is passed to the Driver Logics (DL). It controls two operational amplifiers, where two currents called D and P currents shape the high-speed data signal. D can be used to enhance the high-speed data signal global strength. P allows to compensate for the

[1] In the charge-pump system, as shown in Figure H.2, one source is connected to the positive supply rail while the another to the negative supply rail. The sources are separated by two switches – S_1 and S_2 respectively – that cannot work simultaneously. When U is high and D is low then, S_1 is ON and S_2 is OFF. This causes current to flow out of the pump and into the loop filter. When U is low and D is high then S_1 is OFF and S_2 is ON which causes current to flow out of the loop filter and into the pump.

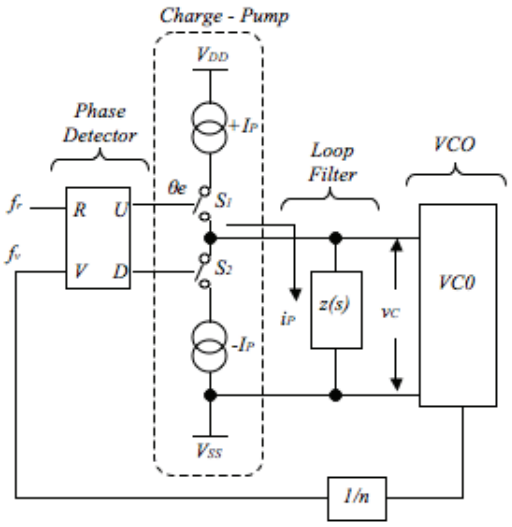

FIGURE H.2. The basic circuit of PLL with CP component (from [233]).

foreseen attenuation of the rising – or falling – edge of the bits during its transmission along the path to the MOSAIC board.

During the functional tests on H-Ds two parameter sets have been used:

(i) D = 4, P = 4 and CP = 8;

(ii) D = 4, P = 10 and CP = 10.

The first set was used in the early qualification days. When too many bad eyes were found, it was decided to revise it. The set D4P10–CP10 gives better results regarding the current configuration of the readout chain, as described in Section 7.1.2, in particular regarding the number of connections[2] involved between the sensors and the MOSAIC board and the total length of the high-speed data cables.

[2]Each additional connection is expected to degrade the quality of the transmitted signal.

List of Figures

List of Tables